

Advances in Sustainability Science and Technology

V. Bindhu

João Manuel R. S. Tavares

Joy long-Zong Chen *Editors*

Proceedings of Fifth International Conference on Inventive Material Science Applications

ICIMA 2022



 Springer

Advances in Sustainability Science and Technology

Series Editors

Robert J. Howlett, Bournemouth University and KES International,
Shoreham-by-Sea, UK

John Littlewood, School of Art & Design, Cardiff Metropolitan University, Cardiff,
UK

Lakhmi C. Jain, KES International, Shoreham-by-Sea, UK

The book series aims at bringing together valuable and novel scientific contributions that address the critical issues of renewable energy, sustainable building, sustainable manufacturing, and other sustainability science and technology topics that have an impact in this diverse and fast-changing research community in academia and industry.

The areas to be covered are

- Climate change and mitigation, atmospheric carbon reduction, global warming
- Sustainability science, sustainability technologies
- Sustainable building technologies
- Intelligent buildings
- Sustainable energy generation
- Combined heat and power and district heating systems
- Control and optimization of renewable energy systems
- Smart grids and micro grids, local energy markets
- Smart cities, smart buildings, smart districts, smart countryside
- Energy and environmental assessment in buildings and cities
- Sustainable design, innovation and services
- Sustainable manufacturing processes and technology
- Sustainable manufacturing systems and enterprises
- Decision support for sustainability
- Micro/nanomachining, microelectromechanical machines (MEMS)
- Sustainable transport, smart vehicles and smart roads
- Information technology and artificial intelligence applied to sustainability
- Big data and data analytics applied to sustainability
- Sustainable food production, sustainable horticulture and agriculture
- Sustainability of air, water and other natural resources
- Sustainability policy, shaping the future, the triple bottom line, the circular economy

High quality content is an essential feature for all book proposals accepted for the series. It is expected that editors of all accepted volumes will ensure that contributions are subjected to an appropriate level of reviewing process and adhere to KES quality principles.

The series will include monographs, edited volumes, and selected proceedings.

V. Bindhu · João Manuel R. S. Tavares ·
Joy Iong-Zong Chen
Editors

Proceedings of Fifth International Conference on Inventive Material Science Applications

ICIMA 2022

 Springer

Editors

V. Bindhu
Department of Electronics
and Communication Engineering
PPG Institute of Technology
Coimbatore, India

João Manuel R. S. Tavares
Faculdade de Engenharia
Universidade do Porto
Porto, Portugal

Joy Iong-Zong Chen
Department of Electrical Engineering
Da-Yeh University
Changhua, Taiwan

ISSN 2662-6829

ISSN 2662-6837 (electronic)

Advances in Sustainability Science and Technology

ISBN 978-981-19-4303-4

ISBN 978-981-19-4304-1 (eBook)

<https://doi.org/10.1007/978-981-19-4304-1>

© The Editor(s) (if applicable) and The Author(s), under exclusive license to Springer Nature Singapore Pte Ltd. 2023

This work is subject to copyright. All rights are solely and exclusively licensed by the Publisher, whether the whole or part of the material is concerned, specifically the rights of translation, reprinting, reuse of illustrations, recitation, broadcasting, reproduction on microfilms or in any other physical way, and transmission or information storage and retrieval, electronic adaptation, computer software, or by similar or dissimilar methodology now known or hereafter developed.

The use of general descriptive names, registered names, trademarks, service marks, etc. in this publication does not imply, even in the absence of a specific statement, that such names are exempt from the relevant protective laws and regulations and therefore free for general use.

The publisher, the authors, and the editors are safe to assume that the advice and information in this book are believed to be true and accurate at the date of publication. Neither the publisher nor the authors or the editors give a warranty, expressed or implied, with respect to the material contained herein or for any errors or omissions that may have been made. The publisher remains neutral with regard to jurisdictional claims in published maps and institutional affiliations.

This Springer imprint is published by the registered company Springer Nature Singapore Pte Ltd.

The registered company address is: 152 Beach Road, #21-01/04 Gateway East, Singapore 189721, Singapore

The conference is dedicated to the outstanding reviewers, authors, editors, and organizer of the conference to commemorate their inevitable contributions to advanced materials science and related fields. Without their participation, it would be impossible to hold the 5th ICIMA 2022 successfully and ensure high quality of papers published in the conference proceedings.

Preface

We are very pleased to introduce the Proceedings of the 5th International Conference on Inventive Material Science Applications (ICIMA 2022). The 5th ICIMA event was held at PPG Institute of Technology from May 6 to 7, 2022.

One of the significant and valuable aspects of this 5th conference edition is the way it brings together researchers, academicians, and engineers from various countries and initiates discussion on relevant issues, challenges, opportunities, and research findings. The primary focus of ICIMA 2022 is to provide an excellent platform for the conference participants to share and exchange novel and innovative ideas of original research, and to build international association. The main intent of this conference is to create a smart and advanced research landscape for the areas of inventive material science.

Out of 182 submissions received from different parts of the world, only 26 submissions were accepted as full papers for publication and presentation in ICIMA 2022. These papers provide a brief illustration of current research on relevant topics, covering sustainable strategy, micro/nanomaterials, biomaterials, hybrid electronic materials, innovative electronic materials processing, computational material science, material characterization, fabrication, and synthesis technologies.

The success of the conference is due to the collective efforts of all the reviewers and advisory/review board members. We would like to express and record our gratitude and appreciation to the authors for their contributions. Many thanks to the reviewers, who helped us to maintain high-quality manuscripts included in the proceedings. We

also express our sincere thanks to the keynote member ‘Dr. M. V. Reddy, Institute of Research Hydro Quebec, Canada’ and members of the conference committees and organizing team for their hard work. We wish that all the authors and delegates find ICIMA 2022 proceedings interesting, exciting, and inspiring.

Dr. V. Bindhu
Professor and Head
ECE

PPG Institute of Technology
Coimbatore, India

Dr. João Manuel R. S. Tavares
Professor
Faculdade de Engenharia
Universidade do Porto (FEUP)
Porto, Portugal

Dr. Joy Iong-Zong Chen
Professor
Department of Electrical Engineering
Da-Yeh University
Changhua, Taiwan

Contents

Wave Energy System Design of the Waraqocha Project	1
Sebastián Chacana, Norman Toro, Diego Herrera, Wagner Fleming, and Iván Salazar	
Performance Characteristics of Mineral Oil Blended with Vegetable Oil	17
P. Prakash, M. Seethraman, L. Santhosh Kumar, S. Jayaprakash, and M. Bakrutheen	
Design of Beam Splitters by Using 1D Defect Ternary Photonic Band Gap Structures	27
Anirudh Banerjee	
Comparative Study Between Different Mechanisms for Determining the Flocculant Dosage in the Sedimentation of Copper Concentrates	33
Aldo Quiero, Ruben Olcay, and Norman Toro	
Investigation on Critical Characteristics of Mineral Oil by Using h-BN Nanoparticles	47
P. Sathya, M. Ravindran, and R. Harichandran	
Implementation of ALU Using Partial Adiabatic Logic Style	59
S. Dhileep Kumar, Kasireddy Vathsalya, and R. Phani Vidyadhar	
High Speed Low Voltage Hybrid Full Adder for Computing Systems ...	77
J. Vineetha, K. Vamsi Krishna, P. Gayathri, M. Taj, and Satyajeet Sahoo	
Fracture Interface Observation After the Mechanical Test of Additively Manufactured CCFRTC Fabricated Under the Controlled Air Flow Cooling Effect	87
Nabeel Maqsood and Marius Rimašauskas	

Influence of Acetic Acids on Performance Parameters of Vegetable Oil Insulation	97
M. Rajesh, J. Salamon Raja, S. Selvakumar, S. Prasanth, and M. Bakruthen	
Design of Gate All Around MOS-Based RADFET Dosimeter	107
Chitikina Neeraj Venkatesh and Guru Prasad Mishra	
Influence of Casting Moulds on the Tensile and Corrosion Characteristics of Palm Kernel Shell Ash Reinforced Al6063-SiC Composite	115
O. O. Ajide, T. O. Dada, N. Idusuyi, F. A. Musa, O. A. Aogo, A. S. Adebayo, and N. Kumar	
Design and Development of Universal Runner Cutting Machine	131
Gopaldas Waghmare, Atharva Nemad, Gaurav Puri, Devyani Teware, Aalapi Banubakode, and Shrinath Ghuge	
Surface Integrity and Corrosion Resistance of AZ31B Magnesium Alloy Processed by Ultrasonic Rolling	145
Gao Honghong, Ma Baoji, Zhu Yuanpeng, and Huo Jinxiang	
Wireless Interface-Based Acquisition, Analysis, and Control System Using Master–Slave Approach for Chemical Laser	155
Rajeev Kumar Dohare, Mainuddin, and Gaurav Singhal	
Finite Element Analysis of Isotropic & Functionally Graded Plate	163
Satadru Singha and S. K. Tiwari	
Designing of an Efficient 4*4 RAM Using Binary Cell	175
Meghana Rao Ravula, Abhishek Potharaju, and R. Phani Vidyadhar	
Mathematical Model of Kirchhoff Mesh Nanoplate Under the Action of Electrostatic and Temperature Fields	185
E. Y. Krylova	
Verification of Wishbone Compliant SPI Using System Verilog	197
Aditya Yadav, Amit Gupta, Adarsh Rana, and Aditya Kumar	
Design and Simulation of MEMS-Based Two-Directional Capacitive Pressure Sensor	211
Yellapragada V. S. Sasank, Chennai J. V. K. Sathya Swaroop, Ghanta Sriram, Satyajeet Sahoo, and M. Taj	
Memristor and Its Modelling: A Review	219
Deneyaz Shaik and Satyajeet Sahoo	
Performance Characteristics of Vegetable Oil and Its Blended Combinations as Alternate Liquid Insulation	235
M. Padmavathy and M. Bakruthen	

Bottom-Up Synthetic Biology Leads to Artificial Cells as Innovative Materials and Calls for the Adoption of Systemic Perspectives	245
Pasquale Stano	
Sensitivity Studies on Low Energetic Pyrotechnic Composition for Future Consumer Fireworks	257
S. Lionel Beneston, S. P. Asok, and V. Harish	
Investigation of Desirable Vibrational Energy Harvester Based on Design Structure and Piezoelectric Material	267
Shaik Riyan, Boppana Bhargav Chowdary, Adil Altom Mohammed Adam, Satyajeet Sahoo, and M. Taj	
Surface Characterization of $Mn_{1.0}Co_{1.9}Fe_{0.1}O_4$ (MCF) Spinel Coating on Metallic Interconnect Used in Solid Oxide Fuel Cells	277
N. Manjunath and B. Rajasekaran	
Performance Optimization of IGZO-Based Junctionless Thin Film Transistor for Low Power Application	285
Shraddha Yogi and Alok Naugarhiya	
Author Index	295

About the Editors

Dr. V. Bindhu received the B.E Degree in Electronics and Communication Engineering from Bharathiar University, Coimbatore, in 2002, and M.E. Degree in Applied Electronics from Anna University, Chennai, in 2007, and Ph.D. Degree from Anna University, Chennai, in 2014. She has 10 years of teaching experience and 5 years of research experience. Currently, she is a professor at PPG Institute of Technology, Coimbatore. Her area of interest includes signal processing and VLSI design.

João Manuel R. S. Tavares graduated in Mechanical Engineering at the Universidade do Porto, Portugal in 1992. He also earned his M.Sc. degree and Ph.D. degree in Electrical and Computer Engineering from the Universidade do Porto in 1995 and 2001, and attained his Habilitation in Mechanical Engineering in 2015. He is a senior researcher at the Instituto de Ciência e Inovação em Engenharia Mecânica e Engenharia Industrial (INEGI) and Full Professor at the Department of Mechanical Engineering (DEMec) of the Faculdade de Engenharia da Universidade do Porto (FEUP). João Tavares is co-editor of more than 75 books, co-author of more than 50 book chapters, 650 articles in international and national journals and conferences, and 3 international and 3 national patents. He has been a committee member of several international and national journals and conferences, is co-founder and co-editor of the book series *Lecture Notes in Computational Vision and Biomechanics* published by Springer, founder and Editor-in-Chief of the journal *Computer Methods in Biomechanics and Biomedical Engineering: Imaging & Visualization* published by Taylor & Francis, Editor-in-Chief of the journal *Computer Methods in Biomechanics and Biomedical Engineering* published by Taylor & Francis, and co-founder and co-chair of the international conference series: CompIMAGE, ECCOMAS VipIMAGE, ICCEBS and BioDental. Additionally, he has been (co-)supervisor of several MSc and PhD thesis and supervisor of several post-doc projects, and has participated in many scientific projects both as researcher and as scientific coordinator. His main research areas include computational vision, medical imaging, computational mechanics, scientific visualization, human-computer interaction and new product development.

Dr. Joy Iong-Zong Chen is currently a full professor of the Department of Electrical Engineering Dayeh University at Changhua Taiwan. Prior to joining the Dayeh University, he worked at the Control Data Company (Taiwan) as a technical manager since September 1985 to September 1996. His research interests include wireless communications, spread spectrum technical, OFDM systems, and wireless sensor networks. He has published a large number of SCI Journal papers in the issues addressed physical layer for wireless communication systems. Moreover, he also majors in developing some applications of the Internet of Things (IoT) techniques, and Dr. Joy Iong-Zong Chen owned some patents authorized by the Taiwan Intellectual Property Office (TIPO).

Wave Energy System Design of the Waraqocha Project



Sebastián Chacana, Norman Toro, Diego Herrera, Wagner Fleming, and Iván Salazar

Abstract Given the need to develop new technologies to supply energy to the mining industry in Chile, and its industries that provide services to mining, the development of a wave project to generate energy through the movement of waves on the northern coasts is presented from the country. For this, an analysis of the different technologies that exist for wave energy generation was carried out, in order to understand the context in which it is designed. Measurements were made in the field regarding the height of the waves in the area where the equipment was installed, in order to size based on the characteristics of the waves. The project is based on the generation of electrical energy through a Pelton turbine, which is fed by fresh water at high pressure, which rotates the impellers of the turbine. There is a transformation of mechanical energy to electrical energy by means of a hydraulic system. Finally, the amount of energy that the system can produce was estimated, together with the valuation of the project.

Keywords Renewable energy · Mining · Sustainability

S. Chacana · I. Salazar (✉)

Departamento de Ingeniería Civil, Universidad Católica del Norte, Angamos Av. 0610, 1270709 Antofagasta, Chile
e-mail: isalazar@ucn.cl

N. Toro · W. Fleming

Faculty of Engineering and Architecture, Universidad Arturo Prat, 1100000 Iquique, Chile
e-mail: notoro@unap.cl

W. Fleming

e-mail: wflaming@ucn.cl

D. Herrera

Gerencia y Desarrollo, Empresa Portuaria Antofagasta (EPA), Antofagasta, Chile
e-mail: dherrera@puertoantofagasta.cl

1 Introduction

Chile is the world's leading copper producer with a 27.9% share and 29% of the reserves of this commodity [1]. Within the national territory, there are 3817 copper mineral deposits, where their exploitation represents 92% of exports by the mining market [2]. Currently, part of the strategy at the country level is to go from 5.78 million tons of fine copper to around 6.2 million tons in 2027, increasing by 1.7% [3]. However, despite these positive figures presented, in recent years copper deposits have shown a drop in their grades, where the average copper grade has dropped from 1% in 2004 to average grades of 0.65 in 2016 [4, 5]. Added to this problem are the greater environmental restrictions, the scarcity of water, and the need to seek new energy sources that are friendly to the environment [6].

One of the challenges for mining companies, especially large ones, brought about by the new Energy Efficiency Law is the implementation of energy management systems in their processes and the obligation to report annually on energy consumption and other indicators [7]. The Corfo Solar Committee indicates that the average cost of MWh in mining is US \$100, with a variation that fluctuates on average between US \$80 and US \$120 MWh, but the cost of MWh for photovoltaic generation is in the order of US \$21 to US \$23 MWh [8]. Currently, 17% of the energy produced in Chile comes from non-conventional renewable sources. Experts say that the country will pass 30% in 2025. The goal, according to the Ministry of Energy, is that by 2035 60% will be clean energy and that it could even reach 100% renewable energy by 2050. Currently, the Solar energy is the one that advances the most: 76% of NCRE projects in development are of this type [9]. However, it is necessary to diversify the energy matrix to be able to meet the consumption needs of mining and its industries that provide support and support [10, 11].

A good inexhaustible alternative source to supply energy is the sea. Chile has a large amount of coastline with unused available energy, according to Henry Jeffrey "on a planetary level, the coast of Chile is a great wave energy hotspot (waves) with an estimated potential of 240 GW, that is, more than ten times the complete matrix of the country (19 GW)" [12].

In the present manuscript, a project carried out on the north coast of Chile is presented, in order to evaluate the energy potential of the waves at the site of the wave system. Subsequently, the design of a buoy arm system for wave energy production is presented, and finally, the technical and economical characterization of the equipment associated with the wave energy system for energy conversion is presented. This project is necessary due to the lack of an energy matrix for mining in Chile, and also the need to generate non-conventional renewable energies taking advantage of the region's climate. In addition, there is no project in Chile that uses wave energy; therefore, this is a pioneering and novelty project. Also, the model is novelty and designed by the authors of this manuscript, and that is currently being applied in the local industry in Chile.

Table 1 Different types of wave energy technologies

Technology type	Model	Generated power
Attenuators	Pelamis	750 kW
Overflowing devices	Wave dragon	4 MW
Oscillating water column	LIMPET	500 kW
Point absorbers	OPT	150 kW
Oscillating wave converter	Oyster	800 kW
Arm-Buoy	Pecem Plant	50 kW
Arm-Buoy	Wave star energy	600 kW

2 Background of Undomotive Energy

Wave energy is the kinetic energy contained in the oscillatory movement of the ocean waters, that is, the energy available in the waves. Wave energy consists of systems that take advantage of the oscillatory movement of the waves, absorbing both their kinetic and potential energy, either with horizontal floating devices or with vertical devices that take advantage of the amplitude of the waves [13].

At a global level wave energy, although it is not one of the best-known energies, there are multiple projects that have been developed to capture wave energy. The energy of the waves depends on the location where the equipment is installed as can be seen in the figure. The southern area of Chile has excellent conditions for the development of this type of technology; however, in the northern sector of the country, the conditions are not so favorable, and it is in this sector where this research was developed [14]. Among the types of devices are those shown in Table 1.

3 System Conceptual Design

The project is based on the generation of electrical energy through a Pelton turbine, which is fed by fresh water at high pressure, which rotates the impellers of the turbine. There is a transformation of mechanical energy to electrical energy by means of a hydraulic system.

The operation of the system (see scheme in Fig. 1) is based on 3 components:

- Mechanical arm-buoy system
- Hydraulic system
- Energy conversion system.

The waves of the sea cause the float or buoy to move, and the buoy is connected to some high pressure cylinders by means of a structure that works as an arm. The cylinders act as a positive displacement pump. These cylinders pump fresh water

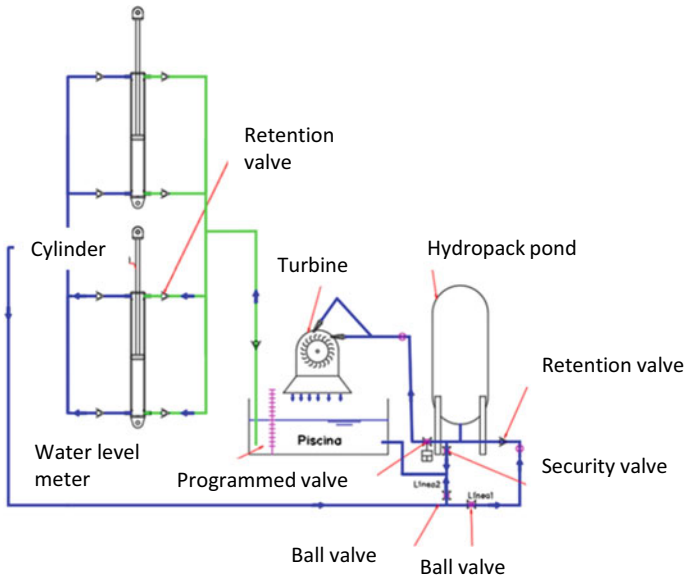


Fig. 1 General scheme of the operation of the system

from an accumulation tank into a hydropneumatic tank, which increases the pressure of the water, which will eventually be delivered to the Pelton turbine.

The Pelton turbine allows the transformation of mechanical energy into electrical energy; after this step, the water returns to the accumulation tank.

The main components of the system are the following:

- Buoy
- Arm
- Cylinders
- Hydraulic system
- Hydropneumatic tank
- Pelton turbine
- Pond
- Control and instrumentation system.

The mentioned elements must meet certain characteristics to have an optimal operation and can be part of the wave power system.

Table 2 Measurement record

Record	Date	Duration		Minimum height ¹	Maximum height
		Hours	Days	cm	cm
1	21-12-2016	279	11.625	759	48
2	18-01-2017	300	12.5	759	0
3	08-03-2017	282	11.75	719	20
4	12-05-2017	396	16.5	756	25

4 Cadastre Data Analysis

The wave system depends entirely on sea conditions; for this reason, the behavior of the sea in the area to be studied must be analyzed. Wave behavior depends on many factors, which will influence the power generation of the system.

In order to have data on the ground of the sector in which the wave power system is to be installed, measurements were made on the ground in the port of Antofagasta, where a wave recording system was installed, this system worked through an ultrasonic distance meter XL-MaxSonar[®]—WR1[™] (MB7060 ultrasonic), which was connected to an Arduino system and this, in turn, transfers the data in text file format to a 16 Gb memory card.

Once the data was collected, it was passed to a filter where it was processed. Subsequently, having a comprehensive and processed record, the data was entered into the energy calculation model, which gives a theoretical value of energy production in the system.

Analysis of data obtained by the sensor: Several records are available. For the analysis, the 4 most reliable records were used (see Table 2), since they were long periods of measurement and had fewer irregularities.

The minimum and maximum heights can be highlighted from Table 2. The minimum height includes from the sensor located at the height of the surface of the molo and the lowest distance that reaches the surface of the wave. The maximum height is the shortest distance between the surface of the wave and the sensor. Sensor scheme is shown in Fig. 2.

In summary, from the four records the information shown in Table 3 is obtained.

According to this table, it is observed that the average difference between the lower peak (average of the greatest distance or lowest wave height) and the upper peak (average of the lowest distance or highest wave height) is 262 cm.

From this, it follows that on average the float must move vertically 262 cm, in normal operation.

Figure 3 shows the levels registered by the sensor and subsequently corrected:

- In yellow, you can see the maximum and minimum levels of the first record
- In magenta, you can see the maximum and minimum levels of the second register

¹ With respect to the surface of the molo.

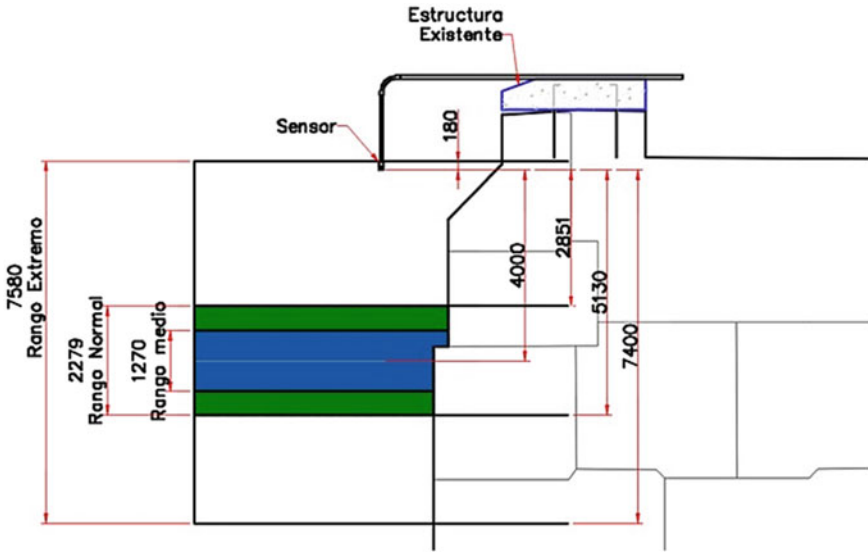


Fig. 2 Sensor schematic

Table 3 Registered information

Item/Record (cm)	1	2	3	4	Mean
Lower peak	505	513	526	537	520
Upper peak	291	248	256	239	258
Difference	214	266	271	298	262
Middle point	398	380	391	388	389
Minimum wave	580	570	610	592	588
Maximum wave	180	60	140	157	134
Distance to center	107	133	135	149	131

- The maximum and minimum levels of the third register are shown in blue.
- Green shows the maximum and minimum levels of the fourth register
- In red, it looked like the sonar reduction level (sea level 0).

5 Mechanical Design

5.1 Float

The float shall be round-based and have a one-degree-of-freedom hinge (see Fig. 4).

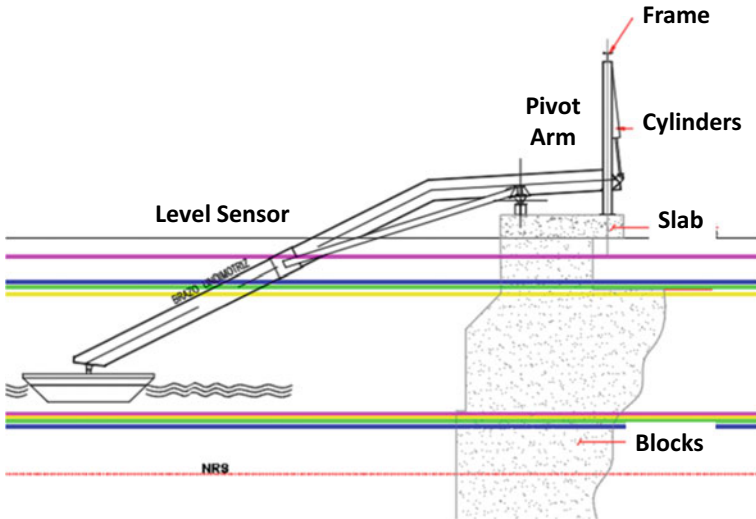


Fig. 3 Records height

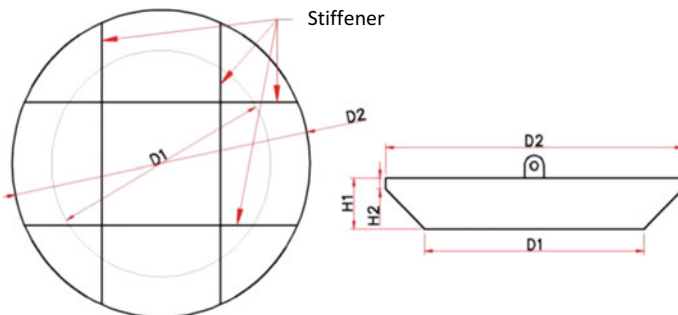


Fig. 4 Float design

It will have a flat bottom, and the outer faces will be made of 8-mm steel plate. In addition, it will have 4 inner ribs in 8-mm steel plate.

The characteristics of the float are shown in Table 4.

For the design, a float with a weight of 3.052 (ton) was established, which added to the 2.0 (ton) applied by the arm, giving a total force of 5.052 (ton). It is observed that the total flotation capacity is 9.45 (ton), the water level being 510 (mm) from the base, which is the lowest value it will have.

Table 4 Float dimensions

Parameter	Unit	Model
<i>D1</i>	mm	2.950
<i>D2</i>	mm	4.500
<i>H1</i>	mm	800
<i>H2</i>	mm	125
Thickness <i>D1</i>	mm	8
Thickness <i>D2</i>	mm	8
Mantle thickness	mm	8
Total weight	Kgf	3.052
Vertical force <i>F</i>	Kgf	2.000
Final weight	Kgf	5.052
Total volume	m ³	9.45
Metacenter	mm	510
Gravity center	mm	502

5.2 Arm

The arm must be long enough to be able to make the path that the buoy makes when rising and falling with the waves (see scheme in Fig. 5), it must also have an inclination so that it does not hit the surface of the molo.

The arm will be 18.1 m in plan, with an angle of 157°.

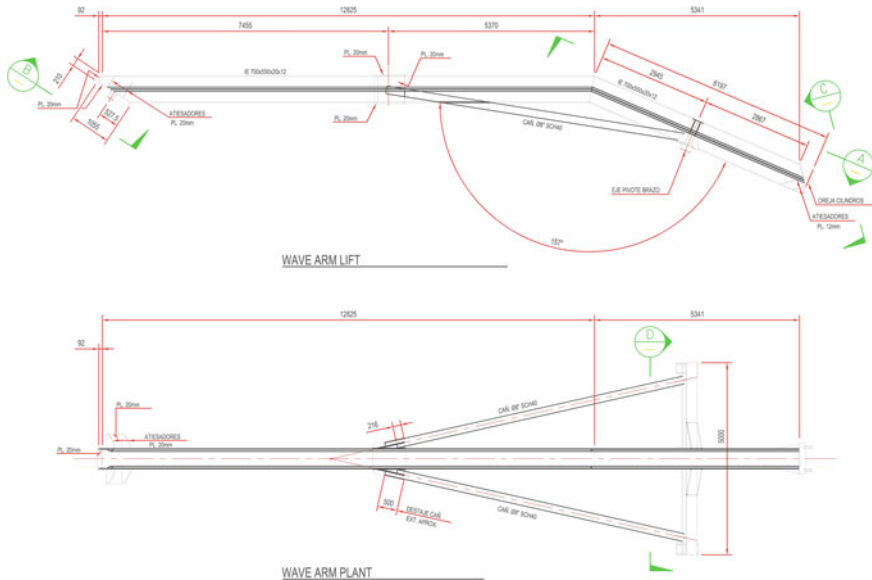


Fig. 5 Arm design

5.3 Cylinders

The cylinder used in the project is the 250 mm diameter cylinder (see scheme in Fig. 6), since it has an adequate volume for the operation of the project.

6 Hydraulic Design

The hydraulic system works through the cylinders, which act as a pump, sucking the water from the accumulation tank and driving it to the hydropneumatic tank and later to the Pelton turbine. This system is divided into two subsystems which are divided into the cylinder: Suction system and Drive system.

The hydraulic system has common design criteria, among which the materiality, layout, and parts that it will have are first defined, to later calculate the system. Figure 7 shows a general operation of the system, in green the suction line and in blue the impulsion line.

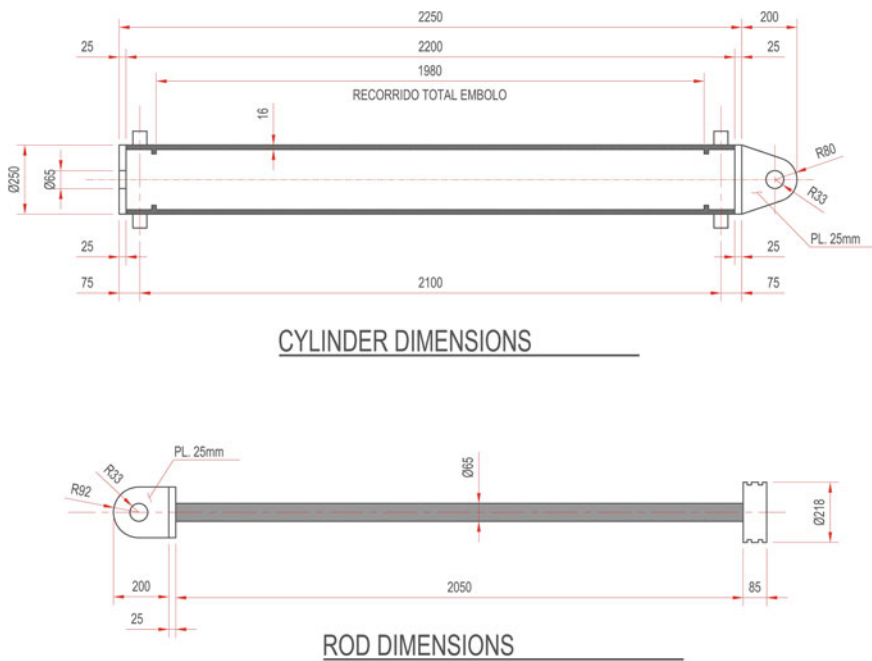


Fig. 6 Hydraulic cylinder

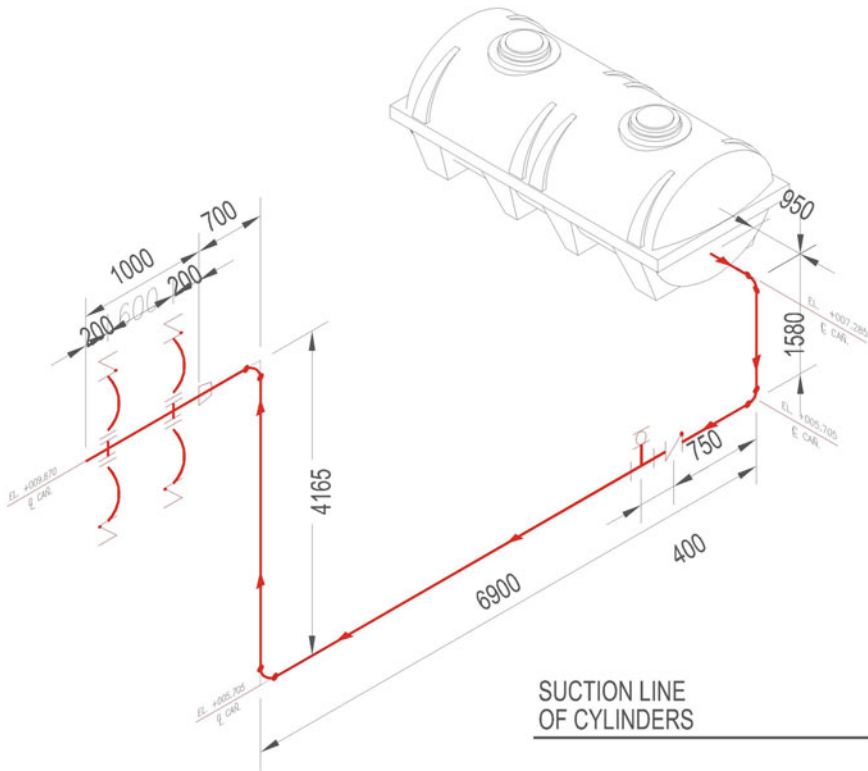


Fig. 7 Suction scheme

6.1 Suction System

The suction system (see scheme in Fig. 7) is basically the conduction from the pond to the cylinder. To design this system, it must be established that the cylinder acts as a pump. The system was designed to avoid cavitation. To avoid this phenomenon, the net positive suction head (NPSH) is calculated, which is a modification of the Bernoulli energy equation. While the energy branches were calculated, they are shown in Table 5.

Table 5 Suction calculations summary ($A > B$, does not cavitate)

Flow (lt/min)	Lower section		Verification	Upper section		Verification
	NSPH Available A	NSPH Required B		NSPH Available A	NSPH Required B	
276	8.362	0.565	$A > B$	6.217	0.565	$A > B$
936	3.602	1.25	$A > B$	1.71	1.25	$A > B$

From this table, it can be deduced that the system works in limit conditions for the maximum flow. For medium flow, it works perfectly. The maximum flow condition is very extreme, and it is unlikely for this reason that the little cavitation clearance is accepted.

6.2 Drive System

The drive system consists of the operation of the hydraulic system after the cylinders. These work as a pump which drives the fluid into the hydropneumatic tank. This increases the pressure of the water by driving it toward the Pelton turbine.

In addition, this system has different control valves between the valves as follows: Solenoid valves; Safety valves; and Non-return valves (check valve).

These valves will control that the system works correctly according to the established parameters. To calculate the pressure and the operation of the system, it was analyzed with a maximum pressure of 15 tons applied to the cylinder, since this is the maximum load that could affect the cylinder, according to the maximum weight of the system. The layout can be seen in the following diagram (see Fig. 8) of the isometric view of the system.

To calculate each section of the pipeline, the Bernoulli energy equation was used. Table 6 shows the system calculations:

It is verified that the pipe resists the requested pressures; in addition, the diameter of the pipes is adequate so that the losses are minimal.

7 Turbine and Electric Generation

7.1 Pelton Turbine

Finally, the Pelton turbine is in charge of energy production; for this reason, it was designed in accordance with the system requirements. In order for the turbine to function optimally and avoid prolonged downtime, it was designed according to the following characteristics:

- The programmed valve is activated with a pressure of 8 bar
- The working flow is 6.3 lt/s
- The operating time is 900 s
- Turbine stop time is 90 s
- 19 mm nozzle.

The operation of the system is presented in Fig. 9.

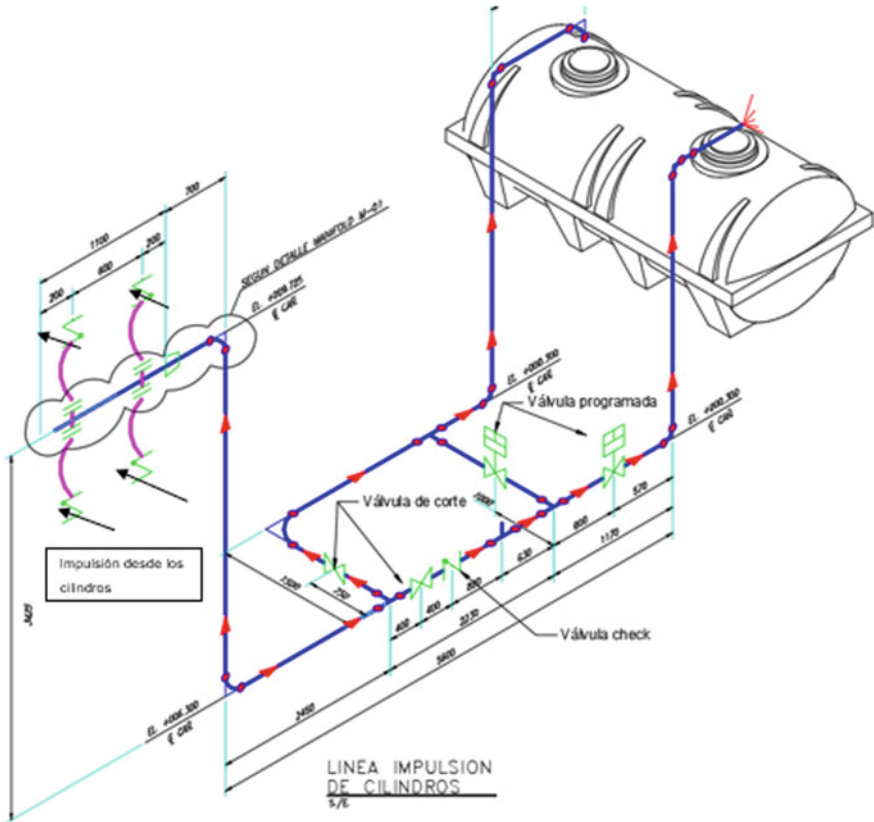


Fig. 8 Drive scheme

7.2 Estimated Generation

To calculate the estimated power generated by the system, the four normalized registers were analyzed, according to the envelope. For each of these registers, the force exerted on the arm was calculated, which translates into a discharge of flow and pressure by the effect of the hydraulic cylinders, which finally delivers a power generated by the Pelton turbine.

According to the modeling carried out, it is estimated that the proposed wave system could generate the following power, according to each record (see Table 7).

On average, the system is capable of producing 2.93 kW, this is taking the last two records as valid, since they are the most stable and extensive depending on the wave conditions.

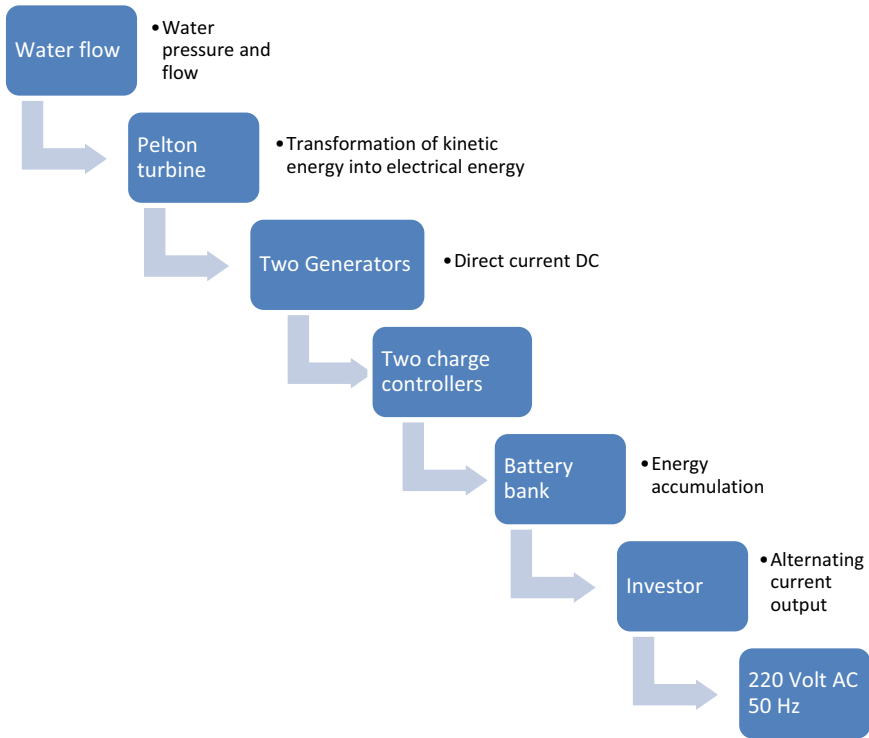


Fig. 9 System operation scheme

Table 7 Estimated power

Record	1	2	3	4
Measurement date	12-21-2016	18-01-2017	08-03-2017	12-05-2017
Generated power (kW)	713.82	766.86	826.65	1161
Hours	279.45	300.01	282.47	396
Days	11.64	12.5	11.77	16.5
Average power (kW)	2.55	2.56	2.93	2.93

8 Conclusion

According to the analysis of the data registered on different dates, it was observed that the generation was similar for different sampling dates, which according to the calculations would allow the system to generate approximately 2.9 kW. It should be remembered that this depends on the wave variation, which can change and the volume of the actual generation of the system can only be known once it has been put into operation. The wave power system proposed in comparison with the other

models reviewed generates a lower power; however, it must be considered that the maritime conditions are not the same, nor are the dimensions of the prototypes, although the system is not economically viable, it can be easily modifiable in order to optimize generation.

Regarding the design, it can be established that it is a simple model that uses a hydraulic system which depends on the movement of the waves. Compared to the other models, the system occupies a small surface of water, since it uses a single buoy. It could be optimized by using a larger surface area in the water, in order to use more buoys with the same hydraulic system, similar to the Wave Star Energy model. Another modification to the system would be to try to reduce energy losses, experiment with magnetic energy systems, such as a dynamo and crank, and crank mechanism. Another relevant point is to analyze different configurations of equipment, in order to direct the project to be an electricity generating plant and not just an experimental prototype, that is, perhaps adding more pistons, or analyzing the operation of several arms with a hydropneumatic tank common and a common turbine, thus generating a continuous system of electricity generation.

Finally, it is concluded that the present system can be a good alternative source to generate renewable electricity, to supply the industry that provides services to local mining companies in northern Chile.

As current limitations and future improvements, the energy transformation system must be improved to reduce energy losses and thus improve the energy efficiency of the project.

Acknowledgements Iván Salazar acknowledges funding support from FIC-R BIP project 30413374-0.

References

1. Flanagan, D.M.: Copper. In: Mineral Commodity Summaries 2021, pp 52–53. U.S. Geological Survey, Reston, Virginia, USA (2021)
2. Torres Alborno, D.A.: Copper and manganese extraction through leaching processes (2021)
3. Montes, C.: Proyección de consumo de agua en la minería del cobre 2019–2030. In: COCHILCO. <https://www.cochilco.cl/Listado%20Temtico/proyeccion%20agua%20mineria%20del%20cobre%202019-2030%20VF.pdf> (2019). Accessed 6 Jan 2022
4. SERNAGEOMIN.: Anuario de la Minería de Chile. Santiago, Chile (2020)
5. Toro, N., Jeldres, R.I., Ordenes, J.A., et al.: Manganese nodules in Chile, an alternative for the production of Co and Mn in the future—a review. *Minerals* **10**, 674 (2020). <https://doi.org/10.3390/min10080674>
6. Saldaña, M., Rodríguez, F., Rojas, A., et al.: Development of an empirical model for copper extraction from chalcocite in chloride media. *Hemijaska Industrija* **74**, 285–292 (2020). <https://doi.org/10.2298/HEMIND200424031S>
7. 4e Chile.: Evento abordará los desafíos que trae la Ley de Eficiencia Energética para la minería chilena. In: Programa de Energías Renovables y Energéticas en Chile. <https://www.4echile.cl/noticias/evento-abordara-los-desafios-que-trae-la-ley-de-eficiencia-energetica-para-la-mineria-chilena/> (2021). Accessed 7 Jan 2022

8. Los desafíos energéticos de la minería. In: *Electricidad: La Revista Energética de Chile*. <https://www.revistaei.cl/reportajes/los-desafios-energeticos-la-mineria/> (2018). Accessed 7 Jan 2022
9. El 17% de la energía producida en Chile proviene de fuentes renovables no convencionales. In: *Electricidad: La Revista Energética de Chile*. <https://www.revistaei.cl/2017/04/24/17-la-energia-producida-chile-proviene-fuentes-renovables-no-convencionales/> (2017). Accessed 7 Jan 2022
10. Grágeda, M., Escudero, M., Alavia, W., et al.: Review and multi-criteria assessment of solar energy projects in Chile. *Renew. Sustain. Energy Rev.* **59**, 583–596 (2016). <https://doi.org/10.1016/j.rser.2015.12.149>
11. Toro, N., Robles, P., Jeldres, R.I.: Seabed mineral resources, an alternative for the future of renewable energy: a critical review. *Ore Geol. Rev.* **126**, 103699 (2020). <https://doi.org/10.1016/j.oregeorev.2020.103699>
12. Henry, J.: Experto en energías marinas: “La costa de Chile es un gran hotspot de energía.” In: *AQUA: Acuicultura y Pesca*. <https://www.aqua.cl/entrevistas/henry-jeffrey-experto-energias-marinas-la-costa-chile-gran-hotspot-energia/> (2016). Accessed 7 Jan 2022
13. Terrero González, A., Dunning, P., Howard, I., et al.: Is wave energy untapped potential? *Int. J. Mech. Sci.* **205** (2021). <https://doi.org/10.1016/j.ijmecsci.2021.106544>
14. Jin, S., Zheng, S., Greaves, D.: On the scalability of wave energy converters. *Ocean Eng.* **243**, 110212 (2021). <https://doi.org/10.1016/j.oceaneng.2021.110212>

Performance Characteristics of Mineral Oil Blended with Vegetable Oil



P. Prakash, M. Seethraman, L. Santhosh Kumar, S. Jayaprakash,
and M. Bakruthen

Abstract For a long time, oil-based commodities have dominated the world's energy requirements across a wide range of businesses. Vegetable-based ester oil is provided as an environmentally friendly fluid protection option to determine if it may be used to replace standard mineral oil. Various mineral and ester oil ratios were blended in this study to evaluate the essential characteristics of blended liquid as liquid insulation. Sunflower, safflower, and rice bran oils are being investigated. Viscosity, breakdown voltage, flash point, and pour point are tested according to industry standards for various combinations (IEC and ASTM). According to the study, blended combinations indicate variances in attributes towards positive signs for replacement with the mineral oil.

Keywords Vegetable oil · Blending · Liquid insulation · Transformers

1 Introduction

The insulating oil used in electrical power transformers is known as transformer oil. It is obtained via fractional distillation and subsequent treatment of crude petroleum. Transformers function by combining the core and winding motions. When a high electric field is applied, heat is generated inside the transformer. As a result, the primary purpose of transformer oil is to avoid corona and arc discharges. Pyrolysis should be decreased when using a coolant. Allowing ambient oxygen to come into touch with insulation is not good [1–3].

Mineral oil is a complex mixture of hundreds of distinct chemical compounds, with the majority of the molecules consisting of carbon and hydrogen. Mineral oil is divided into three types. Normal paraffin (straight chain wax-type molecules) and paraffins are two paraffinic crudes containing a modest percentage of naphthenic hydrocarbons (branched paraffins). When compared to these three oils, naphthenic crudes have a number of advantages, including the fact that they contain extremely

P. Prakash · M. Seethraman · L. S. Kumar · S. Jayaprakash · M. Bakruthen (✉)
Department of EEE, National Engineering College, Kovilpatti, Tamil Nadu, India
e-mail: bakruthenme@gmail.com

© The Author(s), under exclusive license to Springer Nature Singapore Pte Ltd. 2023
V. Bindhu et al. (eds.), *Proceedings of Fifth International Conference on Inventive Material Science Applications*, Advances in Sustainability Science and Technology,
https://doi.org/10.1007/978-981-19-4304-1_2

little wax. Because naphthenic oils are thinner than paraffinic oils, they have a lower viscosity. Even if they continue to be an excellent technical vs. cost answer, mineral oils must be assessed in terms of their environmental impact [4–7].

Natural and synthetic ester-based dielectric fluids have gained popularity amongst researchers and businesses interested in liquid dielectrics worldwide. Triglycerides are formed spontaneously when the tri-alcohol glycerol is etherified with three fatty acids in vegetable oil [8–10].

Blended oil is a novel mineral oil substitute developed by combining two insulating liquids. When compared to mineral oil, blended oil offers anti-ageing benefits. This Blended oil has a low dielectric loss, a low degradation ratio, a low acid number, and a low moisture content. However, depending on the type of ester oil and the acid level. The ester oil's miscibility determines the performance characteristics. The biodegradability of ester-based dielectric fluids is particularly important. As a result, current knowledge and literature on these new insulating fluids must be updated urgently. Based on the literature, this study aims to explore the qualities of natural esters-based oil samples as well as a blended mixture of natural ester oil and mineral oil [8–12].

2 Experimental Details

2.1 Oil Samples

Sunflower Oil (SUO), Safflower Oil (SAO), and Rice Bran Oil (RBO) have been chosen as vegetable oil samples for evaluation based on geographical availability, affordability, and previous study. Vegetable oil samples and mineral oil (MO) in their raw form are collected from a nearby factory. To meet the CIGRE Work Group's Study Committee Report 12.17 criteria for good oil quality, all are filtered to remove suspended particles from their composition. Various combinations for blended oil are shown in Table 1.

Table 1 Proposed oil samples

Sample	Composition
Base sample 1	100% MO
Base sample 2	100% SUO
Base sample 3	100% SAO
Base sample 4	100% RBO
Mixed sample 1	50% MO + 50% SUO
Mixed sample 2	50% MO + 50% SAO
Mixed sample 3	50% MO + 50% RBO

2.2 Mixed/Blended Oil Sample Preparation Process

A 500 mL glass spherical reactor with a thermostat, mechanical stirring, and a sample exit is used for the reaction. The technique used is described in the following paragraphs. The REACTOR is warmed to 75 °C to remove moisture before adding each vegetable oil sample as per the proposed samples. The stirring system is initiated when the reactor achieves the reaction temperature, designating this event as the reaction's time zero. Each mixture is vigorously agitated and refluxed for the required reaction time.

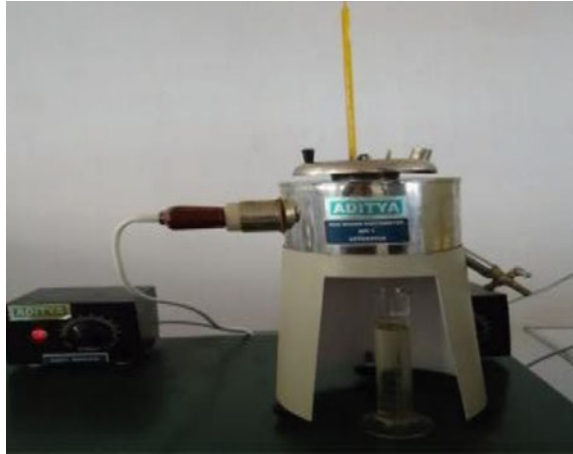
2.3 Measurement of Breakdown Voltage

The breakdown voltage is the most essential aspect in determining whether or not to utilise oil as a transformer protection. Some of the factors that effect the breakdown voltage esteem include dampness pressure, air pockets, strong particles, and causticity. At room temperature, the breakdown voltage of the examples was computed using an oil test unit in compliance with IEC 60156 [13] regulations. The estimation limit of the oil test pack is 60 kV. The oil test box includes a standard oil test cup with a round cathode. The oil test cup is shown in Fig. 1.

During the estimation, the hole separating the cathodes was kept at 2.5 mm, as per the norm. Before determining the fraction of breakdown voltage, the oil test cup was flushed with the supplied example. Then it was loaded with the example, which required the calculation of the breakdown voltage. From the terminal's highest point, the example was filled to a height of at least 40 mm. The stockpile was shifted at a rate of 2 kV/s using the control handle. The breakdown voltage estimation was repeated many times for each sample. The average of these variables was used to calculate the breakdown voltage in that scenario.

Fig. 1 Breakdown voltage kit



Fig. 2 Redwood viscometer

2.4 Measurement of Viscosity

Shearstress causes a barrier in a liquid, which is known as viscosity. Liquids of varying thicknesses, as well as liquids of varying thicknesses, can be successfully transferred without encountering any obstacles. With the anticipated of a supplemental oil course in the transformer tanl for cooling purposes—the transformer oil should have a medium consistency The temperature affects the thickness of the oil. A redwood viscometer was used to test the thickness at room temperature in accordance with ASTM D445 [14]. Figure 2 depicts the viscometer setup.

The sample was placed in a silver plated oil cup Allow the sample to flow through the ball valve (orifice) and into the test beaker. Calculate how long it takes to collect 50 ml of sample in a given amount of time.

2.5 Measurement of Flash Point

The flashpoint and fire point of transformer oil determine the temperature at which the oil will ignite if a fire source is present. The minimum temperature at which the oil would dissolve to frame a mixture of start in the air is known as the streak point. The temperature at which the framed fume prepared to consume [8, 10] is known as the fire point. The flash point and fire point were calculated at room temperature using Pensky Martin Flash point Apparatus as in accordance with ASTM D 93 [15]. The Pensky Martin Flashpoint Apparatus (Fig. 3) is a closed cup analyzer. The sample was placed in a brass test cup, and the temperature was raised using an electric heater with temperature control. Test fire was coordinated into the test. Essentially, the temperature comparing to the firepoint was related to ceaseless fire on the oil surface whenever a little test fire was coordinated into the example.

Fig. 3 Pensky Martin flash apparatus



2.6 Measurement of Pour Point

One of the important elements depicting the ability of fluid protection in chilly climate zones is low temperature execution. The minimum temperature at which fluid streams under authorised conditions is known as the pour point of fluid protection. Oil stream below the pour point might be problematic, and the stream is further constrained by consistency. In difficult working conditions such as cold areas, pour point estimation might be useful in determining the type of fluid protection for specific apparatus (IEEE Std. C57.14, 2018). The setup is shown in Fig. 4.

In accordance with ASTM D97, 2017 pour point temperature was calculated using a four-chamber pour point equipment. In a test tube, 50 ml of oil is placed in a

Fig. 4 Pour point apparatus kit



copper holder that is submerged in cooling media. Oil test in test tube is made easier by lowering the temperature of the cooling media.

3 Experimental Results and Discussion

3.1 Properties of Base Oil Samples

Breakdown voltage, viscosity, flash point, and pour point are measured as per standards for preliminary research on selected oils. Values of properties of oil samples are listed in Table 2.

The following inferences are drawn from the experimental results of properties by comparing them to the IEEE Guide for Acceptance and Maintenance of Insulating Liquid in Transformers.

The breakdown voltage of any liquid insulation is a critical parameter that determines the liquid insulation's ability to tolerate electrical stress generated inside the transformer during operation. According to IEEE guidelines, the minimum breakdown voltage should be 35 kV. All oil samples had a breakdown voltage more than 35 kV, according to the primary study of attributes of selected oil samples for this investigation. Based on these findings, it is discovered that certain natural esters have potential as liquid insulation for use in transformers due to a key trait of breakdown voltage.

The viscosity of liquid insulation is one of the key features that affects its effectiveness as a coolant and other liquid insulation components in the transformer. For acceptance as liquid insulation, the maximum acceptable range for viscosity values of natural esters and mineral oil given in IEEE guide is 50 cSt and 15 cSt, respectively. The viscosity of vegetable oil-based liquid insulations is often higher than that of standard mineral oil used in transformers. The discovered viscosity values for vegetable oil samples are similarly substantially greater than the stated standard value in this experiment. Natural esters may cause problems with cooling performance if used directly. Some approaches for lowering viscosity values have been proposed in the literature. As a result, viscosity reduction techniques should be used to apply the researched natural esters as liquid insulation in transformers.

Table 2 Properties of base oil samples

Properties	MO	SUO	SAO	RBO
Breakdown voltage (kV)	35	35	36	38
Viscosity at 40 °C (cSt)	12	52	50	56
Flash point (°C)	150	280	270	290
Pour point (°C)	-6	9	6	12

Flash point temperature is used for fire risk assessment as one of the important component. Natural esters and mineral oil, according to the IEEE Guide, must have a minimum flash point temperature of 275 °C and 140 °C, respectively, to be accepted as liquid insulation. All oil samples' flash point temperatures meet the specified standard specification. According to these findings, the tested oil samples exhibit a wide range of flash point temperatures for use as liquid insulation in transformers.

The pour point of liquid insulation is one of the most important features that indicates a temperature range where unrestricted circulation is possible without trouble. According to IEEE guidelines, the minimum pour point temperature for accepting as liquid insulation is -10 °C. All the samples except mineral oil have a positive value of pour point temperatures. These values are indicated that there are possibilities of freezing or crystal formation inside oil samples before sub-zero conditions. From results, it is observed inferred that fatty acid components are influential in pour point values. Because the pour point temperature of researched natural esters should be substantially lower than the measured values for their use in cold climates. Based on the literature available for pour point reduction, some procedures should be used to lower pour point from its normal value to a given range.

3.2 Properties of Mixed/Blended Oil Samples

Blended oil samples are prepared according to methodology, and property measurements are performed according to conventional protocols. The attributes of oil samples after mixing are given in Table 3.

The following conclusions can be drawn from the preceding experimental findings. The 50–50 combination has no effect on the breakdown voltage value after blending the oil samples. After testing, the viscosity and pour point of vegetable oil samples showed a decrease in value blending. The oil samples' flash point temperature decreases somewhat from its normal value.

Table 3 Properties of mixed oil samples

Properties	50% MO + 50% SUO	50% MO + 50% SAO	50% MO + 50% RBO
Breakdown voltage (kV)	35	35	36
Viscosity at 40 °C (cSt)	27	22	25
Flash point (°C)	200	200	210
Pour point (°C)	3	3	6

4 Conclusion

Today, the entire globe is witnessing the transition from oil-based items that are environmentally harmful to vegetable oils that are inexhaustible and eco-friendly. These limitless resources have excellent dielectric qualities and can be used with little risk. Mineral and normal ester oil-based mixed oil characteristics will be investigated further in this work. Mineral oil testing demonstrate that mixed oil mixes have better properties than mineral oil tests. This blended oil can be used in any electrical hardware depending on the application region and desired properties. In comparison to conventional mineral oil, the investigated mixed example has the potential to be a viable alternative. The biggest difficulty is that normal esters are more expensive than mineral oil. The following works will be completed in the future scope The investigation could be expanded to look at different blending combinations. More research on the performance of bio-modified vegetable oil and factors of life estimation is needed.

References

1. Senthilkumar, Karthick, Madavan, Arul Marcel Moshi, Sundara Bharathi, Saroja, S.R., Sowmya Dhanalakshmi: Optimization of transformer oil blended with natural ester oils using Taguchi-based grey relational analysis. *Fuels* **11**(1813) (2019)
2. Siva, S., Balaji, Akileshwaran, Hemanathan.: Experimental analysis on the combination of jatropha oil and silk cotton oil for transformer. In: International Conference on Science Technology Engineering and Mathematics (ICONSTEM) (2019)
3. Rakesh, C., Thomas, M.J.: Pongamia oil, an eco-friendly alternative for mineral oil used in high voltage transformers. *IEEE Trans. Dielectr. Electr. Insul.* **5** (2018)
4. Bandara, K., Fernando, M.: Possibility of blending sesame oil with field aged mineral oil for transformer applications. *IEEE Trans. Dielectr. Electr. Insul.* **21**(7) (2018)
5. Kamal, A., Bashir, M.: Insulating properties of vegetable oils and their blend. In: IEEE 7th International Power Engineering and Optimization Conference (2018)
6. Raof, N., Yunus, R.: Effects of palm-based trimethylolpropane ester/mineral oil blending on dielectric properties and oxidative stability of transformer insulating liquid. *IEEE Trans. Dielectr. Electr. Insul.* **26**(6) (2019)
7. Liang, S., Wang, F., Huang, Z., Chen, W., Wang, Y., Li, J.: Significantly improved electrical breakdown strength of natural ester liquid dielectrics by doping ultraviolet absorbing molecules. *IEEE Trans Dielectr Electr Insul* (2019)
8. Khaled, U.: Statistical investigation of AC breakdown voltage of natural ester with electronic scavenger additives. *IEEE Trans. Dielectr. Electr. Insul.* **26**, 6 (2019)
9. Trnka, P., Hornak, J., Prosr, P., Michal, O., Wang, F.: Various aging processes in a paper-natural ester insulation system in the presence of copper and moisture. *IEEE Trans. Dielectr. Electr. Insul.* (2020)
10. Cai, S., Zhou, X., Chen, J., Yu, H., Zhou, C.: Transesterification reaction reduce viscosity of vegetable insulating oil. In: International Conference on High Voltage Engineering and Application (ICHVE), pp. 648–650 (2012)
11. Devasia, A., Chattopadhyay, M.: Macroscopic characterization of grating coupled waveguide structures for optical notch filtering. In: International Conference on Innovative Data Communication Technologies and Application, pp 27–36. Springer, Cham (2019)

12. Saheb, S.H., Babu, G.S.: Modeling and evaluation of performance characteristics of redundant parallel planar manipulator. In: International Conference on Innovative Data Communication Technologies and Application, pp. 229–236. Springer, Cham (2019)
13. IEC 60156, Insulating Liquids—Determination of Breakdown Voltage at Power Frequency—Test Method, 3rd Ed (2003)
14. ASTM D445, Standard Test Method for Kinematic Viscosity of Transparent and Opaque liquids (and Calculation of Dynamic Viscosity) (2011)
15. ASTM D93, Standard Test Methods for Flash Point by Pensky-Martens Closed Cup Tester (2012)

Design of Beam Splitters by Using 1D Defect Ternary Photonic Band Gap Structures



Anirudh Banerjee

Abstract In this paper, beam splitters based on 1D defect ternary Photonic crystals are proposed. These beam splitters can split lights of different wavelengths into two beams having 50% of i/p optical power. The 50% of i/p light power of the splitted wavelength will be transmitted by the structure and 50% of i/p light power will be reflected by the structure. These splitted light beams will be available at the o/p and i/p ports, respectively. The wavelength to be splitted by this beam splitter and wavelength range of operation can be changed and controlled by changing the structural parameters.

Keywords Ternary · Photonic crystal · Photonic band gap · Transmission · Reflection · Beam splitter

1 Introduction

A beam splitter is a device that splits an i/p light beam into two light beams with 50% optical power. These beam splitters can be made by using different optical structures. Recently, 1D photonic crystal (PC) have been used for making different optical devices [1–6] and purpose of study [7–12]. In this paper, beam splitters based on 1D defect ternary photonic crystals are proposed. The wavelength of light to be splitted in this beam splitter can be chosen by changing the structural parameters. The i/p light beam falling on this 1D PC can be divided into two beams with 50% power of i/p light beam. One of the splitted beams will emerge from opposite side of the incident beam while other splitted beam will emerge from the same side as that of the i/p light beam. The wavelength range of operation of this beam splitter can be chosen by choosing different values of structural parameters. For designing beam splitters 2D and 3D PBG structures can be considered, but the major challenges associated with 2D and 3D PC structures are that they are costly and complicated to fabricate. The advantage

A. Banerjee (✉)

Department of Electronics and Communication, Amity School of Engineering and Technology, Amity University, Lucknow, Uttar Pradesh, India

e-mail: anirudhelectronics@yahoo.com

$$M_D = \begin{bmatrix} \cos \beta_D & \frac{-i \sin \beta_D}{q_D} \\ -i q_D \sin \beta_D & \cos \beta_D \end{bmatrix} \quad (4)$$

where

$$\beta_1 = \frac{2\pi}{\lambda} n_1 d_1 \cos \theta_1, \beta_2 = \frac{2\pi}{\lambda} n_2 d_2 \cos \theta_2, \beta_3 = \frac{2\pi}{\lambda} n_3 d_3 \cos \theta_3, \beta_D = \frac{2\pi n_D d_D \cos \theta_D}{\lambda_0}$$

are the layerwise phase thicknesses.

Here q_1, q_2, q_3 and q_D are given below.

$q_1 = n_1 \cos \theta_1, q_2 = n_2 \cos \theta_2, q_3 = n_3 \cos \theta_3$ and $q_D = n_D \cos \theta_3$ for TE polarization and

$q_1 = \cos \theta_1 / n_1, q_2 = \cos \theta_2 / n_2, q_3 = \cos \theta_3 / n_3$ and $q_D = \cos \theta_D / n_D$ for TM polarization.

$\theta_1, \theta_2, \theta_3$ and θ_D are the layer ray angles inside four layers, respectively, and these are related to the angle of incidence θ_0 by

$$\cos \theta_1 = \left[1 - \frac{\sin^2 \theta_0}{(n_1)^2} \right]^{\frac{1}{2}},$$

$$\cos \theta_2 = \left[1 - \frac{\sin^2 \theta_0}{(n_2)^2} \right]^{\frac{1}{2}},$$

$$\cos \theta_3 = \left[1 - \frac{\sin^2 \theta_0}{(n_3)^2} \right]^{\frac{1}{2}}$$

and

$$\cos \theta_D = \left[1 - \frac{\sin^2 \theta_0}{(n_D)^2} \right]^{\frac{1}{2}}$$

the total transmission matrix for this beam splitter is

$$\begin{aligned} M &= M_1 M_2 M_3 M_1 M_2 M_3 M_1 M_2 M_3 M_1 M_2 M_3 M_1 \\ &\quad M_2 M_3 M_1 M_2 M_3 M_1 M_2 M_3 M_1 M_2 M_3 M_D \\ &\quad \times M_1 M_2 M_3 M_1 M_2 M_3 M_1 M_2 M_3 M_1 M_2 M_3 \\ &\quad M_1 M_2 M_3 M_1 M_2 M_3 M_1 M_2 M_3 M_1 M_2 M_3 \\ &= \begin{bmatrix} m_{11} & m_{12} \\ m_{21} & m_{22} \end{bmatrix} \end{aligned} \quad (5)$$

For normally incident light on the PC from air, the transmission coefficient is

$$t = \frac{2}{(m_{11} + m_{12}) + (m_{21} + m_{22})} \quad (6)$$

and the transmissivity is

$$T = |t|^2 \quad (7)$$

3 Results and Discussion

Figure 2 shows the o/p spectrum of the first 1D defect ternary PC considered. The structural parameters for this 1D ternary defect PC are $n_1 = 3.3$, $n_2 = 2.05$, $n_3 = 1.46$, $n_D = 3.45$, $d_1 = 110$ nm, $d_2 = 99$ nm, $d_3 = 261.017$ nm and $d_D = 1.4$ μm . The o/p spectrum of this structure has a transmission peak at 1.572 μm wavelength with 50% transmittance and 50% reflectance.

Figure 3 shows the o/p spectrum of the second 1D ternary defect PC structure considered. The structural parameters for this 1D ternary PC structures are $n_1 = 3.3$, $n_2 = 2.05$, $n_3 = 1.46$, $n_D = 3.45$, $d_1 = 116$ nm, $d_2 = 99$ nm, $d_3 = 263$ nm and $d_D = 1.4$ μm . The o/p spectrum of this structure has a transmission peak at 1.585 μm wavelength with 50% transmittance and 50% reflectance.

It is clearly evident from figures that these 1D defect ternary PC structures can split i/p light beam into two parts with 50% transmittance each. The wavelength to be splitted by this beam splitter can be chosen or tuned by the changing the thickness of the defect layer and/or by changing structural parameters. The range of operation of this beam splitter will also be changed by changing the value of structural parameters.

Fig. 2 Output spectrum of first 1D ternary defect PC structure beam splitter

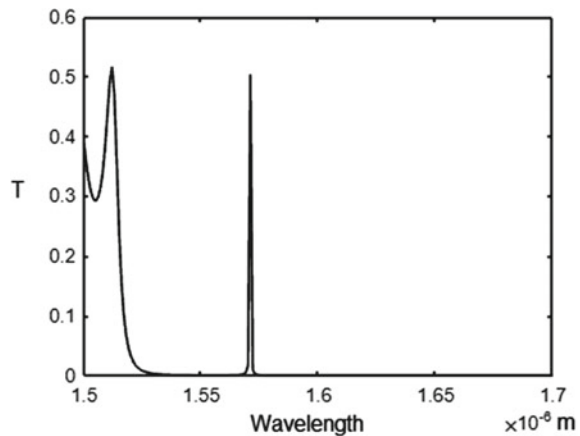
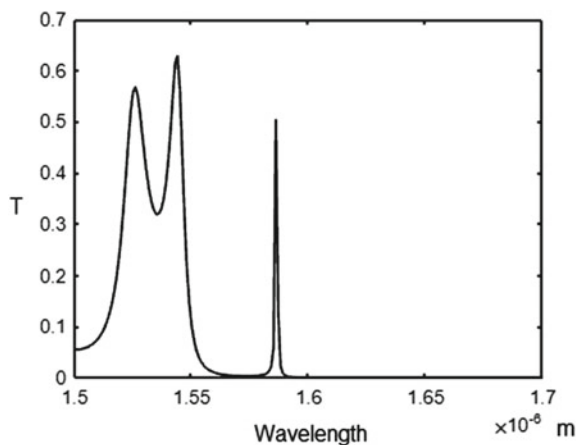


Fig. 3 Output spectrum of second 1D ternary defect PC structure beam splitter



4 Conclusion

In this paper, beam splitters based on 1D defect ternary PC structure were proposed. These 1D ternary defect PC structure beam splitters can split different optical wavelengths. The intensities of the splitted output beams of a wavelength are of 50% of the intensity of input beam. These beam splitters can operate in visible, infrared and other regions of electromagnetic spectrum depending on the values of structural parameters. Further, these 1D ternary defect PC structure beam splitters have advantages like low cost and ease of fabrication. These beam splitters find application in optical instrumentation.

References

1. Abadla, M.M., Tabaza, N.A., Tabaza, W., Ramanujam, N.R., Wilson, K.S.J., Vigneswaran, D., Taya, S.A.: Properties of ternary photonic crystal consisting of dielectric/plasma/ dielectric as a lattice period. *Optik* **185**, 784–793 (2019)
2. El-Amassi, D.M., Taya, S.A., Vigneswaran, D.: Temperature sensor utilizing a ternary photonic crystal with a polymer layer sandwiched between Si and SiO₂ layers. *J. Theor. Appl. Phys.* **12**, 293–298 (2018)
3. Taya, S.A.: Ternary photonic crystal with left-handed material layer for refractometric application. *Opto-Electron. Rev.* **26**, 236–241 (2018)
4. Abohassan, K.M., Ashour, H.S., Abadla, M.M.: One-dimensional ZnSe/ZnS/BK7 ternary planar photonic crystals as wide angle infrared reflectors. *Results Phys.* **22**, 103882 (2021)
5. Banerjee, A.: Enhancement in sensitivity of blood glucose sensor by using 1D defect ternary photonic band gap structures. *J. Opt.* **48**, 262–265 (2019)
6. Banerjee, A.: Design of enhanced sensitivity gas sensors by using 1d defect ternary photonic band gap structures. *Indian J. Phys.* **94**, 535–539 (2020)
7. Banerjee, A.: Enhanced incidence angle based spectrum tuning by using one-dimensional ternary photonic band gap structures. *J. Electromagn. Waves Appl.* **24**, 1023–1032 (2010)

8. Banerjee, A.: Enhanced refractometric optical sensing by using one-dimensional ternary photonic crystals. *Progr. Electromagn. Res.* **89**, 11–22 (2009)
9. Banerjee, A.: Enhanced temperature sensing by using one-dimensional ternary photonic band gap structures. *Progr. Electromagn. Res. Lett.* **11**, 129–137 (2009)
10. Yadav, A., Kumar, A., Sharan, P.: Sensitivity enhancement of a plasmonic biosensor for urine glucose detection by employing black phosphorous. *J. Opt. Soc. Am. B* **39**, 200–206 (2022)
11. Banerjee, A., Rizvi, S.: Suitability of 1d photonic band gap structures for electrical tuning of transmission spectrum in optical filters. *IEEE Xplore* (2018)
12. Singh, A.K., Kulshreshtha, A., Banerjee, A., Singh, B.R.: Nanotechnology in road construction. *AIP Conf. Proc.* **2224**, 0500021–0500024 (2020)

Comparative Study Between Different Mechanisms for Determining the Flocculant Dosage in the Sedimentation of Copper Concentrates



Aldo Quiero, Ruben Olcay, and Norman Toro

Abstract Three methods are studied to determine the adequate flocculant dose in an industrial pulp, sedimentation and compression parameters must be obtained from discontinuous sedimentation tests, carried out in a 1 L test tube, and in a 10 L column. The results obtained show different flocculant dose values for the three analyzed methods, since the maximum sedimentation speed method indicates that the chosen dose would be 4 (g/t); However, the analysis of the granulometry of the sediment shows that the addition of flocculant is not necessary; and finally the thickener design method (Adorjan's method), and prioritizing as the most relevant result the unit sedimentation area over the height of the thickener, indicates that the optimal value for the range under study would be 20 (g/t).

Keywords Sedimentation · Compression · Design · Thickener · Adorjan

1 Introduction

Solid–fluid separation operations at mining sites are of relevant importance due to the geographic location of these sites, where specifically in the North of Chile, the water resource is scarce; and in the future it will be even more so. For this reason, research into processes that include water recoveries will be increasingly important in the future mining development of Chile.

A. Quiero (✉) · R. Olcay · N. Toro

Faculty of Engineering and Architecture, Universidad Arturo Prat, 1100000 Iquique, Chile

e-mail: aquiero@unap.cl

R. Olcay

e-mail: rolcay@unap.cl

N. Toro

e-mail: notoro@unap.cl

Thickeners are the first equipment used in the solid–fluid separation stage, in copper sulfide mineral treatment mining operations, which use flotation as a concentration process; The objectives of which are the sedimentation and clarification of the pulp from the flotation process, either as a concentrate or as a tail for the process.

The design of conventional thickeners had its first proposals with the Mishler equation [1] and with the Coe and Clevenger method [2]. Later, Kynch's kinematic theory [3] is developed, presenting various design methods that use this theory, such as the methods of Talmage and Fitch [4] and Yoshioka and Hassett [5–8]; finally, models are developed that consider the behavior of flocculated pulps, incorporating the consolidation of dense sediments, with the use of dynamic models; such as the model proposed by Adorjan [9, 10].

A critical analysis of these methods was carried out by Concha and Barrientos [7], and a general evaluation of these methods was made by Quiero [11], for a tailings ore flocculated pulp, demonstrating that the method that precisely described the design and subsequent simulation of the thickeners working at their respective sites, was the Adorjan method; presenting differences of less than 5% of the actual operating values.

Later, Zambra and Quiero [12] carried out the study for a tailings flocculated pulp, but from another mining site, in which it was concluded that the design and simulation of the thickener operation, using the Adorjan method, also presented differences, less than 5%.

Another aspect to be studied in this work refers to the determination of the optimum flocculant dose in the operation of a thickener, since the conventional method consists of carrying out various discontinuous sedimentation tests, for the same pulp concentration, and then calculating the sedimentation rate of the pulp, and with these values, calculate the necessary sedimentation area and choose the largest of them, then apply a safety factor to it, and choose the value obtained as the design parameter of the industrial thickener. In this work, a study of the granulometry of the sediment at the bottom of the test tube was also carried out, to which the discontinuous sedimentation test was carried out, since the flocculant, in addition to increasing the sedimentation speed, must also homogenize the pulp. sedimented, avoiding size segregation in the thickener compression zone, located at the bottom of said equipment. Finally, a study of the values obtained in the design of the thickener will also be carried out, for all the doses of flocculant used in this work, and compare them with the two previous methods and analyze if the values obtained for each of the mentioned methods agree.

Currently in Chile and worldwide copper mining, the water resource is scarce and of vital importance within the existing concentration processes for copper ore, and for this reason, the improvements made in the liquid separation processes are of vital importance in copper mining.

For this reason, the present study is carried out to improve solid–liquid separation processes. Methods were studied and proposed to help determine the optimal dose of flocculant in a copper concentrate ore, and thus have more information to contribute to the improvement of the use and recovery of process water in thickeners, which currently values of 75% recovery of this vital element are reached.

2 Adorjan Thickeners Design Method

This method [9, 10] considers the forces existing between the particles that make up the pulp under study; Therefore, he believes that the solid concentration of the compression zone depends on the pressure of the latter, therefore, on the height of the sediment in compression. In this regard, Adorjan when studying this phenomenon indicated that: “if a pulp presents significant compressive forces, the dimensions of a thickener cannot be calculated from the discontinuous sedimentation test”, therefore, compression and permeability parameters must be applied on a new line and should be grouped per affiliation.

2.1 Thickener Area

The Area required by a Thickener calculated by the Adorjan method is:

$$A = \frac{Q_F}{\rho_s v_S} \left(\frac{1}{\phi_F} - \frac{1}{\phi_D} \right) \quad (1)$$

where Q_F is the flow of feed to the thickener, ϕ_F is the volumetric fraction of feed solids to the thickener, ϕ_D is the volumetric fraction of solids from the thickener discharge, ρ_s is the density of the solid, ρ_f is the density of the fluid, and v_S is the sedimentation rate of the feed pulp.

To calculate the sedimentation rate, the Richardson and Zaki equation [13] shown below was used:

$$v_S = v_\infty (1 - \phi)^n \quad (2)$$

where v_∞ and n are parameters of the equation, and v_S is the terminal velocity of a particle that is, the sedimentation rate of a particle in an infinite dilution medium.

To calculate the critical volumetric fraction of solids, the Michaels and Bolger Equation [14] shown below was used:

$$v_S = v_\infty \left(1 - \frac{\phi}{\phi_m} \right)^{4.65} \quad (3)$$

where v_∞ and ϕ_m are parameters of the equation.

The operation of a thickener under critical conditions requires additional consideration of an appreciable height so that the pulp can settle, since any increase in the feed rate will take the solids to the overflow zone. Therefore, a thickener should be operated up to a certain fraction of the critical feed flow. Adorjan defined a factor to control this condition, and called it “load factor”, which is defined by:

$$Q = \lambda QF, \quad \text{donde } 0 < \lambda < 1 \quad (4)$$

Choosing a suitable load factor λ will result in a successful thickener operation, since fluctuations do not affect efficient operation, even under critical conditions.

Replacing (2) and (4) in (1), we finally have that the area required by the thickener is:

$$A = \frac{Q}{\lambda \rho_s v_\infty} \frac{\left(\frac{1}{\phi_F} - \frac{1}{\phi_D}\right)}{(1 - \phi_F)^n} \quad (5)$$

2.2 Thickener Height

To calculate the compression parameters of the pulp to be studied, the equation of Concha and Barrientos [8, 11, 12] was used, shown below:

$$\sigma_e = a e^{b\phi} \quad (6)$$

Using this equation, Adorjan's method returns the following expression:

$$\frac{dh}{d\phi} = \frac{a b e^{b\phi}}{\Delta \rho \phi g \left[1 - \frac{Q J^*}{\rho_s A v_\infty (1 - \phi)^n} \right]} = f(\phi), \quad \phi > \phi_c \quad (7)$$

where $J^* = (1/\phi - 1/\phi_D)$.

Equation (7) gives us a relationship between the concentration of the solid and its height in the thickener.

As all the parameters of the previous equation are separable variables, the fourth order Runge–Kutta method was used, whose values are calculated with an increase in the volumetric fraction of solids of δc , obtaining: $k_1 = F(c_j)$, $k_2 = F(c_j + \delta c/2)$, $k_3 = F(c_j + 2\delta c/3)$ y $k_4 = F(c_j + \delta c)$. Therefore, the value of the height of the thickener is given by

$$h_{j+1} = h_j + \frac{1}{8}(k_1 + 3k_2 + 3k_3 + k_4) \quad (8)$$

At this point an additional value must be added for the feeding, clear water area and the conical base that it must have in the discharge. The extra height is around 1 m.

3 Experimental Procedure

The mineral used corresponds to copper concentrate from columnar flotation. To obtain the solid sample, a 300 kg drying stage was carried out. Initial sample in an electric stove, which later with the use of the rifle cutter and the cone and quartering, respectively, a representative sample of 2 kg was obtained for the purposes of granulometric analysis and determination of the density of the copper concentrate.

For the granulometric analysis, the Ro-Tap equipment was used and 500 g of mineral were weighed, where the Tyler (#) meshes were considered: from 14 to 400. The determination of the mineral density was carried out by means of the pycnometer method, conventional. The flocculant solution used for the discontinuous sedimentation tests was SH-913 with a concentration equal to 0.1 (g/L) of solution.

To determine the optimal dose of flocculant (by sedimentation rate and sediment granulometry method), discontinuous sedimentation tests were carried out, for a volumetric fraction of 0.0824 (value used in industrial operation), in 1000 mL test tubes for the flocculant doses of: 0, 1, 2, 3, 4, 5, 6, 7, 8, 9, 10, 12, 14, 16, 18 and 20 (g/t). To determine the sedimentation rate of the pulp, it was used in the Design of Conventional Thickeners (DEC) program [15]. To obtain the granulometry of the sediment, it was decided to consider a height of 5 cm from the bottom, as a representative sample of the sediment to be studied; therefore samples of approximately 5 cm were taken for each discontinuous sedimentation test with the different doses of flocculant mentioned (0 to 20 g/t). These samples were filtered and dried in the electric oven and their granulometry was subsequently calculated considering the coarse fraction as +270 # and the fine fraction as -325 #.

To calculate the area and height of a thickener by the Adorjan method, it is necessary to determine the sedimentation and compression parameters of the pulp. In the case of determining the sedimentation parameters, discontinuous sedimentation tests were performed for the doses of 0, 4, 7, 10, 14 and 20 (g/t), for the range of volumetric concentrations of: $\phi = 0.025, 0.030, 0.035, 0.040, 0.045, 0.050, 0.055, 0.060, 0.065, 0.070, 0.080, 0.090, 0.100, 0.110, 0.120$ and 0.130. The sedimentation parameters calculated correspond to the parameters of the equation Richardson and Kaki [13] (v_∞ and n) and Michaels and Bolger [14] (ϕ_c), which were calculated for each of the aforementioned doses of flocculant, using DEC software [15].

To determine the compression parameters, discontinuous sedimentation tests were carried out, with an initial concentration of $\phi_0 = 0.20$, for the flocculant doses of 0, 4, 7, 10, 14 and 20 (g/t), which are the same as the previous case, in a 10 cm sedimentation column, diameter and 10 L of total capacity, which has a series of samplers that allow the measurement of the concentration at different heights in a quasi-stationary state, as presented in Fig. 1 and thus be able to measure the volumetric fraction versus height of the sediment, and with these data calculate the effective solid effort versus the sediment height, and calculate the parameters of the Concha and Barrientos equation.

In these tests, the samples were taken when the sedimentation rate had values close to 1 (mm/min), which was considered a quasi-stationary state. Samples of

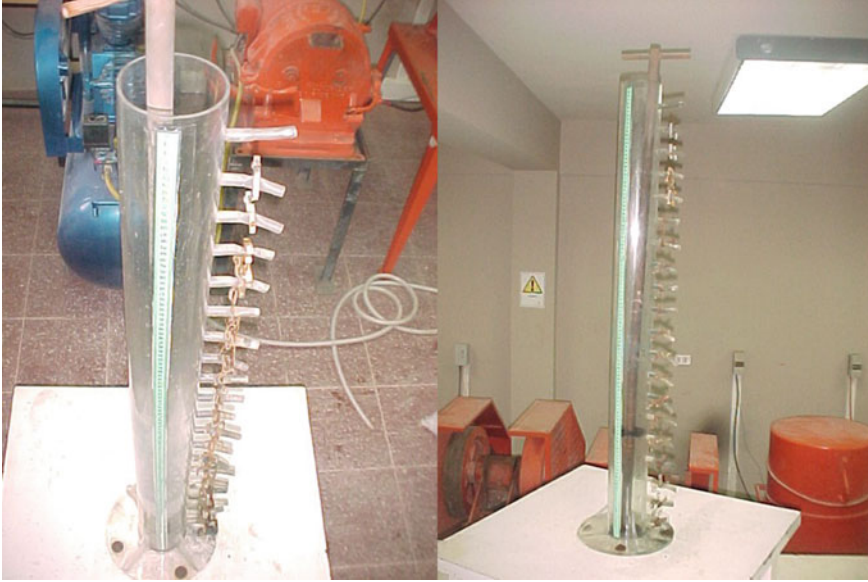


Fig. 1 Column of sedimentation used to determine the profile of concentration in tests of batch sedimentation

approximately 50 mL of the pulps taken at different compression heights, were weighed and dried to determine the percentage of solids and the volume fractions (ϕ) at these different heights of the sediment in the column.

4 Results

4.1 *Maximum Sedimentation Rate Method*

The results of the experimental tests of discontinuous sedimentation for a volumetric fraction of 0.0824, and for flocculant doses between 0 and 20 (g/t), according to the procedure already described, are shown in Fig. 2.

The analysis of this figure gives the result that for Flocculant doses greater than 4 (g/t) a significant increase in sedimentation rate is not achieved, so this method indicates that the optimal dose would be 4 (g/t).

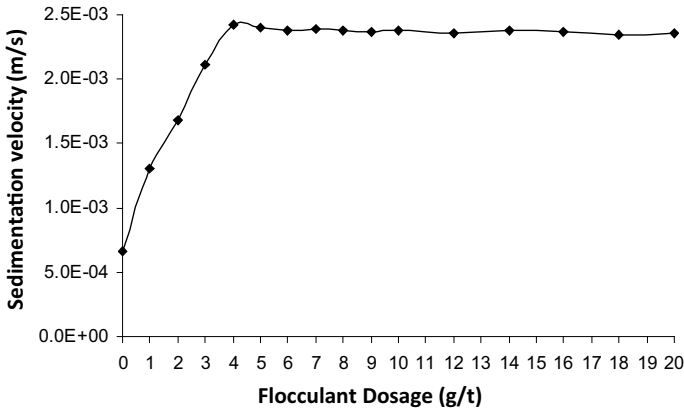


Fig. 2 Velocity of sedimentation against flocculant’s rate, for tests of batch sedimentation in a column of 1000 (cm³) and with $\phi_0 = 0.0824$

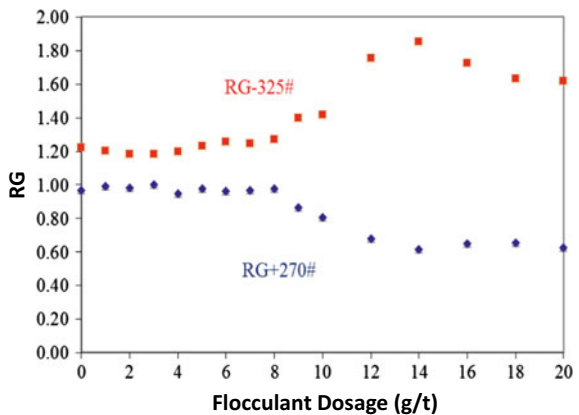
4.2 Sediment Granulometry Method

For the same experimental tests of the previous point, the granulometry of the sediment was calculated, and a dimensionless number called “granulometric ratio (RG)” is used, defined as:

$$RG(\text{accumulated/retained mesh}) = \frac{\% \text{accumulated/retained mesh in sediment}}{\% \text{accumulated/retained mesh in the sample}} \tag{9}$$

In this case, the RG (+270 #) and RG (−325 #) were studied, which are shown in Fig. 3.

Fig. 3 Granulometer ratio against flocculant’s rate, for tests of batch sedimentation in a column of 1000 (cm³) and with $\phi_0 = 0.0824$



In this figure, it is observed from the non-use of flocculant that the mineral does not have size segregation when settling, since the RG (+270 #) in this condition is 0.97, therefore the amount of thicknesses in the sediment it is practically the same as in food. For this same dose, the RG (−325 #) is 1.22; which indicates that the fines sediment in a greater proportion than the coarse ones. When increasing the dose up to 7 (g/t) there are no significant changes in the thicknesses, since the RG (+270 #) since it increases from 1.22 to 1.25; and for fines the RG values (−325 #) vary between the order of 0.95 and 0.97, so it can be considered constant. For higher doses, an increasing trend in the amount of fines is obtained in the sediment until obtaining a RG (−325 #) of 1.85 at 14 (g/t), a value that decreases slightly (up to 1.61) for higher flocculant doses; which shows that there is 85% more fines present in the final sediment, with respect to the initial quantity; Furthermore, with respect to the amount of coarse, the best value is also obtained for a dose of 14 (g/t) which corresponds to a RG (+270 #) of 0.61, which indicates that at that dose the fines settle preferentially by on the coarse mineral, maintaining a constant tendency to continue increasing the dose.

The global behavior of the mineral indicates that there is no segregation of sizes, by not using flocculant, and that it is only possible to have an increase in the amount of fines in the sediment, from a dose of 8 (g/t) obtaining a maximum value in sedimentation of fines for 14 (g/t). In addition, the explanation of this behavior must be supported by the measurement of yield stress [16] and also a study, not carried out so far, to analyze the effect of adding flocculant on each pure mineral species, and also see the synergistic effect when there are other mineral species.

4.3 Thickener Design Evaluation Method

To use the Adorjan method [9, 10], it is necessary to determine the sedimentation parameters, therefore, discontinuous sedimentation tests were performed for flocculant doses of 0, 4, 7, 10, 14 and 20 (g/t), for: $\phi = 0.025, 0.030, 0.035, 0.040, 0.045, 0.050, 0.055, 0.060, 0.065, 0.070, 0.080, 0.090, 0.100, 0.110, 0.120$ and 0.130 ; It is also necessary to determine the compression parameters, for which discontinuous sedimentation tests were carried out with $\phi_0 = 0.20$, for flocculant doses of 0, 4, 7, 10, 14 and 20 (g/t).

Sedimentation parameters

The values obtained are shown in Tables 1 and 2, shown below.

The parameter v_∞ increases in a linear way with the increase in the flocculant dose, which is verified by performing a linear regression, the equation $y = 5.51 * 10 - 4x + 1.9515$ is obtained, where “y” is the dilution rate infinite and “x” is the flocculant dose, and the parameter $r^2 = 0.9841$. The trend of the parameter “n” will be mentioned later in conjunction with the capacity of the thickener.

The critical concentration has the lowest value for sedimentation without flocculant, which is logical since the limit concentration value between free and obstructed

Table 1 Parameters of sedimentation of the slurry, of the Richardson and Zaki [13] equations

Sedimentation parameters	Flocculant dosage (g/t)					
	0	4	7	10	14	20
$v_{\infty} * 10^2$ (m/s)	1.95	2.16	2.29	2.54	2.80	3.00
N	31.29	28.58	28.20	29.02	30.54	27.46
r^2	0.987	0.996	0.999	0.998	0.999	0.999

Table 2 Parameters of sedimentation of the slurry, of the Michaels y Bolger [14] equations

Sedimentation parameters	Flocculant dosage (g/t)					
	0	4	7	10	14	20
ϕ_c	0.051	0.053	0.058	0.061	0.062	0.069
r^2	0.977	0.993	0.999	0.999	0.998	0.998

sedimentation will increase as I add flocculant, since the addition of the latter increases the speed of sedimentation of the pulp, causing the pulp to settle in a free form that is, without interference between particles for slightly higher concentrations; therefore the critical concentration must grow until reaching a limit value [12, 17], a situation that is not reached in this working range. The explanation of this behavior is suggested to study considering sedimentation studies of pure mineral species and in controlled mixtures, and to integrate the measurement of the pulp yield effort, in the sedimentation conditions to be studied [16].

Compression parameters

The values obtained are the following (Table 3).

The trend presented by parameter “a” will be discussed later, since it will be carried out together with the analysis of the height obtained for the thickener.

Thickener Design

Using as design values, a feed of 2500 (t/d), feed volume fraction ϕ_F of 0.146, discharge volume fraction ϕ_D of 0.239, ore density of 4.77 (g/cm³) and a load factor λ of 0.90; the values obtained are the following (Table 4).

The trend shown by the Sedimentation Unit Area as a function of the flocculant dose, has an expected behavior for flocculant doses from 0 to 14 (g/t), in which a

Table 3 Parameters of sedimentation of the slurry, of the Concha and Barrientos equations

Sedimentation parameters	Flocculant dosage (g/t)					
	0	4	7	10	14	20
a (N/m ²)	216.074	0.270	21.230	18.690	1.576	1.101
b	4.672	19.604	9.961	10.428	16.947	19.242
r^2	0.99	0.92	0.98	0.98	0.73	0.94

Table 4 Design valor's of the thickener, for the Adorjan [9, 10] methods

Sedimentation parameters	Flocculant dosage (g/t)					
	0	4	7	10	14	20
Height (m)	1.77	1.04	1.33	1.32	1.13	1.16
Diameter (m)	23.9	16.5	15.3	16.0	18.3	12.3
A.U. (m ² /t)	0.180	0.086	0.074	0.081	0.105	0.048

maximum value of the designed unit area is shown without the addition of flocculant, which is obvious, under these conditions, the sedimentation will be of lower quality when compared to the sedimentation of a flocculated pulp; for higher doses the values of unit sedimentation area decrease until reaching a minimum value of 7 (g/t), which increases together with the greater addition of flocculant doses up to a dose of 14 (g/t), which shows an intuitively expected behavior, since in general the thickener design methods present a behavior of this type. However, when the flocculant dose is increased to 20 (g/t), there is a further decrease in the sedimentation unit area, which cancels the dose of 7 (g/t) as a minimum value. The explanation for this behavior is observed when comparing the trend of the parameter “n” of the Richardson and Zaki equation together with the unit sedimentation area with respect to the flocculant dose (see Fig. 4), which are exactly the same, therefore that it is concluded that this parameter “n” has a great influence on the values of the unit sedimentation area; However, a physical explanation of this behavior is not possible to obtain from the measurements made, so it is suggested to append to the quantified variables, the measurement of the yielding effort of the pulp, as well as to verify this behavior, using a pilot thickener to validate this behavior, making direct measurements of continuous sedimentation; since it is possible that the Richardson and Zaki equation is not suitable for use in the design of thickeners by the Adorjan method and that it

Fig. 4 Thickener unitary area design and parameter “n” against flocculant’s rate

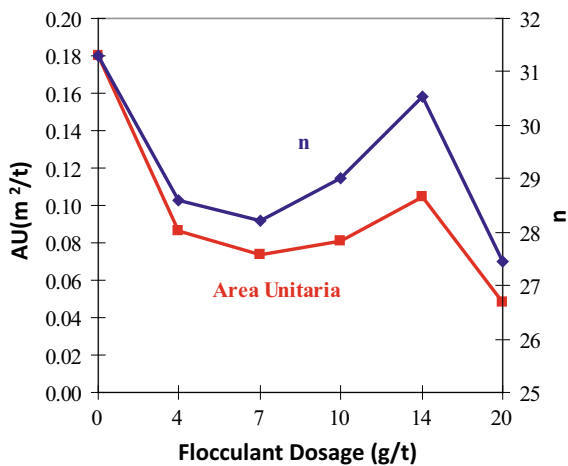
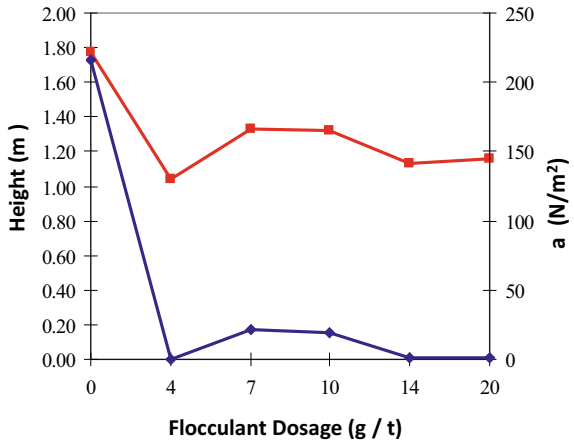


Fig. 5 Thickener height design and parameter “a” against Flocculant’s rate



does not correctly represent the aforementioned behavior. It is convenient to point out that in a study carried out for tailings ore from this same mining company [12], the behavior shown by both mentioned variables versus the flocculant dose was exactly the same as that obtained in this study, and for this reason it was postulates to validate the use of the Richardson and Zaki equation for the design of thickeners using the Adorjan method.

With respect to the trend shown by the design values of Thickener Height with respect to the dose of flocculant, it shows a value of maximum height necessary for a pulp without flocculant, which is obvious due to sedimentation in the most adverse conditions studied; to reach a minimum value for a dose of 4 (g/t) and for doses between 7 and 20 (g/t) the height varies between 15 and 30 cm (discounting the value of an additional meter mentioned with the description of the method), which are values that for equipment design purposes are slight differences, as to affect the decision to purchase a thickener, so they can be considered negligible.

Notwithstanding the observation, it should be noted that the behavior obtained for the height of the thickener versus the flocculant dose is exactly the same as the trend shown by the parameter “a” of the Concha and Barrientos equation; This leads to the same previous conclusion, referring to the fact that the behavior must be explained by making measurements of other parameters such as the yield stress measurement, in addition to being validated by a study carried out on a pilot thickener (Fig. 5).

5 Conclusion

- The use of the maximum sedimentation speed method indicates that the optimum flocculant dose is 4 (g/t).

- The sediment granulometry method shows that there are no great differences in the segregation of solids in the sediment, when using flocculant doses between 0 and 7 (g/t), so this method informs that the use of flocculant.
- When evaluating the design method of the Thickener Unit Area, it informs that when analyzing the sedimentation unit area values, they have a behavior that needs to be corroborated, carrying out continuous sedimentation operation measurements in a pilot thickener, to question the validation of use, of the Richardson and Zaki equation, within the equation proposed by Adorjan. Notwithstanding the previous comment, the optimal value of the sedimentation unit area is for a flocculant dose of 20 (g/t).
- When evaluating the design method of the Thickener Height, as in the previous case, its behavior must be corroborated, with experimental tests of continuous sedimentation carried out in pilot thickeners. The relationship of the values obtained for the height of the thickener are clearly dependent on the parameter “a” of the Concha and Barrientos equation.
- It is suggested to annex to this work, the study of sedimentation of mineral pulp, controlling the amount of mineral species within the pulp, in order to know the direct influence of the flocculant additive, on each mineral species, and on the controlled mixture of species minerals.
- It is suggested to annex to this work measurements of the yield stress of the mineral pulps, in all the studied conditions, since it is required to have a rheological support in the explanations of the obtained behaviors.
- The corroboration of the design of a thickener using the Adorjan method is required, as well as the possibility of generating a new model, from the validation of the results obtained by verifying them with the direct operation of a pilot thickener.

The present study evaluates a specific concentrate for a certain mining company, in a future study it is necessary to evaluate different types of copper concentrates from different origins.

References

1. Mishler, R.: *Eng. Mining J.* **94**(14), 643–646 (1912)
2. Coe, H., Clevenger, G.: *Trans. AIME* **55**, 356–385 (1916)
3. Kynch, G.: *Trans. Faraday Soc.* **48**, 166–176 (1952)
4. Talmage, W., Fitch, E.: *Ind. Eng. Chem.* **47**, 38–41 (1955)
5. Yoshioka, N., Hotta, Y., Tanaka, S., Naito, S., Tsugami, S.: *Chem. Eng. Japan* **21**, 66–74 (1957)
6. Hassett, N.: *Min. Sci.* **1**, 24–40 (1968)
7. Concha, F., Barrientos, A.: *Kona*, No 11, pp. 79–104 (1993)
8. Concha, F.: *Manual de Filtración y Separación, CETTEM, Univ. de Concepción*, pp. 41–232 (2001)
9. Adorjan, L.: *XI IMPC, Caglary*, pp. 1–22 (1975)
10. Adorjan, L.: *Trans. Inst. Min. Met., Sec C*, **85**, 157–163 (1976)
11. Quiero, A.: *Memoria de Ingeniero Civil Metalúrgico, Facultad de Ingeniería, Universidad de Concepción* (1994)

12. Zambra, R.: Memoria de Ingeniero Civil Metalúrgico, Departamento de Ingeniería, Universidad Arturo Prat (2005)
13. Richardson, R., Zaki, W.: Part. I. Trans. Inst. Chem. **32**, 35–53 (1954)
14. Michaels, A., Bolger, J.: Ind. Eng. Chem. Fund. **1**(1), 1962 (1962)
15. SOFTWARE DEC, Diseño de Espesadores Convencionales (2000)
16. Bustamante, O., Aguilera, G., Gomez, H.: VII Jornadas Argentinas de Tratamiento de Minerales (2004)
17. Valenzuela, R.: Memoria de Ingeniero Civil Metalúrgico, Facultad de Ingeniería, Universidad de Concepción (1994)

Investigation on Critical Characteristics of Mineral Oil by Using h-BN Nanoparticles



P. Sathya, M. Ravindran, and R. Harichandran

Abstract This work shows how the physical, electrical, and thermal properties of mineral oil vary according to the mixture of nanoparticles. Nanoparticles of h-BN were injected into the mineral oil individually, with particle volume portions ranging from 0.1 to 0.4%, to create nanofluids (NFs) that act on the oil's fundamental properties. The qualities like flash point, breakdown voltage (BDV), fire point, and viscosity were estimated at the room temperature where it depends upon the standards such as IEC and ASTM standards. When the mineral oil is heated in the presence of nanoparticles, the breakdown voltage will increase. Meanwhile, the flash point and fire point have increased, expanding from 10 to 15 °C, and the viscosity has changed as nanoparticles have grown in size.

Keywords Mineral oil · Nanoparticles · Nanofluids · Blending · Transformers

1 Introduction

In the transmission and circulation organization, transformers are the most urgent and significant part. The protecting oil (transformer oil) is utilized to give electrical protection to inside components of transformers just as fill in as a hotness trade medium. The transformer's optimal activity is determined by the transformer oil's electrical, physical, and chemical properties [1]. The dielectric protection method is to be faulted for most of the transformer disappointments. Nanoparticles, of course,

P. Sathya

High Voltage Engineering, National Engineering College, Kovilpatti, Tamil Nadu, India
e-mail: 2054003@nec.edu.in

M. Ravindran (✉)

EEE, National Engineering College, Kovilpatti, Tamil Nadu, India
e-mail: ravindranm786@gmail.com

R. Harichandran

Mechanical, National Engineering College, Kovilpatti, Tamil Nadu, India

are mixed into transformer oil to work on securing properties [2]. The transformation of magnetite nanoparticles into transformer nanoparticles increases the dielectric strength of the AC and driving circuits. The outer attractive field direction, on the other hand, determines the scattering of magnetite nanoparticles in transformer oil. The magnetite nanoparticles constructed a scaffold across the field hole between the anodes in an attractive field, bringing down the transformer oil's dielectric strength [3]. These liquids ought to have adequate dielectric solidarity to support the possible scope of electrical pressure produced during administration. The dielectric strength of half and half nanofluids was analyzed, and a decrease was noted when contrasted with unadulterated oil [4, 5]. It has explored lightning motivation breakdown voltage of regular and engineered ester oil-based Fe_2O_3 , Al_2O_3 , and SiO_2 nanofluids [6]. The dielectric consistent increments and the dielectric misfortune steady decline with the consideration of nanoparticles. From the writing study, larger part properties have chosen TiO_2 , Al_2O_3 , CuO , and SiO_2 as nanoparticles. The principle worry of the previously mentioned nanoparticles is that they have a lower grating coefficient esteem and are more costly. Most of distributed examination centers around the effect of nanoparticles on the warms and dielectric properties of greasing up oils [7]. The dielectric and warm properties of non-edible cottonseed oil were investigated by infusing h-BN nanoparticles. The nanofluids were used to overcome cottonseed oil's confined dielectric and warm properties. CSO-based nanofluids were studied for their dielectric and warm properties [8]. The impact of nanoparticles blends on AC breakdown voltage of mineral oil. They have seen that the combinations of nanoparticles (Al_2O_3 , SiO_2 , and Fe_3O_4) is additionally performed utilizing typical and Weibull laws [9]. In the existing work, TiO_2 , SiO_2 , Al_2O_3 , and CuO nanoparticles are used; I now use h-BN nanoparticles, because they have higher dielectric and thermal properties. Mineral oil is a complex compound of hundreds of different chemical compounds, with many molecules comprising carbon and hydrogen. Although mineral oil continues to be a major technological solution compared to the economy, its environmental impact must be considered.

Nanoparticles are added to transformer oil in this paper, and their attributes are investigated at room temperature with the purpose of increasing the physical and electrical properties of mineral oil. This work is to expand the presentation of dielectric and actual properties utilizing hexagonal boron nitride. In this current work, the h-BN nanoparticle scattered in mineral oil orchestrated, and its viscosity, flash point, fire point, and breakdown voltage and execution were researched for different volume centralizations of h-BN nanofluids.

2 Experimental Details

A. Preparation of Nanofluids

In our review, the h-BN nanoparticles were included in a mineral oil to create the nanofluids. The h-BN nanofluids were arranged utilizing underneath referenced cycle with different volume focuses from 0.1 to 0.4% (Fig. 1).

Utilizing an attractive stirrer, the mixture of h-BN nanoparticles and base oil takes place. During the scattering of nanoparticles, the magnetic stirrer's speed and the temperature of the examples were kept at 1500 rpm and 40 °C, individually, for a measure of 3 h. From that point forward, the determined measure of h-BN is added to the arrangement and upset for an additional 30 min at a similar temperature. From that point onward, a test sonicator is utilized to sonicate for an hour to get steady scattering. The h-BN nanofluid samples at different volume concentrations are shown in Fig. 2.

B. Breakdown voltage measurements

The breakdown voltage of fluid protection is a proportion of the capacity of fluid protection to endure electrical pressure created in working circumstances.

At the room temperature, by using oil test cup the sample's breakdown voltage was measured with specified standard (IEC 60156). Figure 3 shows the oil test cup. The oil testing cup has set up transformer capable of giving up to 60 kV.

For the breakdown voltage measurement of oil, the gap space is set as 2.5 mm. First, the oil cup is washed with given transformer oil. It is then loaded up with transformer oil, whose dielectric strength is not set in stone. It is permitted to stand adequately and regardless to a stature at least 40 mm from the highest point of the cathode. The oil test is given two anodes. The oil is filled inside the cup, and the bar



Fig. 1 Magnetic stirrer setup



Fig. 2 Preparation of samples

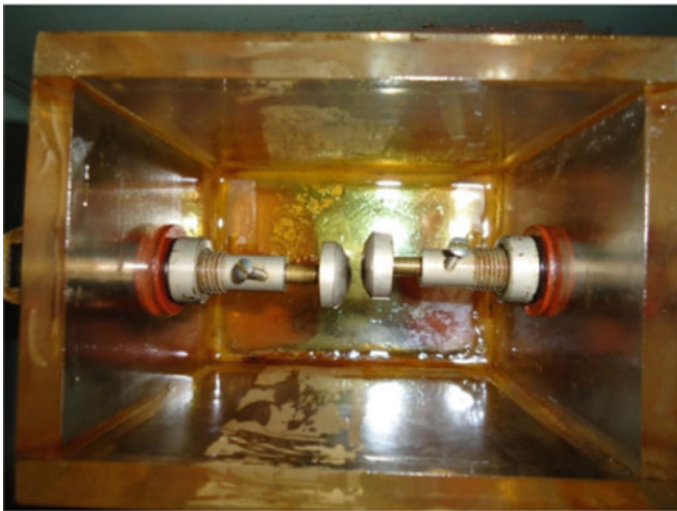


Fig. 3 Oil test cup

of the testing pack is inundated in the oil for a profundity of 40 mm. The stock is shifted through the variac, and the breakdown of the optional voltage is noted.

C. Flash point and Fire point measurements

Low combustibility is one of the significant contemplations being developed toward better fluid protection. The temperature at which the molded smoke is ready to burn-through is known as the fire point. From the room temperature, the flash point



Fig. 4 Pensky martin apparatus

and fire points are measured with the use of Pensky Martin closed cup apparatus as shown by the standard ASTM D 93. Figure 4 shows the Pensky Martin shut cup analyzer. The model was placed in a metal test cup, and the temperature was raised with the help of an electric boiler with temperature control. When a little test fire was put into the model, the temperature corresponding to the flash point was determined with smolder improvement and ephemeral fire on the oil surface. By warming 50 ml oil test under controlled conditions in test cup, flash point is estimated at which temperature, combustible fume on the outer layer of oil test is delivered when misleadingly presented a fire in test hole.

D. Viscosity measurement

The transformer oil should have a medium consistency, with the idea that oil will flow freely in the transformer tank for cooling purposes. The temperature affects the oil's consistency.

The viscosity is the physical property of transformer oil which is measured by the apparatus called redwood viscometer by the standard ASTM D 445. The redwood viscometer is displayed in Fig. 5.

In a silver-plated oil cup, the model was filled. Allow the movement of test through the ball valve (orifice) to accumulate the model in the test receptacle by opening the ball valve (orifice). Measure the amount of time required for a social gathering with 50 mL of test in a receptacle. Since then, viscosity has not been fixed in stone. There is a little aperture of normal size beneath the falling head.



Fig. 5 Redwood viscometer

3 Results and Discussions

A. Properties of Base oil

The properties of base oil (transformer oil) were measured at room temperature according to the standards ASTM and IEC. The properties are shown in Table 1.

B. Breakdown voltage

The breakdown voltage of transformer oil-based nanofluids should be addressed in light of the fact that transformer oil is designed to act as an electrical cover in transformer devices that operate in high-voltage environments. If the oil's breakdown voltage cannot keep the transformer from reaching the maximum electric field strength, the oil will fizzle. In this vein, a high breakdown voltage is a critical characteristic of high-quality transformer oil. The breakdown voltage of h-BN-containing transformer oil-based nanofluids was investigated. The after-sample measurements

Table 1 Properties of base fluids

Properties	Values
Breakdown voltage (kv)	32
Flash point (°C)	160
Fire point (°C)	175
Viscosity (csk)	40

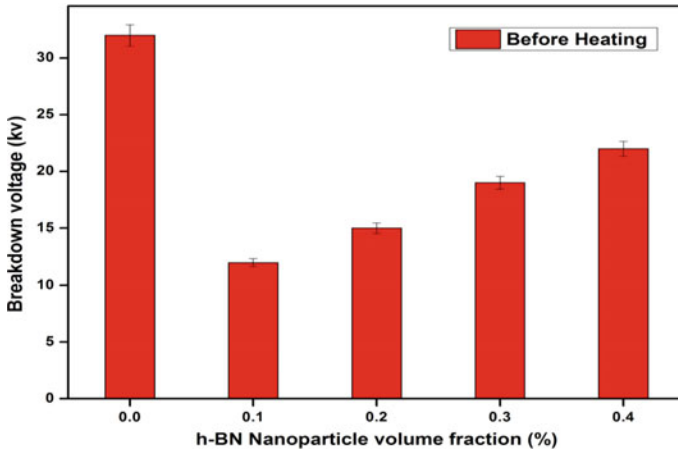


Fig. 6 Breakdown voltage (after sample preparation)

Table 2 Nanofluid measurements of breakdown (after sample preparation)

h-BN nanoparticle volume fraction (vol%)	Breakdown voltage (kv)
0.1	12
0.2	15
0.3	19
0.4	22

are shown in Table 1. The after-sample measurement graph is shown in Fig. 6. The sample of the nanofluids was prolonged when compared to the basic fluid, as shown in Table 2. Figure 7 shows the breakdown voltage assessment curve of the models before they were warmed up to 100 °C. The breakdown voltage was developed in the particle volume section of nanoparticles, according to the breakdown voltage assessment. Before heating, the breakdown voltage was minimum range, because the moisture was presented; after heating the samples, the moisture was removed and the breakdown voltage is maximum range.

C. Flash point and Fire point

The flash point and fire point are the thermal properties of the transformer oil which indicates the ignition of air. At room temperature, Table 3 displays the deliberate fire point and flash point of mineral oil and nanofluids. Estimating a fluid’s flash point requires start is eliminated. This is not to be mistaken for the autostart temperature, which requires no start source. At the flash point, the fume might stop to consume when the wellspring of start is eliminated. Streak guide alludes toward both combustible fluids just as flammable fluids. Fire point is utilized to get to the danger of the materials capacity to help burning.

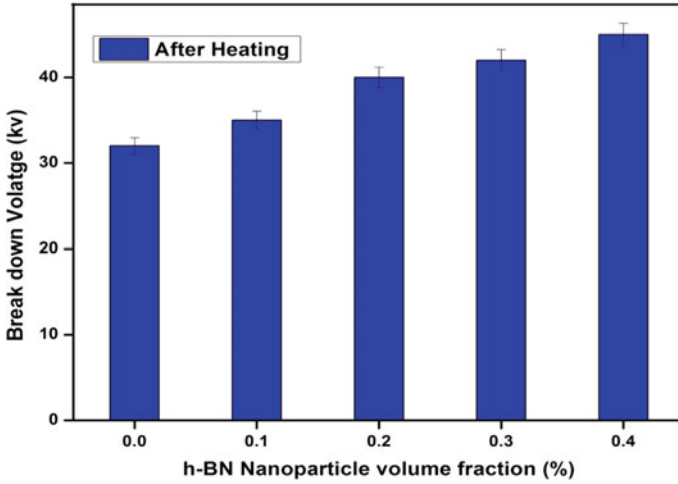


Fig. 7 Breakdown voltage (after heated up to 100 °C)

Table 3 Nanofluid measurements of breakdown voltage (after heating of samples up to 100 °C)

h-BN nanoparticle volume fractions (vol%)	Breakdown voltage (kv)
0.1	35
0.2	40
0.3	42
0.4	45

The fire point and flash point of nanoparticles are shown to be continuously expanding as the volume portion of the nanoparticles expands. Table 3 demonstrates that the flash point of nanofluids is similar to that of base liquids, whereas the fire point of nanofluids increases from 10 to 15 °C when compared to base liquid. The example will maintain ignition for 5 s at the fire location. Figures 8 and 9 provide a graphic depicting the analysis of fire point and flash point. The flash point and fire points are increased because the ignitions repeat as the liquid temperature continues to rise.

D. Viscosity

A high viscosity indicates good stream protection, whereas a low consistency indicates poor stream protection; viscosity changes were directly proportional to temperature. Pressure also has an effect on viscosity; high pressure causes the consistency to increase, and thus the oil’s heap conveying limit to increase.

The viscosity upsides of base mineral oil and arranged distinctive volume rates of nanofluids at various temperatures are given in Fig. 10. The consistency of base and nanofluids diminishes quickly with expanding temperature. Table 4 shows that the thickness of nanofluids diminishes in various volume portions. When the viscosity

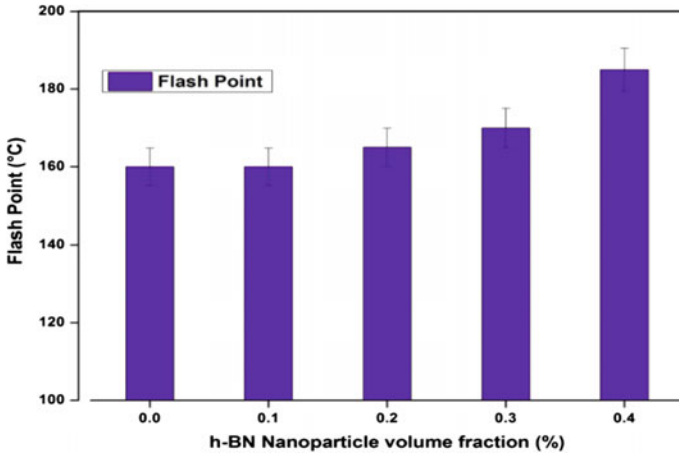


Fig. 8 Various samples of flash point measurements

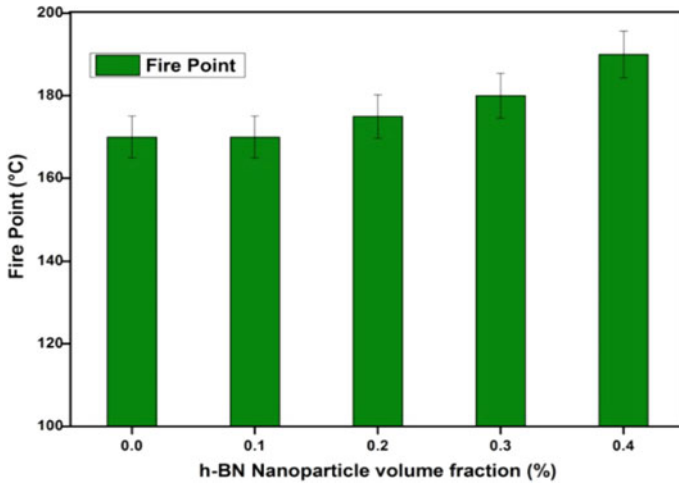


Fig. 9 Various samples of fire point measurements

analysis temperature for mineral oils intended for internal use is relatively normal. The viscosity of the mineral oil is more standard value when compared to the vegetable oil. Some approaches for lowering viscosity values have been proposed in the literature. As a result, the viscosity increased techniques should be used to operate the research mineral oil as transformers (Table 5).

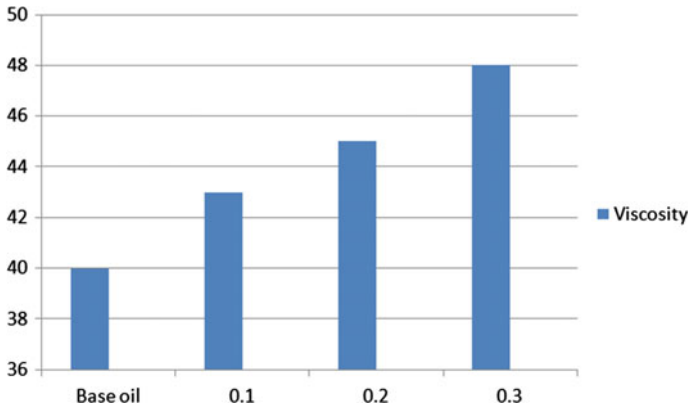


Fig. 10 Various sample measurement of viscosity

Table 4 Nanofluid measurements of flash and fire point

h-BN nanoparticle volume fractions (vol%)	Flash point	Fire point
0.1	160	170
0.2	165	175
0.3	170	180
0.4	185	190

Table 5 Viscosity measurements of nanofluids

h-BN nanoparticle volume fractions (Vol%)	Viscosity (cSk)
0.1	40
0.2	43
0.3	45
0.4	48

4 Conclusion

Nanofluids were created in this study by dispersing nanoparticles in mineral oil. At normal temperature, the essential features of nanofluids were examined.

1. The h-BN nanoparticles are added into the mineral oil which assembles the breakdown voltage, according to the assessment results. The breakdown voltage of nanofluids is increasing as the particle volume part of nanoparticles expands.
2. The flash point of the mineral oil is increased by including nanoparticles. Meanwhile, the temperature of the fire sites has increased from 10 to 15 °C.
3. When h-BN nanoparticles get dissolved in mineral oil, it results in increase of viscosity range.

According to the findings, adding nanoparticles to mineral oil increases the breakdown voltage and fire point while also increasing the viscosity.

For the future work, replacement of mineral oil by various vegetable oil will be done to determine the performance characteristics.

References

1. Khaled, U., Abderrahmane, B.: AC dielectric strength of natural ester oil—based Fe_3O_4 , Al_2O_3 and SiO_2 Nano—fluids. *IEEE Access* **7**, 60594–60601 (2019)
2. Salles, V., Bernard, S.: Investigated of structural and thermal properties of boron nitride nanoparticles. **168**, 287–295 (2011)
3. Javed, M., Aziz, A.: Synthesis of stable waste palm oil based CuO nanofluid for heat transfer applications. **54**(12), 3739–3745 (2018)
4. Mansour, D.A., Shaalan, E.M.: Multiple nanoparticles for improvement of thermal and dielectric properties of oil nanofluids. **13**(7), 968–974 (2019)
5. Yao, W., Wu, L.: Enhanced electrical insulation and heat transfer performance of vegetable oil based nanofluids. **2018**(4504028) (2018)
6. Yang, N., Huo, J.: Preparation and properties of thermally conductive polyimide/boron nitride composites. **6**(22), 18279–18287 (2016)
7. Hameed, A., Mukthar, A.: Synthesis, characterization, stability, thermo-physical properties and rheological behavior of MCWNTs—kapok seed oil based nanofluid. **277**, 812–824 (2019)
8. Muthu, R.N., Rajashabala, S.: Hydrogen storage performance of lithium borohydride decorated activated hexagonal boron nitride nanocomposite for fuel cell applications. **42**(23), 15586–15596 (2017)
9. Mansour, D.E., Elsaeed, A.M.: The role of interfacial zone in dielectric properties of transformer oil—based nanofluids. **23**(6), 3364–3372 (2016)

Implementation of ALU Using Partial Adiabatic Logic Style



S. Dhileep Kumar, Kasireddy Vathsalya, and R. Phani Vidyadhar

Abstract In the world we live in, new technologies are emerging and existing ones are being updated with new methods. Similarly, VLSI technology is also transforming their chips into smarter ones with the transition of technologies, but the complexity of the design increases which creates a higher level of power dissipation. Furthermore, with the increasing reliance on electronics, battery life is also an important factor, which makes power dissipation a concern (Yadav et al. Adiabatic Approach for Charge Restoration in Low Power Digital Circuits, pp. 473–477 [1]). One technique for reducing dissipating power while maintaining good performance is adiabatic logic in low-power VLSI. Computing consists of arithmetic operations on binary numbers, which are performed by all digital computers through arithmetic units. ALUs are one of the most crucial parts of a CPU (Central Processing Unit). Those basic building blocks are adopted using Cadence Virtuoso 90 nm technology (Sapna et al. in Comparative Analysis of ECRL and TSEL Adiabatic Logic Style [2]). Results obtained from the study indicate that designing ALUs using ECRL logic consumes less power than designing them using traditional logic.

Keywords VLSI (Very large scale integration) · ALU (Arithmetic logic unit) · Adiabatic · ECRL (Efficient charge recovery logic) · Full adder · Full subtractor

S. D. Kumar (✉) · K. Vathsalya · R. P. Vidyadhar
Department of Electronics and Communications, Vardhaman College of Engineering,
Shamshabad, Hyderabad, India
e-mail: sdhileep_18ec@vardhaman.org

K. Vathsalya
e-mail: kasireddyvathsalya_18ec@vardhaman.org

R. P. Vidyadhar
e-mail: rphaniv@vardhaman.org

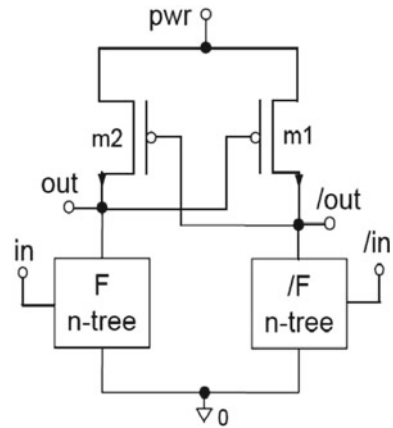
© The Author(s), under exclusive license to Springer Nature Singapore Pte Ltd. 2023
V. Bindhu et al. (eds.), *Proceedings of Fifth International Conference on Inventive Material Science Applications*, Advances in Sustainability Science and Technology,
https://doi.org/10.1007/978-981-19-4304-1_6

1 Introduction

An Arithmetic and Logic Unit (ALU) is a common component in every digital device which enables a device to perform different mathematical operations. Some of those operations are logical, Arithmetic, and shift operations. Logical operations which used in our design are AND, OR, XOR, and XNOR; similarly arithmetic operations which we used are addition and subtraction [3]. The ALU includes much more operations which makes the circuit's power consumption high. So, to reduce the power dissipation of ALU we are using a Partial Adiabatic logic style instead of conventional CMOS logic design. Partial Adiabatic logic style consists of four different types of forms, i.e., ECRL, 2N2N-2P, PFAL, and clocked adiabatic logic [4]. The form we used to design ALU is ECRL Fig. 1.

Efficient Charge Recovery Logic (ECRL) is one of the power reduction techniques in Partial Adiabatic Logic [5]. In ECRL, the pull-up network consists of two cross-coupled PMOS transistors and the pull-down network realizes the input function. In a pull-down network, one block realizes the true input logic and the other realizes the complement of the true logic function. ECRL logic gives two outputs: one is true logic output and the other is the complement of true logic output [6].

Fig. 1 ECRL block diagram



2 Literature Review

2.1 *Power Reduction of Half Adder And Half Subtractor using different Partial Adiabatic Logic Styles*

Rajan and Akshitha [7] used partial adiabatic logic techniques to reduce the power dissipation of half-adder and half-subtractor. They implemented half-adder and half-subtractor in ECRL, 2 N-2N2P, PFAL, CAL, and conventional CMOS logic. They calculated the average power for every technique and did a power analysis comparison. They concluded that when compared to the standard half-adder design, the ECRL adiabatic approach saves around 90.28 percent in power (average power), while the 2 N-2N2P, PFAL, and CAL half-adder techniques save about 87.54, 96.8, and 86% in power consumption. This is because the transistors in adiabatic logic are switched under specific conditions, and the energy dissipation is decreased by slowing down the pace of operation. They concluded that when compared to the standard half-subtractor design, the ECRL adiabatic approach saves around 84.97% in power (average power), while the 2 N-2N2P, PFAL, and CAL half-adder techniques save about 90.56, 96.45, and 84% in power consumption. Because the switching transition rate is reduced, the circuit uses the least amount of energy stored in node capacitance during a particular calculation step, allowing it to use that energy for the next level of computation. This is the reason why we chose adiabatic logic to implement ALU.

2.2 *An Alternative Approach To Low Power Application Circuits Using Adiabatic Logic*

To minimize the power dissipation of 2×1 MUX, full adder sum, and full adder carry, Bhati and Rizvi [8] employed partial adiabatic logic approaches. In PFAL and standard CMOS circuitry, they built 2×1 MUX, full adder sum, and full adder carry. They estimated the average power for each approach and compared the results in a power analysis. They found that the PFAL adiabatic technique saves roughly 87.32% in power dissipation when compared to the typical 2×1 mux design (average power). This is because in adiabatic logic, the transistors are switched under specified conditions, and the energy dissipation is reduced by slowing down the operating speed. They found that the PFAL adiabatic approach saves around 83.29% in power dissipation (average power) when compared to the standard full adder sum design and that the PFAL adiabatic approach saves around 88.29% in power dissipation (average power) when compared to the standard full adder carry design (average power). The circuit consumes the least amount of energy stored in node capacitance during a given calculation step because the switching transition rate is lowered, allowing it

to utilize that energy for the following level of computation. This is why adiabatic logic was chosen to build ALU.

3 ALU

3.1 Logical Block of ALU

Logic Block comprises four operations: AND, OR, XOR, and XNOR. The output of AND gate is high only when both inputs are high and vice versa. The output of OR gate is high when any one input is high and vice versa [9]. The output of the XOR gate is high when both inputs are distinct and vice versa. The output of the XNOR gate is high when both inputs are the same and vice versa Fig. 2.

$$AND = A.B$$

$$OR = A + B$$

$$XOR = A \wedge B$$

$$XNOR = A \odot B$$

Fig. 2 Logical block of ALU

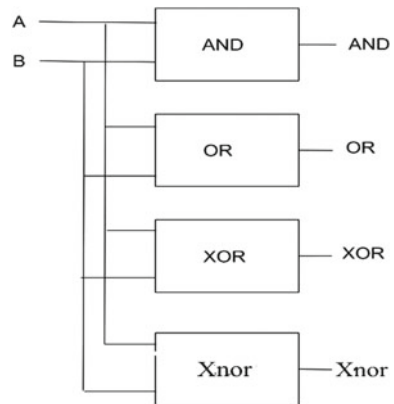
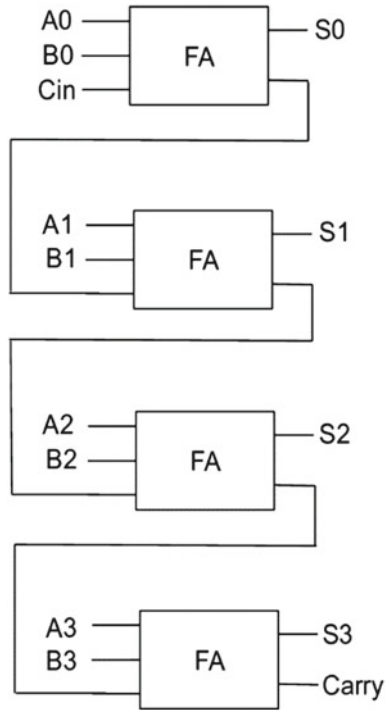


Fig. 3 Block diagram of 4-bit full adder



3.2 4-Bit Full Adder

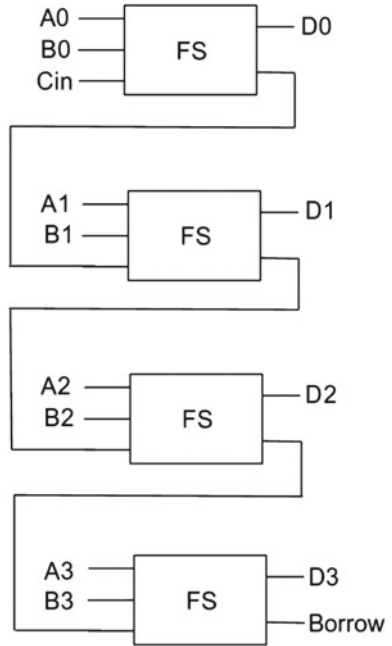
The 4-bit Full adder is a circuit that executes an addition operation on given two 4-bit binary numbers. As it is a full adder, the no. of inputs is three, i.e., A , B , C_{in} , and in each stage A , B inputs are given but C_{in} is given only for the LSB bit, and for the rest bits, the Carry which is resulted from the output of LSB bit is carry forwarded to next bit as C_{in} and the same goes for next bits also [10] Fig. 3.

$$\begin{aligned}
 \text{ADDER} &= A \wedge B \wedge C \\
 \text{CARRY} &= AB + BC + CA
 \end{aligned}$$

3.3 4-Bit Full Subtractor

The 4-bit Full subtractor is a circuit that executes a subtraction operation on given two 4-bit binary numbers [11]. As it is a full subtractor, the no. of inputs is three, i.e., A , B , C_{in} , and in each stage A , B inputs are given but C_{in} is given only for the LSB bit, and for the rest bits, the borrow which is resulted from the output of LSB

Fig. 4 Block diagram of 4-bit subtractor



bit is carry forwarded to next bit as C_{in} and the same goes for next bits also Fig. 4.

$$\text{DIFFERENCE} = A \wedge B \wedge C$$

$$\text{BORROW} = A' C_{in} + A' B + B C_{in}$$

3.4 4-Bit ALU

ALU is a unit that executes logical and arithmetic operations in digital computers. The ALU we designed is made using an 8×1 multiplexer [12]. It consists of four logical operations, i.e., AND, OR, XOR, and XNOR, and two arithmetic operations, i.e., adder (sum, carry) and subtractor (difference, borrow) Fig. 5.

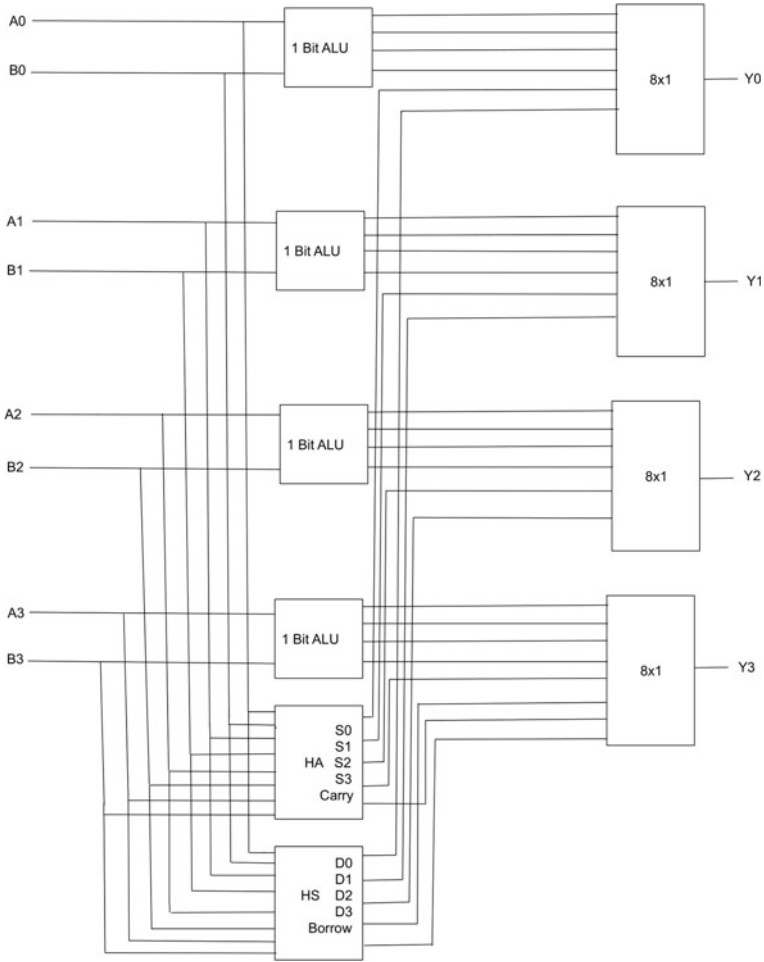


Fig. 5 Block diagram of 4-bit ALU

4 Simulations and Results

4.1 Conventional Circuits

4.1.1 Logical Block Circuit

Figure 6 is the picture of the logical schematic diagram. The outputs of this circuit are AND, OR, XOR, and XNOR. Figure 7 shows the logical block transient analysis.

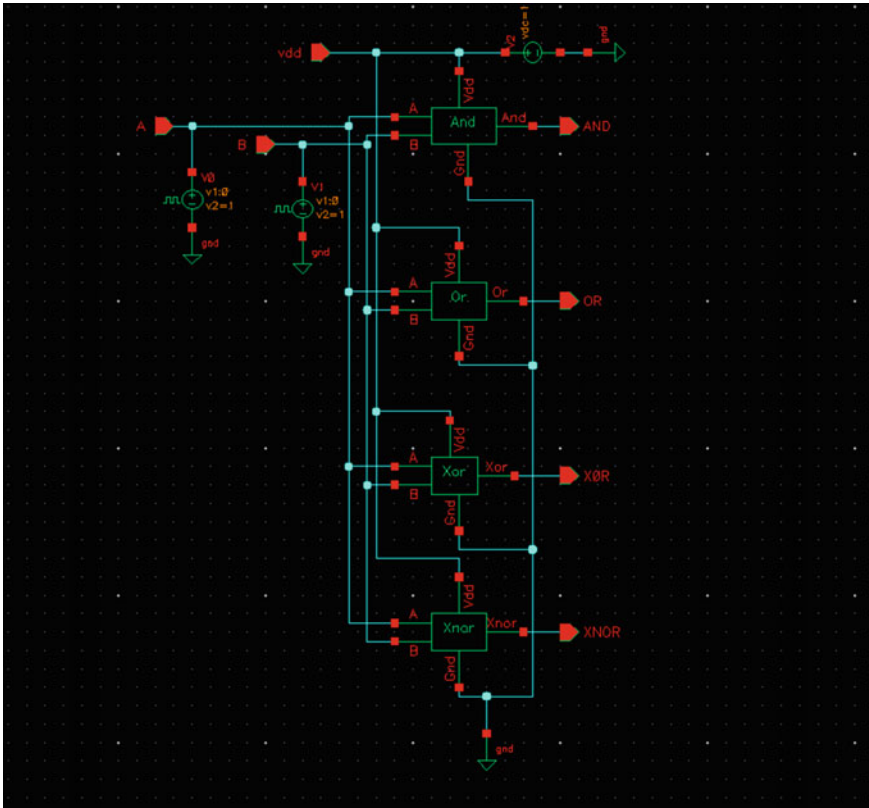


Fig. 6 Schematic of conventional logical block

4.1.2 4-Bit Full Adder

Figure 8 is the picture of the 4-bit adder schematic diagram. The outputs of this circuit are sum (S_0, S_1, S_2, S_3) and carry. Fig. 9 shows the full adder transient analysis.

4.1.3 4-Bit Full Subtractor

Figure 10 is the picture of the 4-bit subtractor schematic diagram. The outputs of this circuit are difference (D_0, D_1, D_2, D_3) and borrow. Fig. 11 shows the full subtractor transient analysis.

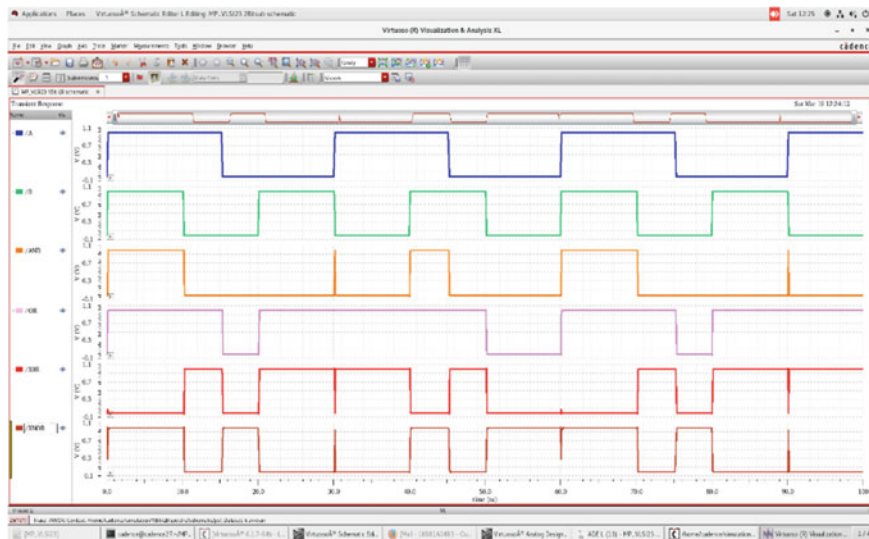


Fig. 7 Waveform of conventional logical block

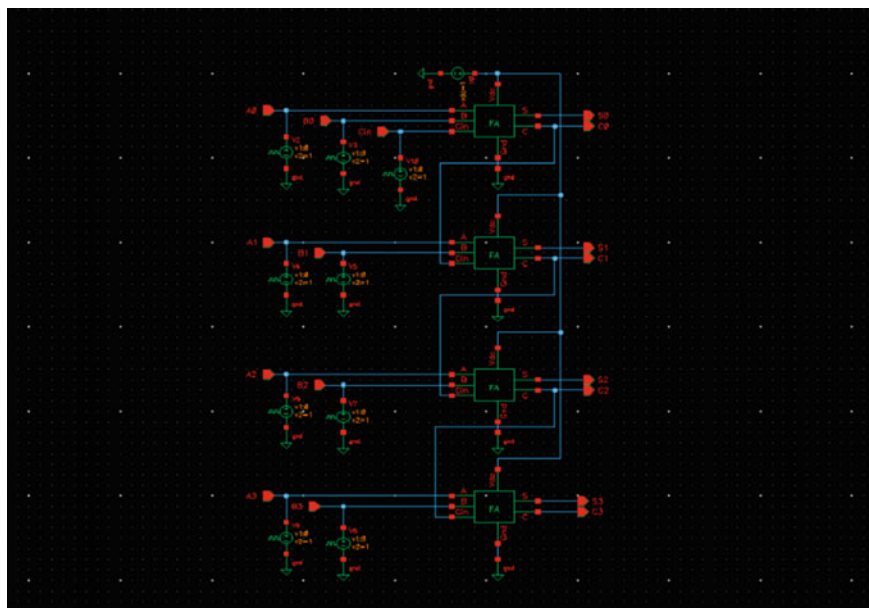


Fig. 8 Schematic of conventional full adder

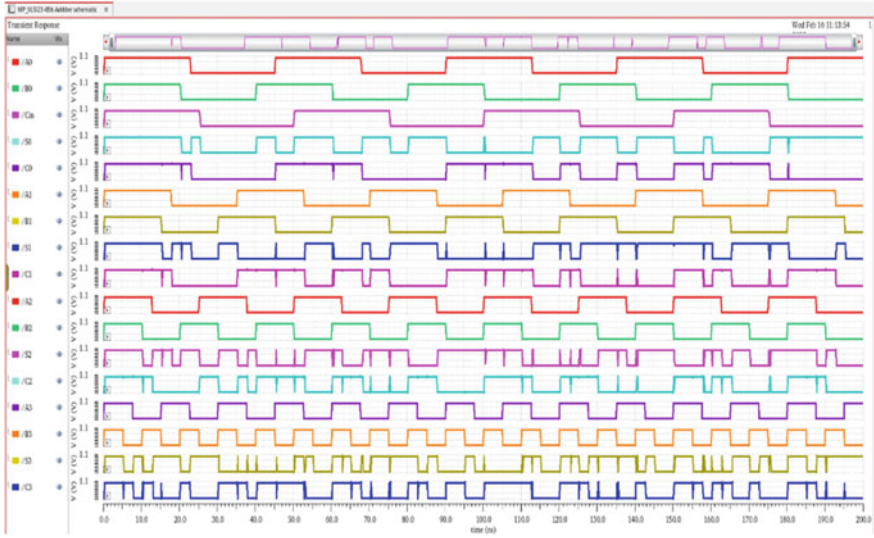


Fig. 9 Waveform of conventional full adder

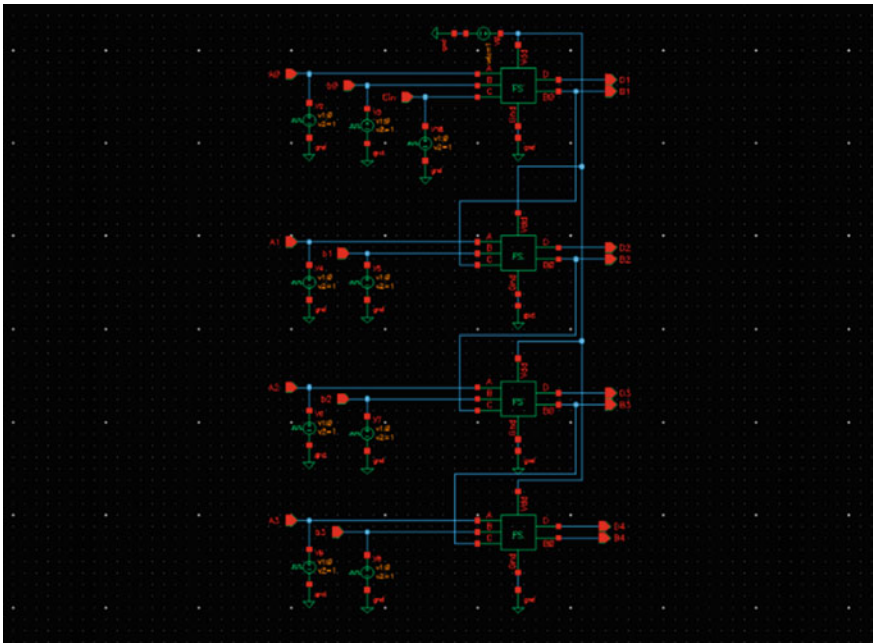


Fig. 10 Schematic of conventional full subtractor

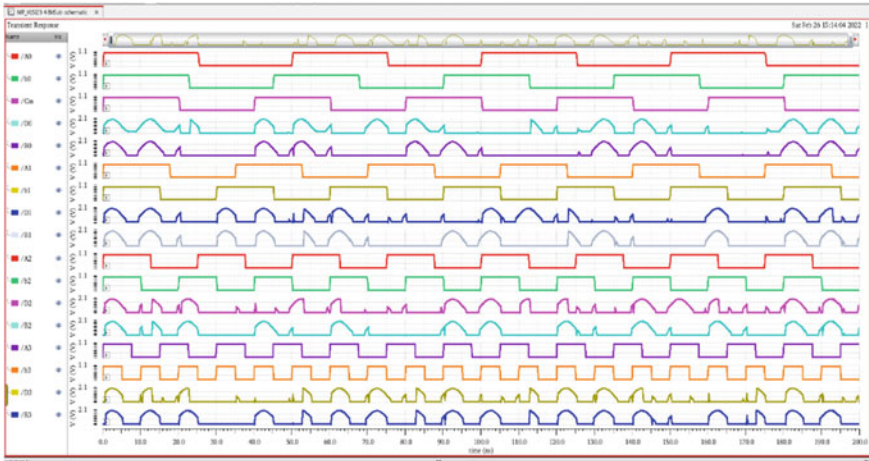


Fig. 11 Waveform of conventional full subtractor

4.1.4 4-Bit ALU

Figure 12 is the picture of the 4-bit ALU schematic diagram. The outputs of this circuit are Y0, Y1, Y2, and Y3. Figure 13 shows the logical block transient analysis.

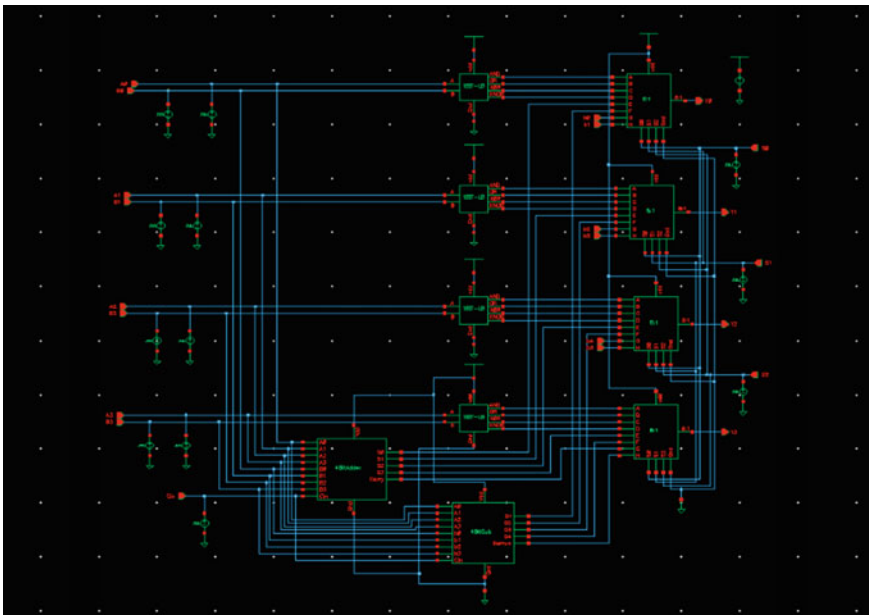


Fig. 12 Schematic of conventional 4-bit ALU

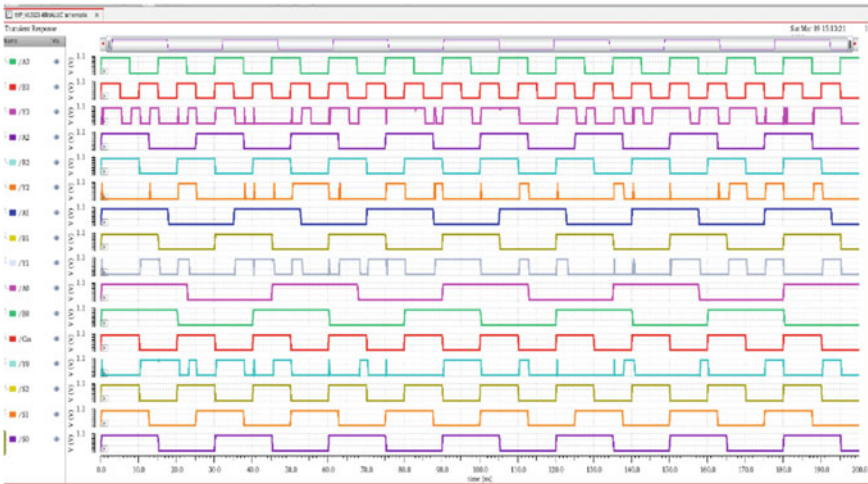


Fig. 13 Waveform of conventional 4-bit ALU

4.2 Adiabatic Logic Circuits

4.2.1 Logical Block

Figure 14 is the picture of the logical schematic diagram. The outputs of this circuit are AND, OR, XOR, and XNOR. Figure 15 shows the logical block transient analysis.

4.2.2 4-Bit Full Adder

Figure 16 is the picture of the 4-bit adder schematic diagram. The outputs of this circuit are sum (S_0, S_1, S_2, S_3) and carry. Fig. 17 shows the full adder transient analysis.

4.2.3 4-Bit Full Subtractor

Figure 18 is the picture of the 4-bit subtractor schematic diagram. The outputs of this circuit are difference (D_0, D_1, D_2, D_3) and borrow. Figure 19 shows the Full Subtractor transient analysis.

4.2.4 4-Bit ALU

Figure 20 is the picture of the 4-bit ALU schematic diagram. The outputs of this circuit are $Y_0, Y_1, Y_2,$ and Y_3 . Figure 21 shows the logical block transient analysis.

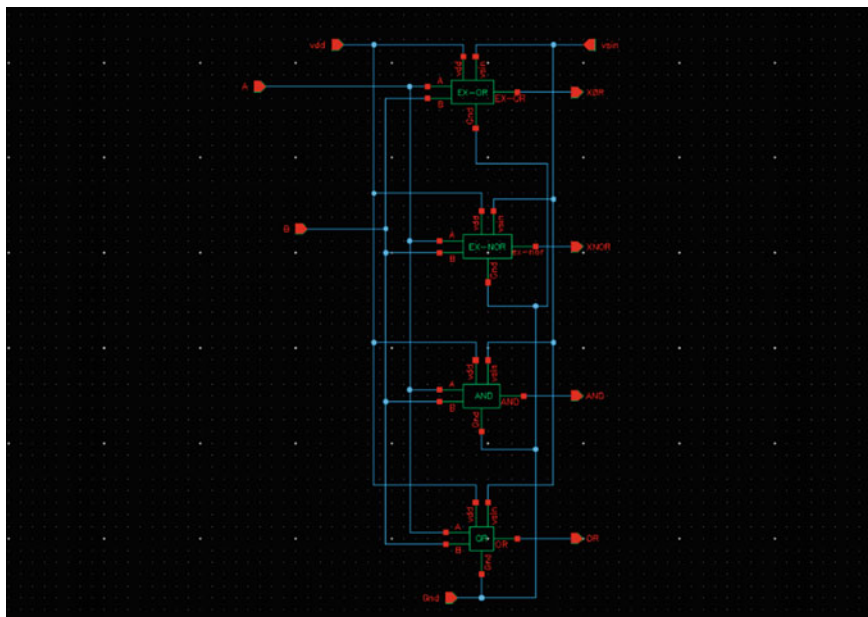


Fig. 14 Schematic of adiabatic logical block

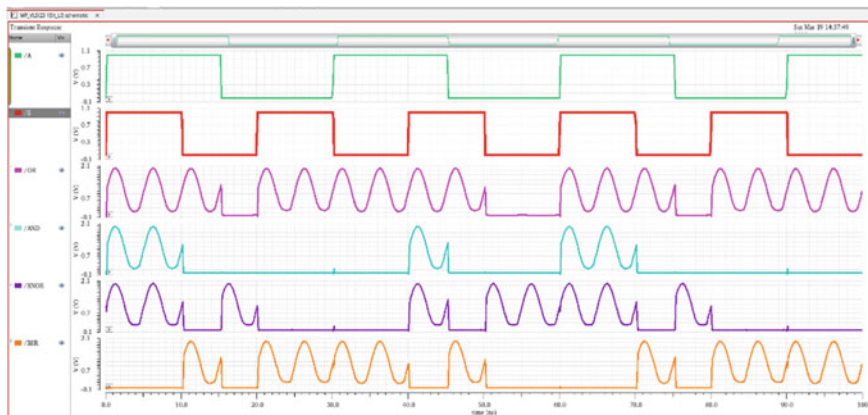


Fig. 15 Waveform of adiabatic logical block

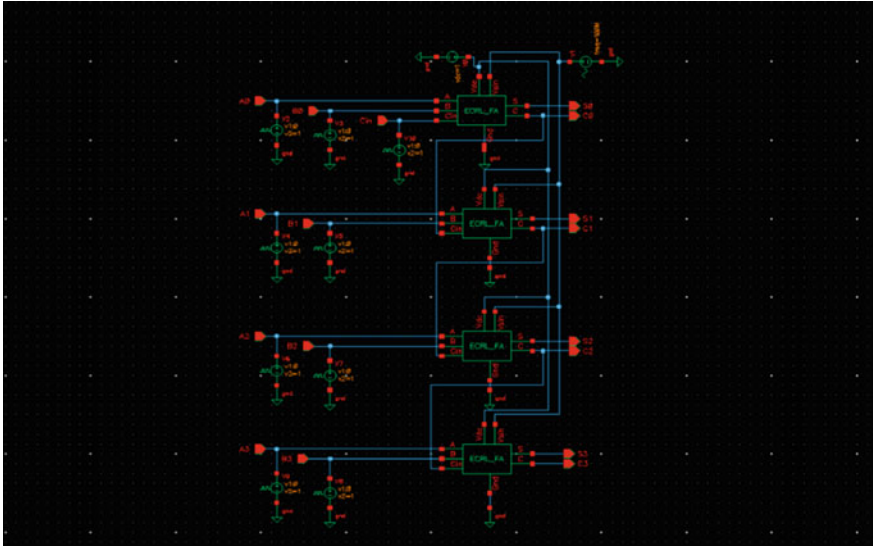


Fig. 16 Schematic of adiabatic 4-bit full adder

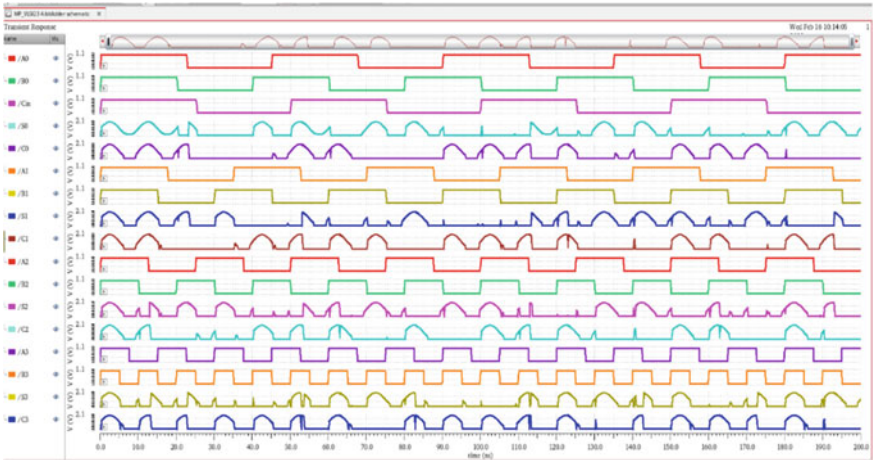


Fig. 17 Waveform of adiabatic 4-bit full adder

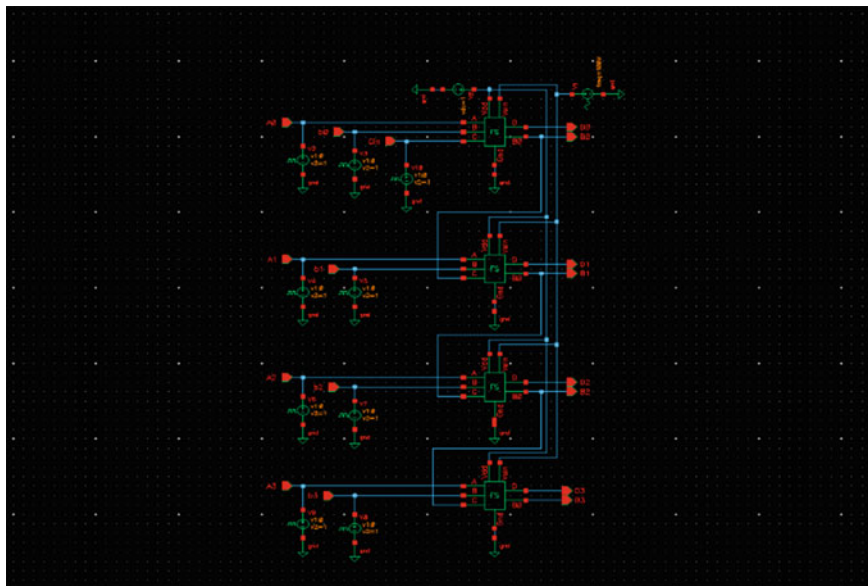


Fig. 18 Schematic of adiabatic 4-bit full subtractor

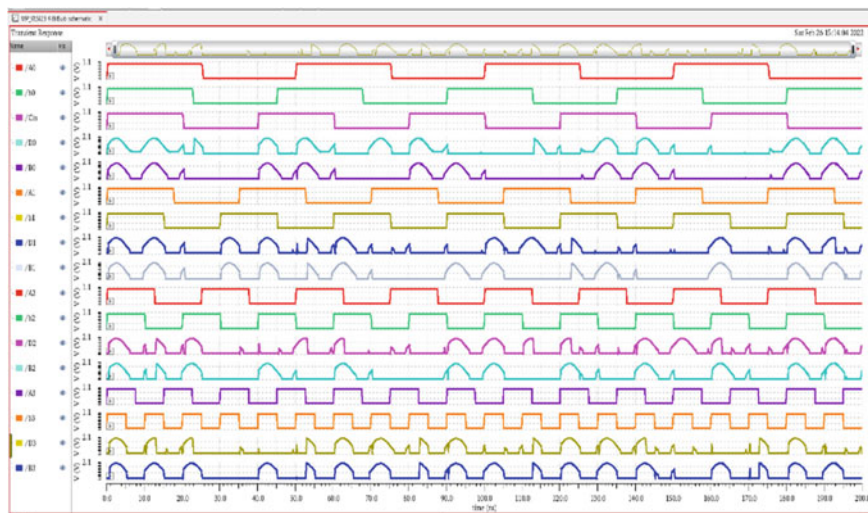


Fig. 19 Waveform of adiabatic 4-bit full subtractor

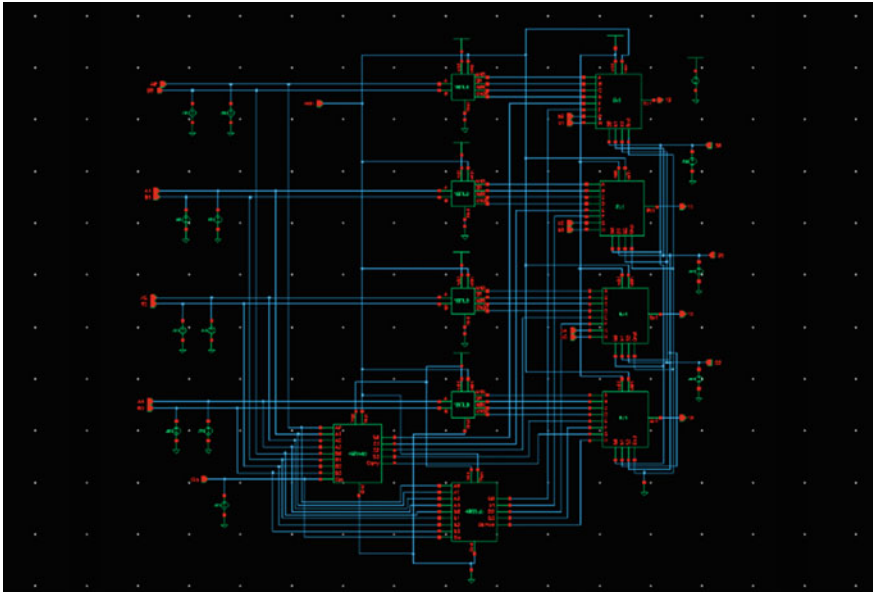


Fig. 20 Schematic of adiabatic 4-bit ALU

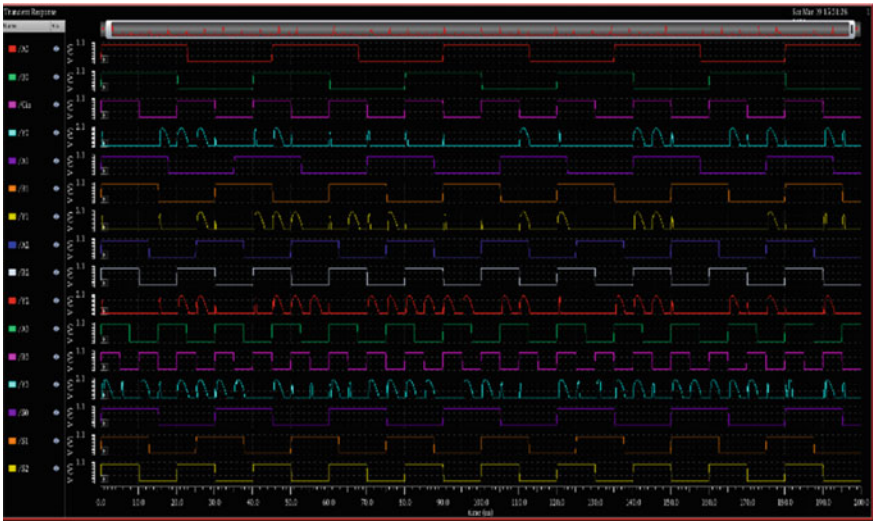


Fig. 21 Waveform of adiabatic 4-bit ALU

5 Power Analysis

Table 1 Power analysis between conventional and adiabatic

Design	Power
Conventional	502.6E
Adiabatic	310E–6

6 Conclusion

In adiabatic logic, the energy accumulated in the load capacitors is re-addressed by the load without dispersing it into the ground. As a result, the circuit consumed less power as well as reduced power dissipation [13]. Results obtained from the study indicate that designing ALUs using ECRL logic consumes less power than designing them using traditional logic. In this logic, the power supply voltage varies over time, not a constant voltage, and supplied voltage is 1 V.

References

1. Yadav, R., Bakshi, A., Chowdhury, J. Das, J.K.: Adiabatic approach for charge restoration in low power digital circuits. In: IEEE ICISC, pp. 473–477, 2018
2. Sapna, R.D., Sarbhai, Y., Sharma, G.: Comparative analysis of ECRL and TSEL adiabatic logic style. In: International Conference on Current Trends towards Converging Technologies (ICCTCT), 2018
3. Singh, S., Singh, G., Singh, J.: Adiabatic approach to design low power energy efficient CMOS circuit. In: International Journal of Emerging Research in Management and Technology, pp. 498–504, ISSN: 2395-0072
4. Chaudhuri, A., Bhowmik, M., Nath, S., Das, P.S.: Implementation of circuit in different adiabatic logic. In: IEEE 2nd International Conference on Electronics and Communication System (ICECS), pp. 353–359, 2015
5. Maxwell, C.: A Treatise on Electricity and Magnetism, 3rd ed., vol. 2, pp. 68–73. Clarendon, Oxford (1892). <https://ieeexplore.ieee.org/document/9391609J>
6. Khurana, S., Kaur, K.: Implementation of ALU using FPGA. Int J Emerg Trends Technol Comp Sci (IJETTCS) **1**(2) (2012)
7. Akshitha, Rajan, N.: Power reduction of half adder and half subtractor using different partial adiabatic logic styles. In: 2019 International Conference on Intelligent Sustainable Systems (ICISS), 2019
8. Bhati, P., Rizvi, N.Z.: Adiabatic logic: an alternative approach to low power application circuits. In: 2016 International Conference on Electrical, Electronics, and Optimization Techniques (ICEEOT), pp. 4255–4260, 2016. <https://doi.org/10.1109/ICEEOT.2016.7755521>
9. Sharma, A., Tiwari, R.: Low power 8-bit ALU design using full adder and multiplexer. In: IEEE WiSPNET 2016 Conference

10. Shreelakshmi, Sendamarai, P.: Enhancement of design quality for an 8-bit ALU. *ABHIYANTRIKI* **3**(5) (May, 2016)
11. Ando, Y., Sato, R., Tanaka, M., Takagi, K., Takagi, N.: 80-GHz operation of an 8-Bit RSFQ arithmetic logic unit. In: 2015 15th International Superconductive Electronics Conference (ISEC), Nagoya, 2015, pp. 1–3
12. Sarkar, S., Chatterjee, H., Saha, P., Biswas, M.: 8-bit ALU design using m-GDI technique. In: 2020 4th International Conference on Trends in Electronics and Informatics (ICOEI)(48184), pp. 17–22 (2020). <https://doi.org/10.1109/ICOEI48184.2020.9142881>
13. Gadda, N., Eranna, U.: 64-bit ALU design using vedic mathematics. In: 2020 International Conference on Emerging Trends in Information Technology and Engineering (ic-ETITE), pp. 1–4 (2020). <https://doi.org/10.1109/ic-ETITE47903.2020.122>

High Speed Low Voltage Hybrid Full Adder for Computing Systems



J. Vineetha, K. Vamsi Krishna, P. Gayathri, M. Taj, and Satyajeet Sahoo

Abstract The XOR–XNOR circuit determines how well a Full Adder performs in terms of power, latency, and driving capability. Here a hybrid full adder is designed using Transmission Gate Logic (TGL) and Pass Transistor Logic (PTL). The main motive of the proposed hybrid full adder design is to achieve high speed. The proposed circuit is designed with a less number of transistors to achieve better results. The circuit's performance is evaluated using 45-nm CMOS technology in cadence virtuoso tool. The proposed design has reduced the delay atleast by 50% than available full adders and PDP reduced to 41.69%. The parameters are calculated and the results have been tabulated.

Keywords Hybrid logic · PTL · TGL · Delay · PDP

1 Introduction

In electronic devices, digital signal processing (DSP) is a crucial component. Video processing, filtering, and the rapid Fourier transform are all performed with DSP-based processors (FFT). These modules carry out a long list of addition, subtraction, multiplication, and division calculations. In arithmetic circuits, addition is the simplest basic operation. Multiplication, division, and address calculations all use full adders in the critical path of a complex arithmetic circuit. These are the most important components of any system, and they can have a big impact on how well it works. As a result, improving the 1-bit adder cell's performance can improve the entire system performance.

The entire adder cell can be implemented using a variety of logic methods. Each reasoning approach has its own set of benefits and drawbacks. Static CMOS full adders are based on a conventional CMOS construction. In spite of voltage and

J. Vineetha · K. V. Krishna · P. Gayathri · M. Taj · S. Sahoo (✉)
Department of Electronics and Communication Engineering, Vignan's Foundation for Science,
Technology and Research (Deemed to be University), Vadlamudi, Guntur, Andhra Pradesh
522213, India
e-mail: drss_ece@vignan.ac.in

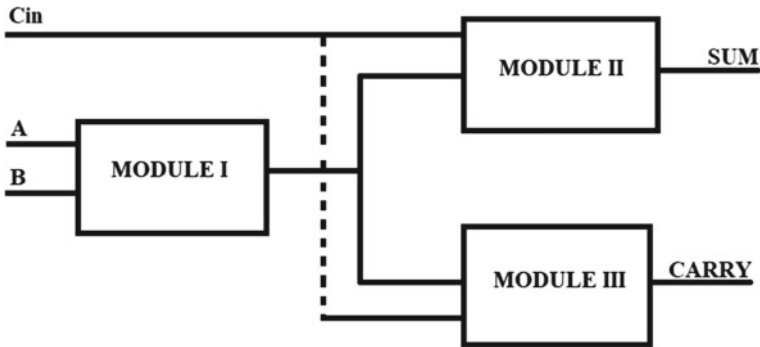


Fig. 1 Hybrid FA cell

transistor sizing, this adder gives full swing at output. This design's constraints include a larger size and slower speed. Full adder can also be designed using Hybrid logic style. To enhance the performance of the system, the adders are developed using a combination of multiple logic styles. The main motive of hybrid style is to reduce the number of circuit elements and power dissipation [1] (Fig. 1).

In CMOS circuits, there are three basic components to calculate power consumption, which can be estimated using the equation:

$$P = V_{dd}I_l + \sum_i V_{dd}I_{sc} + \sum_i V_{dd}V_{sw}C_l P_i F \quad (1)$$

Dynamic power is the third and largest component in the Eq. (1). It is responsible in discharging and charging the circuit capacitance during transistors switching operation [2]. This component accounts for 85–90% of the system's total power usage. Circuit capacitance are generally included diffusion, gate and wiring capacitance, calculated by their lengths and number of connections. To optimize the circuit's performance, it is critical to choose the logic style wisely. Short circuit power takes place during transistor switching due to creation of short paths between ground and supply voltage. The static power because of leakage current is represented by the first term. Power consumption is minimized by reducing short circuit power components and dynamic power components.

Exclusive-OR (XOR) gate can be used to design a full adder, the sum expressed as XOR of the inputs while carry is a multiplexer with XOR function for the control signal. The procedure of pass transistors are extended to combined CMOS XOR–XNOR cell design.

2 Pass Networks

The input signal is sent to the source of a pass transistor, and the output signal is taken from the drain. A pass network is a connection of number of pass transistors to obtain a particular switching function. The signal applied to the gate controls the signal propagation through transistor [3]. A path for the input from source to drain is provided when the Logic 1 is provided at the gate and logic 0 at the gate opens the path in the case of NMOS transistor. With a control signal of logic level 0 PMOS shows similar behavior. If signal X is connected to the gate and signal Y is connected to the source of the NMOS/PMOS transistor respectively, then it is denoted as $X(Y)$. A CMOS transmission gate is a circuit where a PMOS and NMOS transistors are connected in parallel to pass the signal Y . Figure 2 shows the logic symbols and expressions of the pass gates.

A nMOS transistor gives weak '1' and strong '0'. A pMOS transistor gives weak '0' and strong '1'. Transmission gate gives strong '1' and strong '0'.

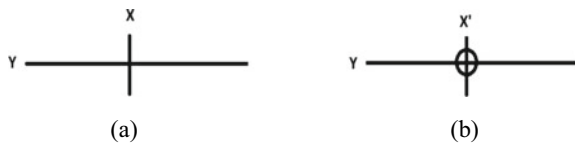
The significant difference in designs of pass network and gate network is that in the minimization algorithm 1's and 0's of the function are necessarily considered in case of pass network [4]. The pass network design procedure selects all of the function's important pass prime implicants first, then a small selection of pass prime implicants to cover the entire function.

In pass network design if in the implicant the pass variable is 0, a pure nMOS transistor passes it to the output without any signal degradation and if the pass variable is 1, a pure pMOS transistor passes it without any degradation in the signal. The output signal of a pure pMOS or nMOS chain is degraded when a variable other than 1 or 0 is fed through it. Because of this drawback pass transistors can be replaced by transmission gates to achieve full swing but additional inverters are required to complement the control signals. CMOS pass network is used when drive requirements of outputs are critical [5].

2.1 Pass Logic Implementation of XOR Cell

Figures 3a–f demonstrate various implementations of XOR circuits. The goal is to show how these circuits can be designed in a formal way using the network design procedures discussed above. The pass variables are 1s and 0s in the minimization indicated in Fig. 3a [6]. The XOR gate in CMOS is represented by this. As a result, this paper does not go into detail about it.

Fig. 2 Symbols of pass transistors **a** transistor (nMOS), **b** transistor (pMOS)



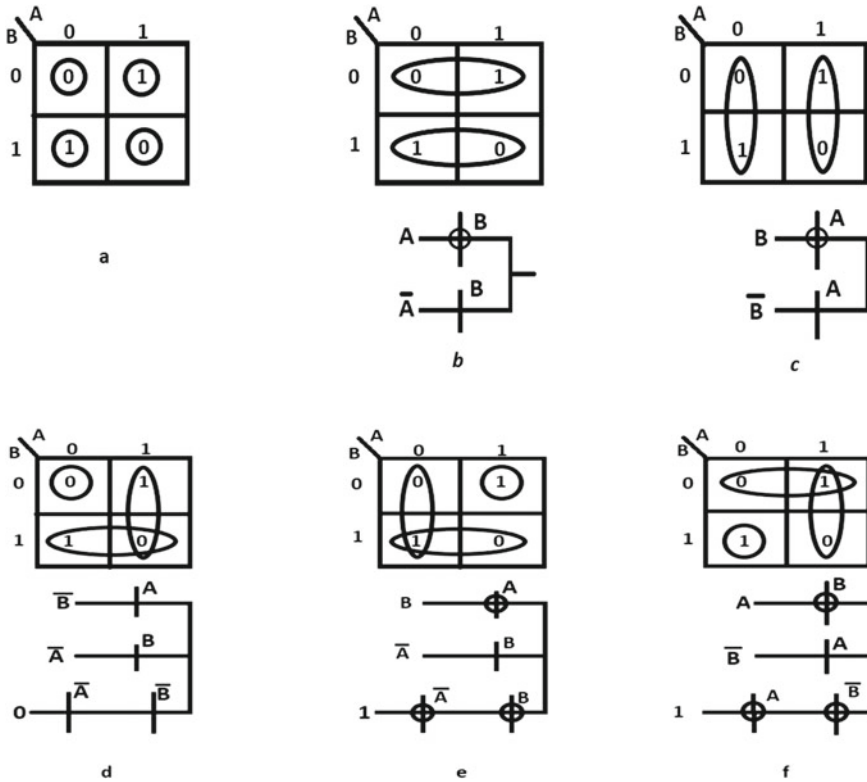
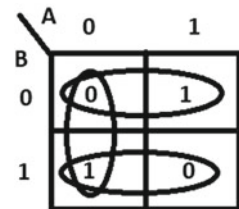


Fig. 3 Analysis of XOR logic

When the control variable is complemented (not complemented) corresponding to a pass variable that is not either 1 or 0, the thumb rule is to utilize a pMOS (nMOS) for the implementation in order to reduce the inverter count in the design. Complementary pass variables (A and B) are required for the pass logic realization shown in Fig. 3b–d. Figure 3f, e are not good implementations. Further leaves the implementations shown in Fig. 4. For $A = B = 0$, both P-type MOS passes a weak '0' to the output in Fig. 4. For the creation of XOR gate, the transmission gate can be replaced in the place of P-type MOS which in merit of 5 transistors and the count

Fig. 4 Pass network of XOR cell



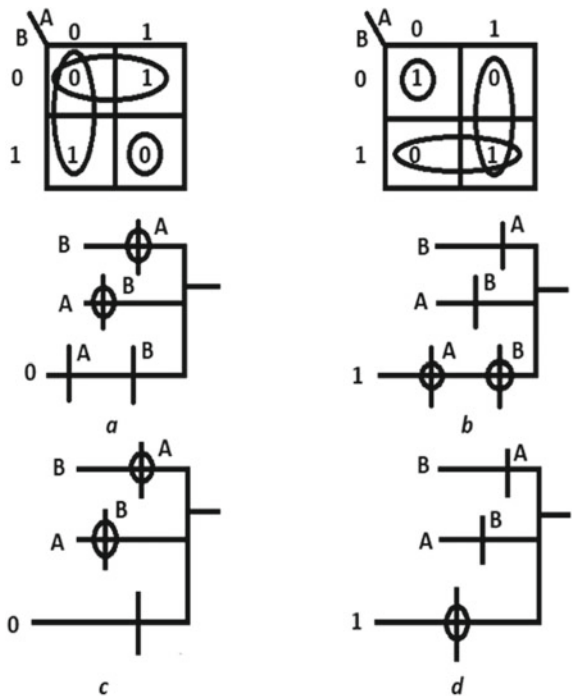
goes up to 7 on inclusion of an inverter. This XOR arrangement was simulated and found that there was no threshold voltage loss with a lower power supply voltage, i.e., 2 V, allowing voltage with full swing (0–2 V) at output [7]. Both P-type MOS in Fig. 4 pass a weak ‘0’ to the output when $A = B = 0$. The output becomes a strong ‘0’ by replacing PMOS transistor controlled by A (variable) with transmission gate. This is redrawn in Fig. 4 and only requires four transistors (six with an inverter) [8]. This XOR circuit was implemented in [14] and found to use the least amount of power.

3 Full Adder Cell

3.1 XOR–XNOR Cell Using Pass Transmission Logic

The circuit which is having lowest average power consumption was the one represented in Fig. 5a, b with an eight-transistor count, but the minimal transistor count produced using this method was just six. The succeeding diagram shows the design of a new six transistor completely restored XOR–XNOR cell that does not require any inverters, hence improving the circuit’s whole performance [9].

Fig. 5 Analysis of XOR–XNOR circuit



In Fig. 5a, b, the XOR and XNOR k-maps have been redrawn. It must be observed that the AB (0) pass implicant in Fig. 5a is merely employed to produce the ‘0’ output in accordance with $A = B = 1$ and is made up of two nMOS transistors.

Similarly, in Fig. 5b, pass implicant $A'B'$ (1) generates 1 output, which corresponds to $A = B = 0$. When the two k-maps are compared, it can be observed that the complimentary values created by the cross-coupled MOS executing another circuit match to the previously described states in each k-map.

When $A = B = 1$, for example, the cross-coupled n-type MOS arrangement related to the k-map in Fig. 5b outputs logic 1. Instead of AB (0), output can also be utilized as a gate signal to transfer logic 0 to the output for the circuit in Fig. 5a via a n-type MOS, completing the circuit layout as illustrated in Fig. 5c for the XOR gate.

The cross-coupled p-type MOS setup corresponding to the k-map in Fig. 5a provides logic 0 at the output when $A = B = 0$. Instead of using $A'B'$ (1), a PMOS transistor is used to pass a logic 1 to the output of the XNOR gate in Fig. 5b, as shown in Fig. 5d. As a result, XOR and XNOR functions are generated by coupling the two circuits via feedback. Compared to the original configuration, this arrangement saves two transistors. Figure 6 shows transistor circuit schematic of combined circuit. The transistors are labeled with numbers ranging from 1 to 6. Threshold voltage drop is totally removed from XOR–XNOR outputs in Fig. 6 because of the regenerative feedback produced by the n-type MOS and p-type MOS, resulting in the full voltage swing. This can be seen in the following example: Consider the instance where A is equal to 0 and B is equal to 1. $(A \wedge B)'$ is totally discharged to ground, while $(A \wedge B)$ is fully charged to VDD. If B shifts from 1 to 0 the second p-type MOS discharges the output $(A \wedge B)$ toward 0. Because a p-type MOS only passes weak ‘0,’ the output $(A \wedge B)$ is only drained to the threshold voltage, $|V_{tp}|$ [10, 11].

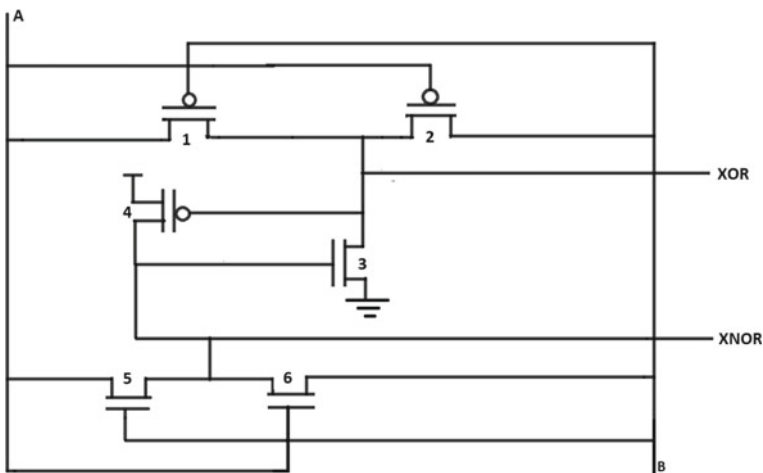
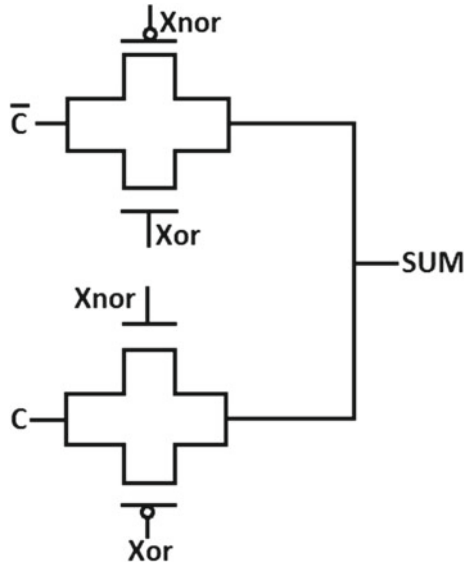


Fig. 6 Proposed XOR–XNOR circuit

Fig. 7 Proposed SUM circuit



3.2 Proposed Sum Module

Kindly the inputs of sum module are XOR–XNOR circuit outputs and C_{in} . The main objective is to produce sufficient driving power. Transmission Gate logic (TGL) is used to implement sum module as 2:1 MUX and it has four transistors. Within this circuit, the inputs to the gate are XOR and XNOR signals and the inputs for the sources of two Transmission Gates are C_{in} and C'_{in} . This circuit achieves high speed and low power consumption with full swing output (Fig. 7).

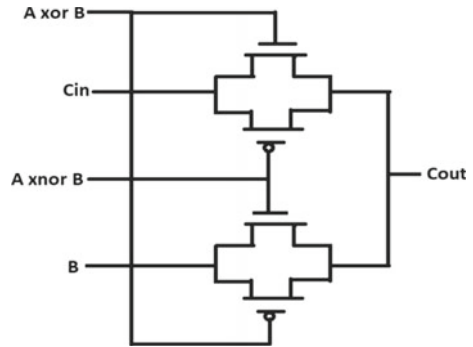
$$SUM = (A \wedge B) \wedge C'_{in} + (A \wedge B)' \wedge C_{in} \tag{2}$$

3.3 Proposed Carry Module

In general, full adder circuit delay is mainly dependent on carry signal. The transistors used in carry module are pass transistors [9]. Pass transistors are mainly used in low power circuits. In each combination of the input vectors, carry signal passes through a single transistor thus it reduces propagation path of carry. Delay of the carry signal reduces automatically when the propagation path of the carry signal is reduced (Fig. 8).

$$C_{Out} = (A \wedge B)'B + (A \wedge B)C_{in} \tag{3}$$

Fig. 8 Proposed carry circuit



3.4 Proposed Full Adder

A hybrid Full Adder can be designed by merging three modules (XOR–XNOR circuit, sum circuit, and carry circuit, respectively). A unique XOR–XNOR circuit is suggested, and prior sections address certain sum and carry circuits [12].

By following the full adder design processes detailed below, number of transistors can be reduced while preserving full output voltages. The inputs are A , B , and C_{in} , and sum S and carry out C_{out} are two outputs, make up a complete adder (Fig. 9).

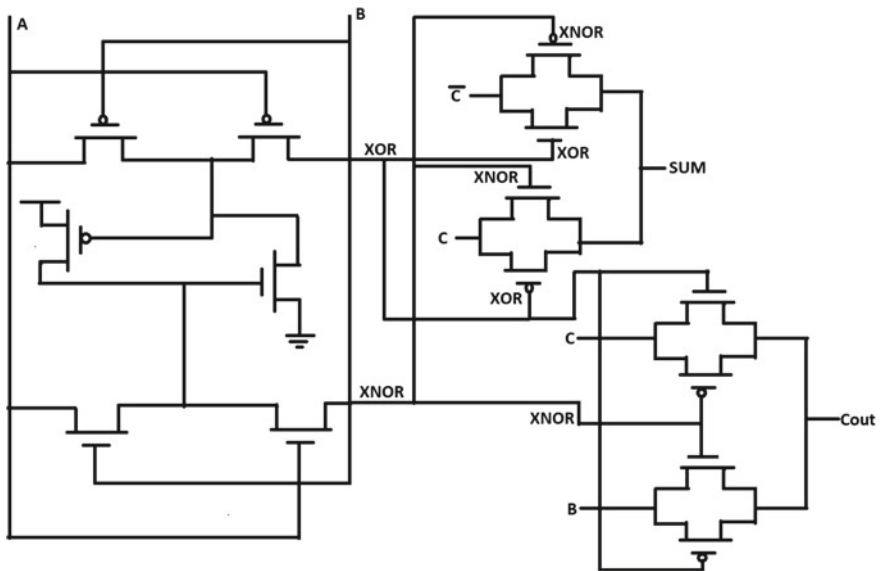


Fig. 9 Proposed full adder circuit

4 Simulation Results

The two 1-bit adders (20T [1], 16T) have been designed and simulated using 45-nm GPDK CMOS technology. The design is analyzed in cadence virtuoso at a power supply voltage of 0.4 V.

With reference to power consumption, worst-case latency and PDP, the suggested circuit’s performance is compared to that of existing circuits. For rise and fall time transitions, delay is computed from a voltage level of 50% at the input to a voltage level of 50% at the output, and the worst-case latency is chosen. The PDP is calculated using worst-case delay of the outputs.

The design described provides the finest performance with regard to power usage. The proposed circuit, however, has the lowest PDP of all the circuits. The suggested circuit is better than other circuits in terms of PDP and delay by up to 41.69% and 50.55%, respectively (Fig. 10; Table 1).

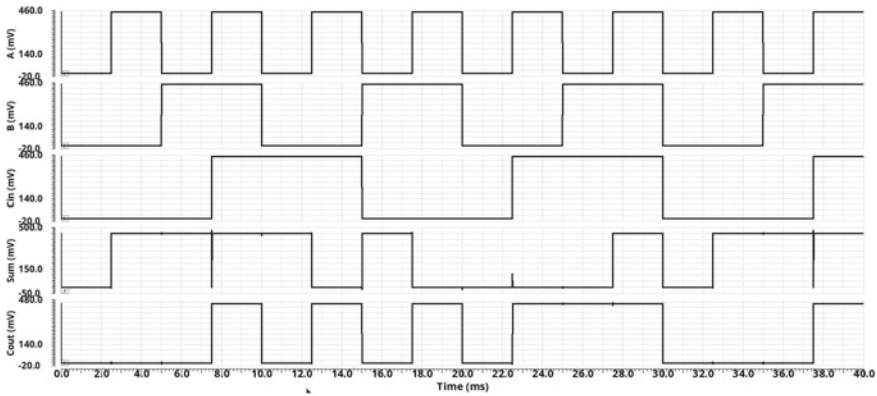


Fig. 10 Simulation results of proposed full adder

Table 1 Comparison of results

Full adder@45 nm	[1]	Proposed FA
No. of transistors	20	14
Delay	0.726 nS	0.367 nS
Power	0.196 uW	0.156 uW
Power delay product (PDP)	137.9 aJ	57.5 aJ

5 Conclusion

A new design with combined XOR–XNOR cell was proposed based on Pass Transistor Logic. On the basis of latency, power dissipation, and PDP, the circuit's performance was compared to that of a previous Full adder design. As per the simulation the proposed circuit showed better and more competitive than possible alternatives. In comparison to prior designs, it has a good driving capability without any degradation in the output voltage. As per the enhanced performance, the proposed circuit was more suitable for low power electronic devices.

References

1. Kandpal, J., Tomar, A., Agarwal, M., Sharma, K.K.: High-speed hybrid-logic full adder using high-performance 10-T XOR–XNOR Cell. *IEEE Trans. Very Large Scale Integr. (VLSI) Syst.* **28**, 1413–1422 (2020)
2. Hasa, M., Hossein, Md. J., Hossain, M., Zaman, H.U., Islam, S.: Design of a scalable low-power 1-bit hybrid full adder for fast computation. *IEEE Trans. Circ. Syst.* **67**, 1464–1468 (2020)
3. Kishore, S., Sakthivel, R.: Ultra-low-voltage GDI-based hybrid full adder design for area and energy-efficient computing systems. *IET Circ. Dev. Syst.* **13**, 465–470 (2019)
4. Lakshmi, S., Meenu, R.C., Krishnadas, D.: Optimization of hybrid CMOS designs using a new energy efficient 1 bit hybrid full adder. *IEEE Trans. Very Large Scale Integr. (VLSI) Syst.* **18**, 905–908 (2018)
5. Bhattacharyya, P., Kundu, B., Ghosh, S., Kumar, V., Dandapat, A.: Performance analysis of a low-power high-speed hybrid 1-bit full adder circuit. *IEEE Trans. Very Large Scale Integration. (VLSI) Syst.* **23**, 2001–2008 (2015)
6. Sahoo, S., Prabakaran, S.R.S.: Nano-ionic solid state resistive memories (Re-RAM): a review. *J. Nanosci. Nanotechnol.* **17**, 72–86 (2017)
7. Valashani, M.A., Mirzakuchaki, S.: A novel fast, low-power and high-performance XOR–XNOR cell. In: *Proceedings of IEEE International Symposium on Circuits Systems (ISCAS)*, pp. 694–697 (2016)
8. Hernandez, M.A., Aranda, M.L.: CMOS full-adders for energy-efficient arithmetic applications. *IEEE Trans. Very Large-Scale Integr. (VLSI) Syst.* **19**, 718–721 (2011)
9. Dreslinski, R.G., Wieckowski, M., Blaauw, D., et al.: Near-threshold computing: reclaiming Moore's law through energy efficient integrated circuits. *Proc. IEEE.* **98**, 253–326 (2010)
10. Sahoo, S., Manoravi, P., Prabakaran, S.R.S.: Titania based nano-ionic memristive crossbar arrays: fabrication and resistive switching characteristics. *Nanosci. Nanotechnol.—Asia* **9**(4), 486–493 (2019)
11. Sahoo, S.: Conduction and switching behavior of e-beam deposited polycrystalline Nb₂O₅ non-volatile memory applications. *J. Alloys Compd.* **866**, 158394 (2021)
12. Shams, A.M., Darwish, T.K., Bayoumi, M.A.: Performance analysis of low power 1-bit CMOS full adder cells. *IEEE Trans. VLSI Syst.* **10**, 20–29 (2002)

Fracture Interface Observation After the Mechanical Test of Additively Manufactured CCFRTC Fabricated Under the Controlled Air Flow Cooling Effect



Nabeel Maqsood and Marius Rimašauskas

Abstract Additive manufacturing (AM) is an advance manufacturing process that creates a layered structure followed by the 3D CAD model and manufacturing process parameters opposed to traditional and conventional manufacturing process. The parameters of the printing process play an important role in determining the mechanical strength, design properties and failure mechanisms of 3D printed composite structures. Analytical investigation of the refractive mechanism can lead to improvements in printing parameters and production processes. In this study, the fracture interface analysis is performed of 3D printed continuous carbon fiber-reinforced thermoplastic composite (CCFRTC) structure after performing the mechanical (tensile and flexural) testing. The study explains how the continuous carbon fiber (CCF) was able to support the composite during the loading and how the load was distributed from matrix to reinforcement fiber.

Keywords CCFRTC · Fused deposition modeling · Fracture interface · Microscope's micrograph

1 Introduction

Additive manufacturing (AM) or 3D printing is an advance manufacturing process in which the solid structure is created layer upon layer creation followed by the 3D CAD model and manufacturing process parameters opposed to traditional and conventional manufacturing process [1, 2]. Fused deposition modeling (FDM) is a most common AM technology for fabricating solid parts of pure polymers as well as composite parts with complex geometry shape with least wastage of the material and time consuming. These are some of the factors that have advantage of the 3D

N. Maqsood (✉) · M. Rimašauskas
Department of Production Engineering, Faculty of Mechanical Engineering and Design, Kaunas University of Technology, 51424 Kaunas, Lithuania
e-mail: nabeel.maqsood@ktu.edu

M. Rimašauskas
e-mail: marius.rimasauskas@ktu.lt

© The Author(s), under exclusive license to Springer Nature Singapore Pte Ltd. 2023
V. Bindhu et al. (eds.), *Proceedings of Fifth International Conference on Inventive Material Science Applications*, Advances in Sustainability Science and Technology,
https://doi.org/10.1007/978-981-19-4304-1_8

printing technologies over the conventional manufacturing technologies [3, 4]. Pure polymers produced with AM technology have low strength and stiffness, which may make them unsuitable for use as target parts due to their low mechanical strength, due to which it could not be used for high structural applications [5, 6].

In order to improve their mechanical properties, additive in the form of reinforcement is added to make such materials to be used for high strength applications. Continuous carbon fiber (CCF) is lightweight and stiff material which can be used as a reinforcement in the thermoplastic polymers forming CCF-reinforced thermoplastic polymer composite (CCFRTC) parts which are used in the wide range of engineering applications [7, 8]. CCF has shown better mechanical performance compared to the short carbon fiber [9].

The printing of the CCF using FDM technique is itself a challenging factor in order to find the optimum printing parameters and maintain the quality of the fabricated parts consistently. A number of researches have been performed to improve the quality and mechanical properties using the optimized parameters. Printing parameters greatly affect the mechanical properties, quality and fracture mechanism of the composite structure [10]. The printing process parameters were studied eventually and importance of the layer height, line width, extrusion multiplier, infill structure and density, printing speed and content of reinforcement were explained and their effect on the strength levels, porosity and quality were determined and explained [11, 12]. The mechanical and microstructural properties of short carbon fiber-reinforced ABS matrix composites with maximum tensile and flexural strengths of 42 MPa and 65 MPa, respectively [13], were investigated, and the results showed that gaps between the printing layers were created by increasing the fiber content, while the tensile strength of the 3D printed samples increased [14]. Most studies have shown that the strength level can be improved by optimizing the pressure parameters; only limited studies were found to illustrate the failure mode and mechanical behavior of the AM CCFRTC [15].

Fracture interface analysis and mechanism is also one of the most important factors when determining the quality and mechanical performance of the 3D printed CCFRTC structure. The fracture mechanism explains how the load was carried out when subjected to mechanical loading and the importance of the distribution of the matrix material and reinforcement in the composite. This analysis also helps in improving the structure and quality of the composite.

In this study, the CCFRTC parts were fabricated using various printing process parameters (extrusion multiplier, extrusion temperature and line width) and subjected to mechanical loading. The fracture interface analysis was studied using the microscope's micrograph after the mechanical testing of the ruptured area.

Table 1 Parameters of 3D printing

Nozzle diameter (mm)	1.5 mm
Extrusion multiplier	0.5, 0.7, 0.8, 0.9
Extrusion width (mm)	1.2, 1.3, 1.4, 1.5
Layer height (mm)	0.5
Printing speed (mm/s)	3.0
Extruder temperature (°C)	210
Bed temperature (°C)	90
Infill pattern	Rectilinear
Internal infill angle offsets	0°

2 Fabrication Process of CCFRPC Specimens Using Control Cooling Effect

In this study, Polymaker polylite PLA material was used as matrix material, while CCF from Toray company was used as reinforcement. Before the printing process, the standard CFF was impregnated with PLA pellets and di-chloromethyl to improve the quality of the printing [16]. The impregnation process was performed prior to printing process in order to ease the printability with better adhesion and quality. McCreator 2 FDM printer was used to fabricate the composite specimens. The 3D printer's extruder was also modified with two input channels and one output that enable the CCF to print with the PLA. Printing process parameters are presented in Table 1. Throughout the experimentation, 0° unidirectional composite specimens were fabricated with the range of printing process parameters (extrusion multiplier, extrusion temperature and line width). The major amendment made in this research was introducing the control cooling effect during the printing process parameters in order to maintain high quality concern. The control cooling effect enables the composite specimens to improve the quality of the printing by ensuring the uniform distribution of the layers and lines of the specimens during the printing that also decreases the void content as well as improve mechanical performance. The flow rate of 40 l/m was kept constant throughout the printing process. The flow rate was selected according to the best result shown in terms of quality. ASTM D3039 and ASTM D790 standard was used to perform the tensile and flexural test, respectively. Figure 1 shows the experimental methodology of the study.

3 Observation of the Manufactured Composite Specimens

After the fabrication process of the composite specimens, it was observed visually, and microscope's micrographs were carried out to observe the distribution of the composite layers and lines which represent its quality. The composite specimens were also weighing after the fabrication process printed with the range of printing process parameters to compare their masses presented in Fig. 2. The figures show

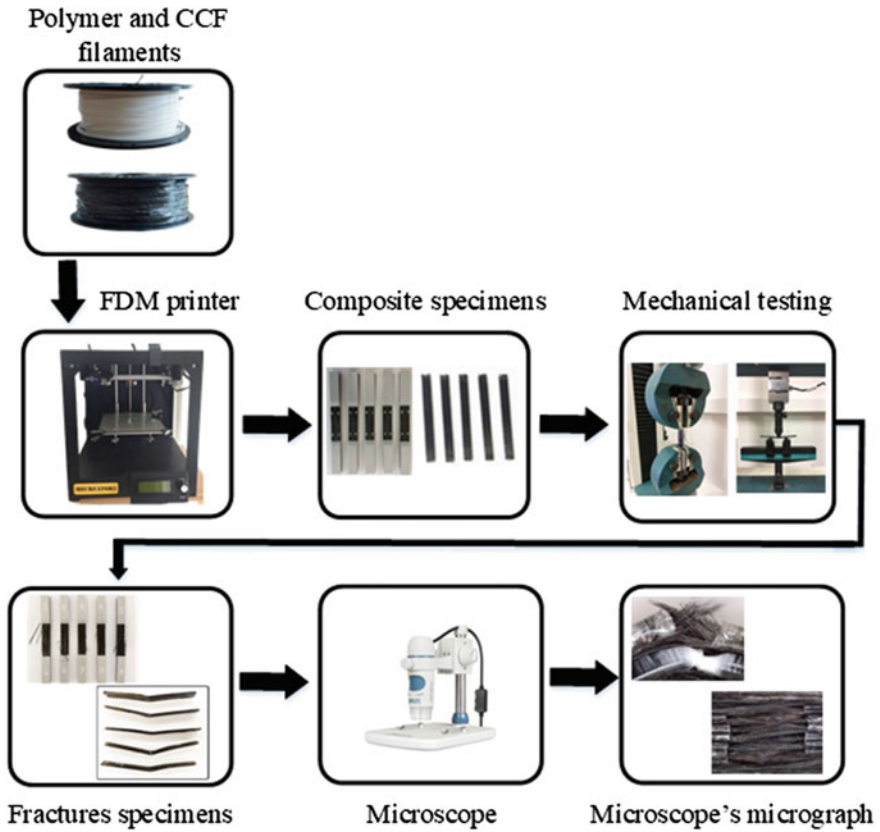
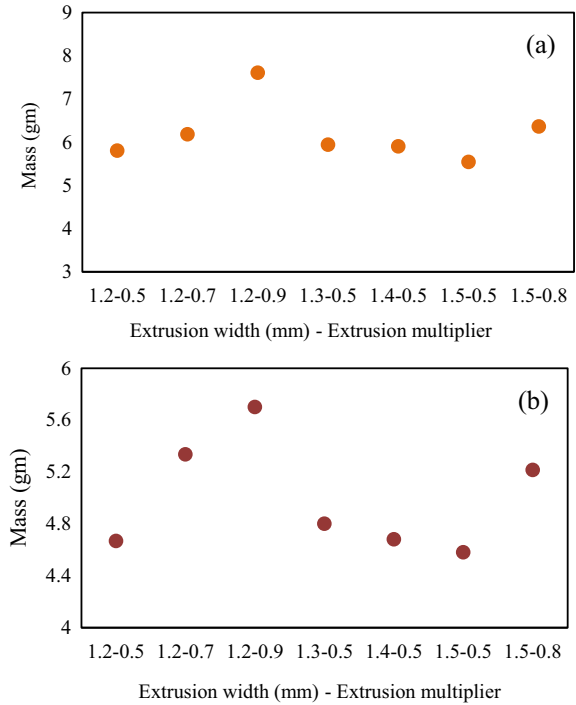


Fig. 1 Flow chart of the experimental methodology

that the composite specimen with the printing process parameters of extrusion width of 1.2 mm and extrusion multiplier of 0.9 showed the highest mass in both the cases (tensile and flexural) due to minimum width between the printed lines and excess extruded thermoplastic. The mass varies in each fabricated composite specimen due to change in the width of printed lines and extruded thermoplastic matrix. Such selection of printing process parameters depends on the availability of the parameters in the software and compatibility of the composite specimens using FDM 3D printing technique.

Fig. 2 Mass versus printing parameters specimens of **a** tensile and **b** flexural



4 Fractured Interface Analysis of the CCFRPC Specimens After Performing Mechanical Testing

The fracture interface plays an important role in determining the quality and failure mechanism of composite specimens. Based on the experimental analysis of tensile and flexural tests of composites, it was decided to study the fracture rate after mechanical testing. Fracture interface analysis was performed to monitor and study the deformation behavior and how failure occurs during mechanical testing. To study this event, the fracture interface of each group of CCFRPC samples was observed under a light microscope. For these results, samples from each group were chosen to better reflect the failure mode.

Figure 3 represents the microscope’s micrograph after the tensile test printed with the range of extrusion temperatures shows the rupture occurred within the composite during the tensile loading. Although the specimen with the extrusion temperature of 230 °C showed the best mechanical strength, all the fractured specimens showed the same behavior. The matrix was initially broke at the outer layer of the composite. The fibers behind it hold it but still separated at various instant. The results revealed that the fibers hold during the tension by distributing their loads [17]. But the major failure caused due to fractured fibers [18].

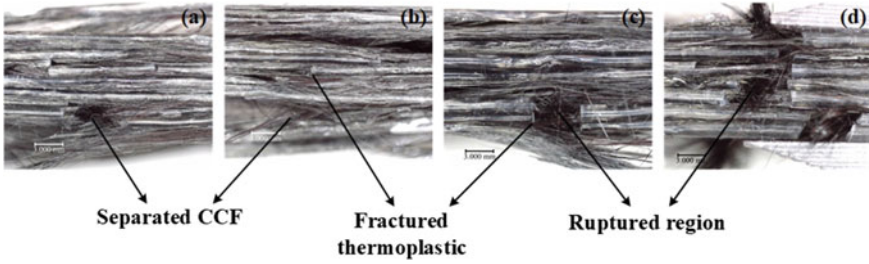


Fig. 3 Microscope’s micrograph of the fractured composite specimens after tensile test printed with the extrusion temperature of **a** 200 °C, **b** 210 °C, **c** 220 °C and **d** 230 °C parameters

CCF can be observed to separate from the thermoplastic matrix when produced using different parameters of the printing process, as shown in Fig. 4. The fibers and matrix are joined into parts to support the load, but gaps appear. It is between the layers, but the carbon fiber is still hold together. Although, the carbon fibers separated from the PLA matrix during the tensile testing and cracked areas can be clearly seen after the test, leaving voids. A void or gaps refers to the internal structure of a component containing multiple voids representing the fill of a 3D production part. Similar behavior was observed when the CCF fracture occurred after the reinforcing bar was detached and a gap was formed during loading [7, 17].

Microscopic examination of the microscopic sample after the bending test using the parameters of the printing process (Fig. 5) and the extrusion temperature range (Fig. 6) shows the broken area and the broken layer where the maximum bending force is applied. It is clear that separated fibers have emerged from the matrix material after the experiment, but the fibers remain together at different times. This suggests that the composite structure can be used to support loads during bending, as the fracture interface shows efficient load transfer from the PLA thermoplastic matrix to the carbon fiber reinforcement. Delamination was one of the major failures caused

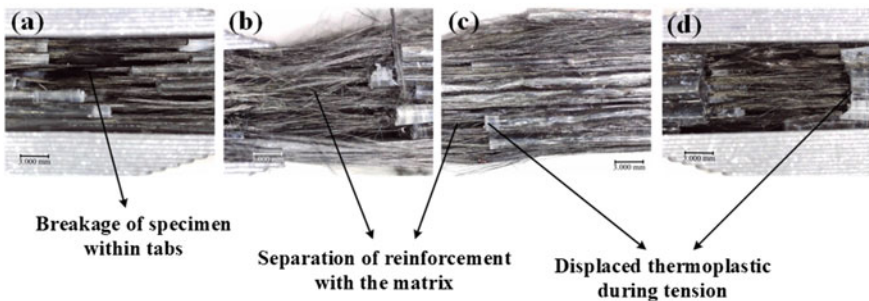


Fig. 4 Microscope’s micrograph of the fractured composite specimens after tensile test fabricated with printing parameters of extrusion width, extrusion multiplier of **a** 1.2 mm, 0.7, **b** 1.3 mm, 0.5, **c** 1.4 mm, 0.5 and **d** 1.5 mm, 0.8

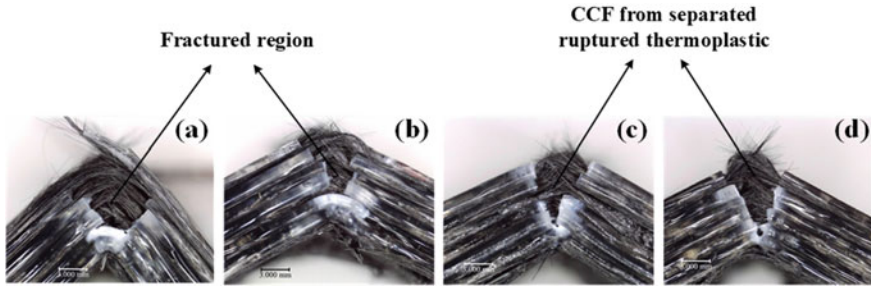


Fig. 5 Microscope's micrograph of the fractured composite specimens after flexural test fabricated with printing parameters of extrusion width, extrusion multiplier of **a** 1.2 mm, 0.7, **b** 1.3 mm, 0.5, **c** 1.4 mm, 0.5 and **d** 1.5 mm, 0.8

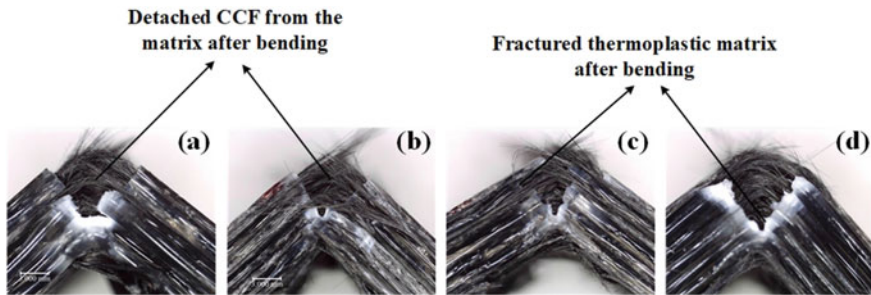


Fig. 6 Microscope's micrograph of the fractured composite specimens after flexural test printed with the extrusion temperature of **a** 200 °C, **b** 210 °C, **c** 220 °C and **d** 230 °C

usually during the bending [9]. The experimental results revealed that the fabricated composite structure showed the capability to withstand during the mechanical loading that still holds together even after the fracture which indicates the distribution of the load from the matrix to the reinforcement. This behavior mainly seen in the composites with continuous fiber reinforcement.

5 Conclusion

The analysis of the fracture interface was studied after mechanical testing (tensile and bending) using various parameters of the printing process (extrusion temperature, extrusion width and extrusion multiplier). The microscopic results of the micrographs of the composite samples show that the thermoplastic matrix breaks initially during the two loading processes and then the reinforcing fibers separate at different points in the structure, but the matrix remains unchanged at different instant. The results show that the loads are efficiently transferred from the matrix to the fibers during

loading, which can be used for structural design. Moreover, the experimental results revealed that the fabricated composite structure showed the capability to withstand during the mechanical loading that still holds together even after the failure which indicates the distribution of the load from the matrix to the reinforcement.

Acknowledgements This research was funded by a grant (No. S-M-ERA.NET-20-1) (project: “Additive Manufactured Composite Smart Structures with Embedded Fibre Bragg Grating Sensors,” acronym: “AMCSS”) from the Research Council of Lithuania.

References

1. Nakagawa, Y., Mori, K., Maeno, T.: 3D printing of carbon fibre-reinforced plastic parts. *Int. J. Adv. Manuf. Technol.* **91**, 2811–2817 (2017)
2. Maqsood, N., Rimasauskas, M.: A review on development and manufacturing of polymer matrix composites using 3D printing technologies. In: 9th international scientific conference on defensive technology OTEH, pp. 462–468 (2020)
3. Singh, S., Ramakrishna, S., Singh, R.: Material issues in additive manufacturing: a review. *J. Manuf. Process* **25**, 185–200 (2017)
4. El Moumen, A., Tarfaoui, M., Lafdi, K.: Additive manufacturing of polymer composites: processing and modeling approaches. *Composite Part B Eng.* **171**, 166–182 (2019)
5. Nebe, M., Schmack, T., Schaefer, T., Walther, F.: Experimental and numerical investigation on the impact response of CFRP under 3-point-bending. *Composites Part C : Open Access* **4**, 100079 (2021)
6. Dickson, A.N., Barry, J.N., McDonnell, K.A., Dowling, D.P.: Fabrication of continuous carbon, glass and Kevlar fibre reinforced polymer composites using additive manufacturing. *Addit. Manuf.* **16**, 146–152 (2017)
7. Maqsood, N., Rimašauskas, M.: Characterization of carbon fiber reinforced PLA composites manufactured by fused deposition modeling. *Composite Part C Open Access* **4**, 100112 (2021)
8. Love, L.J., Kunc, V., Rios, O., Duty, C.E., Elliott, A.M., Post, B.K.: The importance of carbon fiber to polymer additive manufacturing. *J. Mater. Res.* **29**, 1893–1898 (2014)
9. Maqsood, N., Rimašauskas, M.: Delamination observation occurred during the flexural bending in additively manufactured PLA-short carbon fiber filament reinforced with continuous carbon fiber composite. *Results Eng.* **11**, 100246 (2021)
10. Moradi, M., Moghadam, M.K., Shamsborhan, M., Bodaghi, M.: The synergic effects of fdm 3d printing parameters on mechanical behaviors of bronze poly lactic acid composites. *J. Compos. Sci.* **4**, 1–16 (2020)
11. Rimašauskas, M., Jasiūnienė, E., Kuncius, T., Rimašauskienė, R., Cicėnas, V.: Investigation of influence of printing parameters on the quality of 3D printed composite structures. *Compos. Struct.* **281** (2022)
12. Türk, D.A., Brenni, F., Zogg, M., Meboldt, M.: Mechanical characterization of 3D printed polymers for fiber reinforced polymers processing. *Mater. Des.* **118**, 256–265 (2017)
13. Ning, F., Cong, W., Qiu, J., Wei, J., Wang, S.: Additive manufacturing of carbon fiber reinforced thermoplastic composites using fused deposition modeling. *Compos. B Eng.* **80**, 369–378 (2015)
14. Tekinalp, H.L., Kunc, V., Velez-Garcia, G.M., Duty, C.E., Love, L.J., Naskar, A.K.: Highly oriented carbon fiber-polymer composites via additive manufacturing. *Compos. Sci. Technol.* **105**, 144–150 (2014)
15. Yu, T., Zhang, Z., Song, S., Bai, Y., Wu, D.: Tensile and flexural behaviors of additively manufactured continuous carbon fiber-reinforced polymer composites. *Compos. Struct.* **225**, 111147 (2019)

16. Rimašauskas, M., Kuncius, T., Rimašauskienė, R.: Processing of carbon fiber for 3D printed continuous composite structures. *Mater. Manuf. Process.* **34**, 1528–1536 (2019)
17. Maqsood, N., Rimašauskas, M.: Tensile and flexural response of 3D printed solid and porous CCFRPC structures and fracture interface study using image processing technique. *J. Market. Res.* **14**, 731–742 (2021)
18. Hao, W., Liu, Y., Zhou, H., Chen, H., Fang, D.: Preparation and characterization of 3D printed continuous carbon fiber reinforced thermosetting composites. *Polym. Testing* **65**, 29–34 (2018)

Influence of Acetic Acids on Performance Parameters of Vegetable Oil Insulation



M. Rajesh, J. Salamon Raja, S. Selvakumar, S. Prasanth, and M. Bakruthen

Abstract For analyzing the presence of oxidative by-product of acid formation in the characteristics of vegetable-based insulating liquids, a study of impact of acid inclusion with the vegetable oil is proposed in this work to analyze the characteristics of selected oil as liquid insulation in transformer under the exposure of acidic condition. For the experimentation purpose, vegetable oils like sunflower oil (SFO), rice bran oil (RBO), sesame oil (SSO), and palm oil (PAO) are taken as base oil samples. The inclusion of acetic acid level in oil samples with the concentrations of 5 ml and 10 ml to study the comprehensive changes in properties of oil samples. The characteristics of samples have been measured as per the international standard. From the experimental results, it is inferred that oil samples have shown the degradation of its performance with an increase in acid. Suitable actions have to be taken for minimization of effects of acids in the performance of oil samples as liquid insulation in transformers.

Keywords Vegetable oil · Acetic acid · Liquid insulation · Transformers

1 Introduction

The demand for electrical apparatus with highly dependable and useful insulating materials has risen in the transmission network of power systems because they will decide the dynamic behavior of the electrical equipment under a variety of operating conditions. Liquid insulations are a common choice among the many forms of insulation used in equipment because they satisfy the criteria for both insulation and cooling [1–7].

Liquid insulation is commonly used to provide insulation and cooling between live conducting elements in oil-filled transformers. Circuit breakers, capacitors, cables, and other devices require liquid insulation. For that, mineral oil made from petroleum has long been used as a liquid insulator. Mineral oil offers the best dielectric and

M. Rajesh · J. S. Raja · S. Selvakumar · S. Prasanth · M. Bakruthen (✉)
EEE, National Engineering College, Kovilpatti, Tamil Nadu, India
e-mail: bakruthenme@gmail.com

© The Author(s), under exclusive license to Springer Nature Singapore Pte Ltd. 2023
V. Bindhu et al. (eds.), *Proceedings of Fifth International Conference on Inventive Material Science Applications*, Advances in Sustainability Science and Technology,
https://doi.org/10.1007/978-981-19-4304-1_9

physicochemical qualities for liquid insulation, but it has a number of disadvantages, including non-biodegradability, toxic gas production, and a limited supply of petroleum for future purposes, to name a few. Researchers are becoming interested in adopting vegetable oil-based liquid insulations in transformers due to their biodegradability, environmental friendliness, and safety when compared to typical mineral oil. Vegetable oil-based insulation was also shown to have better dielectric and physicochemical qualities than the other alternatives when used as an alternate liquid insulation [7].

When exposed to aging conditions over a prolonged length of time, vegetable oils perform better in terms of aging properties [8–12]. Natural sources, such as seeds, plants, and other natural items, are used to make vegetable oils. They are made up of saturated and unsaturated triglyceride fatty acids, which will play a part in assessing the quality of oil samples [1, 2]. Several vegetable oil samples, including sunflower oil, soybean oil, mustard oil, coconut oil, palm oil, and others, were tested in the examination of alternative liquid insulation. Because their compositions vary, vegetable oil in both its unrefined and refined forms was investigated for use as liquid insulation in bio-liquid insulation research [8, 9]. The use of vegetable oil in the transesterification process results in low viscosity liquid insulation [3, 4].

Vegetable oil has been the subject of several studies to test its viability as a liquid insulator. The majority of the studies were focused on experimental property study, assessment of inclusion additives for performance enhancement, aging analysis with paper insulation, dissolved gas analysis, and other similar topics. Mostly on impact of moisture on the properties of oil samples, there is a paucity of literature. Although the presence of acids in oil is undesirable, it cannot be avoided. The presence of acids in liquid insulation is caused by the entry of ambient moisture, as well as the breakdown of paper insulation and oil throughout the aging process. Acid increases the conductivity of oil through ionic generation; therefore, it is one of the most important variables in decreasing the liquid insulation's dielectric breakdown voltage. As a result, investigating the effect of acids on the breakdown voltage is one of the research studies required to evaluate whether oil samples are suitable for use as liquid insulation [10–12]. With all of this in mind, the purpose of this study was to determine how acids influence the performance of oil samples.

2 Experimental Details

2.1 Selection of Base Oil Samples

Along with its low poly and high monounsaturated fatty acid content, natural ester oil is resistant to oxidation. As a result, we will look for the following oil samples: Sunflower oil (SFO), rice bran oil (RBO), sesame oil (SSO), and palm oil (PAO) have been chosen for evaluation based on geographical availability, affordability, and previous study.

Table 1 Proposed oil samples

Sample	Composition
Base sample 1	Sunflower oil
Base sample 2	Rice bran oil
Base sample 3	Sesame oil
Base sample 4	Palm oil
Acid mixed sample 1	Sunflower oil + 5 ml acetic acid
Acid mixed sample 2	Rice bran oil + 5 ml acetic acid
Acid mixed sample 3	Sesame oil + 5 ml acetic acid
Acid mixed sample 4	Palm oil + 5 ml acetic acid
Acid mixed sample 5	Sunflower oil + 10 ml acetic acid
Acid mixed sample 6	Rice bran oil + 10 ml acetic acid
Acid mixed sample 7	Sesame oil + 10 ml acetic acid
Acid mixed sample 8	Palm oil + 10 ml acetic acid

2.2 Proposed Samples

Acid value of vegetable insulating oil increases with the increase in oxidation time, the initial stage of growth is relatively slow, while with the increase in oxidation time, acid value growth rate increases gradually. Moreover, the change of acid value in oil-paper insulation is larger than that of pure insulating oil. For this work, acetic acid is considered, since it is influential acid inside the transformer formed due to oxidation process. Proposed samples and its composition are tabulated in Table 1.

2.3 Oil Preparation Processes

All oil samples are collected from a local manufacturer. They are then filtered to remove the impurities before they are sent to the laboratory. Seeds and nuts must be washed and free of extraneous particles before being turned into oil. The addition of acetic acid to oil samples is done according to procedure, and property measurements are done using industry-standard methods [12–15].

2.4 Measurement of Breakdown Voltage

The breakdown voltage of fluid protection is a proportion of the capacity of fluid protection to endure electrical pressure created in working circumstances. Within the sight of at least one sullyng substance like water, soil, suspended particles, and so forth, low-esteem breakdown voltage might be estimated with the test (IEEE

Fig. 1 Breakdown voltage kit



Std. C57.14, 2018). The breakdown voltage of fluid protection is estimated in light of standard IEC 60,156–11, 2003 [15], with a test cell containing hemispherical terminals. Cathodes are organized on a level plane with 2.5 mm hole dividing. Oil tests are filled in a test cell with the total submersion of terminals. Assuming that air pockets are shaped in the oil test, they are appropriately taken out by giving longer rest season in excess of 15 min at room temperature condition to try not to misdirect and low voltage breakdown. By applying a voltage across the cathode at an increasing pace of 2 kV/s, the breakdown voltage of oil tests is estimated at a specific voltage, which causes breakdown between anodes under endorsed test conditions. For processing dielectric breakdown voltage of oil tests, the test is rehashed for five to multiple times, and the mean of acquired breakdown voltage is considered as the last breakdown voltage of oil test. Breakdown voltage unit is displayed in Fig. 1.

2.5 Measurement of Viscosity

The viscosity of fluid protection is a lot of fundamental to be inside the reference and an incentive for typical working temperatures since fluid protection additionally goes about as a coolant. Thickness might make an effect on cooling and execution of related hardware connected with cooling. Thickness is a proportion of stream obstruction presented by fluid to stream (IEEE Std. C57.14, 2018). The consistency of fluid protection is assessed according to ASTM D445 [16] in redwood viscometer by estimating the time taken for the progression of 50 ml of oil tests through the hole in viscometer under controlled conditions. Red wood viscometer is displayed in Fig. 2.

Fig. 2 Redwood viscometer

2.6 Measurement of Flash Point

Low combustibility is one of the significant contemplations being developed toward better fluid protection. Streak point is the least temperature at which fluid protection shapes a combustible fume combination at surface of fluid. Additionally, low worth of glimmer point is the sign of defilement with fluid protection (IEEE Std. C57.14, 2018). Pensky–Marten closed-cup apparatus is utilized for estimating streak point of fluid protection-based ASTM D92, 2012 [17]. By warming 50 ml oil test under controlled conditions in test cup, streak point is estimated at which temperature, combustible fume on the outer layer of oil test is delivered when misleadingly presented a fire in test hole. Pensky–Marten shut-cup technique is displayed in Fig. 3.

2.7 Measurement of Pour Point

Low temperature execution is one of the significant elements portraying capacity of fluid protection in chilly environments. Pour point of fluid protection is the most minimal temperature at which fluid streams under endorsed conditions. Underneath pour point, oil stream may be troublesome, and furthermore, stream is restricted by consistency. Pour point estimation can be helpful in deciding sort of fluid protection for specific hardware in troublesome working circumstances like cold areas (IEEE Std. C57.14, 2018). Temperature is estimated with pour point contraption with four chambers. 50 ml of oil is taken in test tube and put in copper compartment which is overwhelmed in cooling medium. By lessening temperature of cooling media, oil test in test tube is checked by setting test tube in even way for hardening for each

Fig. 3 Pensky–Marten flash apparatus



3 °C decrease. Pour point temperature is estimated at which temperature, oil tests halted its pouring inside test cell. The pour point estimation arrangement is displayed in Fig. 4.

Fig. 4 Pour point apparatus kit



3 Experimental Results and Discussion

3.1 Properties of Base Oil Samples

For initial investigations on selected oils, properties such as breakdown voltage, viscosity, flash point, and pour point are measured as per standards. Values of properties of oil samples are listed in Table 2.

From the test aftereffects of properties of consumable and non-eatable normal esters, the accompanying derivations are made by contrasting outcomes and IEEE Guide for Acceptance and Maintenance of Natural Ester Insulating Liquid in Transformers, IEEE Std. C57.14, 2018.

The breakdown voltage of any fluid protection is a significant property which estimates the capacity of fluid protection to endure electrical pressure created inside the transformer during working. According to the IEEE guide, the base worth of breakdown voltage of normal esters ought to be 35 kV. In the essential examination of properties of chosen oil tests for this examination, all oil tests have breakdown voltage above 35 kV. From these perceptions, observed chosen regular esters have possible qualities as fluid protection for applications in transformers in light of a significant property of breakdown voltage.

The thickness of fluid protection is one of the significant attributes which impact execution as a coolant and different parts related with fluid protection in the transformer. The most extreme suitable reach for thickness worth of normal esters indicated in IEEE guide is 50 cSt for tolerating as fluid protection. Vegetable oil-based fluid protections for the most part have higher gooey qualities than conventional mineral oil utilized in transformers. In this examination likewise, it is seen that got consistency values for vegetable oil tests are a lot higher than the predefined standard worth. From writing, it is deduced that unsaturated fat parts in vegetable oil are the essential justification for the higher worth of thickness. Since these scopes of thickness for examined vegetable oil are not inside standard worth, direct execution of regular esters might cause issues in cooling execution. For decreasing consistency esteems, a few procedures are proposed in the writing. Subsequently, consist decrease strategies ought to be finished utilization of examined regular esters in transformers as fluid protection.

Fire point temperature is utilized for fire risk appraisal as one of the significant parts. According to IEEE Guide, regular esters ought to have least blaze point

Table 2 Properties of base oil samples

Properties	SFO	RBO	SSO	PAO
Breakdown voltage (kV)	35	38	38	36
Viscosity at 40 °C (cSt)	42	46	55	48
Flash point (°C)	280	290	295	280
Pour point (°C)	9	12	3	3

temperature of 275 °C for tolerating as fluid protection. Streak point temperatures of all vegetable oil tests are fulfilling out the necessary guidelines. From these perceptions, observed explored oil tests have a decent scope of glimmer point temperature as fluid protection for applications in transformers.

Pour point of fluid protection is one of the fundamental properties which demonstrate a scope of temperature with the expectation of complimentary flow easily. Least pour point temperature of regular esters is $-10\text{ }^{\circ}\text{C}$ for tolerating normal esters as fluid protection in light of IEEE guide. Every one of the examples has a positive worth of pour point temperatures. These qualities demonstrated that there are conceivable outcomes of freezing or precious stone development inside oil tests before freezing conditions. From results, it is noticed that unsaturated fat parts are persuasive in pour point values. Since pour point temperature should be a lot of lower than got values for explored regular esters for their utilization in chilly locales, a few methods ought to be embraced to decrease pour guide from its generally expected esteem toward indicated range in view of the writing accessible for decrease in pour point.

3.2 Properties of Acid-Included Oil Samples

Acetic acid inclusion with the oil samples is carried out as per methodology, and measurement of properties is carried out as per standard procedures. The properties of oil samples after inclusion of acid are tabulated in Tables 3 and 4, respectively, for 5 ml and 10 ml inclusion of acetic acid.

From the above experimental results, the following inferences were observed. Even as acid content grows, the rate of decrease in breakdown voltage becomes

Table 3 Properties of 5 ml acetic acid included samples

Properties	SFO + 5 ml Acetic acid	RBO + 5 ml Acetic acid	SSO + 5 ml Acetic acid	PAO + 5 ml Acetic acid
Breakdown voltage (kV)	30	30	28	30
Viscosity at 40 °C (cSt)	55	58	60	53
Flash point (°C)	280	285	285	275
Pour point (°C)	6	15	9	6

Table 4 Properties of 10 ml acetic acid included samples

Properties	SFO + 10 ml Acetic acid	RBO + 10 ml Acetic acid	SSO + 10 ml Acetic acid	PAO + 10 ml Acetic acid
Breakdown voltage (kV)	18	20	19	18
Viscosity at 40 °C (cSt)	60	62	67	59
Flash point (°C)	275	280	275	270
Pour point (°C)	9	18	12	9

noticeable. The breakdown voltage of the oil samples lowers to nearly half of what it was before the acid was applied when 10 ml of acetic acid is added externally. Viscosity and pour point of vegetable oil samples have shown increment in its value after inclusion of acids. Flash point temperature value of the oil samples slightly reduces from normal value without acid inclusion. This indicates the lesser impact created with the acetic acid in the vegetable oil's thermal characteristics.

4 Conclusion

Today, whole world is witnessing the period of shifting from the petroleum products that are depicting and environmentally unfriendly into vegetable oils that are renewable and environmentally friendly. In the study presented in this paper, an attempt was made to develop and characterize a bio-based insulating fluid. This study investigates the impact of acid addition on the properties of vegetable oil-based oil samples. The data demonstrated that acid has a considerable impact on changes in oil sample properties; however, the rate of change differs depending on the acid employed. Increased ionic conductivity, changes in fatty acid content, bubble creation due to dissolved hydrogen gas, and high-pressure development in oil samples are all probable explanations for acid inclusion property changes. In the future, more experiments with oil samples may be undertaken to validate the consistency of vegetable oil as a suitable replacement to mineral oil. For the future, the following work can be focused. Investigation may be extended to analyze the impact of acids from categories of low molecular weight acids and high molecular weight acids. Further investigation can be done to measure the performance of bio-modified vegetable oil and aspects of life estimation. Compatibility analysis can be done to develop the suitable oil insulation to work along with paper insulation.

References

1. Ahamadkamal, M.S., Bashir, N., Muhammad, N.A.: Insulating properties of vegetableoils and their blends. *IEEE Conf. Publ.* 455–458 (2013)
2. Akure, N., Akinola, A.O.: The effects of transesterification and blending on the fatty acid profiles of vegetable oils. *Saudi J. Eng. Technol.* **1**(2), 2415–6264 (2016)
3. Aliyu, A.O., Tijjani, A.: Transesterification and epoxidation of oil extracts from selected plants for use as bio-transformer oil transesterification and epoxidation of oil extracts from selected plants for use as bio-transformer oil. *Int. Res. J. Pure Appl. Chem.* 2231–3443 (2017)
4. Antony Pradeep, J., Kishore Kumar, K., Balasubramanian, D.: Biofuel production using butanol and used transformer oil. *Am. J. Eng. Res. (AJER)* **5**, 285-293 (2016)
5. Bakruthen, M., Karthick, R., Madavan, R.: Investigation of critical parameters of insulating mineral oil using semi conductive nano particles. *IEEE Int. Conf. Circ. Power Comput. Technol.* 294–299 (2013)

6. Ranga, C., Kumar Chandel, A., Chandel, R.: Performance analysis of alternative solid dielectrics of power transformers with a blend of mineral and silicon oils. *IETE Tech. Rev.* (2017)
7. Fofana, I.: 50 years in the development of insulating liquids. *IEEE Electr. Insul. Mag.* **29**(5), 13–25 (2014)
8. Sitorus, H.B.H., Setiabudy, R., Bismo, S., Beroual, A.: Jatrophacurcas methyl ester oil obtaining as vegetable insulating oil. *IEEE Trans. Dielectr. Electr. Insul.* **23**(4), 2021–2028 (2016)
9. Yu, H., Yu, P., Luo, Y.: Renewable low-viscosity dielectrics based on vegetable oil methyl esters. *J. Electr. Eng. Technol.* 2093–7423 (2017)
10. Nasrat, L.S., Kassem, N., Shukry, N.: Aging effect on characteristics of oil impregnated insulation paper for power transformers. *Engineering* **5**, 1–7 (2013)
11. Raof, N.A., Rashid, U., Yunus, R., Azis, N., Yaakub, Z.: Development of palm-based neopentyl glycol diester as dielectric fluid and its thermal aging performance. *IEEE Trans. Dielectr. Electr. Insul.* **23**(4), 2051–2058 (2016)
12. Arroyo, O.H., Fofana, I., Jalbert, J., Ryadi, M.: Relationships between methanol marker and mechanical performance of electrical insulation papers for power transformers under accelerated thermal aging. *IEEE Trans. Dielectr. Electr. Insul.* **22**, 6 (2015)
13. Shah, G.B., Sajja Priti, S.: Implementation of words and characters segmentation of gujarati script using MATLAB. In: *International conference on innovative data communication technologies and application*, pp. 247–256. Springer, Cham (2019)
14. Hamdan, Y.B.: Construction of statistical SVM based recognition model for handwritten character recognition. *J. Inf. Technol.* **3**(2), 92–107 (2021)
15. IEC 60156.: *Insulating liquids-determination of breakdown voltage at power frequency—test method, Third Edition* (2003)
16. ASTM D445.: *Standard test method for kinematic viscosity of transparent and opaque liquids (and calculation of dynamic viscosity)* (2011)
17. ASTM D93.: *Standard test methods for flash point by pensky-martens closed cup tester* (2012)

Design of Gate All Around MOS-Based RADFET Dosimeter



Chitikina Neeraj Venkatesh and Guru Prasad Mishra

Abstract This article proposes gate all around (GAA) MOSFET as a radiation sensitive metal oxide field effect transistor (RADFET) for radiation sensing in space applications. The proposed RADFET uses gate all around technology as it has minimal short channel effects and good electrostatic stability. Analysis is carried out to investigate surface potential, threshold voltage, sensitivity and drain current characteristics. It was proved to be a good one as it achieves high I_{on}/I_{off} value of 8.95×10^{10} and sensitivity of 1.56 mv/Gy. The device implementation and simulations are carried out using 3D technology computed-aided design (TCAD) tool. The sensitivity curves report that GAA RADFET can be a good candidate for space applications.

Keywords RADFET · Surface potential · Threshold voltage · Gate all around MOSFET · Sensitivity

1 Introduction

With advancements in technology, there is need for a device which serves better in terms of area and power consumption. In large-scale devices, leakage current (off-state) is of less significance because devices are operated at higher voltages. But with small scale devices, as the channel length decreases short channel effects like hot carrier injection, punch through, DIBL and V_t roll off are of major concern [1, 2]. To minimize these short channel effects, SOI technology was introduced. This SOI technology has reduced the short channel effects to a certain extent as double gate, triple gate, quadruple and pi gate structures are made using this technology. The major advantage of this technology includes reduction in short channel effects and higher drive current but it suffers from corner effects. Due to corner effects,

C. N. Venkatesh (✉) · G. P. Mishra
Department of Electronics and Communication Engineering, National Institute of Technology Raipur, Raipur, India
e-mail: cvenkatesh.mtech2020.etc@nitrr.ac.in

G. P. Mishra
e-mail: gpscmishra.etc@nitrr.ac.in

excess of heat will be produced resulting in self-heating of the device degrading its performance [3–6]. To avoid this problem, structures with sharp corner are to be avoided, and a device with smooth surface without 90-degree bends is required. Hence, the proposed device gate all around MOSFET is introduced [7].

In this device, the channel is cylindrically surrounded by gate. As the channel is cylindrically surrounded by gate, there are several advantages like better control over the channel, high on current, negligible leakage current, low subthreshold slope and reduced parasitic capacitance [8–11]. One of the disadvantages of the device is its self-heating, but it can be modelled as shown in [12, 13]. This device can be used for low-power applications like designing memories, amplifiers, logic circuits and high frequency application like RF circuits [14, 15].

Since the instruments used for radiation dosimetry are exposed to very high radiation, there is high possibility of device damage [16]. The sensitivity obtained by the conventional RADFETs is very less, and it has been found that MOSFETs can be served as RADFET [17]. But due to high radiation densities, there exist a very high chance of occurrence of short channel effects in RADFET. Hence, a device with good electrostatic stability is required to serve as a dosimeter [18]. Therefore, the proposed device the gate all around MOSFET can be analysed to study its radiation sensing behaviour as it is less prone to short channel effects.

The contents of the paper are illustrated as follows: in Sect. 2 models and parameters related to the device are presented. Section 3 discusses about the results obtained in the simulator in terms of threshold voltage and sensitivity. Section 4 concludes the work.

2 Device Physics

2.1 Theory

The base for the structure is a silicon substrate made using SOI technology. Using self-alignment technique, a cylindrical structure of silicon is prepared. The gate oxide layer is deposited over the channel region of the silicon substrate. Upon the gate oxide region, another dielectric material like spacer is wrapped. A trench is made in the spacer region to accommodate the gate with respect to the channel. The divided spacer regions are known as spacer 1 (SP1) and spacer 2 (SP2). Finally, ion implantation technique is used to form the source and drain regions the MOSFET (Fig. 1).

To study the behaviour of the partially irradiation, the dielectric region around the channel is divided into three regions, namely R1, R2 and R3. These regions are analysed for different irradiation densities [19, 20]. The parameters of the structure used are given in the Table 1.

To analyse the device behaviour, various physics models are used which are as follows: CONMOB and FLDMOB are used to study the mobility characteristics of

Fig. 1 2D cross-sectional view of gate all around RADFET

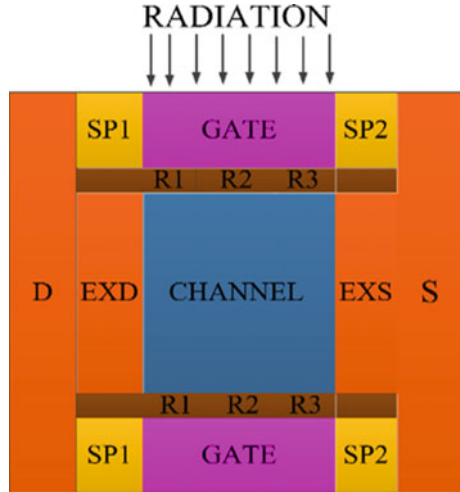


Table 1 Parameters of the device

Parameter	Value
Source/Drain doping	2×10^{20}
Source/Drain extension doping	1×10^{20}
Channel doping	1×10^{16}
Oxide thickness	2 nm
Channel length	40 nm
Spacer length	15 nm
Spacer thickness	10 nm
Gate radius	10 nm
Channel radius	8 nm
Source/Drain thickness	16 nm

the device. DRIFT.DIFF model is used in calculation of drain current and to deal with recombination charges, SRH model is used. Newton trap method is used for simulator mathematical calculations at 300 k. Silvaco TCAD is used as the simulator [21].

The principle behind the working of RADFET is that when a device is subjected to radiation then trap charges get accumulated in the oxide region. These accumulated trap charges help in decreasing or increasing the threshold voltage of the device. This change in threshold voltage for radiated and unirradiated device for a certain radiation dose is termed as sensitivity [19, 20]. Hence, sensitivity of RADFET is proportional to change in threshold voltage and inversely proportional to radiation dose. Therefore, sensitivity can be given as

$$\text{Sensitivity}(s) = \frac{\Delta v_{th}}{D} \tag{1}$$

where D is radiation dose whose value is 104 Gy for simulation.

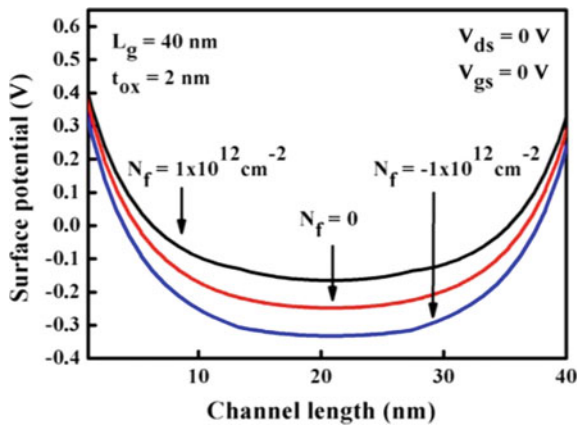
3 Results and Discussion

This section of the paper deals with the radiation exposed behaviour of the gate all around MOSFET. On irradiation, trap charges will be induced in the oxide layer. The presence of these trap charges results in change of surface potential. The surface potential change on irradiation for positive and negative trap charges is depicted in the Fig. 2.

Above figure illustrates the effect of uniform radiation on the device. It can be visualized that presence of positive trap charges supports for channel formation increasing the surface potential compared to conventional device. On the other hand, negative trap charges in the oxide layer opposes the formation of the channel formation decreasing the surface potential.

Effect on surface potential for nonuniform radiation is shown in Fig. 3. It can be concluded from both figures that as the density of radiation increases then the variation in surface potential increases. Figure 3a shows the nonuniform radiation condition where region 1 (R1) and region 3 (R3) are given same amount of negative trap charges and region 2 (R2) is unirradiated. Hence, there is a difference in the potential of region 1 and region 3 to that of region 2 but it is also get effected by radiation. Figure 3b depicts the step increment of charges where increment in positive trap charges further enhances the surface potential and increment in negative trap charges further reduces the surface potential.

Fig. 2 Surface potential plot for various uniform trap charge densities



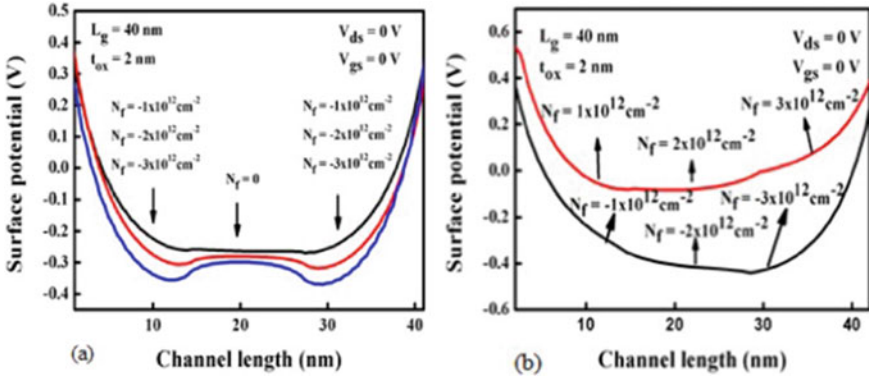
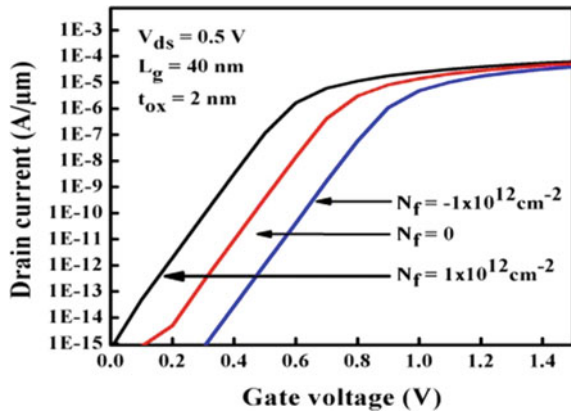


Fig. 3 Surface potential variation for various nonuniform trap charge densities

Fig. 4 Transfer characteristics curve for proposed RADFET with different trap charges



From the drain current plot in Fig. 4, it can be said that device has good electrostatic characteristics and is less prone to short channel effects. The device has a good I_{on}/I_{off} ratio of the order 10^{10} and as shown in graph drain curve shifts left when radiated by positive charges reducing the threshold voltage, and it moves right when irradiated by negative charges increasing the threshold voltage.

Threshold voltage shown in below Fig. 5 follows a linear pattern with increase in trap charge density, and the sensitivity of the proposed gate all around RADFET is large for negative trap charges compared to same density of positive trap charges.

On obtaining the threshold voltage curves, sensitivity of the RADFET is calculated. The sensitivity curves for different trap charges show that sensitivity is high for negative trap charge density and increases with increase in thickness of the oxide layer (Fig. 6).

Finally, a table can be drawn to represent the performance characteristics of the device, where it shows good I_{on}/I_{off} ratio of the order 10^{10} and subthreshold slope below 60 mV/dec and sensitivity greater than 1 mV/gy (Table 2).

Fig. 5 Threshold voltage variation with increase in trap for different oxide thickness

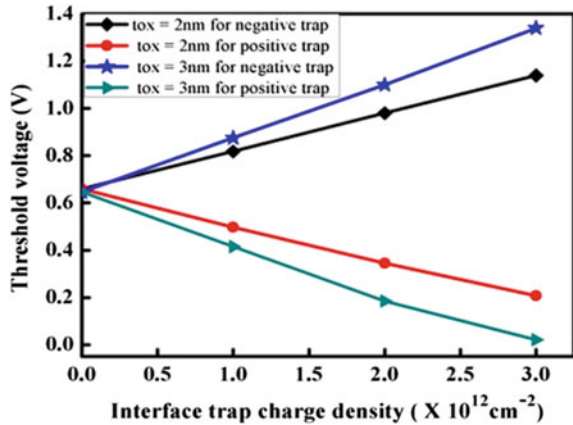


Fig. 6 Sensitivity variation with respect to positive and negative trap charges for oxide thickness of 2 nm and 3 nm

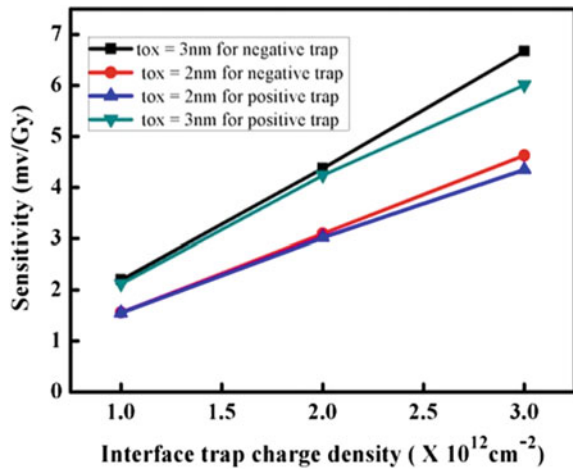


Table 2 Various parameters for proposed GAA RADFET

Parameter	GAA RADFET
I_{on}/I_{off}	8.95×10^{10}
SS (mv/dec)	59.7
Vth (V)	0.659
S (mv/Gy)	1.56

4 Conclusion

This paper presents the gate all around MOSFET for designing a radiation sensitive device called the RADFET. Various electrical characteristics like the surface potential, threshold voltage, transfer characteristics and sensitivity are investigated in the

paper. Analysis is done for both uniform and nonuniform irradiation and found that gate all around RADFET achieves a sensitivity of 1.56 mv/Gy.

References

1. Bohr, M.: A 30 year retrospective on Dennard's MOSFET scaling paper. *IEEE Solid-State Circ. Soc. Newslett.* **12**, 11–13 (2007)
2. Firdous, R.: Future of wireless mobile communication with nanotechnology and application of CNT in MOSFETs (nano transistors). *Int. Res. J. Eng. Technol. (IRJET)*, **5**, 503–507 (2018)
3. Reddy, G.V., Kumar, M.J.: A new dual-material double-gate (DMDG) nanoscale SOI MOSFET—two-dimensional analytical modelling and simulation. *IEEE Trans. Nanotechnol.* **4**, 260–268 (2005)
4. Ernst, T., Ritzenthaler, R., Faynot, O., Cristoloveanu, S.: A model of fringing fields in short-channel planar and triple-gate SOI MOSFETs. *IEEE Trans. Electron Devices* **54**, 1366–1375 (2007)
5. Gupta, S., Rawat, A., Mishra, V.: Linearity distortion analysis of junctionless quadruple gate MOSFETs for analog applications. *SILICON* **11**, 257–265 (2019)
6. Park, J., Colinge, J.P.: Multiple-gate SOI MOSFETs: device design guidelines. *IEEE Trans. Electron Devices* **49**, 2222–2229 (2002)
7. Sachdeva, T.K., Aggarwal, S.K., Kushwaha, A.K.: Design, analysis and simulation of 30 nm cylindrical gate all around MOSFET. *Int. J. Adv. Res. Comput. Commun. Eng.* **5**, 358–360 (2016)
8. Takato, H.: Impact of surrounding gate transistor (SGT) for ultra-high-density LSI's. *IEEE Trans. Electron Devices* **38**, 573–578 (1991)
9. Jena, B., Pradhan, K.P., Dash, S., Mishra, G.P., Sahu, P.K., Mohapatra, S.K.: Performance analysis of undoped cylindrical gate all around (GAA) MOSFET at subthreshold regime. *Adv. Nat. Sci. Nanosci. Nanotechnol.* **6**, 035010 (2015)
10. Jena, B., Pradhan, K.P., Sahu, P.K., Dash, S., Mishra, G.P., Mohapatra, S.K.: Investigation on cylindrical gate all around (GAA) to nanowire MOSFET for circuit application. *Facta Universitatis, Series: Electron. Energetics* **28**, 637–643 (2015)
11. Jena, B., Dash, S., Routray, S.R., Mishra, G.P.: Inner-gate-engineered GAA MOSFET to enhance the electrostatic integrity. *NANO* **14**, 1950128 (2019)
12. Su, Y., Lai, J., Sun, L.: Investigation of self-heating effects in vacuum gate dielectric gate-all-around vertically stacked silicon nanowire field effect transistors. *IEEE Trans. Electron Devices* **67**, 4085–4091 (2020)
13. Shin, S.H.: Direct observation of self-heating in III–V gate-all around nanowire MOSFETs. *IEEE Trans. Electron Devices* **62**, 3516–3523 (2015)
14. Kushwaha, P., Dasgupta, A., Kao, M.-Y., Agarwal, H., Salahuddin, S., Hu, C.: Design optimization techniques in nanosheet transistor for RF applications. *IEEE Trans. Electron Devices* **67**, 4515–4520 (2020)
15. Andri, S., Fhager, L.O., Wernersson, L.E.: Millimeter-wave vertical III-V nanowire MOSFET device-to-circuit co-design. *IEEE Trans. Nanotechnol.* **20**, 434–440 (2021)
16. Pejovic, S., Pejovic, M.: VDMOSFET as a prospective dosimeter for radiotherapy. *Appl. Radiat. Isot.* **132**, 1–5 (2018)
17. Yilmaz, E., Kahraman, A., McGarrigle, A.M., Vasovic, N.: Investigation of RadFET response to X-ray and electron beams. *Appl. Radiat. Isot.* **127**, 156–160 (2017)
18. Farroh, H.A., Nasr, A., Sharshar, K.A.: A study of the performance of an N-channel MOSFET under gamma radiation as a dosimeter. *J. Electron. Mater.* **49**, 5762–5772 (2020)
19. Dubey, A., Ajay, Narang, R., Saxena, M., Gupta, M.: Modeling and simulation of junctionless double gate radiation sensitive FET (RADFET) dosimeter. *IEEE Trans. Nanotechnol.* **17**, 49–55 (2018)

20. Ghosh, S., Saha, P., Mukherjee, A., Bose, S., Venkateswaran, P., Sarkar, S.: Analytical modeling of core-shell junctionless RADFET dosimeter of improved sensitivity. **13**, 1–12 (2022)
21. ATLAS Device Simulation Software, Silvaco. Santa Clara, CA, USA (2016)

Influence of Casting Moulds on the Tensile and Corrosion Characteristics of Palm Kernel Shell Ash Reinforced Al6063-SiC Composite



O. O. Ajide, T. O. Dada, N. Idusuyi, F. A. Musa, O. A. Aogo, A. S. Adebayo, and N. Kumar

Abstract In this work, SiC particles were partially replaced with agro-based Palm Kernel Shell Ash (PKSA) in Al6063-SiC-based composites and the impact of two mould types on their tensile and corrosion properties was investigated. Tensile, corrosion and microscopic tests were carried out on the stir cast produced composites. The composite produced with metal mould had the highest UTS and elongation at 193.55 MPa and 19.15%, respectively. The lowest corrosion penetration rate and current density were achieved with the composite produced using metal mould at 0.000739 mm/yr and 6.36E-08 A/cm², respectively. The presence of agglomerated particles in microstructures of Al6063-SiC-PKSA composites produced with sand mould can be attributed to their general lower tensile and corrosion properties in comparison with the composites produced with metal mould. This study showed that the use of metal mould is better than sand mould for production of Al6063-SiC-PKSA composites with enhanced tensile and corrosion properties.

Keywords Al6063-SiC-PKSA composites · Casting mould · Tensile properties · Corrosion and microstructure

O. O. Ajide (✉) · N. Idusuyi · F. A. Musa · A. S. Adebayo
Department of Mechanical Engineering, University of Ibadan, Ibadan, Oyo state, Nigeria
e-mail: ooe.ajide@ui.edu.ng; ooe.ajide@gmail.com

T. O. Dada
Department of Mechanical Engineering, University of Manitoba, Winnipeg, MB, Canada

O. A. Aogo
Research and Development Unit, Standard Connections Limited, Lagos, Nigeria

N. Kumar
School of Materials Science and Technology, Indian Institute of Technology (BHU), Varanasi
221005, India

1 Introduction

As part of efforts towards meeting the global demand for lightweight, low-cost and high-performance structural materials, there has been a gradual shift from monolithic alloys to Metal Matrix Composites (MMCs) materials [1]. The potential advantages of MMCs over monolithic alloys may have accounted for the recent resurgence of research interest in the field [2, 3]. Aluminium Matrix Composites (AMCs) are highly sought-after in aerospace, automotive, marine and other structural engineering applications due to their superior mechanical properties, light weight and stability under challenging operating conditions [2, 4–6]. There are many methods for fabricating composite materials; hence, researchers can choose one depending on the matrix and reinforcement used [7]. Stir casting is the most frequently used manufacturing method for AMCs due to its simplicity and low cost [8]. A study on properties of AMCs fabricated via stir casting by Rao et al. [4] showed that stir casting is well suited and economical for the preparation of AMCs with desired properties.

The performance of AMCs materials is primarily determined by their microstructures. Other critical parameters are the distribution of reinforcement within the alloy, particulate size and shape of the resulting composite [7]. In Rao et al. [4], it was shown that by increasing volume fraction and decreasing particle size of reinforced material in AMCs, the hardness, tensile strength and yield strength increase. The use of SiC, Al₂O₃, B₄C, TiB₂ and other synthetic reinforcements in AMCs had been substantially explored [7, 9–15]. Several studies have examined the use of either single or hybrid ceramic reinforcement for improving the mechanical, tribological and microstructural properties of AMCs. For instance, Ram et al. [16] investigated the mechanical properties of Al6061 reinforced with SiC and Al₂O₃ particles at wt% of 2.5wt% and 5wt%, respectively, and vice versa. The outcome of the study indicated improved mechanical properties in Al6061 reinforced with 5wt% SiC and 2.5wt% Al₂O₃.

Due to the cost implications of synthetic ceramic reinforcements and environmental concerns [17], researchers have intensified efforts in exploring low cost and eco-friendly agro-residues and industrial wastes such as groundnut shell ash, Rice Husk Ash (RHA) and fly ash [2, 3 18–21] as a partial or wholly replacement for ceramic reinforcement in AMCs [21]. The mechanical behaviour of Al–Mg–Si alloy matrix reinforced with Al₂O₃ and RHA in ratio (10:0, 8:2, 7:3 and 6:4) was investigated by Alaneme et al. [22]. Findings obtained showed that sample with 2wt% RHA had higher value of specific strength, percentage elongation and fracture toughness when compared to the single Al₂O₃ reinforced. The physico-mechanical properties of Al 6063-based composites reinforced with SiC and Palm Kernel Shell Ash (PKSA) were investigated by Ikubanni et al. [21] The results showed a reduction in the density of composites with a corresponding increase in the wt% of the PKSA particulates. It was also found that the mechanical properties improved as the volume fraction of PKSA increased at fixed 2wt% SiC content. The observed general improvement in physico-mechanical properties of Al6063-SiC-PKSA was attributed to the homogeneous dispersion of both reinforcements in the alloy. However, deteriorations in the

percentage elongation and fracture toughness of the composites were observed due to the presence of weak phases of PKSA and intermetallics. In [15], the influences of fly ash and carbonized eggshells as reinforcements on the mechanical, wear and corrosion of properties of Al-Si12-based composite were studied. It was revealed that increase in the weight fraction of the reinforcements generally improved the microhardness, wear and corrosion properties of the composite.

Aside the influence of reinforcements on the properties of cast AMCs, many authors have also shown that the type, materials characteristics and temperature of the mould as well as conditions of mould–metal interface can remarkably impact on the resulting properties of the monolithic alloys/composites [23–29]. For instance, Ayoola et al. [24] compared the influence of metal mould, cement-bonded sand mould and naturally bonded sand mould on the tensile strength, hardness and impact strength properties of as cast Al6063 alloy. The outcome of the study revealed that naturally bonded sand mould had superior tensile strength and ductility when compared to metal mould and cement-bonded sand mould. The authors' findings however showed that casting of Al6063 alloy with metal mould yielded the best impact strength when compared with cement-bonded sand mould and naturally bonded sand mould. Despite the reported influence of mould types in the aforementioned, there is paucity of information in respect of their impact on properties of Al6063-SiC-based composites. In this work, attempt was made to partially replace SiC particles with agro-based PKSA in Al6063-SiC-based composites and investigate the impact of two mould types on mechanical and corrosion properties of the resulting Al6063-SiC-PKSA composites. The motivations for this study were the potential benefits of reduction in cost implication and environmental concerns associated with use of agro-based reinforcement in Al6063-based composites as well as data to be made available for appropriate choice of casting moulds for production of Al6063-SiC-PKSA composites.

2 Methodology

The experimental methodology at glance used for this study is presented in Fig. 1.

2.1 Materials

The materials used in the study were Aluminium magnesium-silicon (Al6063), Silicon Carbide (SiC) and Palm Kernel Shell Ash (PKSA). Al6063 was obtained from NIGALEX, Lagos State, Nigeria. The chemical composition of Al6063 is presented in Table 1. SiC powder particle size 30 μm was obtained from Show Crown Ventures Nigeria, while processed PKSA was procured at Olorunda Market in Nigeria. SiC and PKSA were added as the reinforcement for the Al6063-based composite.

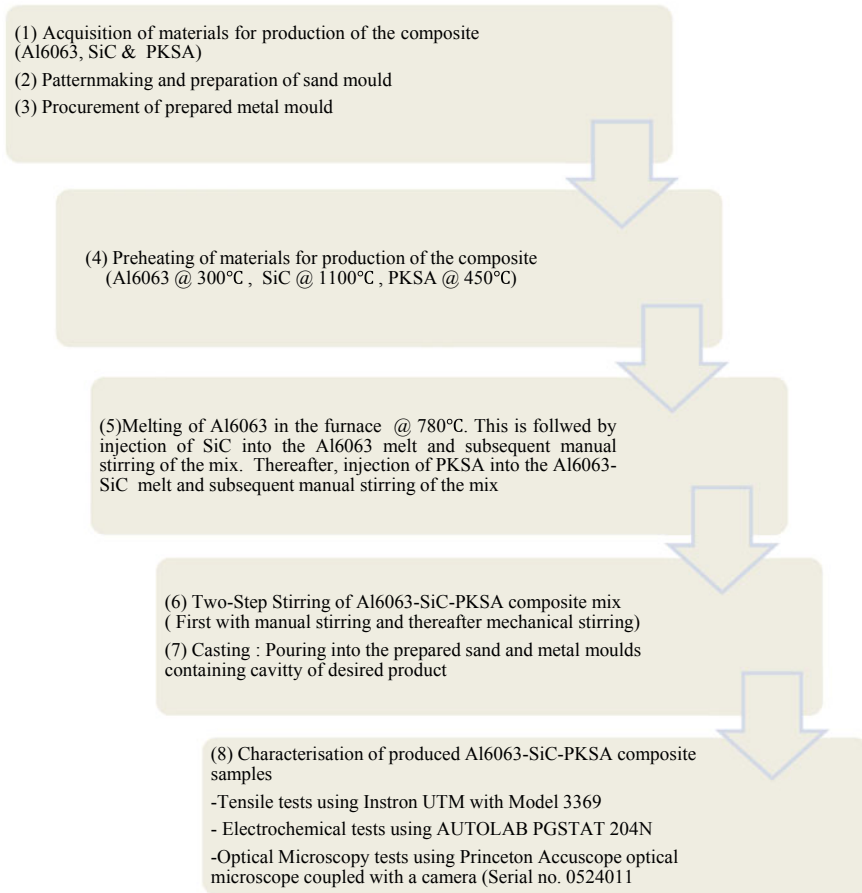


Fig. 1 Block schematic of the experimental methodology

Table 1 Chemical composition of Al6063 alloy

Constituents	Si	Mg	Fe	Cu	Mn	Cr	Zn	Ti	Al
%Composition	0.4649	0.4682	0.2143	0.0030	0.0140	0.0020	0.0010	0.0050	98.6900

2.2 Production of Composites

The Al6063-SiC-PKSA composite was produced using the two-step stir casting method. SiC and PKSA were incorporated at concentrations of 10, 11, 12 and 13 wt%, based on SiC to PKSA ratios (10:0, 10:1, 10:2 and 10:3). Al6063 alloys containing 87, 88, 89 and 90% by weight were first heated to a temperature of 300 °C for 45 min to improve wettability. The SiC powder and PKSA were preheated to 1100 °C and 450 °C, respectively. The Al6063 particles were then heated to 780 °C and allowed

Fig. 2 Mechanical stirring setup for the Al6063-based composite slurry



to cool until the alloy reached a semi-solid state at approximately 600 °C. At this temperature, the SiC powder and PKSA particles were added to the furnace and the mix manually stirred for 5 min. The composite slurry was placed in the furnace and reheated until it reached a liquid state, at which point mechanical stirring (as shown in Fig. 2) at 300 rpm began for approximately 15 min. The furnace temperature was maintained at 770°C during the final stages of mixing. After mixing, the slag was removed from the composite slurry and the composite was slightly cooled to approximately 750 °C before being carefully poured into the previously prepared sand and fixed metal moulds.

2.3 Mechanical Test

Tensile Test

Instron Universal Testing Machine (UTM) with Model 3369 as shown in Fig. 3 was used to conduct the tensile strength test using standard procedures. The composite samples as shown in Fig. 4a, b were machined on a lathe to the required standard test piece size, a cylindrical shape with a diameter of 5 mm and a length of 30 mm, with dog bone-shaped ends (Fig. 4c). The Ultimate Tensile Strength (UTS), Modulus of Elasticity (MOE) and Percentage Elongation were determined from the tests.

Metallographic Test

Fig. 3 Tensile tests setup with UTM (model 3369)

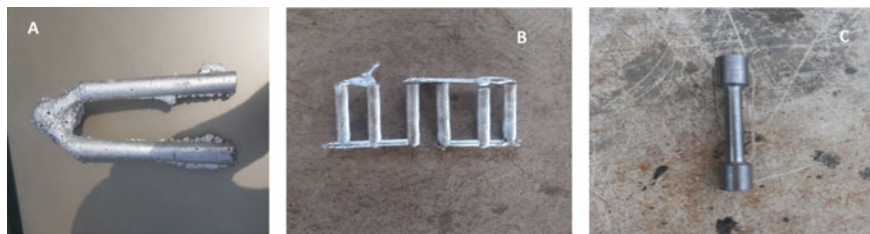


Fig. 4 a Al6063-SiC-PKSA sand mould, b Al6063-SiC-PKSA metal mould, c tensile test sample

Silicon Carbide paper of various grades was placed on the grinding machine in the following order: 220, 320, 400 and 600 (i.e. coarse grade to fine grade) followed by polishing to mirror like surface. The surfaces were etched with 2% sodium hydroxide and examined at 400X magnification using Princeton Accuscope optical microscope coupled with a camera (Serial no. 0524011) as shown in Fig. 5.

Corrosion Test

The samples were cut into small pieces measuring 10 mm in diameter and 5 mm in height. The cutting was accomplished with the aid of a student lathe machine. The experiments on potentiodynamic polarization and Open Circuit Potential (OCP) were conducted using AUTOLAB PGSTAT 204 N instrument as indicated in Fig. 6. At room temperature, electrochemical studies were conducted using a three-electrode cell assembly. The working electrode was a composite of 0.785 cm² geometric area embedded in resins, the counter electrode was platinum, the reference electrode was saturated silver/silver chloride, and the electrolyte was sea water. The working electrode was polished using emery paper of various grades. Prior to performing the potentiodynamic polarization measurement, 30 min of OCP measurements were



Fig. 5 Optical microscopy tests setup

Fig. 6 Electrochemical tests setup using AUTOLAB PGSTAT 204 N



conducted, which was found to be sufficient to achieve a stable value of E_{corr} . To determine the current density, corrosion rate, and polarization resistance, a linear polarization study was conducted from a cathodic potential of -250 mV to an anodic potential of $+250$ mV at a scan rate of 1.0 mVs¹.

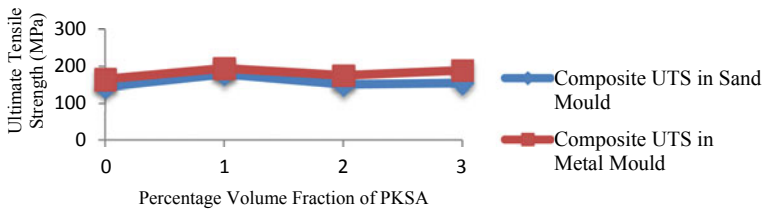


Fig. 7 Effect of PKSA content on UTS of the composites produced using sand and metal moulds

3 Results and Discussion

3.1 Ultimate Tensile Strength (UTS)

Figure 7 shows the effect of increasing the volume fraction of PKSA on the UTS of the composites produced using sand and metal moulds. Figure 3 generally shows that UTS increased with increasing volume fraction of PKSA in the composites produced using the two mould types chosen for this study. The foregoing observation is in agreement with the findings of [3]. It was found by Edoziuno et al. [3] that the use of PKSA as reinforcement for AA6063 alloy improved the tensile and yield strengths. The authors attributed the improvement to grain refinement which was the consequential homogeneous dispersion of PKSA in the matrix. However, the composite prepared using the metal mould had higher UTS values when compared to that of sand mould at all investigated volume fractions of PKSA. The highest obtained UTS was 193.55 MPa with 1% PKSA content. The comparably better UTS of the composites synthesized with metal mould can be explained based on structural features of castings observed by Ayoola et al. [24] in respect of their study on effects of metal mould on cast aluminium 6063 alloy.

3.2 Modulus of Elasticity (MOE)

As shown in Fig. 8, the inclusion of PKSA in the composites up to 1% increased the MOE of those produced using sand mould and decreased those produced using metal mould. Perhaps, the difference in the initial temperature of the moulds was responsible for variation in response pattern. The findings of [26] can be used to support the explanation offered in this regard. Adeosun et al. [26] observed that the type of mould with higher prior to casting mould temperature had detrimental mechanical properties. The maximum MOE of 9852.43 MPa was obtained when the composite had 1% PKSA. Even at ambient temperature, metal mould being a good conductor of heat has higher prior to casting mould temperature in comparison to that of sand mould. However, with PKSA content above 1%, the MOE of those produced using sand mould decreased, while that of those produced using metal mould increased. The

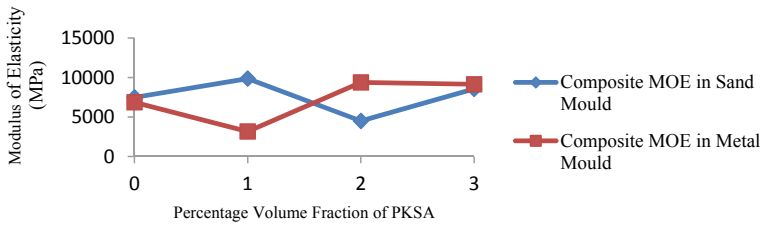


Fig. 8 Effect of PKSA content on MOE of the composites produced using sand and metal moulds

observed comparably increase in MOE at PKSA content beyond 1% for composite castings synthesized with metal mould can be attributed to high thermal conductivity of metal mould resulting to higher cooling rate and the consequential solidification condition of the composite melt [26, 27]. Drawn from the inspiration of the findings reported by [3, 24], the higher rate of solidification yielded grain refinement and equiaxed microstructures of composite castings synthesized with metal mould.

3.3 Elongation

Figure 9 shows the effect of increasing volume fraction of PKSA on the percentage elongation of the composite. Figure 5 reveals that the percentage elongation exhibited fluctuating response as the percentage of PKSA was increased for both sand and metal moulds. Notwithstanding, it can be inferred that percentage elongation generally increases as the PKSA content increases. The aforementioned observation is in line with findings of [3] which found that inclusion of PKSA as reinforcement promotes ductility behaviour of AA6063-based composites. However, the highest percentage elongation occurred when the composite contained 1% PKSA for both the metal and sand moulds which were 19.15% and 10.58%, respectively. Fig. 9 also shows that the composites prepared with metal mould had higher percentage elongation than that of the sand moulds at all investigated percentages of PKSA. The better percentage

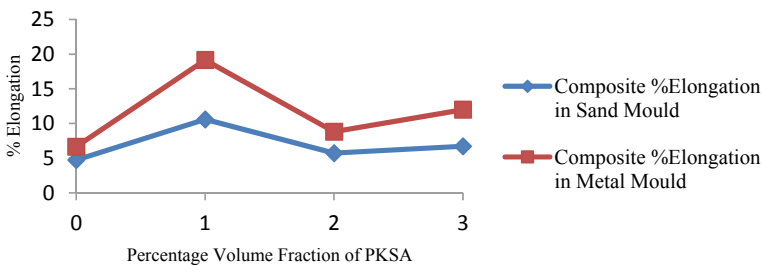


Fig. 9 Effect of PKSA content on percentage elongation of the produced Al6063-SiC-PKSA composites

elongation response of the composites produced with metal mould can be explained based on the observed structural features of castings studied by Ayoola et al. [24].

3.4 Metallographic Examination

Figure 10a, b shows the micrographs of Al6063-SiC composites prepared with sand mould and metal mould, respectively, containing no PKSA. The microstructural studies revealed a more uniform distribution of reinforcement particles in the metal mould than in the sand mould characterized with macro-segregation of particles in some places. The characteristics of the microstructures observed conforms to the findings of [24] where it was found that castings produced with metal mould exhibited equiaxed grain structures and finer microstructures features as against the coarseness compared to those synthesized with sand mould. Figure 10c, d shows the micrographs of Al6063-SiC composite prepared with sand mould and metal mould, respectively, containing 1% PKSA. A close examination of the microstructures revealed the presence of agglomerated particles of SiC and PKSA in the composite prepared with sand

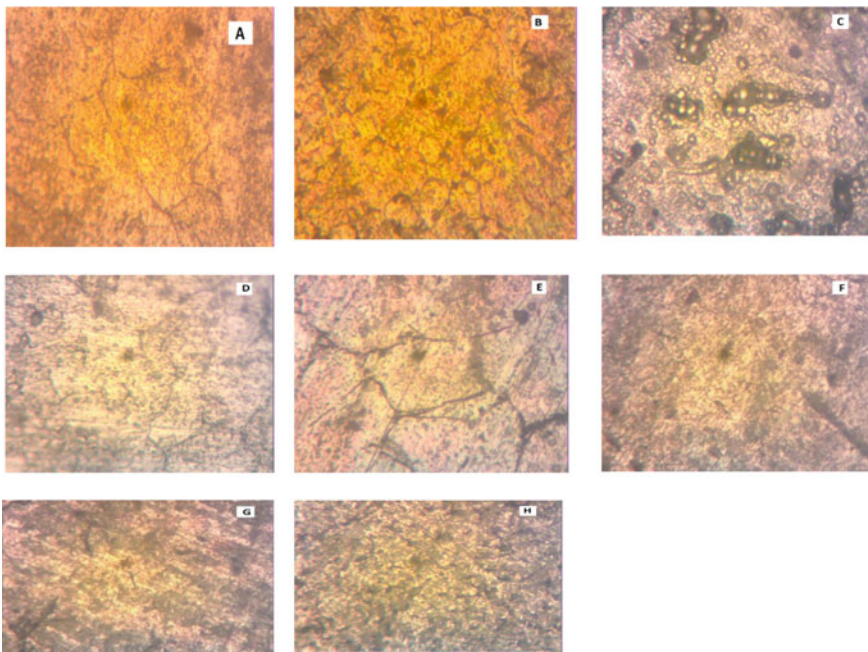


Fig. 10 Micrographs of **a** AL6063-SiC for sand mould, **b** Al6063-SiC for metal mould, **c** Al6063-SiC + 1% PKSA for sand mould, **d** Al6063-SiC + 1% PKSA for metal mould, **e** Al6063-SiC + 2% PKSA for sand mould, **f** Al6063-SiC + 2% PKSA for metal mould, **g** Al6063-SiC + 3% PKSA for sand mould, **h** Al6063-SiC + 3% PKSA for metal mould

mould than that prepared with the metal mould which is in close agreement with the findings of [24]. These clusters of SiC and PKSA are likely to be responsible for the increased UTS and elongation for the composites prepared with metal mould than that of the sand mould. The composite prepared with sand mould had its highest MOE at this percentage, but the reverse was the case for the metal mould. This also might be due to agglomeration in the composite matrix. Figure 10e, f shows the micrographs of Al6063-SiC composite prepared with sand mould and metal mould, respectively, containing 2% PKSA. The microstructure revealed the presence of rather thick grain boundary lines and may be attributed to agglomeration which often occur at higher volume fraction of the reinforcements. The agglomeration of SiC and PKSA is not as pronounced as the samples containing 1% PKSA for the sand mould. Generally, the sample shows good mixability of the matrix and the fibres added. The composite prepared with the metal mould shows a better and more refined structure than that prepared with sand mould. Perhaps, this is why the composite prepared with metal mould has higher UTS and percentage elongation than that of sand mould. Figure 10g, h shows the micrographs of Al6063-SiC composite prepared with sand mould and metal mould, respectively, containing 3% PKSA. Very visible from the micrograph is the good spread of PKSA and SiC along the matrix. The composite prepared with metal mould still shows better grain structure and homogeneity than that of the sand mould. This still further explains the higher UTS and percentage elongation of composites produced with metal mould compared to that of sand mould.

3.5 Corrosion Test

It can be observed that the corrosion rates reduced as the percentage of PKSA increased in both sand and metal moulds as shown in Figs. 11, 12 and 13. But as the volume fraction of PKSA increased above 2%, the corrosion rate began to increase. The lowest value of the corrosion penetration rate for the sand mould occurred between 0.003488 mm/yr and 0.000838 mm/yr with 1 and 2wt. % PKSA content, respectively. Figure 13 also shows the lowest value of the corrosion penetration rate

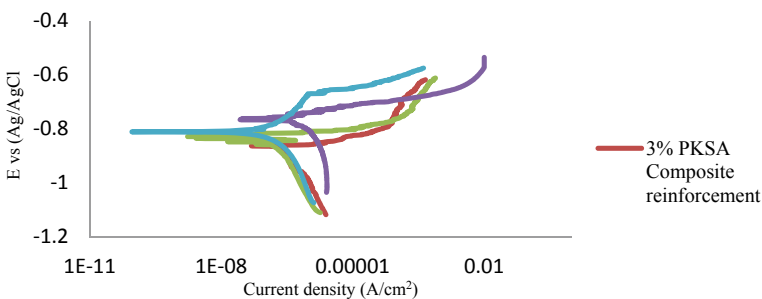


Fig. 11 Tafel diagram of composites developed using sand mould

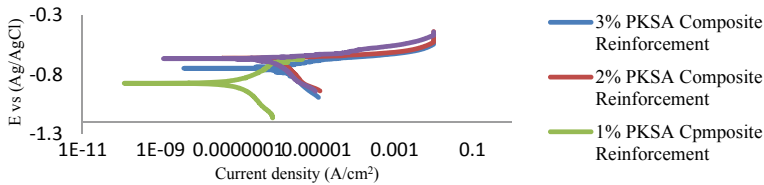


Fig. 12 Tafel diagram of composite developed with metal mould

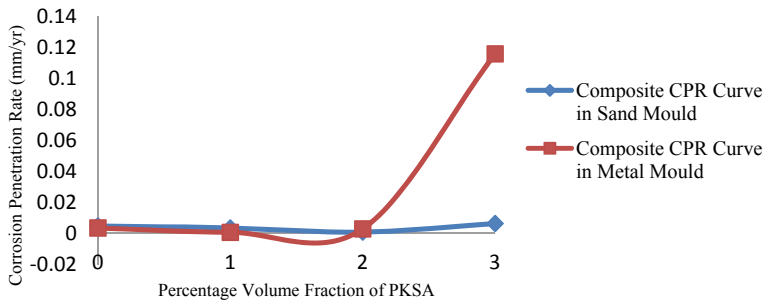


Fig. 13 Effect of mould types on corrosion resistance of Al6063-SiC-PKSA in seawater

for the metal mould occurred between 0.000739 mm/yr and 0.00291 mm/yr which also correspond to 1 and 2% PKSA, respectively. The highest value of the corrosion penetration rate occurred with samples containing 3% PKSA for both the sand mould and metal mould which were 0.00636 mm/yr and 0.1158 mm/yr, respectively. This shows that the corrosion penetration rate was lower in the metal mould than that of the sand mould at 0–2% volume fraction of PKSA. However, as the volume fraction of PKSA increased above 2%, the sand mould comparably exhibited lower corrosion penetration rate. The results show that PKSA does reduce the rate of corrosion of the Al6063-SiC composite when added in small quantities. The result also shows that composites developed with the metal mould had lower corrosion rate than that developed with sand mould when small quantities (between 0 and 2%) of PKSA are added. The current density curve is alike with the corrosion penetration curve. The lowest value of the current density for the sand mould occurred between 3.00×10^{-7} A/cm² and 7.21×10^{-8} A/cm² which corresponds to 1 and 2% PKSA, respectively. The lowest value of the current density for the metal mould occurred between 6.36×10^{-8} A/cm² and 2.50×10^{-7} A/cm² which also corresponds to 1 and 2% PKSA, respectively. Highest value of the current density occurred with samples containing 3% PKSA for both the sand mould and metal mould which were 5.47×10^{-7} A/cm² and 9.97×10^{-6} A/cm², respectively, with lowest value occurring in metal mould between 0 and 2% volume fraction of PKSA as shown in Fig. 14. However, as the volume fraction of PKSA increased above 2%, the sand mould exhibited lower current density. The results show that PKSA does reduce the current density of the Al6063-SiC composite when added in small quantities. The result also showed that

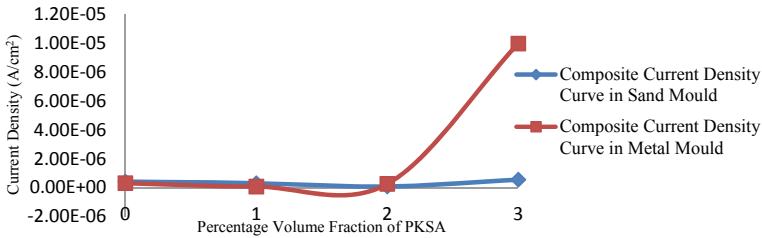


Fig. 14 Effect of mould types on the current density of Al6063-SiC-PKSA in seawater

composites developed with the metal mould have lower current density compared to that developed with sand mould when content added is not above 2% of PKSA. The attainment of equiaxed grain structures with castings produced with metal mould [24] implies a lesser presence of corrosion prone features and that accounted for higher corrosion resistance when compared to those castings produced with sand mould. Corrosion prone features and sites (such as pores, pits and agglomeration) adversely affected the corrosion resistance response of composite castings synthesized with sand mould.

4 Conclusions

Aluminium-based composites are sought-after in aerospace, automotive and other structural engineering applications due to their superior physical and mechanical properties [2, 4–6]. The performance of Aluminium Matrix Composites (AMCs) is primarily determined by their microstructures. Aside the influence of fabrication method, volume fractions, particle size and type of reinforcement materials on the microstructures and subsequent performance characteristics of AMCs [4, 7, 8], literature have also revealed that the type, materials characteristics and temperature of the mould as well as conditions of mould–metal interface can remarkably impact on the resulting properties of the monolithic alloys/composites [23–29]. However, information is sparse in respect of impact of mould types on properties of Al6063-SiC-based composites. In this paper, the effects of mould types on tensile and potentiodynamic corrosion properties of PKSA-reinforced Al6063-SiC-based composites were studied. The following conclusions were drawn from this work:

1. Although Al6063-SiC-PKSA composite produced with metal mould had the highest UTS and elongation at 193.55 MPa and 19.15%, respectively, the tensile properties of the produced composites generally exhibited improvement with increase in PKSA for both sand and metal moulds.
2. Inclusion of PKSA up to maximum of 2% enhanced potentiodynamic corrosion behaviour of Al6063-SiC-PKSA composites. However, composites developed with metal mould showed better corrosion resistance response when compared to those developed with sand mould. The lowest corrosion penetration rate and

current density were achieved with the composite produced using metal mould at 0.000739 mm/yr and $6.36 \times 10^{-8} \text{ A/cm}^2$, respectively.

3. The microstructural features of composites developed with metal mould were refined and comparably better than that of sand mould. The presence of agglomerated particles in microstructures of Al6063-SiC-PKSA composites produced with sand mould can be ascribed to their lower tensile and corrosion resistance characteristics.

References

1. Gowri, S.M.C., Jayashree, P.K., Raviraj, S., Achutha, K., Sharma, S.S.: Individual and combined effect of reinforcements on stir cast aluminium metal matrix composites—a review. *Int. J. Curr. Eng. Technol.* **3**(3), 922–934 (2013). <http://inpressco.com/category/ijcct>
2. Idusuyi, N., Ajide, O.O., Oluwole, O.O., Arotiba, O.A.: Electrochemical impedance study of an Al6063–12% SiC–Cr composite immersed in 3wt% sodium chloride. *Procedia Manuf.* **7**, 413–419 (2017). <http://creativecommons.org/licenses/by-nc-nd/4.0/>
3. Edoziuno, F.O., Nwaeju, C.C., Adediran, A.A., Odoni, B.U., Prakash, V.R.: Mechanical and microstructural characteristics of aluminium 6063 alloy/palm kernel shell composites for light weight applications. *Sci. Afr.* **12**, 1–12 (2021). <https://doi.org/10.1016/j.sciaf.2021.e00781>
4. Rao, V.R.K., Balaji, A., Krishna, D.S., Bhavabhuthi, B.P.R., Sreevatsavam, G., Abhiram, K.: A review on properties of aluminium based metal matrix composites via stir casting. *Int. J. Sci. Eng. Res.* **7**(2), 742–749 (2016). <https://www.ijser.org/researchpaper/A-Review-on-Properties-of-Aluminium-Based-Metal-Matrix-Composites-via-Stir-Casting.pdf>
5. Shuvho, M.B.A., Chowdhury, M.A., Hossain, N., Roy, B.K., Kowser, M.A., Islam, A.: Tribological study of Al-6063-based metal matrix embedded with SiC–Al₂O₃–TiO₂ particles. *SN Appl. Sci.* **2**(2), 1–14 (2020). <https://doi.org/10.1007/s42452-020-2064-1>
6. Fayomi, J., Popoola, A.P.I., Fayomi, O.S.I.: Effect of the parametric processes in stir-casting technique for aluminium based composite development: a review. *IOP Conf. Series: Mater. Sci. Eng.* **1107**(012070), 1–6 (2021). <https://doi.org/10.1088/1757-899X/1107/1/012070>
7. Raghuvaran, P., Suresh, M., Aakash, S., Balaji, M., Kumar, K.D., Prasath, S.H.: A review on mechanical behaviour of aluminium reinforced composites. *IOP Conf. Series: Mater. Sci. Eng.* **995**(012040), 1–9 (2020). <https://doi.org/10.1088/1757-899X/995/1/012040>
8. Kant, S., Singh, V.A.: Stir casting process in particulate aluminium metal matrix composite: a review. *Int. J. Mech. Solids* **12**(1), 61–69 (2017). <http://www.ripublication.com/ijms.htm>
9. Nagaral, M., Bharath, V., Aurad, V.: Effect of Al₂O₃ particles on mechanical and wear properties of 6061al alloy metal matrix composites. *J. Mater. Sci. Eng.* **2**(1), 1–4 (2013). <https://doi.org/10.4172/2169-0022.1000120>
10. Aravindan, M.K., Kulendran, B., Murali, G.: Effect of reinforcement of Al-6063 with SiC on mechanical behavior and microstructure of metal matrix composites. *Carbon Sci. Technol.* 388–394 (2014). <http://www.applied-science-innovations.com/>
11. Kumar, G.S.P., Keshavamurthy, R., Kumari, P., Dubey, C.: Corrosion behaviour of TiB₂ reinforced aluminium based in situ metal matrix composites. *Perspect. Sci.* **8**, 172–175 (2016). <https://doi.org/10.1016/j.pisc.2016.04.025>
12. Ajide, O.O., Otesile, A.O., Salau, T.A.O., Ismail, O.S., Oyewola, O.M.: Investigating effect of zinc content on the mechanical and corrosion responses of Al6063-SiC composite. *Curr. J. Appl. Sci. Technol.* **22**(3), 1–10 (2017). <https://doi.org/10.9734/CJAST/2017/34886>
13. Lyczkowska, K., Adamiec, J., Dolata, A.J., Dyzia, M., Wiczorek, J.: Regeneration of aluminium matrix composite reinforced by SiCp and GCsf using gas tungsten arc welding technology. *Materials* **14**(6410), 1–12 (2021). <https://doi.org/10.3390/ma14216410>

14. Saikrupa, C., Reddy, G.C.M., Venkatesh, S.: Aluminium metal matrix composites and effect of reinforcements—a review. *IOP Conf. Series: Mater. Sci. Eng.* **1057**(012098), 1–10 (2021). <https://doi.org/10.1088/1757-899X/1057/1/012098>
15. Ononiwu, N.H., Ozoegwu, C.G., Madushele, N., Akinribide, J.O., Akinlabi, E.T.: Mechanical properties, tribology and electrochemical studies of Al/Fly ash/eggshell aluminium matrix composite. *Bioint. Res. Appl. Chem.* **12**(4), 4900–4919 (2022). <https://doi.org/10.33263/BRIAC124.49004919>
16. Ram, K.S., Ramakrishnan, S., Risvak, M., Thaufeek, S., Yuvaraj, T.: Experimental analysis and characterization of mechanical, physical properties of aluminium (Al6061) metal matrix composite reinforced with SiC and Al₂O₃ using Stir casting. *IOP Conf. Series: Mater. Sci. Eng.* **1145**(012109), 1–10 (2021). <https://doi.org/10.1088/1757-899X/1145/1/012109>
17. Seetharaman, S., Subramanian, J., Singh, R.A., Wong, W.I.E., Nai, M.I.S., Gupta, M.: Mechanical properties of sustainable metal matrix composites: a review on the role of green reinforcements and processing methods. *Technologies* **10**(32), 1–27 (2022). <https://doi.org/10.3390/technologies10010032>
18. Kulkarni, P.P., Siddeswarappa, B., Kumar, K.S.H.: A survey on effect of agro waste ash as reinforcement on aluminium base metal matrix composites. *Open J. Mater.* **9**, 312–326 (2019). <https://doi.org/10.4236/ojcm.2019.93019>
19. Parveez, B., Maleque, M.A., Jama, N.A.: Influence of agro-based reinforcements on the properties of aluminum matrix composites: a systematic review. *J. Mater. Sci.* **56**, 16195–16222 (2021). <https://doi.org/10.1007/s10853-021-06305-2>
20. Shekhar, P.S., Kumar, S.A., Rao, P.S.: A concise view point on effects of agro and industrial waste as reinforcement on characteristic properties of aluminium alloy-based metal matrix composites. *Adv. Mech. Process. Des. Lect. Notes Mech. Eng.* 261–268 (2021). https://doi.org/10.1007/978-981-15-7779-6_23
21. Ikubanni, P.P., Oki, M., Adeleke, A.A., Omoniyi, P.O.: Synthesis, physico-mechanical and microstructural characterization of Al6063/SiC/PKSA hybrid reinforced composites. *Sci. Rep.* **11**(14845), 1–13 (2021). <https://doi.org/10.1038/s41598-021-94420-0>
22. Alaneme, K.K., Akintunde, I.B., Olubambi, P.A., Adewale, T.M.: Fabrication characteristics and mechanical behaviour of rice husk ash-alumina reinforced Al-Mg-Si alloy matrix hybrid composites. *J. Market. Res.* **2**(1), 60–67 (2013). <https://doi.org/10.1016/j.jmrt.2013.03.012>
23. Oji, J.O., Kareem, B., Idusuyi, N.: Effects of mould and pouring temperatures on the ultimate tensile strength of aluminium alloy sand castings: an ANOVA approach. *Leonardo Electron. J. Pract. Technol.* **19**, 97–108 (2011). <http://lejpt.academicdirect.org>
24. Ayoola, W.A., Adeosun, S.O., Sanni, O.S., Oyetunji, A.: Effect of casting mould on mechanical properties of 6063 aluminium alloy. *J. Eng. Technol.* **7**(1), 89–96 (2012). https://www.researchgate.net/publication/287590221_Effect_of_c
25. Sayuti, M., Sulaiman, S., Baharudin, B.T.H.T., Arifin, M.K.A., Vijayaram, T.R., Suraya, S.: Effect of mould vibration on mechanical properties of particulate reinforced aluminium alloy matrix composite. *Adv. Mater. Res.* **445**, 475–480 (2012). <https://doi.org/10.4028/www.scientific.net/AMR.445.475>
26. Adeosun, S.O., Akpan, E.I., Abiodun, D.: Mould temperature and mechanical properties of cast aluminium-silicon carbide composite. *Int. J. Mater. Chem.* **3**(4), 75–83 (2013). <https://doi.org/10.5923/j.ijmc.20130304.02>
27. Yildirim, M., Özyürek, D.: The effects of mould materials on microstructure and mechanical properties of cast A356 Al. *J. Adv. Mater. Process.* **2**(4), 3–12 (2014). http://jmatpro.iaun.ac.ir/article_553674_bd0f13ff8edb1d222c6291a
28. Abdel-Aziz, K., Abo, E.A.A., Elfasakhany, A., Saber, D., Helal, M.: Influence of casting mould wall thickness on the properties and microstructure of A356 alloy reinforced with micro/nanoalumina particles. *Arctic J.* **71**(7), 26–39 (2018). https://www.researchgate.net/publication/326718942_Influence_of_casting_mould_wall_thick
29. Barenji, R.V.: Effect of reinforcement, mold temperature, superheat, and mold thickness on fluidity of in-situ Al-Mg₂Si composites. *Overseas Foundry* **15**(1), 66–74 (2018). <https://doi.org/10.1007/s41230-018-7095-5>

Design and Development of Universal Runner Cutting Machine



Gopaldas Waghmare, Atharva Nemad, Gaurav Puri, Devyani Teware, Aalapi Banubakode, and Shrinath Ghuge

Abstract Now a days, every industry is moving toward automation. In order to increase the rate of production and increase the efficiency, automation is necessary. Due to automation, the time required for production is reduced which benefits the industries to increase the yield. As we know that the plastic industries use the injection molding process where unwanted material like runners and sprue are attached to the product which are to be separated. Cutting processes are those in which a piece of sheet metal is separated using great enough force. CAD model was used for design and development of machine, and ANSYS was used for the analysis of the machine.

Keywords Runner · Cutting · Plastic · Injection molding · De-gating

1 Introduction

This machine provides us an option to remove molded products, i.e., a process of cutting off gates of molded products. The various types of products which have different gate positions are separated from the gates with high accuracy with the help of a single cutting member [1]. Other than this method, science has provided us with various methods such as the use of supersonic waves for cutting the plastic mold, by the use of vibrational energy from the horn or by using supersonic oscillator, which gives the supersonic waves [2]. Addition to the supersonic energy, ultrasonic energy is also used for separating the runners and the product. There are predefined frequencies for different materials with respect to the required ultrasonic energy for degating [3]. As there are numerous types of gate structures, it increases the diversity of the mold. Another method used to cope up with this versatility is the use of a laser beam as a cutting source [4]. Cutting techniques are the ones, wherein a chunk of sheet steel is separated through making use of an exceptional sufficient pressure to purpose the cloth to fail. The maximum not unusual place slicing techniques are done through making use of a shearing pressure, and are consequently now and again

G. Waghmare (✉) · A. Nemad · G. Puri · D. Teware · A. Banubakode · S. Ghuge
Yeshwantrao Chavan College of Engineering, Nagpur, India
e-mail: gwaghmare@gmail.com

© The Author(s), under exclusive license to Springer Nature Singapore Pte Ltd. 2023
V. Bindhu et al. (eds.), *Proceedings of Fifth International Conference on Inventive Material Science Applications*, Advances in Sustainability Science and Technology,
https://doi.org/10.1007/978-981-19-4304-1_12

131

known as shearing techniques. When an exceptional sufficient shearing pressure is implemented, the shear pressure within side the cloth will exceed the last shear power, and the cloth will fail and separate on the reduce location. This shearing pressure is implemented through gear, one above and one underneath the sheet. Whether the gears are a punch and die or higher and decrease blades, the device above the sheet provides a brief downward blow to the sheet steel that rests over the decrease device. A small clearance is gift among the rims of the higher and decrease gear, which allows the fracture of the cloth. The length of this clearance is usually 2–10% of the cloth thickness and relies upon the numerous factors, which include the unique shearing process, cloth, and sheet thickness the outcomes of shearing at the cloth ex-trade because the reduce progresses and are seen on the threshold of the sheared cloth. While the blade or punch affects the sheet, the clearance among the equipment permits the sheet to plastically deform and “rollover” the area. As the device invades the sheet further, the cutting effects in a vertical are burnished quarter of cloth. Finally, the shear pressure is simply too remarkable and the cloth fractures at perspective with a small burr shaped on the area. The peak of every quantities relies on numerous factors, which include the sharpness and clearance among the equipment. As cited above, numerous reducing procedures exist that make use of shearing pressure to reduce sheet metal, and the term “shearing” itself refers to a selected reducing system that produces directly line cuts to split a chunk of sheet metal. Usually, shearing is used to reduce a sheet which is parallel to the current area that is held square; however, angled cuts may be made as well. For this reason, shearing is by and large used to reduce sheet inventory into smaller sizes in education for different procedures. Shearing has the subsequent capabilities: sheet thickness: 0.005–0.25 inches, tolerance: ± 0.1 inches (± 0.005 inches feasible), surface finish: 250–one thousand μ in (125–2000 μ in feasible). The shearing system is completed on a shear machine, regularly known as a squaring shear or electricity shear, that may be operated manually (through hand or foot) or through hydraulic, pneumatic, or electric-powered electricity. A traditional shear device consists of a desk with aid palms to preserve the sheet, stops or courses to stable the sheet, top and decrease straightedge blades, and a gauging tool to exactly function the sheet. The sheet is located among the top and decrease blade, which can be then compelled collectively toward the sheet, reducing the material. In maximum devices, the decrease blade stays desk bound at the same time as the top blade is compelled downward. The top blade is about 5–10% thick as compared to sheet thickness and is barely offset from the decrease blade. The top blade is commonly angled in order that the reduce progresses from one stop to the other, as a consequence decreasing the desired force. The blades utilized in those machines usually have a rectangular side as opposed to a knife side and are to be had in specific materials, together with low alloy metallic and high-carbon metallic.

2 Previous Work

Karmakar et al. [1] and team fabricated Pedal-Operated Hydraulic Sheet Metal Shearing Machine that electrical energy can be obtained by utilizing the kinetic energy of the exhaust gases. In this project, hydraulic jack is used as hydraulic component. The objective of this project was to lessen the efforts required for cutting sheets of metals with various thicknesses as compared to the effort required when using a simple hand-operated mechanical shear cutter.

Momoh Bello et al. [2] designed and constructed a manually operated foot leverage pedal with adjustable blades guillotine cutter. It was designed to shear variety of materials with various thicknesses and sizes depending on cutting blade capacity and shearing angle. The machine uses a foot lever to operate the blades. The machine cuts the material with a rake angle of 0.5 degrees. The test which was carried out shows that the machine was capable to shear the sheet of metal with thickness of 0.5 mm as maximum.

Gaikwad et al. [3] theoretically designed a Pneumatic Shearing Machine, their main objective was to the efforts and provide the workers with good environmental conditions and facilities and to increase production rate and to have best quality product.

Bahaley et al. [4] described the need of shearing machine in the industries for cutting 5-mm-thick stainless-steel sheets. Here, a CAD model was designed, and the analysis was done using FEA technique for shearing machine.

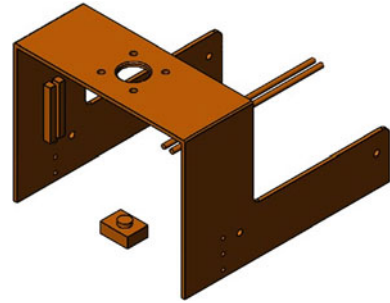
Sibanda et al. [5] presented the methodology for the design of a reconfigurable guillotine shear and bending press machine. The main motive was the exploration of developing machines with best possibility.

3 Construction and Working of Model

The main parts of universal runner cutting machine are as follows: (1) Work table (2) Lower blade (Die) (3) Cutting blade (Punch) (4) Pneumatic cylinder (5) Workpiece and cutting blade holding device (6) Workpiece/part (7) Transparent protective glass (8) Camera (9) Gripper (10) Workpiece guide. Figure 1 shows machine frame.

Details of Tools

1. Frame: The frame not only supports the structure of the complete machine but it also guides the workpiece toward the cutting blade. It is made up of mild steel structure having all the required holes and cutouts for mounting of various working parts of machine, like pneumatic cylinder, upper cutting blade, work holding table, camera, and guiding rods. The guiding rods play a crucial role to feed the component toward the cutting blade as the vertical riser is put between the two guiding rods.

Fig. 1 Machine frame

2. **Holding table:** Holding table acts as support and workpiece holding element of the machine. The workpiece before cutting is placed and guided with the help of holding table. It is also made up of 1.5-mm-thick mild steel plate, and four holes are drilled on the side of the holding table to fasten it to the main frame.
3. **Blade Holder:** Blade holder is an integrated part which is used for coupling of blade with the piston rod of pneumatic cylinder. Blade holder is a part which takes up or transmits the axial force delivered by pneumatic cylinder to the cutting edge of the upper cutting blade. It has a big 20-mm hole on the top for coupling the cylinder rod, and the three holes are for mounting of cutting blade.
4. **Gripper Mechanism:** Gripper is a material handling tool that enables robots to hold and pick up objects. When grippers are combined with collaborative (or “cobot”) industrial robot arm, they allow manufacturers to automate key processes, such as inspection, assembly, pick & place, and machine tending [6]. Figure 2 shows gripper mechanism.

All the workpiece has a spurge attached to it; we can use that spurge to hold the workpiece and feed it to the cutting blade; the guide rods can be used to guide the workpiece into straight line. Gripper can move in Y and Z direction, i.e., toward the direction of blade, and it can rotate the workpiece by 360 degrees to cut the other symmetric rows of the workpiece. Hence, to feed the workpiece toward the blade, we have installed the gripper. The gripper grabs the vertical riser which put in place by the worker in between the guiding rods. The gripper motion is controlled by the microprocessor. For providing Y and Z direction to gripper, mechanisms similar to CNC router machine can be used. Figure 3 shows gripper mechanism actuation.

With the help of gripper, the manufacturer can make whole part separation process automatic in which no human intervention is needed. Hence, the process can work automatically once the parts are fed to the machine.

5. **Pneumatic Cylinder:** Pneumatic cylinder is modeled with the help of dimensions specified in manufacturer’s catalog. The pneumatic cylinder is mounted on frame to produce the axial thrust required to shear the runners from the plastic components [7]. The pneumatic cylinder is mounted on frame to provide

Fig. 2 Gripper mechanism

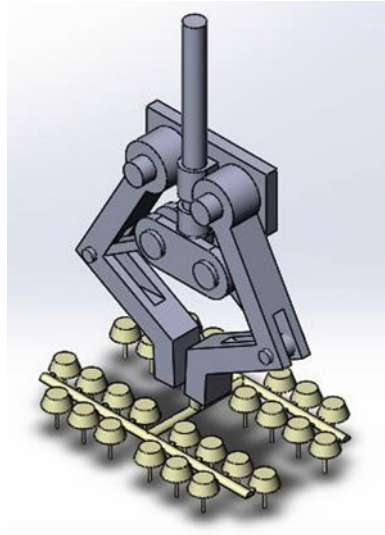
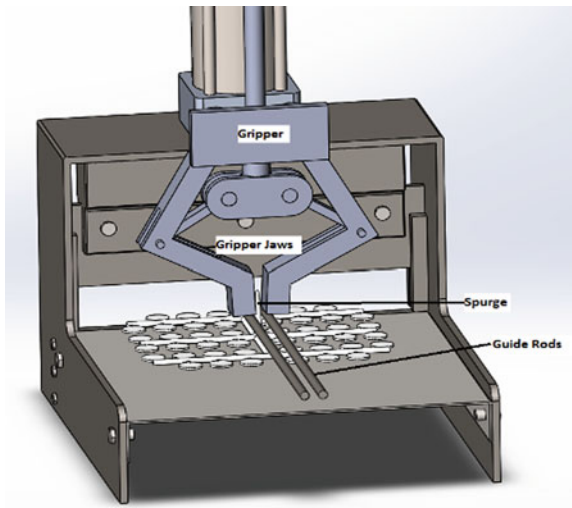


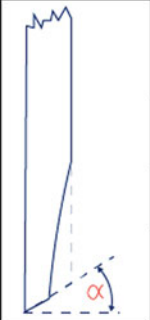
Fig. 3 Gripper mechanism actuation



the force required to shear the runners from the plastic component. The pneumatic cylinder is connected to the compressor with the help of pneumatic hose.

6. Design of blade: As per study, it has been observed that for cutting of metals, laminates, plastic materials the cutting edge having less cutting bevel angle is selected. Generally, the angle “ α ” is set in range of 0° – 10° and 30° for paper, foils, cardboards, etc., and 60° for special cases where sensitive cutting edges are required.

Fig. 4 Cutting edge geometry

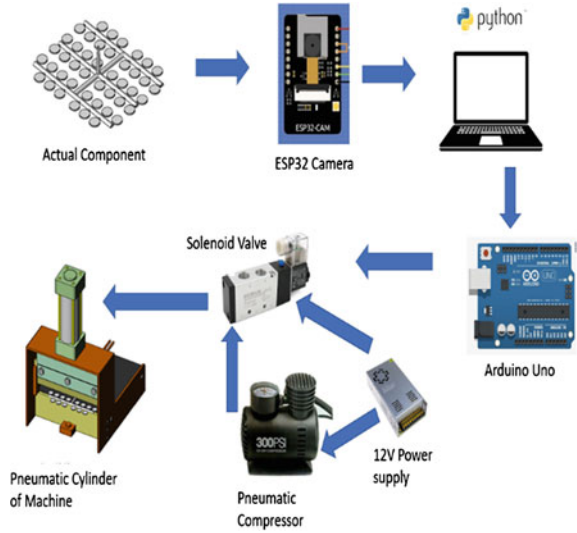
CUTTING EDGE GEOMETRY Top Knife		
Cutting Bevel	Angle of Bevel α	Application Areas
	0-10°	Metals, Laminates, Plastic Materials, Low Edge Distortion
	30°	Paper, Foils, Laminates, Fleece, Cardboard
	45°	
	60°	Special Cases, Film Industry, Sensitive Cutting Edges

Hence, to reduce the effort required, appropriate dimensions of blade should be selected. Figure 4 shows cutting-edge geometry.

- Process: As described above, the component used for removal of the product from extra material is the blade. The blade is attached to the pneumatic cylinder which is mounted on the frame. As shown in the camera is below the holding table in the slot provided in the frame. The material handling is done by the gripper. The gripper holds the workpiece by the surge (vertical projection in the cast). This process is assisted by the guideways provided. The main purpose to provide guideways is to ensure that while the process the workpiece is in the desired orientation and position [8]. The desired orientation is when the workpiece is feed toward the blade the side reaching the blade should be the largest that will ensure that maximum no. of parts are separated simultaneously. This is because of the row-wise symmetry in the product to be processed. The guide ways also ensure that the gripper will hold the spurge (the vertical projection of the workpiece) firmly. The camera, the gripper, and the pneumatic cylinder trigger are connected to a microprocessor. The microprocessor is the main decision-making component of the machine. Figure 5 shows the process flow.

The microprocessor signals the gripper to move the workpiece steadily toward the blade. The microprocessor is the part where the image processing code is saved. The code is written in Python programming language. The code is designed to take the photo captured as the input and after processing the photo give the signal to the pneumatic cylinder to perform forward stroke. The photos are taken spontaneously as the gripper will move the workpiece on the holding table toward the camera a cutting blade. The program is designed to detect the smallest cross-section in the photo received as input and to draw a straight line passing through all the detected area. After this, line is drawn, and as soon as the line comes in line with the cutting edge of the blade, it

Fig. 5 Process flow



will signal the pneumatic cylinder to perform forward stroke. This will be continued till a cast is processed, and all the parts are separated. The process mentioned above is a generalized process for the cutting stroke in this machine. Till the time the gripper reaches the blade, half of the workpiece is processed. The gripper then takes the workpiece back and rotates the workpiece 180°, and again, the process is repeated. When the gripper again reaches, the blades of the workpiece is fully processed. After this, the gripper holds the next workpiece in line, and the process is repeated. Figure 6 shows Universal runner cutting machine.

Fig. 6 Universal runner cutting machine

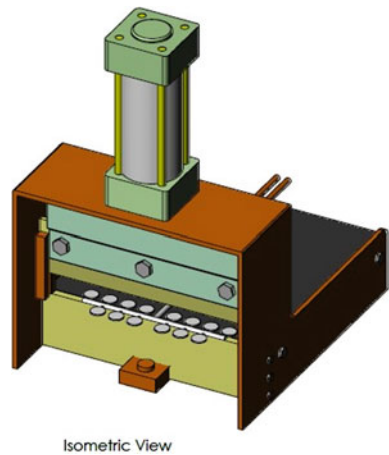
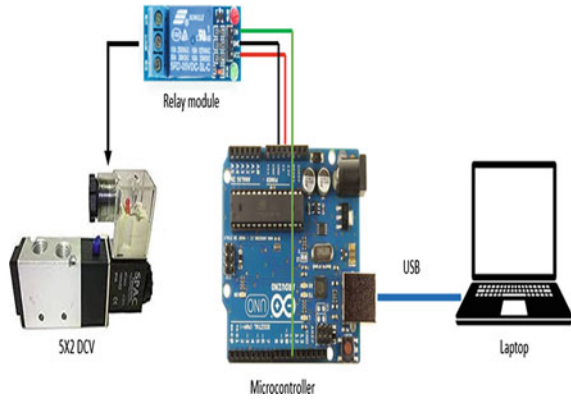


Fig. 7 Interface diagram

8. **Image processing Logic and Code:** With the help of gripper or any material handling device, the workpiece is moved forward row by row. This motion is controlled by microcontroller with the help of program in it. The camera captures the image row by row and sends it to the microcontroller where the image processing code is used to detect and analyze the image captured from the camera. Figure 7 shows interface diagram.

The code makes the decision whether to initiate the cutting stroke or not. The cutting stroke is to be performed when the smallest cross-section areas are in-line with the blade. The code is design to draw a blue line in the image captured by the camera. As soon as the blue line is detected, one command signal is triggered which actuates the directional valve to operate the pneumatic cylinder cutting or return stroke. All the runners are horizontal and parallel to each other, as soon as the first-row image is fed to microcontroller, the code detects the horizontal runners and draws as parallel line below. One blue color line is generated which is nothing but the cutting edge where the cutting action has to be performed. The microcontroller is connected with laptop USB port through which it communicates with Python code using serial communication. As soon as the blue line is detected with the help of Python code, the code will send Boolean values in the form of (Relay pin = 1 and relay pin = 0) which will trigger the relay module which is connected to microcontroller using pin relay data pin.

9. **Material Selection for cutter blade:** A2 tool steel is an alloy of iron, chromium, and molybdenum. It is a type of stainless steel. A2 tool steel is very tough and strong. It contains 5% of chromium steal which gives high hardness after the heat treatment with good dimensional stability. It is also resistant to corrosion. Wherever we require good toughness and good wear resistance, we use A2 tool steal.
10. **Shear Force calculation:** For calculating shear force first, we need to consider all the workpiece dimensions which undergoes direct shear stress; with the help of dimensions, we can calculate the total area under shear, and from

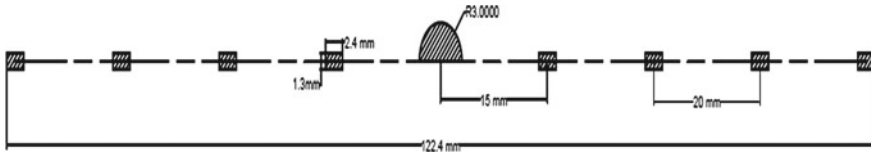


Fig. 8 Actual cut section of the area under shear

workpiece material table, we can get the shear strength value. The formula for shear stress is mentioned below, and efficiency (η) is considered as 85% for further calculations.

$$\text{Shear Force(N)} = \text{Shear stress(N/m}^2) \times \text{Area under shear(m}^2)$$

Shear Force calculation:

$$\text{Shear Force Runner(N)} = \text{Shear Stress(N/m}^2) \times \text{Runner C/s Area(m}^2)$$

$$\text{Shear Force Gate (N)} = \text{Shear Stress(N/m}^2) \times \text{Gate C/s Area(m}^2)$$

$$\text{Total Shear Force(N)} = \text{Shear Force Runner} + 8(\text{Shear Force})$$

For calculating shear force, first, we need to consider all the workpiece dimensions which undergoes direct shear stress; with the help of dimensions, we can calculate the total area under shear. Figure 8 shows actual cut section of the area under shear.

4 Results and Analysis

For design, SolidWorks is used, and for FEA simulation, ANSYS Mechanical Workbench is used to perform dynamic analysis; ANSYS Explicit dynamics is used. If your product needs to survive impacts or short-duration high-pressure loadings, designs can be improved with ANSYS explicit dynamics. Specialized problems require advanced analysis tools to accurately predict the effect of design considerations on product or process behavior. Gaining insight into such a complex reality is especially important when it is too expensive—or impossible—to perform physical testing. The ANSYS explicit dynamics suite enables to capture the physics of short-duration events for products that undergo highly nonlinear, transient dynamic forces. To perform explicit dynamics on the upper blade and workpiece, we need to fix the lower blade, guideways, and bottom and second row of circular part; the first row of parts is kept free, and on the upper face of blade, force of 1335 N is applied which is calculated with the help of pneumatic cylinder. With the help of these boundary conditions, the simulation is run, and the generated outputs are recorded documented.

Figure 9 shows equivalent stress in lower blade, and Fig. 10 shows total deformation in lower blade. Figure 11 shows total deformation in upper blade.

Fig. 9 Equivalent stress in lower blade

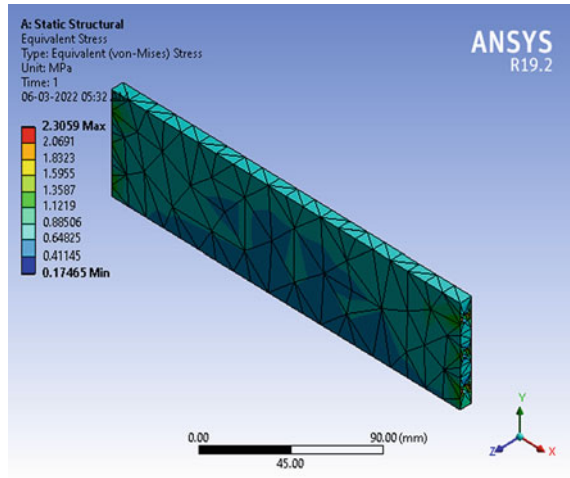
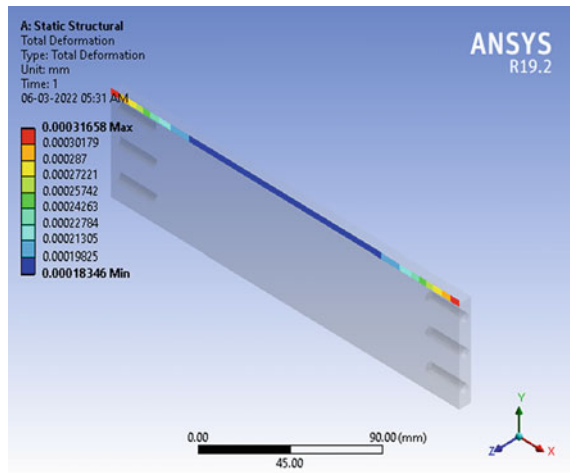


Fig. 10 Total deformation in lower blade



For lower blade, the maximum stress generated is 2.30 MPa, and total deformation is about 0.000183 mm.

For upper blade, the maximum stress generated is 1.27 N/m², and maximum deformation is 1.132e−5 m. Figure 12 shows equivalent stress in upper blade, and Fig. 13 shows total deformation of workpiece. Figure 14 shows equivalent stress of workpiece. Figure 15 shows equivalent stress of workpiece (zoomed view).

The maximum stress generated on the workpiece as per simulation is about 707 MPa, and maximum deformation is 17.11 mm.

Fig. 11 Total deformation in upper blade

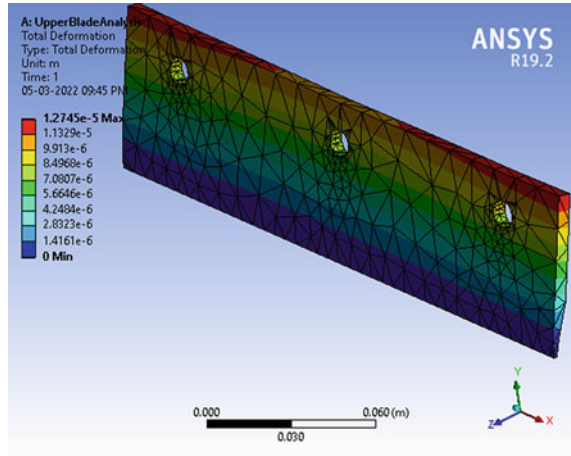
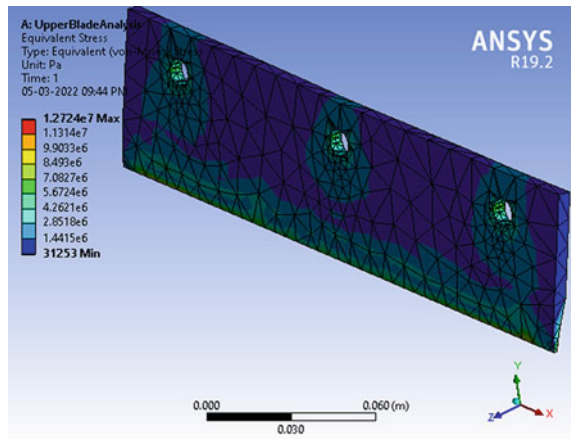


Fig. 12 Equivalent stress in upper blade



5 Conclusion

In this paper, we have described about a universal runner cutting machine. The pneumatic component used here is the pneumatic cylinder. The objective was to automate and reduce the effort required in shearing the runners of the injection molding parts which is a scrap material. This work is carried out by workers which is affected by availability of workers, efficiency, and consistency to do the job. The code takes only 2 s to detect the line, and if any corrections have to be made in alignment, then it will take 2–6 s, and then, cutting action is performed within 1 s; hence, minimum 6 to maximum 8 components can be easily separated from the runners; hence, we can say that for 48 components the machine will require at least

Fig. 13 Total deformation of workpiece

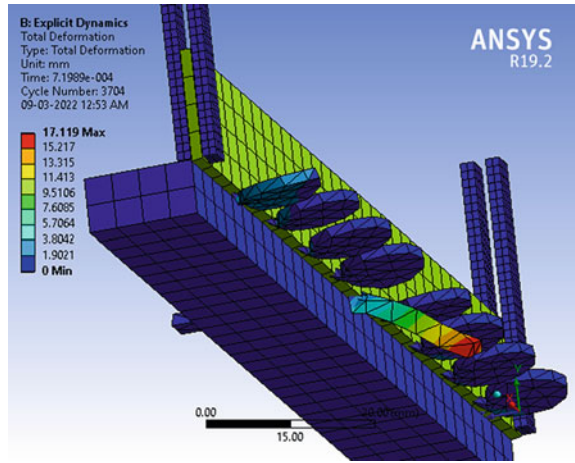
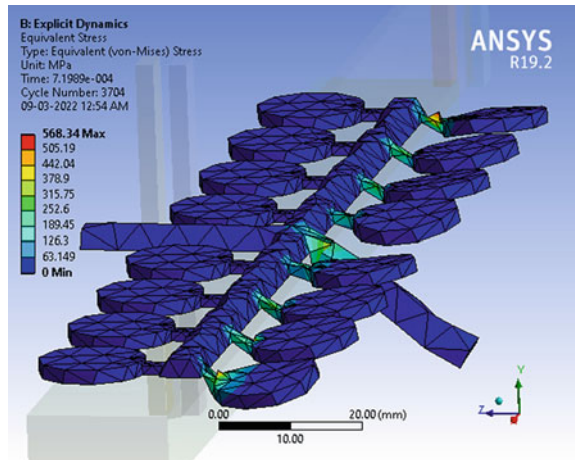
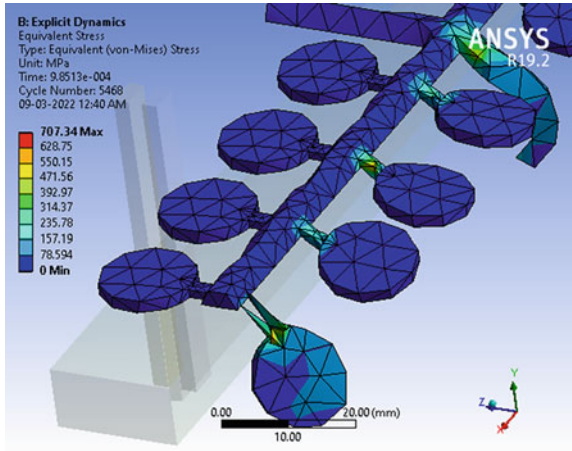


Fig. 14 Equivalent stress of workpiece



54–60 s which is less than the time required by manual operation of cutting single component.

Fig. 15 Equivalent stress of workpiece (zoomed view)



References

1. Karmakar, A.: Fabrication of a pedal operated hydraulic shearing machine. Phd Diss., Dibrugarh University, Dibrugarh (2017)
2. MomohBello, O.I., DanielOmomoh, I., Egwakhide, O.P., Olubiyi, O.D., Vincent, C.: Development of a Manually Operated Guillotine Cutter (2014)
3. Gaikwad, S.L., et al.: Design and development of pneumatic shearing machine **06(01)** (2017)
4. Bahaley, S.G., Khairkar, R.S.: Design and optimization of a shearing machine using FEA. *Development* **181**, 192 (2017)
5. Sibanda, V., Mpofu, K., Trimble, J.: Methodology for the design of a reconfigurable guillotine shear and bending press machine (RGS&BPM). *J. Eng. Des. Technol.* (2021)
6. Sumioka, K., Haji, M., Suzuki, T, Sonobe, M, Naitoh, N.: Device for removing runners from molded products. U.S. Patent 5,556,649, issued September 17, 1996. In: Spencer, T.F., Walter, G.N. both of Rochester, N.Y. Method and apparatus for cited precision degating mechanism. Patent Number: 5,596,915 Date of Patent (1997)
7. Sager, T.B.: Method and apparatus for degating parts using ultrasonic energy. U.S. Patent 4,585,152 (1986)
8. Hama, T.: Plastic-mold cutting apparatus using supersonic waves. U.S. Patent 4,685,602 (1987)

Surface Integrity and Corrosion Resistance of AZ31B Magnesium Alloy Processed by Ultrasonic Rolling



Gao Honghong, Ma Baoji, Zhu Yuanpeng, and Huo Jinxiang

Abstract Ultrasonic rolling was carried out to improve the corrosion resistance of the turning surface of magnesium alloy. The effects of rolling process parameters on surface roughness were studied, and the relationship between surface integrity and electrochemical corrosion characteristics was analyzed. The results showed that the ultrasonic amplitude and rolling passes have great influence on the surface roughness, while the static pressure and feed rate have little influence on the surface roughness. The two-dimension surface roughness of ultrasonic rolling samples is reduced by at least 88.0%, compared with that of the turning sample. The surface grain of ultrasonic rolling sample with the smallest surface roughness is significantly refined, and the thickness of grain refinement layer reaches 200 μm . The difference of corrosion resistance between turning and ultrasonic rolling surfaces is revealed via the electrochemical impedance spectroscopy. The surface integrity and corrosion resistance of AZ31B magnesium alloy are significantly improved after ultrasonic rolling.

Keywords Ultrasonic rolling · Magnesium alloy · Surface roughness · Grain refinement · Electrochemical impedance spectroscopy

1 Introduction

Magnesium (Mg) alloys are considered as potential orthopedic implant materials, due to the biocompatibility, degradability, and similar mechanical properties to natural bone [1]. However, Mg in the alloy is easy to react with water and chloride ions in body fluids, leading to premature loss of overall mechanical strength and failing to provide required mechanical support at the initial stage of implantation [2]. In addition, many other challenges also impede the clinical application of magnesium

G. Honghong (✉) · M. Baoji · Z. Yuanpeng · H. Jinxiang
School of Mechatronic Engineering, Xi'an Technological University, Xi'an 710021, China
e-mail: gaohonghong@xatu.edu.cn

G. Honghong · M. Baoji
Key Laboratory for Non-Traditional Machining Technology of Shaanxi Province, Xi'an 710021, China

alloys, due to the limited understanding of the reaction of magnesium alloys in the complex environment of body fluids [3]. Thus, it is an urgent problem to improve the corrosion resistance of magnesium alloys at the initial stage of *in vitro* immersion.

The surface integrity of magnesium alloy is the main factor affecting the corrosion resistance at the initial stage of immersion. Therefore, it is of great theoretical and practical significance to improve the corrosion resistance of magnesium alloys by changing the surface integrity.

Surface roughness is an important character of surface integrity. Yayoglu et al. found that magnesium alloy surface roughness has little influence on corrosion behavior through short-term immersion experiment *in vitro* [4]. Nguyen et al. found that the non-pitting corrosion rate decreases by reducing the surface roughness of magnesium-based implants without affecting the pitting potential of magnesium through hydrogen evolution experiments [5]. The effect of surface roughness on the passivation and pitting behavior of AZ91 magnesium alloy was studied in the environment containing chloride ions by electrochemical polarization experiment. It was found that the corrosion current and pitting tendency of AZ91 decrease with the decreasing of surface roughness [6]. Most of the existing studies reported that reducing the surface roughness of magnesium alloy is beneficial to improve its corrosion resistance.

Surface roughness can be reduced by mechanical surface modification and coating. The mechanical surface modification induces plastic deformation and cold work hardening on the surface, which changes the phase transformation, macroscopic and microscopic features of the processing area, to influence the surface corrosion features of the material [7]. The *in-situ* modification method is especially suitable for the surface modification of biomedical magnesium alloy. The corrosion rate of the deep rolling surface of MgCa3.0 is obviously slower than that of the turning surface, and the corrosion potential in simulated body fluids (SBFs) shifts slightly to a higher direction [8]. Therefore, the corrosion behavior of the mechanically modified surface is not only related to surface roughness but also affected by the microstructure and the thickness of plastic deformation layer.

Ultrasonic rolling (UR) is one of the mechanical surface modification technologies, in which, the tool head is guided to contact surface with ultrasonic frequency, inducing strong plastic deformation and grain refinement, even grain nanocrystallization. It effectively restrains the expansion of the corrosion from grain to grain; thus, the corrosion rate of metal is significantly reduced [9]. By comparing ultrasonic rolling with the undirected shot peening and traditional rolling, the surface roughness and hardness are substantially improved, and the surface grain size is reduced [10]. Ultrasonic rolling is more suitable for surface modification of biomedical magnesium alloy to improve the surface corrosion resistance. Therefore, it is very significant to further reveal the relationship between surface integrity (surface roughness and microstructure) and corrosion resistance for the corrosion control of magnesium alloys *in vitro*.

Electrochemical impedance spectroscopy (EIS) can provide instantaneous data of polarized surface impedance proportional to the corrosion resistance, and it has been widely used in the corrosion research of alloys [11]. The corrosion behaviors of AZ31

magnesium alloys with different grain sizes were studied in phosphate buffer solution (PBS) by electrochemical technology [12]. It was found that the AZ31 alloy with the smallest grain size obtains the best corrosion resistance after immersion in PBS solution. Wang et al. studied the microstructure of die cast AZ31 magnesium alloy and the corrosion resistance with EIS after soaking in Hank's SBF for different time. It was pointed out that the relationship between the factor leading to grain refinement and corrosion characteristics needs to be further studied [13]. Therefore, the surface of AZ31B magnesium alloy was modified by turning and ultrasonic rolling. The surface roughness of samples before and after ultrasonic rolling was measured by white-light interferometer, and the effects of rolling parameters on two-dimension (2D) surface roughness were analyzed. The microstructure of the surface layer before and after rolling was observed by metallographic microscope to study the effect of ultrasonic rolling on the thickness and microstructure of plastic deformation layer. The influence of ultrasonic rolling on corrosion characteristics was analyzed by EIS.

2 Experiment and Methods

2.1 Materials and Equipment

AZ31B magnesium alloy bar with a diameter of 30 mm and a length of 100 mm was used in the experiment. The chemical composition is shown in Table 1. Although there is a certain biological toxicity due to the presence of Al, it was shown that magnesium alloys even with 9 wt% of Al show enhanced osteoblastic activity in the surrounding of pig femora [7, 14]. Thus, small amount of Al in AZ31B has little effect on the biological safety. The cylindrical surface was pretreated by turning to obtain a consistent surface before rolling. The turning parameters are as follows: The spindle speed is 1500r/min; the feed rate is 0.3 mm/r; the cutting depth is 1 mm. The diameter of AZ31B bars was machined to 28 mm, and the turning length was 45 mm. Two samples with 10 mm and 30 mm length were cut from one of the turned bars and used as turning group (No. 0).

Ultrasonic rolling was carried out after turning by using ultrasonic rolling equipment attached to the CNC lathe machine. The rolling head at the front of the rolling tool is a rotary hard alloy ball with a diameter of 14 mm. The static pressure applied to the workpiece is provided by the air cylinder, and it is adjusted via the air gauge valve. The vibration signal with the frequency of 25 kHz generated by the ultrasonic generator (HK40G, HAWKING, China) is transmitted to the rolling ball through the ultrasonic transducer and horn. During the rolling process, the rolling head exerts

Table 1 Chemical composition of AZ31B magnesium alloy (wt.%)

Element	Al	Zn	Mn	Si	Cu	Fe	Ni	Mg
Content	2.96	0.52	0.31	0.16	0.006	0.003	0.001	96.04

Table 2 Ultrasonic rolling experiment design with four factors and three levels

Level	Rolling passes	Static pressure (MPa)	Factors	
			Ultrasonic vibration amplitude (μm)	Feed rate (mm/r)
1	1	0.04	5	0.05
2	2	0.07	7	0.10
3	3	0.10	9	0.15

static pressure and periodic ultrasonic vibration to the turned surface of the rotary bars, feeding along the axial direction of the bar to get the designed rolling length.

2.2 Ultrasonic Rolling Experiment Design

The plastic deformation ability of magnesium alloy is poor at room temperature. Thus, a lot of preliminary tests were carried out and showed that the rolling passes, static pressure, ultrasonic amplitude, and feed rate have effects on the rolling surface quality at a certain spindle speed. Rolling passes should not be more than three times to get surface roughness less than 0.5 μm . In this test, the spindle speed was fixed at 800 r/min; other four processing parameters, i.e., rolling passes, static pressure, ultrasonic amplitude, and feed rate, were variable factors. Three levels were set for each variable factor, as shown in Table 2.

Nine groups of ultrasonic rolling tests were designed by orthogonal design method. After the nine groups of rolling tests were completed, two ultrasonic rolling samples with 10 mm and 30 mm length were cut from each rolled bar and used as rolling group (No. 1–9). Each processed sample is immediately cleaned with 75% anhydrous ethanol for 3 min through the ultrasonic cleaning machine. Then, the cylindrical surface of each sample was dried by cold air and wrapped with plastic film. Ten samples each with 10 mm length were used for surface roughness and microstructure tests, and ten samples each with 30 mm length were used for electrochemical corrosion test.

2.3 Surface Roughness and Microstructure Tests

One group of cylindrical samples, including one turning sample and nine ultrasonic rolling samples with 10 mm length, was firstly used for measurement of surface roughness and then microstructure. Surface roughness was measured with a white-light interferometer (Zygo Zegage Plus, Middlefield, CT, USA) [15]. Three points randomly selected on the cylindrical surface of each sample were measured. The arithmetic mean value of 2D surface roughness (Ra) measured in the three points was

Table 3 Ionic composition in PBS solution

Ion	Na ⁺	K ⁺	Cl ⁻	HPO ₄ ²⁻
Molar mass (mmol/L)	144	4.6	138.6	10

regarded as the surface roughness of each sample. Then, the cylindrical surface and one end face of the 10 samples were inlaid; another end face was polished successively with sandpapers of P800#, P1500#, P2000#, P3000#, and P4000#. Finally, the end-surface microstructure was observed by an optical microscopy (Axio Observer 7 M, Zeiss, Germany) after metallographic polishing and 20 s etching.

2.4 Electrochemical Corrosion Test

Electrochemical impedance spectroscopy can provide instantaneous data on the impedance of a surface subject to polarization, which is directly proportional to the corrosion resistance and used to determine the rate at which dissolution is occurring [11, 16, 17]. EIS test was carried out on an electrochemical workstation (Zennium X, Zhanar, Germany) with a classical three-electrode system (magnesium alloy sample as working electrode, R232 saturated calomel electrode as reference electrode, and platinum sheet as counter electrode) [18]. PBS was used to simulate the main ion environment in vivo. The type and mass of the main ions in PBS (Biosharp, pH7.2–7.4) are shown in Table 3.

Another group of cylindrical samples, including one 30 mm turning sample and nine 30 mm ultrasonic rolling samples, were used for electrochemical corrosion test. Each sample was connected to the working electrode of the electrochemical workstation by a copper wire, which was embedded in one end face of the sample, to ensure good electrical conductivity. The reference electrode and the counter electrode were also correctly connected. The frequency of EIS test was set at 10^5 Hz– 10^{-2} Hz, and the sweep direction was from up to down. A sinusoidal signal with an amplitude of 10 mV was applied. The EIS test started after the open-circuit potential become stable. The plots and data of Nyquist and Bode in the EIS test were obtained to analyze the impedance characteristics of the tested samples in PBS solution.

3 Results and Discussion

3.1 Surface Roughness

The 2D surface roughness Ra of the turning sample 0 is 3.604 ± 0.282 μm . Ra of the ultrasonic rolling samples in orthogonal test is shown in Table 4. Ra of sample 7 (0.117 ± 0.028 μm) is the smallest among ultrasonic rolling samples 1–9. Ra

Table 4 Range analysis of surface roughness of ultrasonic rolling samples

Sample No	Rolling passes	Static pressure (MPa)	Ultrasonic amplitude (μm)	Feed rate (mm/r)	Ra (μm)
1	1	0.04	5	0.05	0.121 ± 0.011
2	1	0.07	7	0.10	0.137 ± 0.001
3	1	0.10	9	0.15	0.120 ± 0.016
4	2	0.04	7	0.15	0.251 ± 0.199
5	2	0.07	9	0.05	0.118 ± 0.012
6	2	0.10	5	0.10	0.354 ± 0.009
7	3	0.04	9	0.10	0.117 ± 0.028
8	3	0.07	5	0.15	0.237 ± 0.049
9	3	0.10	7	0.05	0.431 ± 0.078
Rk1	0.126	0.163	0.237	0.223	
Rk2	0.241	0.164	0.273	0.203	
Rk3	0.261	0.302	0.119	0.203	
Range analysis	0.135	0.139	0.154	0.021	

of sample 9 (0.431 ± 0.078) is the largest among ultrasonic rolling samples 1–9. Compared with turning sample 0, Ra of sample 7 and 9 decreases 96.75% and 88.0%, respectively. The results show that ultrasonic rolling reduces the surface roughness of magnesium alloy by more than 88.0%, which greatly smooths the surface and induces the surface modification. Range analysis was used for the orthogonal test results to get the optimal combination of rolling parameters and the influence of four rolling parameters on surface roughness.

The optimal combination of rolling parameters corresponding to the minimum Ra from range analysis is that rolling passes, static pressure, ultrasonic amplitude, and feed rate are 1, 0.04 MPa, 9 μm , 0.15 mm/r, respectively. According to this combination, rolling optimization experiment was carried out, and the rolling sample 10 was obtained with the smallest Ra ($0.115 \pm 0.004 \mu\text{m}$) among all the samples. Ra of the optimized sample 10 decreases 96.8%, compared with that of the turning sample 0, as shown in Fig. 1, indicating that the range analysis results of Ra in this experiment are reliable.

The significance of four ultrasonic rolling parameters on Ra in descending order is ultrasonic amplitude, static pressure, rolling passes, and feed rate. Ra firstly increases and then decreases with the increasing of ultrasonic amplitude. Ra increases with the increase of static pressure and rolling passes. Ra slightly decreases with the increasing of feed rate, as shown in Fig. 2. Therefore, the optimized combination of rolling parameters for sample 10 is ultrasonic amplitude and feed rate at level 3, static pressure and rolling passes at level 1.

Fig. 1 Surface roughness Ra of the samples 0–10

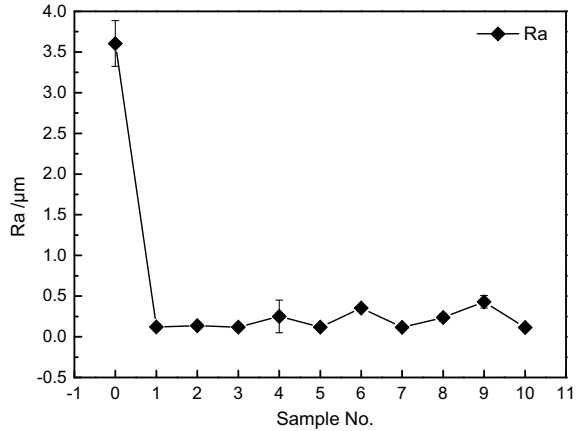
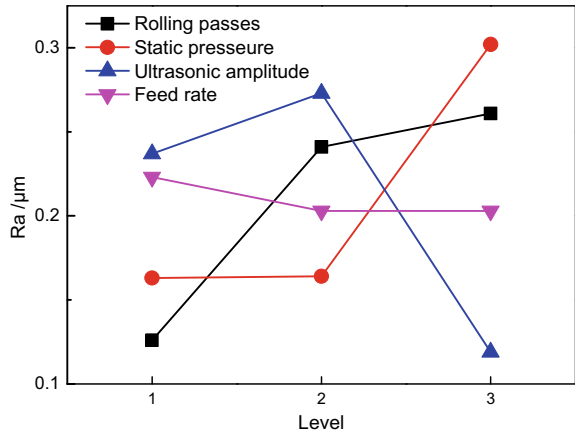


Fig. 2 Relationship between Ra and the four rolling factors



3.2 Metallographic Microstructure

The microstructure of the turning sample 0 and the optimized rolling sample 10 is shown in Fig. 3a, b, respectively. The microstructure of sample 0 is almost not affected by turning since the grain orientation is randomly distributed. The surface grain size of sample 0 is generally more than 20 μm in any direction. The average grain size within 200 μm depth along diameter direction of the optimized rolling sample 10 is less than 10 μm , showing that ultrasonic rolling of AZ31B leads to grain refinement and at least 200 μm thickness of modification layer.

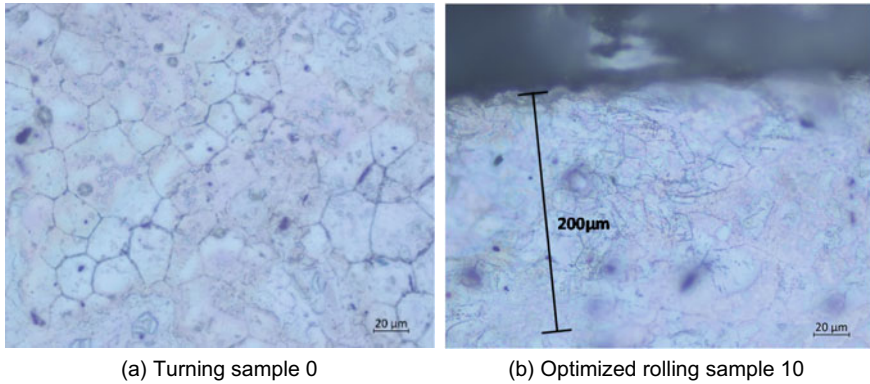
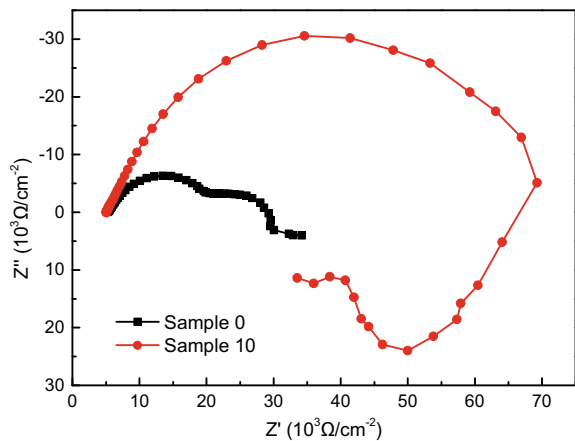


Fig. 3 Microscopic structure of the turning and ultrasonic rolling samples (500X)

3.3 Electrochemical Impedance Spectroscopy

Figure 4 shows Nyquist impedance spectroscopy of the turning sample 0 and the optimized rolling sample 10. Nyquist impedance spectroscopy of the turning sample 0 is composed of two semi-arcs, corresponding to two capacity-reactance arcs, indicating that charge transfer exists in both initial and subsequent stages. Nyquist impedance spectroscopy of the optimized rolling sample 10 consists of a high-frequency capacitive arc and a low-frequency surface relaxation. The diameter of the high-frequency capacitive reactance arc is greater than that of the low-frequency capacitive reactance arc, indicating that the surface corrosion reaction is initially slow, and later, Cl^- comes into the Mg alloy surface, accelerating the corrosion reaction speed. The capacitive arc radius of the optimized rolling sample 10 is obviously larger than that of turning sample 0 during the EIS test. The larger arc radius at high frequency means

Fig. 4 Nyquist impedance spectroscopy of the turning and optimized rolling samples



that the corrosion of the ultrasonic rolling surface is much more difficult to begin than that of the turning surface in the initial stage, so the corrosion current is small. The $\text{Mg}(\text{OH})_2$ film generated later has a protective effect on the surface. Surface relaxation appears at low frequencies, indicating that pitting corrosion occurs, and the film becomes loose. The results show that ultrasonic rolling changes the surface structure, making the rolling surface more difficult to corrode than the turning surface. Even if the corrosion occurs, the generated passivation film provides special protection for the rolling surface, delaying the corrosion of magnesium alloy.

4 Conclusions

- The surface of AZ31B magnesium alloy becomes smooth after ultrasonic rolling. The 2D surface roughness is reduced by at least 88.0%.
- The ultrasonic rolling induces dramatic plastic deformation on the turned surface of AZ31B magnesium alloy. Compared with the turning sample, the surface grain size of the rolling sample is significantly reduced; the thickness of grain refinement layer is increased. The thickness of the plastic deformation layer of the optimized rolling sample with the smallest surface roughness reaches 200 μm .
- The ultrasonic rolling has a great effect on electrochemical impedance spectroscopy. Compared with that of the turning sample, the diameter of the high-frequency capacitive reactance arc of the optimized rolling sample with the minimum surface roughness increases obviously, so the corrosion resistance in the initial stage is significantly improved.
- The processing parameters have effects on the thickness of the plasticity deformation layer and corrosion resistance, so the rolling process needs to be further studied and optimized. In addition, surface treatment, such as, biological safety coating and micro-arc oxidation coating, can be further used on the rolling surface to get better surface corrosion resistance.

Acknowledgements This work is supported by the Key Laboratory Program of Education Department of Shaanxi Province (19JS035).



References

1. Shahri, Z., Allahkaram, S.R., Soltani, R., et al.: Study on corrosion behavior of nano-structured coatings developed on biodegradable as cast Mg–Zn–Ca alloy by plasma electrolyte oxidation. *Surf. Coat. Technol.* **347**, 225–234 (2018)
2. Song, G.L., Atrens, A.: Understanding magnesium corrosion—a framework for improved alloy performance. *Adv. Eng. Mater.* **5**(12), 837–858 (2003)

3. Walker, J., Shadanbaz, S., Woodfield, B.F.T., et al.: Magnesium biomaterials for orthopedic application: a review from a biological perspective. *J. Biomed. Mater. Res. B: Appl. Biomater.* **102B**(6), 1316–1331 (2014)
4. Yayoglu, E.: Corrosion Characteristics of Magnesium Under Varying Surface Roughness Conditions. College of Engineering University of South Florida (2016)
5. Nguyen, T.L., Blanquet, A., Staiger, M.P., et al.: On the role of surface roughness in the corrosion of pure magnesium in vitro. *J. Biomed. Mater. Res. Part B Appl. Biomater.* **100B**(5), 1310–1318 (2012)
6. Walter, R., Kannan, M.B., He, Y., et al.: Effect of surface roughness on the in vitro degradation behaviour of a biodegradable magnesium-based alloy. *Appl. Surf. Sci.* **279**, 343–348 (2013)
7. Schulze, V., Bleicher, F., Groche, P., et al.: Surface modification by machine hammer peening and burnishing. *CIRP Ann. Manuf. Technol.* **65**(2), 809–832 (2016)
8. Denkena, B., Lucas, A.: Biocompatible magnesium alloys as absorbable implant materials adjusted surface and subsurface properties by machining processes. *CIRP Annals Manuf. Technol.* **56**(1), 113–116 (2007)
9. Liu, Y., Zhao, X.H., Wang, D.P.: Determination of the plastic properties of materials treated by ultrasonic surface rolling process through instrumented indentation. *Mater. Sci. Eng., A* **600**, 21–31 (2014)
10. Liu, Y., Zhao, X., Wang, D.: Effective FE model to predict surface layer characteristics of ultrasonic surface rolling. *Mater. Sci. Technol.* **30**(6), 627–636 (2014)
11. Ghali, E.: Conventional and electrochemical methods of investigation. In: Corrosion Resistance of Aluminium and Magnesium Alloys: Understanding, Performance and Testing. John Wiley & Sons, Hoboken, NJ, USA (2010)
12. Alvarez-Lopez, M., Dolores, P.M., Del Valle, J.A., et al.: Corrosion behaviour of AZ31 magnesium alloy with different grain sizes in simulated biological fluids. *Acta Biomater.* **6**(5), 1763–1771 (2009)
13. Wang, H., Estrin, Y., Fu, H., et al.: The effect of pre-processing and grain structure on the bio-corrosion and fatigue resistance of magnesium alloy AZ31. *Adv. Eng. Mater.* **9**, 967–972 (2007)
14. Witte, F., Kaese, V., Haferkamp, H., et al.: In vivo corrosion of four magnesium alloys and the associated bone response. *Biomaterials* **26**(17), 3557–3563 (2005)
15. Gao, H.H., Ma, B.J., Singh, P.R., et al.: Areal surface roughness of AZ31B magnesium alloy processed by dry face turning: an experimental framework combined with regression analysis. *Materials* **13**(10), 2303–2314 (2020)
16. MacDonald, D.D., McKubre, M.C.H.: Impedance measurement techniques. In: Impedance Spectroscopy: Emphasizing Solid Materials and Systems. Wiley, New York (1987)
17. Kirkland, N.T., Birbilis, N., Staiger, M.P.: Assessing the corrosion of biodegradable magnesium implants—a critical review of current methodology and their limitations. *Acta Biomater.* **8**, 925–936 (2012)
18. Daniel, K., Filip, P., Branislav, H.: Corrosion resistance of AZ31 magnesium alloy influenced by conventional cutting fluid. *Mater. Eng.* **24**, 67–71 (2017)

Wireless Interface-Based Acquisition, Analysis, and Control System Using Master–Slave Approach for Chemical Laser



Rajeev Kumar Dohare , Mainuddin , and Gaurav Singhal 

Abstract The abstract is a mandatory element that should summarize the high-power flowing medium lasers being interdisciplinary in nature results in a very complex and huge systems. Acquisition system plays a significant role in demonstration of any laser system in real time, stored data both in numerical and graphical form to analysis decisively for further optimization of laser systems. Although laser systems can be easily established using wired acquisition schemes, they require intricate cabling and suffer from issues such as durability in harsh environments, flexibility, and portability during laser operation. Hence, from the perspective of development of future-ready field weapon systems, it is of the essence to implement a wireless (Wi-Fi) interface supported acquisition, analysis, and control system based on master–slave topology. The proposed scheme facilitates the development of flowing medium lasers and makes the acquisition system compact, flexible, portable with facility of remote and safe operation of flowing medium laser systems.

Keywords Flowing chemical lasers · Data acquisition system · Basic hydrogen peroxide (BHP) · Wireless interface

1 Introduction

With the application in diversified fields like medical, entertainment, printing, cooling, barcode scanners, nuclear fusion, etc., lasers have reached to the stage for use in defense applications in the form of flowing medium lasers like gas dynamic laser

R. K. Dohare (✉)
DIT&CS, DRDO Bhawan, Delhi, New Delhi 110011, India
e-mail: dohare@rediffmail.com

Mainuddin
Jamia Milia Islamia, Delhi, India
e-mail: mainuddin@jmi.ac.in

G. Singhal
CHESS, Hyderabad, India

(GDL) [1], chemical oxygen iodine laser (COIL) [2], hydrogen fluoride/deuterium fluoride (HF/DF) [3, 4], and the very recent liquid laser (LL) [5, 6]. Deployment of flowing laser systems is a matter of time to cater the threats imposed by the UAVs, rockets, mortars, etc., to make the systems future ready, flexible, and portable so that their suitability for the aforesaid applications can be justified in true sense. Wireless interface has been tested in numerous applications like healthcare applications and structural health monitoring system [7], phonocardiography [8], manufacturing equipment [9], brain–computer interface (BCI) system [10], natural gas station [11], land monitoring application [12], long distance data transmission using meteorological sensor network [13], structural data acquisition [14], flight test networks [15], patient care and research [16], traffic control [17], automatic railway gate control [18], and many more.

COIL involves complex technologies for laser generation and optimization. Singlet oxygen is generated as a result of reaction between basic hydrogen peroxide (BHP) and hazardous chlorine gas. It plays role of pumping medium to iodine and stimulates it to the excited levels. Lasing action happens in active medium, iodine, and extraction of COIL laser power is achieved through the use of cavity resonators. Hence, modifications in the direction of development of acquisition systems [19–23] are explicitly the need of the time. It is therefore, a progressive smart acquisition, analysis, and control system [24–26] based on wireless interface scheme with portability and flexibility has been presented here to make them available for the laser systems readiness for future endeavors.

2 Wireless Interface-Based Acquisition, Analysis, and Control System

Figure 1 represents a Wi-Fi interface-based acquisition, analysis, and control system based on master–slave topology developed for the operation of flowing medium lasers. The acquisition and control system is divided into two main parts: master controller and slave unit. Slave unit is an acquisition, analysis, and control unit which performs all the monitoring, acquisition of various laser system parameters in real time, and controls all the valves through actuation process. It also records laser diagnostic data of critical parameters like active and pumping medium characteristics and concentration measurement. Various safety features are also included in slave unit to perform safe operation of laser system during experiments. Master controller controls the slave unit for turning out of the aforesaid functions of the slave control from a remote and safe distance by radio frequency communication via router. It is the master controller which commands the slave controller and executes all the operations from 35 m (with obstacles) to 80 m (without obstacles).

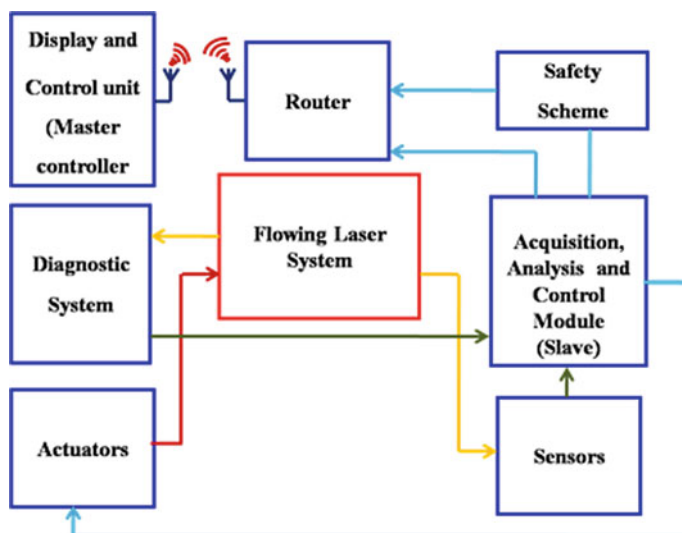


Fig. 1 Master–slave concept-based acquisition, analysis, and control system (using wireless assimilation)

2.1 Assimilation of Acquisition, Analysis, and Control System with Flowing Laser COIL System

Developed acquisition system has been assimilated with subsystems of COIL laser like iodine supply, BHP supply, chlorine supply, safety interlocking, and vacuum creation. Assimilation of wireless interface-based acquisition system with BHP supply system has been discussed in detail and depicted in Fig. 2 with incorporation of safety interlock.

BHP is one of the sources along with chlorine responsible for pumping medium (singlet oxygen) generation during COIL laser generation process. BHP supply system performs various tasks like preparation, storage, and passing BHP to the pumping medium generator (SOG). Due to exothermicity ($\sim 50 \text{ kJ mol}^{-1}$) in BHP preparation process, it is prepared by stepwise gradual supply. Temperature measuring action is performed by using customized k-type thermocouple (Make: Senstech Sensors, Noida, Material: Nickel) with one meter probe length, and its thermal action is maintained at $\sim -20 \text{ }^\circ\text{C}$ by the use of a PID scheme-based temperature controller (Make: Maxthermo) and a suitable capacity chiller system. The BHP solution is stirred continuously by a mixer for uniform cooling. The switching ON/OFF of chiller and mixer is done by the 24 V DC signal through the digital outputs (DO) using ADAM 4069 (8 channel power relay card with MODBUS protocol). ADAM 4069 can handle currents up to 5A, and its turn on and turn off time are 5 ms and 5.6 ms, respectively. Pressure, temperature, and level parameters in BHP tank are incessantly acquired (AI, analog input) by using USB 4716, ADAM 4018, 4117

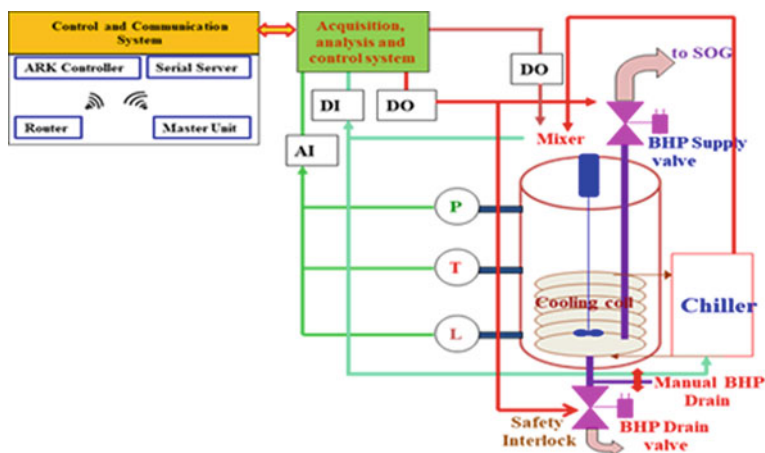


Fig. 2 Interfacing of acquisition system with BHP supply system

and conditioner 3014 cards. Pressure sensors [accuracy: $\pm 0.1\%$ (of FSR), response time—1 ms] fitted with stainless steel diaphragm with Viton seal from M/s Metran, Russia and M/sXi'an Yunyi Instrument Co. Ltd., China, have been used for ranges of 0–100 Torr and 0–10 bar. In order to measure the level of liquid reagent, i.e., BHP inside the tank, level sensors (Metran, Model no. 3536) have been utilized which is compatible with corrosive BHP liquid. These pressure and level sensors provide 4–20 mA current signal and operate with the excitation voltage of 24 V DC. The output 4–20 mA is useful as it is less susceptible to noise as compared to voltage output.

Current status of chiller (DI, digital input), mixer, BHP supply, and BHP drain valves is monitored continuously using ADAM 4051 through a feedback signal. All the actions are performed wirelessly using command produced from the master controller (ARK 1122 C and serial server, EKI-1361) for the slave acquisition, analysis, and control system through a router (D-link, AC-750).

In short, acquisition system performs following functions in controlling the BHP supply from a safe remote distance through master controller:

- Vacuum creation inside the BHP tank for sucking of H_2O_2 to start BHP preparation process.
- Monitoring and displaying the pressures, temperatures, and level inside BHP tank.
- Controlling the mixer and chiller on/off to maintain BHP temperature and displaying their status.
- Implementation of predefined sequencing for commanding of BHP supply and BHP drain valves.
- Incorporation of both manual and automatic safety scheme for opening of drain valve in order to handle any unwanted situation occurred during COIL laser experiments or power failure for a long time under unavoidable circumstances.

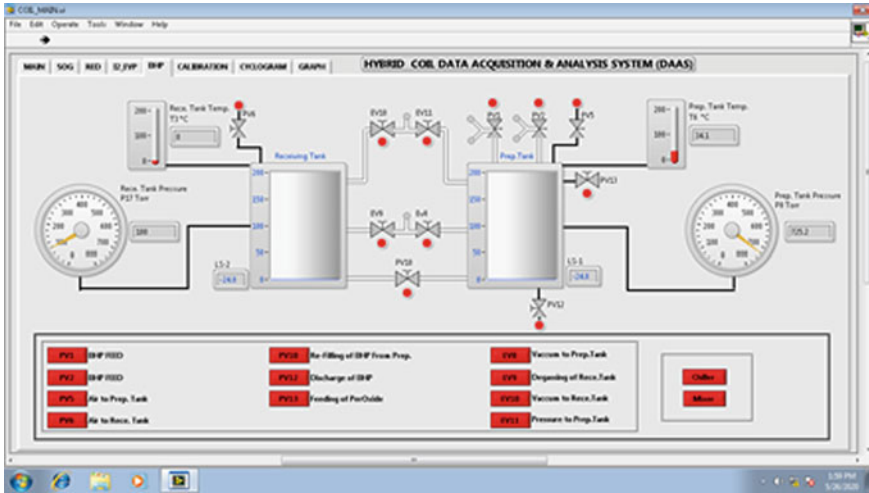


Fig. 3 ‘BHP’ graphical user interface

2.2 Graphical User Interface (GUI)

LabVIEW platform-based application software program has been written, and GUIs for related subsystems have been developed. Figure 3 shows BHP graphical user interface. It describes various valves required for BHP feed, pressure, and vacuum creation in the BHP tanks, discharge of BHP, and refilling of BHP. Temperature, pressure, and level parameters are monitored online, and actuation of different valves is performed with their current status.

3 Conclusion

The discussed wireless interface-based acquisition, analysis, and control system has been successfully utilized for COIL laser processes with 150 channel handling capacity involving both analog and digital acquisition (input) and analog and digital control (output). Numerous experiments were executed using the master–slave approach-based acquisition system, and ~10 kW laser power has been achieved. The presented wireless interface-based acquisition system provides portability, reduction in wire clusters, and flexibility with ease of operation and can process the flowing laser system from safe distance of both line of sight (80 m) and with obstacles (35 m).

Acknowledgements This work is supported by the Ministry of Electronics and Information Technology, Government of India under the Visvesvaraya Ph.D. scheme.

References

1. Boreisho, A.S., Vovk, M.Y., Edigarev, A.D., Kiselev, I.A., KulalaeV, V.V., Morozov, A.V., Orlov, A.E., Smirnov, P.G.: Combustion-driven gas-dynamic CO₂-laser on the basis of modern aviation engines. IOP series, J. Phys. Conf. Seri. **1565**, 012021, 1–6 (2020). <https://doi.org/10.1088/1742-6596/1565/1/012021>
2. McDermott, W.E., Pchlekin, N.R., Benard, D.J., Bonsek, R.R.: An electronic transition chemical laser. J. App. Phy. Letter. **32**, 496 (1978). <https://doi.org/10.1063/1.90088>
3. Behrens, W.H., Lohn, P.D., Endo, M., Walter, R.F.: Hydrogen and Deuterium Fluoride Chemical Lasers in Gas Lasers, pp. 341–367. CRC Press, Ny (2007)
4. Sagar, V., Chhaya, R.K., Mainuddin Borkar, M., Mittal, A.P.: Data acquisition system for arc-drives HF/DF chemical lasers. J. Instrument. Sci. Technol. **40**, 262–274 (2012). <https://doi.org/10.1080/10739149.2012.673197>
5. Luo, G., Chaoqi, H., Bo, P., Dianyuan, F.: A new fluid state laser system realizes laser output, high power lasers and applications. Proc. SPIE **7843**(784311), 1–11 (2010). <https://doi.org/10.1117/12.870197>
6. Chaoqi, H., Haitao, G., She, J., Xiaoxia, Qiao, Z., Fei, G., et al.: Neodymium fluid laser: laser emission in circulating state. J. Opt. Laser Technol. **44**, 1633–1635 (2012). <https://doi.org/10.1016/j.optlastec.2011.12.047>
7. Eroglu, A., Westrick, B.: General purpose wireless communication system using data acquisition. J. Comm. Netw. Sci. Res. **4**, 48–53 (2012). <https://doi.org/10.4236/cn.2012.41007>
8. Sa-ngasoonsong, A., Kunthon, J., Sarangan, V., Cai, X., Satish, T.S.B.: A low-cost, portable, high throughput wireless sensor system for phonocardiography applications. Sensors. ISSN **12**(10851–10870), 1424–8220 (2012). <https://doi.org/10.3390/s120810851>
9. Chen, S.L., Wang, S.R., Lin, Y.C., Chen, Y.Y.: A novel wireless data acquisition infrastructure for manufacturing equipment based on Wi-Fi. J. App. Mech. Mater. **764–765**, 788–791 (2015). <https://doi.org/10.4028/www.scientific.net/AMM.764-765.788>
10. Seungchan, L., Younghak, S., Soogil, W., Kiseon, K., Heung-No, L.: Review of wireless brain-computer interface system. INTECH. Chapter **11**, 215–238 (2013). <https://doi.org/10.5772/56436>
11. Mohamed, M.M., Omar, M.S., Zaghoul, M., Mohamed, E.: Design and development of wireless data acquisition system for natural gas station. J. Wirel. Commun. **7**(5) (2015)
12. Bello, L.L., Kaczynski, G.A., Nolte, T.: Towards a robust real-time wireless link in a land monitoring application. IEEE **449–452** (2006). <https://doi.org/10.1109/ETFA.2006.355237>
13. Dehui Kong, T.L., Xingang, Y., Sun, X., Wang, B., Liu, Q.: The research of long distance transmission based on metrological sensor network. Int. J. Fut. Gener. Commun. Network. **7**(1), 59–70 (2014). <https://doi.org/10.14257/ijfgcn.2014.7.1.06>
14. Xu, N., Rangwala, S., Chintalapudi, K.K., Ganesan, D., Broad, A., Govindan, R., Estrin, D.: A wireless sensor network for structural monitoring. SenSys, Nov 3–5, 2004, pp. 13–24. Baltimore, Maryland, USA (2004). <https://doi.org/10.1145/1031495.1031498>
15. Collins, D.: Wireless data acquisition in flight test networks. In: European Telemetry and Test Conference, pp. 225–232 (2016). <https://doi.org/10.5162/etc2016/8.2>
16. Michael, A., Georgia, D., Kaffashi, F., Jacono, F.J., Loparo, K.A.: Information technology in critical care: review of monitoring and data acquisition systems for patient care and research. Sci. World J. **727694**, 1/7–7/7 (2015). <https://doi.org/10.1155/2015/727694>
17. Gowri, S., Vimali, J.S., Karthik, D.U. Jeffrey, G.A.J.: Real time traffic signal and speed violation control system of vehicles using IOT. In: International Conference on Computer Networks, Big Data and IoT, pp. 953–958. Springer (2019)
18. Subramanian, B., Selvakumar, A.S., Sachithanatham, M.J., Saikumar, S., Radhakrishnan, A.: Automatic railway gate control system using GPS. In: Inventive Communication and Computational Technologies, pp. 441–449. Springer (2021)
19. Beg, M.T., Tyagi, R.K., Rajesh, R., Singhal, G., Dawar, A.L.: Optical spectroscopic based in-line iodine flow measurement system—an application to COIL. Sensors Actuators B **109**, 375–380 (2005). <https://doi.org/10.1016/j.snb.2005.01.004>

20. Tyagi, R.K., Rajesh, R., Singhal, G., Dawar, A.L.: Real time data acquisition and control system for a chemical oxygen-iodine laser. *J. Measur. Sci. Technol.* **14**, 1364–1372 (2003). <https://doi.org/10.1088/0957-0233/14/8/323>
21. Beg, M.T., Tyagi, R.K., Rajesh, R., Singhal, G., Dawar, A.L.: Real time gas flow control and analysis for high power infrared gas lasers. *Int. J. Infrared Millimeter Waves.* **26**(1), 91–105 (2005). <https://doi.org/10.1007/s10762-004-2038-1>
22. Singhal, G., Tyagi, R.K., Maini, A.K.: Development of safe infrared gas lasers, optics and laser technology. *J. Optics Laser Technol.* **47**, 56–63 (2013). <https://doi.org/10.1016/j.optlas tec.2012.07.026>
23. Siddique, M., Singhal, G., Tyagi, R.K., Maini, A.K.: Diagnostics and data acquisition for chemical oxygen iodine laser. *IEEE Trans. Instrum. Meas.* **61**(6), 1747–1756 (2012). <https://doi.org/10.1109/TIM.2011.2178727>
24. Dohare, R.K., Singhal, G.: Hybrid data acquisition system for flowing medium lasers. *Defence Sci. J.* **70**(3), 285–291 (2020). <https://doi.org/10.14429/dsj.70.14902>
25. Dohare, R.K., Kumar, S., Singhal, G.: Data acquisition system for chemical iodine generation suitable for flowing medium chemical oxygen iodine laser. *Defence Sci. J.* **71**(6), 798–806 (2021). <https://doi.org/10.14429/dsj.71.17026>
26. Dohare, R.K., Singhal, G.: Real time flow control system for precise gas feed in COIL. *Defence Sci. J.* **72**(1), 91–97 (2022). <https://doi.org/10.14429/dsj.72.17079>

Mr Rajeev Kumar Dohare obtained his M. Tech (Electronics & Communication Engineering) from Amity University, Noida in 2013. Presently, he is working as a Scientist in DRDO- DIT&CS, DRDO Bhawan, New Delhi, India. His field of interest includes: data acquisition and laser process control/ electronics/ high power lasers/ optical diagnostics and networking.

In the current study, he has carried out for complete design, development scheme, LabVIEW based software and Graphical User Interface windows (GUI) development suitable for laser experiments and written/prepared the manuscript.

Dr Mainuddin received his ME from Delhi College of Engineering, Delhi in 2003 and PhD in 2008 from JMI, New Delhi. He is presently working as a Professor in Department of Electronics & Communication Engineering, JMI, New Delhi. His research interests include: Optical diagnostics, High power lasers, data communication, optical communication and computer networks.

In the current study, he has supervised for design and development scheme.

Dr Gaurav Singhal received BE (Mechanical Engineering) from JMI, New Delhi, in 1998 and PhD from IIT, Delhi, in 2008. Presently, he is working as a Scientist in DRDO- CHES, Hyderabad, India. His research interests include: High power lasers, high speed unsteady flows, turbulent mixing, laser diagnostics, CFD techniques etc

In the current study, he has carried out the entire sensor selection for acquisition of parameters during laser operation.

Finite Element Analysis of Isotropic & Functionally Graded Plate



Satadru Singha and S. K. Tiwari

Abstract In this present work, static analysis is carried out for a functionally graded (FG) and isotropic plate in ABAQUS. The objective is to compare the structural responses of both the plates under different loads, boundary conditions, and analyze the effect of variation in thickness on natural frequencies of the FG plate. The material properties of the FG plate are varying along the thickness. The top and bottom surface of the plate is made up of 100% alumina and aluminum, respectively. In functionally graded plate, the maximum deflection along Y axis is found to be less. Modal analysis was performed on the functionally graded plate with variable thickness to determine the natural frequencies of the first few modes. The natural frequency decreases as the thickness decreases. So, changing the thickness of the plate had a significant effect on its natural frequencies.

Keywords Finite element analysis · Abaqus · Functionally graded materials · Power law

1 Introduction

With advancement of science and technologies, the requirements of different types of materials for various purposes have increased. One such major invention was functionally graded materials commonly known as FGM. These are special kind of composite materials in which the properties of the material such as mass density, Young's modulus, and Poisson's ratio vary as we move from one surface to another [1]. The variation can be along X, Y, or Z direction depending on the purpose that they need to serve. The properties of metal and ceramic together give FGMs a higher edge than any other conventional materials [2]. The ceramic is generally hard and

S. Singha (✉) · S. K. Tiwari
Dr. B R, Ambedkar National Institute of Technology, Jalandhar, India
e-mail: satadrus.de.20@nitj.ac.in

S. K. Tiwari
e-mail: tiwarisk@nitj.ac.in

brittle in nature. Because of their great hardness and strength, they offer good wear resistance. They have high melting point which makes them good heat resistant. Metals are ductile and malleable in nature. They are strong yet deformable.

In early 1990s, the concept of fabricating functionally graded materials (FGMs) came into existence for the first time. These were initially used in aerospace industries to overcome the problems related to heat-resistant coatings. Later, with time, their applications had significantly increased. Functionally graded materials have got a wide range of applications nowadays [3].

- Aerospace industry—due to the capability of resisting high thermal gradient of functionally graded materials, they are used to produce the frames and structures of space crafts, various engine components of rockets.
- Medical science—human bones, teeth, etc., are also functionally graded naturally. FGMs are a good replacement of these living tissues, whenever replacement is required.
- Defense sectors—FGMs have the capability in resisting the crack to propagate because of which, manufacturers use such materials to craft defense equipment for soldiers, e.g., bullet proof jackets.
- FGMs are also used to provide coat over the turbine blades as they are considered to be a good barrier to heat [4].

The following are some of the important studies and analysis on this domain related to FGM.

Pasha & B.M. had studied about FGM, including its applications, limitations, and mainly, the difficulty is making such material with varying properties, and a detailed case study was made on various methods of fabrication of FG materials [5].

Sharma & Singh had performed modal analysis of a FGM beam using general differential quadrature method to find out the natural frequencies and the relationship between volume fraction index, length of the beam, and natural frequencies were shown [6].

Saad & Hadji had studied about the thermal buckling of porous plates where they came to a conclusion that the critical buckling temperature of FGM is lower than that of ceramic under the application of linear and uniform thermal load [7].

Kar & Srinivas had concluded that FGM plate made up of hydroxyapatite/titanium there is a considerable effect of various values of grading indices on bending deflection in the plate and the buckling behavior changes for different values of grading indices; therefore, HA/Ti FGM can be used in bone prosthetic in place of stainless steel [8].

The current analysis focuses on the following points:

- (a) Analysis (static) of isotropic and FG plates using Abaqus.
- (b) Performing modal analysis of the FG plate to find out the natural frequencies of first three modes.
- (c) Studying the effect of variation in thickness in maximum deflections and natural frequencies.

The isotropic plate in this study for static analysis is considered to compare the maximum deflections along Y axis with that of a functionally graded plate, both subjected to different loads and boundary conditions.

2 Methodology

The FEA modeling and analysis of the analysis has been carried out in Abaqus software. The plates considered are thick with a length/width to thickness ratio greater than 5. So, solid element was used to model both the plates in Abaqus. For performing static analysis of isotropic and FG plates, the boundary conditions assumed were both end hinged (H-H) and one end fixed (C-F). The plates were subjected to uniformly varying load (UVL) and concentrated load acting separately. The UVL is assumed to act on the top surface whereas the concentrated load on the right edge. Modal analysis is carried out to find out the natural frequencies (Fig. 1).

The flowchart is a pictorial representation of the methods followed in the analysis. Initially, both the plates have been modeled in Abaqus software. The FG plate was divided into eleven layers along the thickness. The properties of the material evaluated have been assigned to each layer. For assigning these material properties, virtual temperature technique has been used. Continuous variable temperatures have been assigned along the thickness. Then, a one to one relationship between the material properties and temperature has been created. An analytical field has been used to define the temperature distribution along Y axis. It must be noted that all other thermal parameters including conducting factor are zero, and no temperature change takes place during analysis. So, the current study is not a thermal analysis, and therefore, the assigned temperatures act as dummy temperatures only. Poisson's ratio is assumed to be constant along the thickness just for the sake of simplicity.

For the isotropic plate, properties of aluminum have been considered. The analysis (static) to find out the maximum deflection was performed for both the plates. The isotropic plate is considered so that the structural response for the plates can be compared.

To predict the Eigen frequencies of the FG plate, modal analysis was performed. For modal analysis and predicting the natural frequencies in Abaqus, a step has been created with procedure type as linear perturbation, and frequency is chosen further.

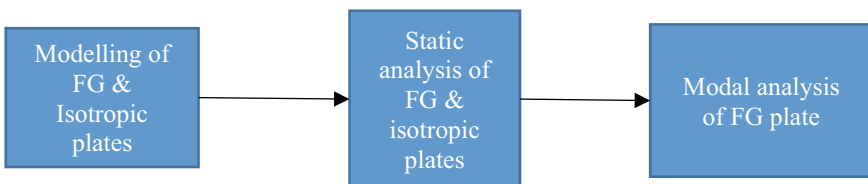


Fig. 1 Flowchart of methodology

The natural frequencies of 1st three modes for the cantilever and hinge-hinge FG plate with thickness 10 and 8 mm have been evaluated.

There are different toolsets used to model both the plates in Abaqus. An analytical field toolset has been used to assign continuous variable temperature distribution along Y axis, i.e., thickness of the functionally graded (FG) plate. Set toolset is used in creating sets, and then, the concentrated load on the right end for both the plates has been applied. The edit mesh toolset has been used in modifying and improving the meshing. The query toolset has been used to get all the information of the model, mesh type, elements, etc.

2.1 Analysis in Abaqus

This include three phases, namely preprocessing, simulation, and post-processing. In the very 1st step, geometry and other properties of the material are to be specified followed by meshing. The global matrix is then evaluated by assembling the stiffness matrices of each material. The required boundary conditions are then applied to obtain the solution. The simulation part runs in the background. The post-processing is the final part where the results are evaluated after the end of simulation. Visualization modules are used to evaluate the results.

3 Materials & Properties of the FG & Isotropic Plates

For the FG plate, aluminum is considered to be the metal, whereas the ceramic is taken as alumina. The Poisson's ratio (μ) of both aluminum and alumina is assumed to be 0.3. The top surface is 100% ceramic, and the bottom surface is fully metal. The isotropic plate has been assumed to be made of aluminum (Fig. 2).

The length (l) and width (w) of the both the plates are assumed to be 100 mm and are constant throughout the analysis, but the variation of thickness from 10 to 8 mm is taken into account.

- (a) Profile 1: length (l) = width (w) = 100 mm & thickness (h) = 10 mm
- (b) Profile 2: length (l) = width (w) = 100 mm & thickness (h) = 8 mm

In the present study, the variation of material properties is assumed to vary only along the thickness of the functionally graded plate. The material properties, i.e., mass density (ρ) and Young's modulus (E) are evaluated from the power law. Also, mass density and Young's modulus depend on volume fraction [9],

$$V_f = \left(\frac{z}{h} + \frac{1}{2} \right)^n \quad (1)$$

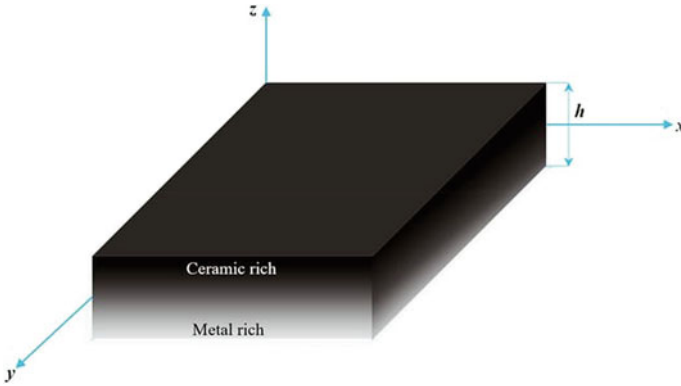


Fig. 2 Coordinate system of the plates

' n ' varies from 0 to infinity and is known as the power law index. In this present study, n is taken as 0.2, 0.5, 1, 2, 10, i.e., for ceramic, n is taken as 10 & 0 for the metal, and z is the distance measured from the middle. At top most surface, $z = h/2$, at bottom most surface, $z = -h/2$ and zero in the middle [10].

Young's modulus and mass density of the FG plate are calculated from the following relations [10],

$$E = (E_c - E_m) \left(\frac{z}{h} + \frac{1}{2} \right)^n + E_m \tag{2}$$

$$\rho = (\rho_c - \rho_m) \left(\frac{z}{h} + \frac{1}{2} \right)^n + \rho_m \tag{3}$$

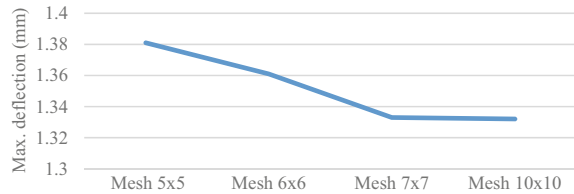
where E_c = Young's modulus of ceramic, E_m = Young's modulus of metal ρ_c = mass density of ceramic and ρ_m = mass density of metal [11].

The functionally graded plate has been divided into 11 layers along the thickness, i.e., Y axis. Each layer has distinct material property. So, Young's modulus and mass density have been assigned to each layer. The Poisson's ratio is assumed to be constant throughout for the sake of simplicity.

The isotropic plate is assumed to be made of aluminum with young's modulus (E) of 70 GPa and mass density (ρ) of 2702 kg/m³. Poisson's ratio (μ) is taken as 0.

4 Research & Analysis

From Fig. 2, it is very much clear that the model converges at mesh size 10×10 when it is subjected to UVL under (Hinge-hinge) HH condition. With a mesh size of 5×5 , the hinged-hinged FG plate showed a maximum deflection of 1.381 mm.

Fig. 3 Convergence study

With increasing the mesh size to 6×6 and 7×7 , the results started converging and finally converged at mesh size of 10×10 (Max. deflection = 1.322 mm). The same mesh size is used in the analysis (Fig. 3).

4.1 Analysis (Static) of FG Plate

The FG plate for static analysis is assumed to be made up of aluminum and alumina. The Young's modulus of aluminum is (70×10^3) MPa and that of alumina is (380×10^3) MPa. The Poisson's ratios of both these materials are assumed to be 0.3. Length and width of the plate is 100 mm and is constant throughout the analysis. The thickness of the square plate is varied from 10 to 8 mm. The loads are applied on the top surface of the plate. The mechanical analysis is performed by the application of UVL and a concentrated force separately. The concentrated load is acting on the right edge of the plate. Two different boundary conditions are assumed, hinge-hinge and one end of the plate is fixed (cantilever). The magnitude of the UVL and concentrated load is 0.5 MPa and 5 N, respectively. The maximum deflection is to be observed along Y axis. The results are enlisted in Table 1.

4.2 Analysis (Static) of Isotropic Plate

The dimensions of the isotropic plate are same as that of functionally graded plate, i.e., length and width of the plate is 100 mm and is constant throughout the analysis. The thickness of the square plate is varied from 10 to 8 mm.

Static analysis of isotropic plate is carried out to find out the deflection suffered by the plate along Y axis. The plate is subjected to different loading and boundary conditions. The maximum deflection in each case is to be noted. To perform the mechanical analysis, it has been assumed that the isotropic plate is subjected to UVL and a concentrated force acting separately. The concentrated force is acting on the right edge of the plate. The two different boundary conditions are assumed are hinge-hinge, and one end of the plate is kept fixed (cantilever). The magnitude of the UVL and concentrated load is 0.5 MPa and 5 N, respectively.

The point load acting on the left edge of the hinged-hinged (H-H) plate caused no deflection as that is hinged. For the functionally graded plate, it is seen that the

Table 1 Max. deflections in FG and isotropic plate under different load & B.C

Boundary condition	Thickness (mm)	Load	Max. deflection of FG plate (mm)	Max. deflection in isotropic plate (mm)
Hinge-hinge (H-H)	10	UVL = 0.5 MPa	0.04927	0.4931
Hinge-hinge (H-H)	8	UVL = 0.5 MPa	0.0962	0.9627
Hinge-hinge (H-H)	10	Point Load = 5 N	0	0
Hinge-hinge (H-H)	8	Point Load = 5 N	0	0
Left end fixed (C-F)	10	UVL = 0.5 MPa	1.332	13.332
Left end fixed (C-F)	8	UVL = 0.5 MPa	5.088	26
Left end fixed (C-F)	10	Point Load = 5 N	2.901	2.901
Left end fixed (C-F)	8	Point Load = 5 N	5.656	5.656

deflection in the plate increases when the plate is fixed at one end compared to that of hinge-hinge condition. The deflection is found less in hinge-hinge boundary condition when compared with that of one end clamped condition. As the thickness of the plate is reduced by 0.8 times keeping all other geometrical parameters constant, the deflection increases by almost 2 times when the plate is subjected to UVL and hinge-hinge boundary condition. The increase in deflection is 3.8 times under UVL and left end fixed condition. Under the application of point load and left end fixed condition, the increase is around 1.95 times. For the isotropic plate, similar results are observed. With decrease in thickness, the deflection further increases. The increase in deflection is almost 1.95 times with reduction of thickness by 0.8 times. Maximum deflection in this case is seen when the plate is subjected to UVL and one end is fixed.

Max. deflection in FG plate subjected to different loads and boundary conditions (Figs. 4, 5, 6 and 7):

Max. deflections in isotropic plate subjected to different loads and boundary conditions (Figs. 8, 9, 10 and 11):

4.3 Modal Analysis of the FG Plate

To find out the natural frequencies of the plate, modal analysis is performed. To perform modal analysis, only, boundary conditions and material properties are required. When designing of a machine is considered, first three or four natural

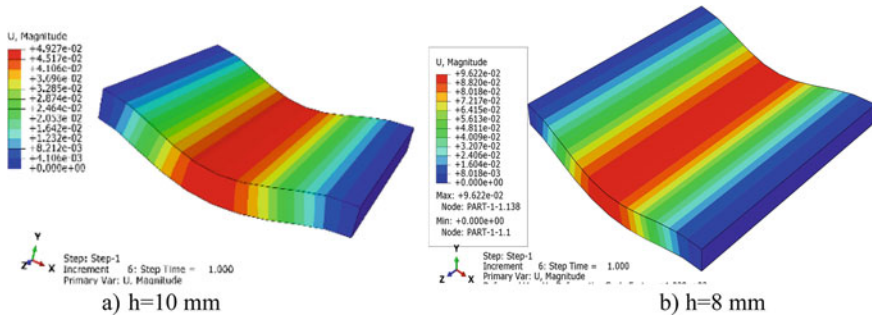


Fig. 4 Max.deflection in HH FG plate subjected to UVL

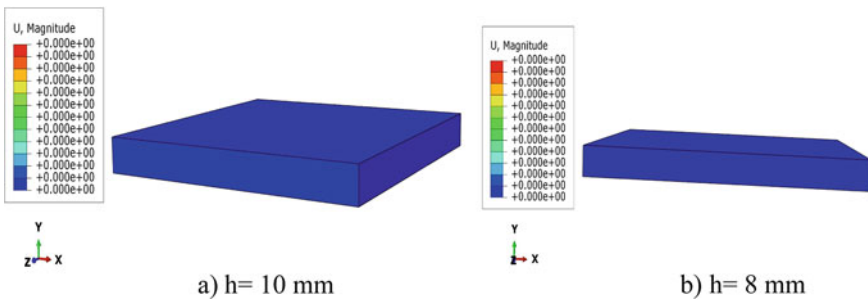


Fig. 5 No deflection in HH FG plate subjected to point load at right edge

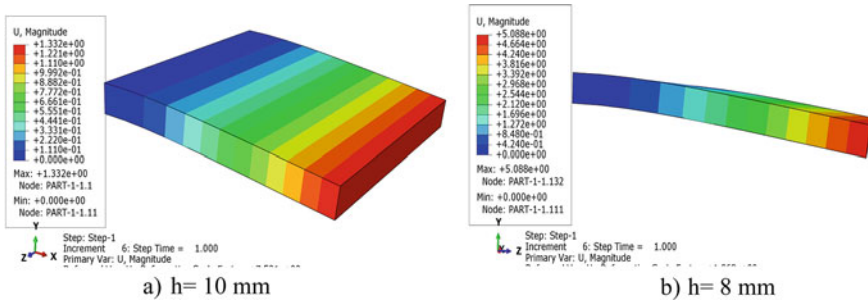


Fig. 6 Max.deflection in C-F FG plate subjected to UVL

frequencies are quite important. The effect of thickness of the plate on the natural frequency is to be observed.

Materials chosen for this analysis is same as earlier, i.e., aluminum as metal and alumina as ceramic, respectively. The magnitudes of the natural frequencies of first three modes of the plate subjected to two different boundary conditions are examined for profile 1 and profile 2 and are enlisted in Table 2.

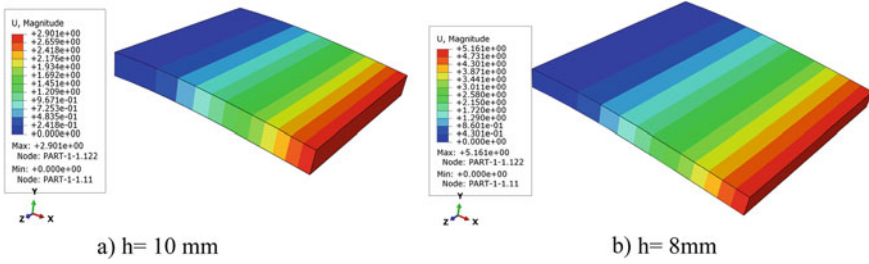


Fig. 7 Max.deflection in C-F FG plate subjected to point load at free end

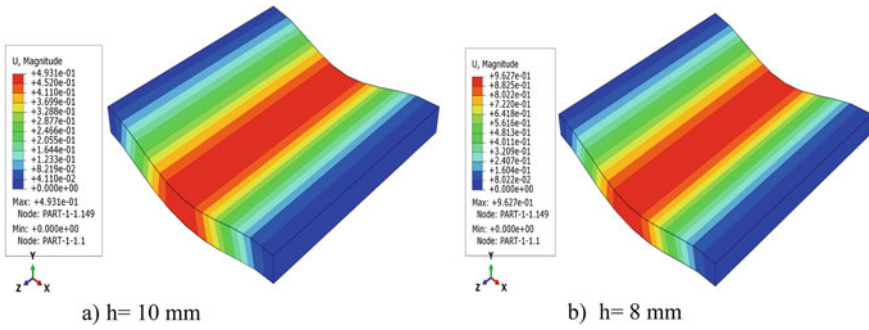


Fig. 8 Max. deflection in HH isotropic plate subjected to UVL

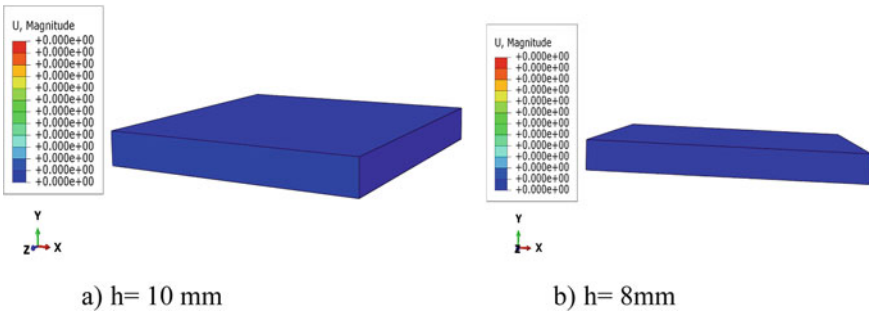


Fig. 9 No deflection in HH isotropic plate subjected to point load at right edge

It is observed that when thickness of the plate is reduced, the natural frequencies are reduced as well. Also, natural frequencies of hinge-hinge plate are higher than that of the cantilever plate.

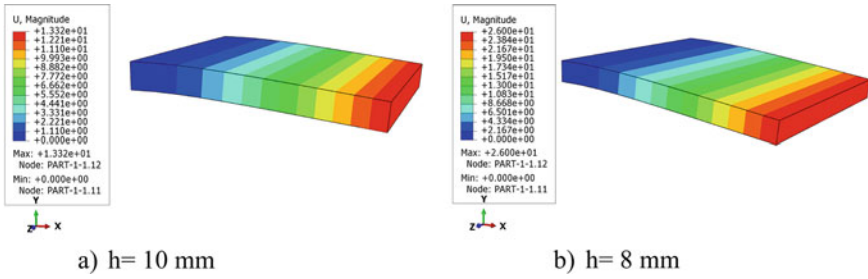


Fig. 10 Max. deflection in C-F isotropic plate subjected to UVL

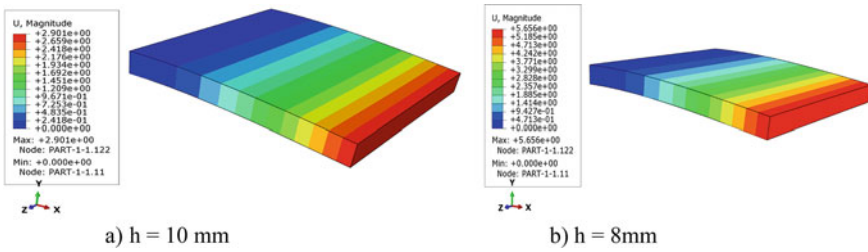


Fig. 11 Max. deflection in C-F isotropic plate subjected to UVL

Table 2 Natural frequencies of FG plate

Boundary cond	Thickness (mm)	Mode	Natural frequency (Hz)
Hinged-hinged (H-H)	10	1	547.97
		2	713.76
		3	1146.8
	8	1	441.04
		2	629.74
		3	1059.7
Left end fixed(C-F)	10	1	85.032
		2	268.60
		3	515.37
	8	1	68.168
		2	252.63
		3	418.07

5 Validation of the Analysis

The result of the study was validated [9] and was found to be within reasonable limit for isotropic plate. Modal analysis of the thin cantilever plate of thickness 10 mm was performed, and the results were compared. The results are in close agreement with the similar kind of work done by [12].

6 Conclusion

In the FG plate, with decrease in the thickness, an increase in the maximum deflection along Y axis is observed. Similar effect can be seen in the isotropic plate. The maximum deflection increases with increase in thickness. The maximum deflection in FG and isotropic plate is observed in C-F condition when the free edge of the plate is subjected to a concentrated load. In almost all the cases, FG plate has showed higher resistance to the static loads than the isotropic plate. Whereas, the maximum deflection of both the plates in C-F condition subjected to concentrated load at the free end is equal. This is possibly because the load is concentrated to particular point and is not distributed over the surface. The modal analysis performed showed that thickness has a significant effect on natural frequencies.

With decrease in thickness of the plate, a reduction in the magnitudes of natural frequencies can be observed.

7 Future Scope

- i. The analysis can be performed taking into account the significance of 2D FG plate where variation of the material properties can be along both thickness and the length of the plate.
- ii. Variable Poisson's ratio can be assigned to the different layers.
- iii. The effect of temperature change can be taken in considered.
- iv. The applications of FG materials are already significant in nuclear, aero, defense, automobile industries, etc. The role of these materials in medical field cannot be ignored, e.g., human teeth, prosthetic bone. Therefore, there should be more researches in this domain in order to contribute more in this noble application.

References

1. Wei, D., Liu, Y., Xiang, Z.: An analytical method for free vibration analysis of functionally graded beams with edge cracks. *J. Sound Vib.* **331**, 1686–1700 (2012)
2. Jha, D.K., Kant, T., Singh, R.K.: A critical review of recent research on functionally graded plates. *Compos. Struct.* **96**, 833–849 (2013)
3. Malekzadeh, P., Heydarpour, Y.: Response of functionally graded cylindrical shells under moving thermo-mechanical loads. *Thin-Walled Struct.* **58**, 51–66 (2012)
4. Nemat-Alla, M.: Reduction of thermal stresses by developing two-dimensional functionally graded materials. *Int. J. Solids Struct.* **40**, 7339–7356 (2003)
5. Pasha, A., Rajaprakash, B.M.: Functionally graded materials (FGM) fabrication and its potential challenges & applications. *Mater. Today Proc.* **52**, 413–418 (2021)
6. Sharma, P., Singh, R.: Materials today: proceedings a numerical study on free vibration analysis of axial FGM beam. *Mater. Today Proc.* **44**, 1664–1668 (2021)
7. Saad, M., Hadji, L.: Materials today: proceedings thermal buckling analysis of porous FGM plates. *Mater. Today Proc.* **53**, 196–201 (2022)
8. Kar, U.K., Srinivas, J.: Materials today: proceedings material modeling and analysis of hydroxyapatite/titanium FGM plate under thermo-mechanical loading conditions. *Mater. Today Proc.* **33**, 5498–5504 (2020)
9. Deepak, S.A., Shetty, R.A.: Materials today: proceedings static and free vibration analysis of functionally graded rectangular plates using ANSYS. *Mater. Today Proc.* **45**, 415–419 (2021)
10. Ferreira, A.J.M., Batra, R.C., Roque, C.M.C., Qian, L.F., Martins, P.A.L.S.: Static analysis of functionally graded plates using third-order shear deformation theory and a meshless method. *Compos. Struct.* **69**, 449–457 (2005)
11. Auad, S.P., Praciano, J.S.C., Barroso, E.S., Jr J.B.M.S., Junior, E.P.: Science direct: isogeometric analysis of FGM plates. *Mater. Today Proc.* **8**, 738–746 (2019)
12. Wangdus, R., Chalak, H.: Free vibration analysis of functionally graded plates using four parameter power law in Abaqus. *JMEST* **3**, 2458–9403 (2016)

Designing of an Efficient 4*4 RAM Using Binary Cell



Meghana Rao Ravula, Abhishek Potharaju, and R. Phani Vidyadhar

Abstract In VLSI, memory cell is an electrical circuit that saves 1 bit of binary data and should be set to cache logic 1 and reset to cache logic 0, and the value is preserved until the set/reset functioning changes. There are two different types of memories; they are RAM and ROM memory, where RAM is used to read, write and alter the data. Here, we considering RAM because it as high-speed memory and used as primary memory. RAM is divided into two types SRAM cell and DRAM cell. SRAM is used because of its huge storage capacity and short access time; it has become a significant component in many VLSI circuits. One of the most difficulties in SRAM is designing low-power sufficient memory; power consumption is high, whereas binary cell has little amount power dissipation. Let's look into comparative study of binary cell, SRAM cell, and SRAM cell using power-gating techniques (sleepy and stack). Here, the proposed 4*4 RAM is designed using binary cell for low-power and high-speed RAM design. The 4*4 RAM modelled and simulated using Cadence Virtuoso 180 nm technology with supply of 1.8 V.

Keywords RAM · ROM · SRAM · DRAM · Binary cell · 4*4 RAM · VLSI

1 Introduction

The technique of combining a millions of transistors into a chip is known as VLSI. By greatly reducing the technology, rapid expansion in the VLSI production process leads in higher integrated circuit density [1]. Simultaneously, enhanced power loss has been a key roadblock to continued VLSI circuit design [2].

As SRAM is designed using six transistors as per shown in Fig. 1, M1, M3 and M2, M4 form two inverters which are connected back-to-back; the output of M1, M3

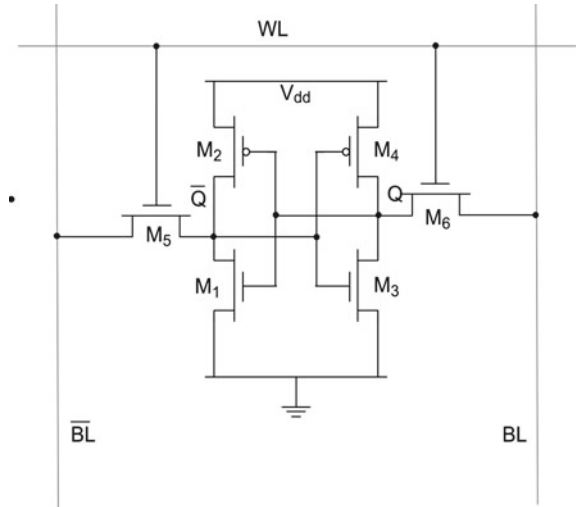
M. R. Ravula (✉) · A. Potharaju · R. P. Vidyadhar
Department of Electronics and Communication Engineering, Vardhaman College Of Engineering,
Hyderabad, Telangana, India
e-mail: meghanaraavula@gmail.com

R. P. Vidyadhar
e-mail: rphaniv@vardhaman.org

© The Author(s), under exclusive license to Springer Nature Singapore Pte Ltd. 2023
V. Bindhu et al. (eds.), *Proceedings of Fifth International Conference on Inventive Material Science Applications*, Advances in Sustainability Science and Technology,
https://doi.org/10.1007/978-981-19-4304-1_16

175

Fig. 1 SRAM (source <https://commons.wikimedia.org>)



inverter is connected as input to M2, M4 inverter; these are bistable cross-coupled inverters. M5, M6 are access transistors; they have access to store the data for read and write functions [3]. The abbreviation of SRAM is static random access memory, whereas static means hold data as long as power is supplied. SRAM performs three operations; they are read, hold and write [4].

Operation of SRAM

Word line, WL, control access.

WL = 0, hold operation.

WL = 1, read or write operation.

OPERATION	Word line (0/1)	Transistor (ON/OFF)
HOLD	0	OFF
WRITE	1	ON
READ	1	ON

If $BL > BLB$, output is 1.

If $BL < BLB$, output is 0.

2 Binary Cell

The binary cell is a device that can store one of two stable states and has two stable states [5]. For developing a memory cell called by binary cell on the basis of flip-flop, three inputs and one output make up the binary cell. When the cell is selected, the

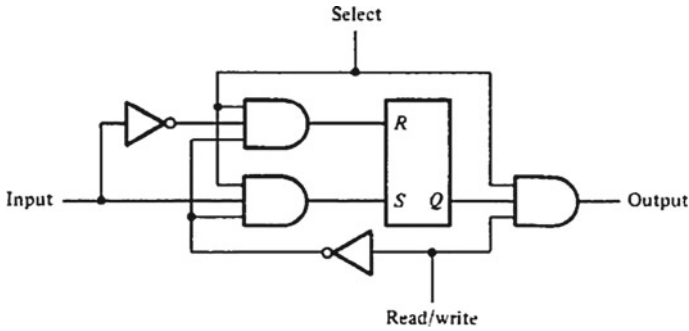


Fig. 2 Schematics of binary cell (source <https://commons.wikimedia.org>)

choose input enables reading or writing. Read/write input specifies cell activity [6] (Fig. 2).

Input “Select” being useful for retrieving and read or write to the cell. A memory action on this cell can be done when the choice line is high [7]. When the choice line of a binary cell is low, the data of the cell are no longer of interest—the cell was not read from it or written to it at the time. By noticing that both the inputs and outputs of “R-S flip-flop” are routed through the gates, “Select” is amongst the input to gates; we can see how “select” is granted this power. Thus, if “select” is low, the R-S flip-inputs flops will stay low, and the cell’s output will be low [8].

“Read/write” is the next input we will look at. This input will be driven by the system clock.

FF Value	Phase
Low (0)	Read
High (1)	Write

During read phase in the cell, we cannot write in the cell, and also unable to examine cell data during write phase (Fig. 3).

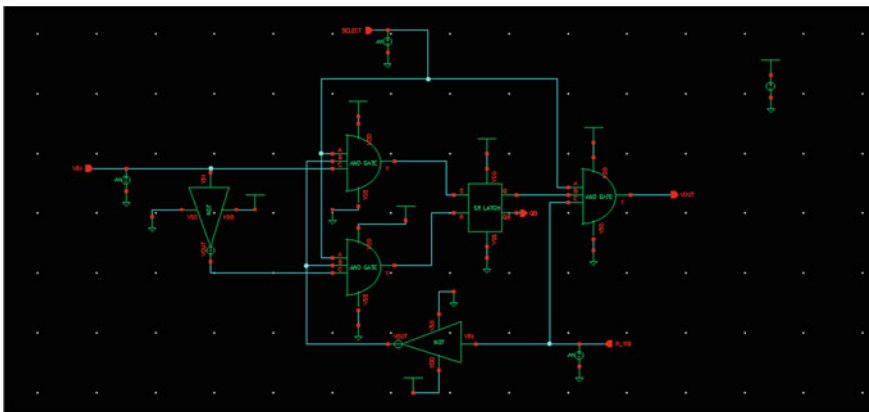


Fig. 3 Schematics of binary cell

3 4*4 Ram Using Binary Cell

The logical layout of a tiny RAM 4*4 is depicted below. It comprises a total of twelve binary cells and is made up of four words of three bits each. The binary cell is represented by each block labelled BC, which has three inputs and one output [9] (Fig. 4).

In 4*4 from there are 16 binary cells, each binary cell is made up of 3 input n and gates and one output n and gate [6]. And also, in the circuit 2*4 decoder which is a combinational circuit with 2 input lines and 4 output lines. Based on the input, one of the outputs will be enabled when memory line is enabled. Read/write is common for all binary cells, and the output is passed through OR gate [9] (Table 1).

Depending on the selection line depending on the mode, the data are either read/write on the binary cell.

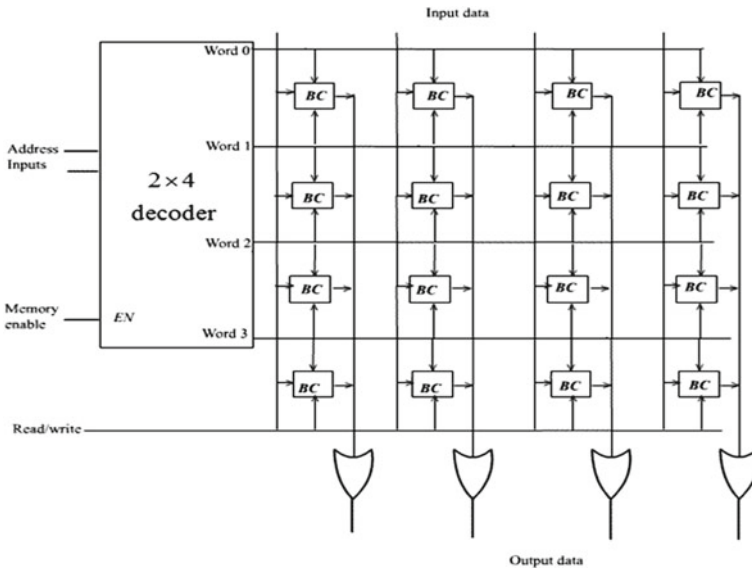


Fig. 4 Circuit of 4*4 RAM using binary cell

Table 1 Decoder truth table

Address line inputs		Outputs	Memory line
0	0	Word 0 is enabled	High
0	1	Word 1 is enabled	High
1	0	Word 2 is enabled	high
1	1	Word 3 is enabled	high

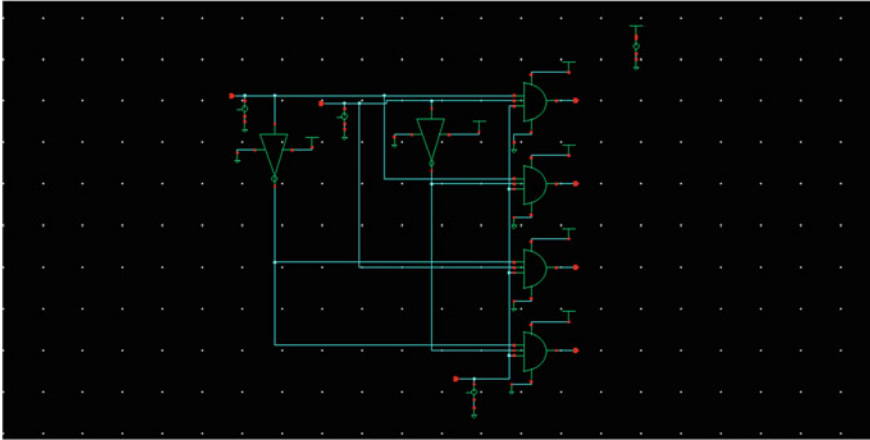


Fig. 5 Schematics of 2 by 4 decoder

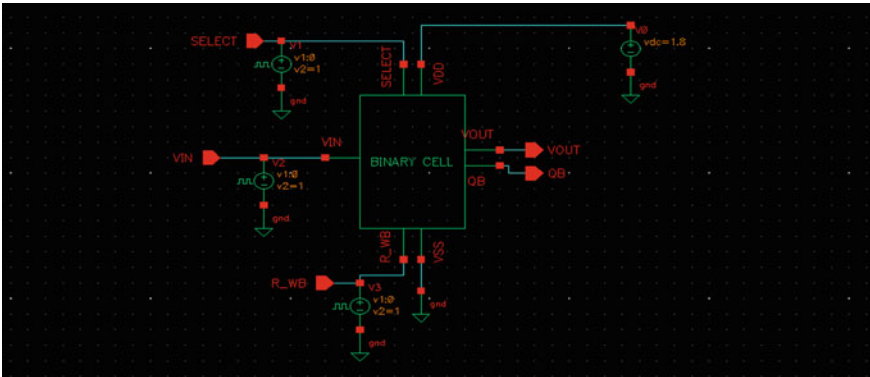


Fig. 6 Schematic of binary cell

4 Simulation Results

See Figs. 5, 6, 7 and 8.

5 Designing SRAM Circuits Using Power Gating Methods

See Figs. 9 and 10.

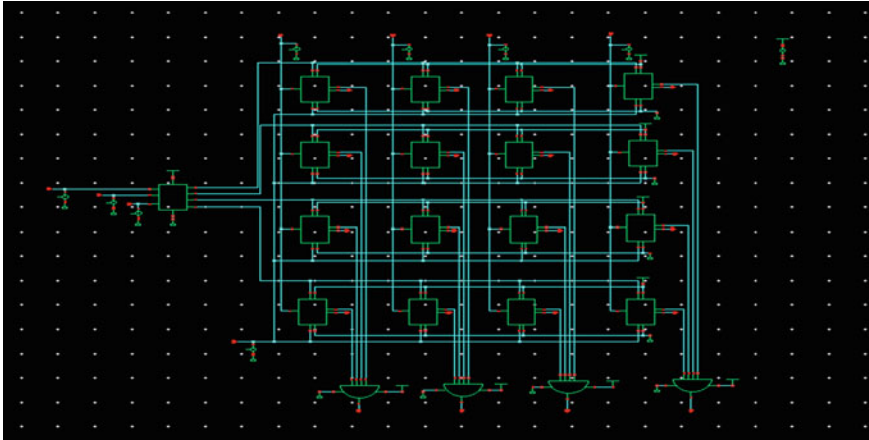


Fig. 7 Schematic of 4*4 RAM using binary cell

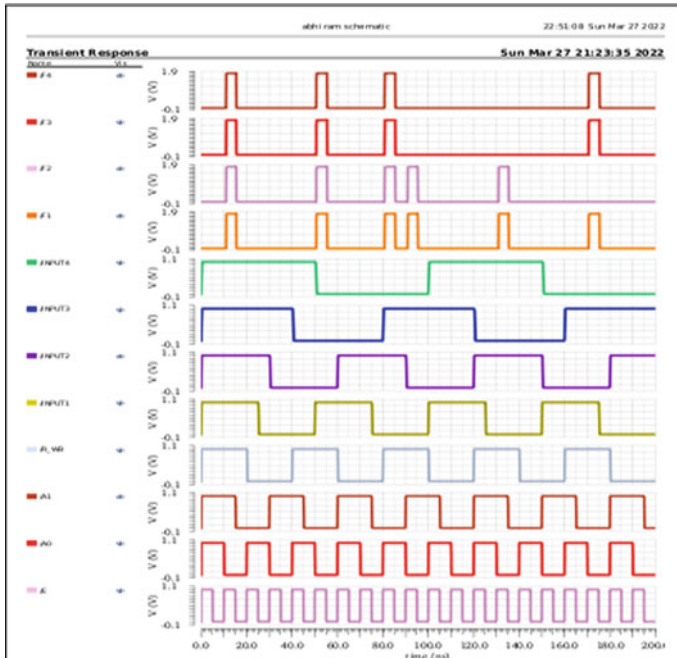


Fig. 8 Waveforms of 4*4 RAM using binary cell

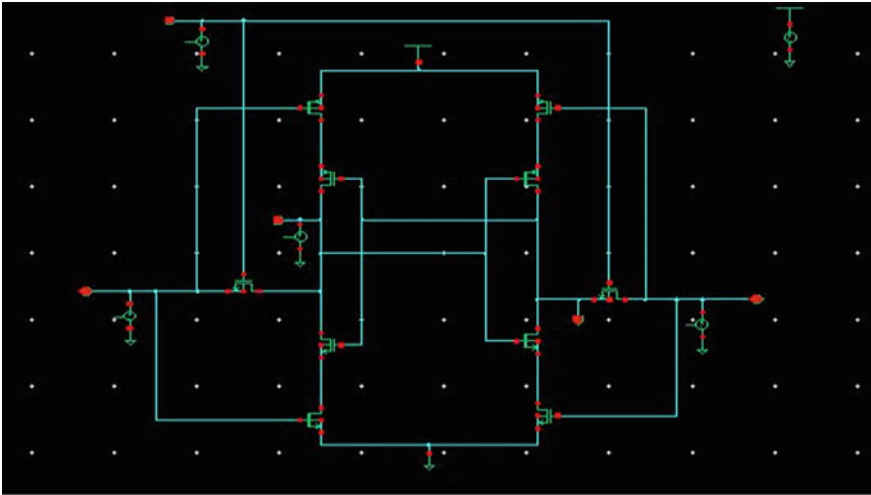


Fig. 9 Circuit implementation of SRAM using stack gating technique

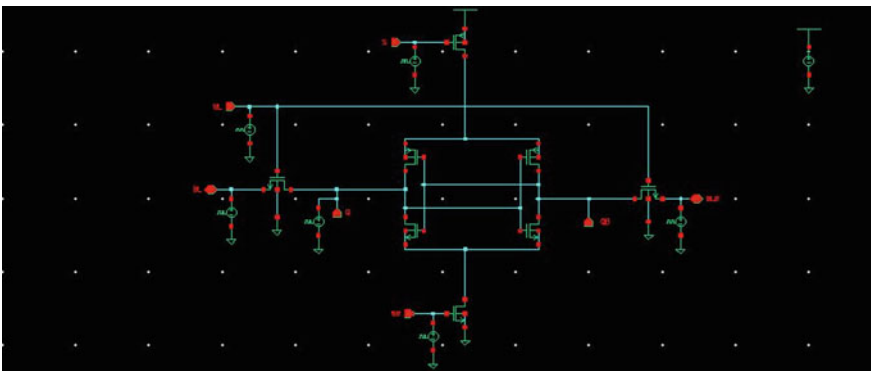


Fig. 10 Circuit implementation of SRAM using sleepy gating technique

6 Comparative Study

See Tables 2, 3, 4, 5 and 6.

Table 2 6 T SRAM.

Parameters	Results
Power	203.6 uW
Delay	503.86 ns

Table 3 SRAM using sleepy technique

Parameters	Results
Power	195.3 uW
Delay	250.4 ps

Table 4 SRAM using stack technique

Parameters	Results
Power	2.446 mW
Delay	68.96 ps

Table 5 Binary cell

Parameters	Results
Power	125.3 uW
Delay	132.6 ps

Table 6 4*4 RAM using binary cell

Parameters	Results
Power	1.87 mW
Delay	10.88 ns

7 Conclusion

The main components used in proposed design 4*4 RAM are binary cell, 2 to 4 decoder and a 4 input OR gate. The RAM is designed by arranging 16 binary cells in a 4*4 array structure. The 6 T SRAM cell is operated in three modes like hold, write and read by changing WL to 0 and 1, and its respective power and delay is calculated. Binary cell is the building block of random access memory and in binary cell whenever the select line is 1, the circuit gets ON then based on the signal given to read/ $\overline{\text{Write}}$ pin when "1" is given (Active high signal), it does read operation, and when "0" is given (Active low signal), write operation is done. On comparing average power consumption between binary cell and SRAM 6 T, binary cell consumes 25% less power. So, it is considered as efficient one. Two power gating techniques are used, namely sleep technique and stack technique. In SRAM using sleep technique additional two sleep transistors that is sleep "S" PMOS and sleep "S Bar" NMOS are used to reduce leakage power consumption, and in SRAM using stack technique in this, total 10 transistors are used; it is also called state maintenance technique. So, by doing comparative study of performance parameters, the 4*4 RAM is considered as efficient one. Entire simulation is done in Cadence virtuoso tool in 180 nm with 1.8 V as supply voltage.

References

1. Tonk, A., Goyal, S.: A literature review on leakage and power reduction techniques in CMOS VLSI design. *Int. J. Adv. Res. Comput. Commun. Eng.* **3**(2), 554–558 (2015)
2. Yeap, G.K., et al.: *Practical Low Power Digital VLSI Design*, p. 233. Kluwer Academic Publishers, Norwell, MA. ISBN: 0792380096 (1998)
3. Lourts Deepak, A., Dhulipalla, L.: Design and implementation of 32nm FINFET based 4×4 SRAM cell array using 1-bit 6T SRAM. In: *International Conference on Nanoscience, Engineering and Technology (ICONSET 2011)*, pp. 177–180 (2011). <https://doi.org/10.1109/ICONSET.2011.6167948>
4. Park, J.: *Sleepy stack: a new approach to low power VLSI and memory*. Ph.D. Dissertation, School of Electrical and Computer Engineering, Georgia Institute of Technology, May 2014
5. Calimera, A., Macii, A., Macii, E., Poncino, M.: Design techniques and architectures for low-leakage SRAMs. *IEEE Trans. Circuits Syst.* **59**(9), 1992–2007 (2012)
6. Wang, L., Li, S., Pan, L.: A pure logic CMOS based low power non-volatile random access memory. In: *2014 International Symposium on Next-Generation Electronics (ISNE)*, pp. 1–2 (2014). <https://doi.org/10.1109/ISNE.2014.6839382>
7. Na, T., Woo, S.-H., Kim, J., Jeon, H., Jung, S.-O.: Comparative study of various latch-type sense amplifiers. *IEEE Trans. Very Large-Scale Integr. (VLSI) Syst.* **12**(6), 1–5 (2013)
8. Geetha Priya, M., Baskaran, K., Krishnaveni, D.: Leakage power reduction technique in deep submicron technologies for VLSI applications. Elsevier-Sciverse Science Direct. *Procedia Eng.* **30**, 1163–1170 (2012)
9. Cathoor, F., Wuytack, S., DeGreef, E.: *Custom Memory Management Methodology Exploration of Memory Organization for Embedded Multimedia System Design*. Kluwer Academic Publishers, Boston (1998)

Mathematical Model of Kirchhoff Mesh Nanoplate Under the Action of Electrostatic and Temperature Fields



E. Y. Krylova

Abstract A new mathematical oscillation's model of a mesh nanoplate under the electrostatic and temperature fields action based on the Hamilton principle is constructed in this work. The mathematical model of the panel's behavior is based on the Kirchhoff hypotheses. The micropolar theory is applied to account for scale effects. It is assumed that the fields of displacement and rotation are not independent. Geometric nonlinearity is taken into account according to the theory of Theodor von Karman. The mesh structure is taken into account based on the Pshenichnov I. G. continuum model, which allows you to replace a regular system of densely spaced edges with a continuous layer. An original software package has been created to study the plate behavior. A numerical experiment was carried out.

Keywords Carbon nanoplate · Meshed plate · Electrostatics · Thermodynamics · Mathematical modeling

1 Introduction

Technical progress and development of science cause necessitates and relevance of the nanomaterials use in instrumentation, optics, radio electronics, robotics, medicine and many other areas. In particular, such structural elements as carbon nanoplates constitute the basis of the new generation field transistors [1]. To model statics and the dynamics of the elements of mechanical systems of micro and nano sizes of classic continual models, there are not enough due to the impossibility of taking into account the size-dependent behavior of such objects. One of the leading places among theories that allow you to take into account large-scale effects is occupied by micropolar (moment) theory [2, 3]. It is chosen by many authors for comprehensive studies of plate-shell elements for MEMS and NEMS [4–11]. MEMS and NEMS often operate at extreme temperatures. Therefore, when modeling their elements behavior, the temperature effects should be taken into account [12, 13]. Many works

E. Y. Krylova (✉)
Saratov State University, Saratov, Russia
e-mail: Kat.krylova@bk.ru

are devoted to the models construction and the study of the continuous micro- and nanoplates and shells behavior under the electrostatic forces influence. Closer to the topic of this study is an article [14] where, on the basis of a micropolar theory, a mathematical model of behavior for a geometrically nonlinear micro-plate is built under the constant and variable electrical load influence. An analysis of the static plate instability was carried out in order to determine critical electrostatic stresses. The scale effect of the plate behavior is investigated. The graphene plate has a mesh structure, when building mathematical models this should be taken into account. At the moment, works devoted to the study of mesh plates, taking into account large-scale effects, are not many [15–17]. In this paper, on the micropolar theory basis, a mathematical model of oscillations for a geometrically nonlinear mesh plate is built under the vibrational, thermal and electrostatic influences.

2 Statement of the Problem

The subject of the study is a mesh rectangular plate that occupies the area in space $\Omega = \{0 \leq x \leq c; 0 \leq y \leq b; -\frac{h}{2} \leq z \leq \frac{h}{2}\}$, the electrode is located at a distance g_0 , c , b —linear dimensions of the plate according to x , y , respectively, h —plate thickness.

The mathematical model was built on the basis of the following hypotheses and assumptions:

- plate material is isotropic and homogeneous (the plate material elastic properties are the same in all directions; at all points of the body with the same stresses, the same deformations occur);
- the geometric nonlinearity is adopted according to the theory of Theodore von Karman (nonlinear dependence of deformations on displacements is considered) [18];
- Duhamel-Neuman relations are considered as defining relations, that is, it is assumed that thermal deformations are the superposition of elastic deformations and thermal expansions;
- the restrictions on the temperature field are not applied according to the plate thickness (the three-dimensional heat equation is considered);
- large-scale effects are taken into account through micropolar theory with constrained rotation of particles [3];
- the mesh structure of the plate is taken into account according to the model of Pshenichnov G.I. [19];
- the mathematical model is based on the kinematic hypotheses of Kirchhoff.

Following the theory of Kirchhoff, the movements vector components are written as follows:

$$u_x = u(x, y, t) - z \frac{\partial w}{\partial x}(x, y, t), u_y = v(x, y, t) - z \frac{\partial w}{\partial y}(x, y, t, u_z) = w(x, y, t) \tag{1}$$

where w —deflation, u, v —the axial displacements of the mid plate surface in directions x, y , respectively.

Nonlinear analysis of the plates behavior of great importance when the nanoplate oscillation’s amplitude exceeds a quarter of the nanoplate thickness, and therefore, a significant nonlinear term must be taken into account in the mathematical model. The nonzero components of the complete deformations symmetric tensor, taking into account the adopted hypotheses and geometric nonlinearity in the form of T. von Karman, take the form:

$$e_{xx} = \frac{\partial u}{\partial x} + \frac{1}{2} \left(\frac{\partial w}{\partial x} \right)^2 - z \frac{\partial^2 w}{\partial x^2}, e_{yy} = \frac{\partial v}{\partial y} + \frac{1}{2} \left(\frac{\partial w}{\partial y} \right)^2 - z \frac{\partial^2 w}{\partial y^2}, \tag{2}$$

$$e_{xy} = \frac{1}{2} \left(\frac{\partial u}{\partial y} + \frac{\partial v}{\partial x} + \frac{\partial w}{\partial x} \frac{\partial w}{\partial y} \right) - z \frac{\partial^2 w}{\partial x \partial y}$$

In the work, a non-classical continuum model of the plate is built. The material of the plate is considered as a Cosserat pseudo-continuum with constrained rotation of particles, in the assumption that displacements and rotations fields are not independent. Thus, the components of the symmetric curvature gradient tensor will have the form

$$\chi_{xx} = \frac{\partial^2 w}{\partial x \partial y}; \chi_{yy} = -\frac{\partial^2 w}{\partial y \partial x}; \chi_{xy} = \frac{1}{2} \left(\frac{\partial^2 w}{\partial y^2} - \frac{\partial^2 w}{\partial x^2} \right); \tag{3}$$

$$\chi_{xz} = \frac{1}{4} \left(\frac{\partial^2 v}{\partial x^2} - \frac{\partial^2 u}{\partial x \partial y} \right); \chi_{yz} = \frac{1}{4} \left(\frac{\partial^2 v}{\partial y \partial x} - \frac{\partial^2 u}{\partial y^2} \right)$$

Defining ratios for the material of the plate, taking into account the hypothesis of the Duhamel-Neuman and the modified moment theory [3], take in the following form:

$$\sigma_{xx} = \frac{E}{1 - \nu^2} [e_{xx} + \nu e_{yy}] - \frac{E}{1 - \nu} \alpha (T - T_0), x \rightleftharpoons y,$$

$$\sigma_{yy} = \frac{E}{(1 + \nu)} e_{xy}, (m_{xx}, m_{xy}, m_{zx}) = \frac{El^2}{1 + \nu} (\chi_{xx}, \chi_{xy}, \chi_{zx}) \tag{4}$$

where σ_{ij} —Cosserat tensor components, m_{ij} —the highest order symmetric moment tensor components, E —Young modulus, ν —Poisson’s ratio of the plate material, l —additional independent material length parameter, α_t —coefficient of the material thermal expansion, $T(x, y, z)$ —the known function of the plate absolute temperature at a time $t \in t_0, t$ and $T_0(x, y, z)$ —the initial plate temperature at time t_0 .

The motion equations of a continuous micropolar plate taking into account thermal, vibrational and electrostatic influences, boundary and initial conditions are obtained from the Hamilton energy principle [20]:

$$\int_{t_0}^t (\delta K - \delta U + \delta W) dt = 0 \quad (5)$$

Here, K —kinetic energy, U —potential energy and W —the external forces work.

Taking into account the micropolar theory, the potential energy U in an elastic body is written as

$$U = \frac{1}{2} \int_{\Omega} (\sigma_{xx} e_{xx} + 2\sigma_{xy} e_{xy} + \sigma_{yy} e_{yy} + m_{xx} \chi_{xx} + m_{yy} \chi_{yy} + 2m_{xy} \chi_{xy} + 2m_{zx} \chi_{zx} + 2m_{zy} \chi_{zy}) dv.$$

The potential energy expression takes into account thermal stresses according to the formula (4).

Kinetic energy

$$K = \frac{1}{2} \rho \int_{\Omega} \left[\left(\frac{\partial u_x}{\partial t} \right)^2 + \left(\frac{\partial u_y}{\partial t} \right)^2 + \left(\frac{\partial u_z}{\partial t} \right)^2 \right] dv.$$

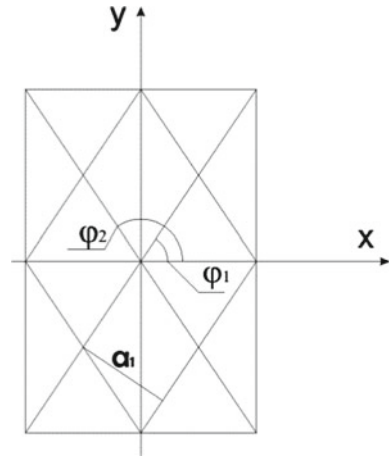
Variation of the external forces work is

$$\delta W = \delta W_{\varepsilon} + \delta W_q + \delta W_{coul},$$

where $\delta W_{\varepsilon} = \int_{\Omega} \rho \varepsilon \frac{\partial w}{\partial t} \delta w dv$ —the term associated with energy dissipation, where ε —the dissipation coefficient of the medium in which the plate operates, ρ —plate material density and $\delta W_q = \int_0^c \int_0^b q(x, y, t) \delta w dx dy$ —the term associated with the external normal distributed load, given by the law $q(x, y, t) = q_0(x, y) \sin \omega_p t$, where q_0 —amplitude, ω_p —vibration load frequency, $\delta W_{coul} = \int_0^c \int_0^b F_{coul} \delta w dx dy$ —the term associated with the work of the electrostatic force (Coulomb force), $F_{coul} = \frac{\varepsilon_r \varepsilon_0 V^2}{2(g_0 - w)^2}$ —Coulomb force, ε_r —dielectric constant of the medium, ε_0 —electrical constant and V —potential difference between the plate and the electrode.

The initial plate has a mesh structure. Suppose it consists of several families of densely spaced edges. According to the continuum theory of G. I. Pshenichny, it is possible to replace a regular system of edges with a continuous layer, as a result of which higher-order stresses and moments arising in an equivalent smooth shell will be associated with higher-order stresses and moments in the edges by the following relations:

Fig. 1 Mesh design scheme



$$\sigma_{xx} = \sum_{j=1}^n \frac{\sigma_x^j \delta_j \cos^2 \varphi_j}{a_j}, \sigma_{yy} = \sum_{j=1}^n \frac{\sigma_x^j \delta_j \sin^2 \varphi_j}{a_j}, \sigma_{xy} = \sum_{j=1}^n \frac{\sigma_x^j \delta_j \cos \varphi_j \sin \varphi_j}{a_j} \tag{6}$$

The latter relations are derived from the conditions of equality of forces acting on the same elementary sites of a plate which consists of an edges system and an equivalent smooth plate. In expressions (7), n —the number of edge families in the mesh plate under consideration and δ_i, a_i, φ_i —the distance between the edges, the width of the edges, the angle between the $O X$ axis and the axis of the edge for j th family, respectively (Fig. 1). The upper index j is assigned to the characteristics of the edges.

Additional conditions for the static equivalence of the initial mesh plate and its equivalent solid (7) are obtained using the Lagrange multiplier method from the condition that the functional reaches stationary values. When constructing the functional, expressions for the potential energy of deformation obtained in terms of stresses and moments of higher orders were used.

$$\sigma_x^j = \sigma_{xx} \cos^2 \varphi_j + \sigma_{yy} \sin^2 \varphi_j + \sigma_{xy} \cos \varphi_j \sin \varphi_j; \\ m_x^j = m_{xx} \cos^2 \varphi_j + m_{yy} \sin^2 \varphi_j + m_{xy} \cos \varphi_j \sin \varphi_j; m_z^j = m_{xz} \cos \varphi_j + m_{yz} \sin \varphi_j. \tag{7}$$

Given (6–7), expressions can be written for all forces and moments of a micropolar smooth plate (with index s) equivalent to the initial mesh plate.

$$N_{xx}^s = A_{40} N_{xx} + A_{22} N_{yy} + A_{31} N_{xy}; N_{yy}^s = A_{22} N_{xx} + A_{04} N_{yy} + A_{13} N_{xy}; \\ N_{yy}^s = A_{22} N_{xx} + A_{04} N_{yy} + A_{13} N_{xy}; M_{xx}^s = A_{40} M_{xx} + A_{22} M_{yy} + A_{31} M_{xy}; \\ M_{yy} = A_{22} M_{xx} + A_{04} M_{yy} + A_{13} M_{xy}; N_{xy}^s = A_{31} N_{xx} + A_{13} N_{yy} + A_{22} N_{xy};$$

$$\begin{aligned}
M_{xy}^s &= A_{31}M_{xx} + A_{13}M_{yy} + A_{22}M_{xy}; Y_{xx}^s = A_{40}Y_{xx} + A_{22}Y_{yy} + A_{31}Y_{xy}; \\
Y_{yy}^s &= A_{22}Y_{xx} + A_{04}Y_{yy} + A_{13}Y_{xy}; Y_{xy}^s = A_{31}Y_{xx} + A_{13}Y_{yy} + A_{22}Y_{xy}; \\
Y_{yz}^s &= A_{11}Y_{xz} + A_{02}Y_{yz}; Y_{xz}^s = A_{20}Y_{xz} + A_{11}Y_{yz}.
\end{aligned} \tag{8}$$

$$\text{Here, } A_{sk} = \sum_{j=1}^n \frac{\delta_j \cos^s \varphi_j \sin^k \varphi_j}{a_j}; s, k = \overline{0, 4},$$

$$\begin{aligned}
\{N_{xx}, M_{xx}\} &= \int_{-\frac{h}{2}}^{\frac{h}{2}} \sigma_{xx} z^{(0,1)} dz; \{N_{xy}, M_{xy}\} = \int_{-\frac{h}{2}}^{\frac{h}{2}} \sigma_{xy} z^{(0,1)} dz; Y_{xx} = \int_{-\frac{h}{2}}^{\frac{h}{2}} m_{xx} dz; \\
Y_{xy} &= \int_{-\frac{h}{2}}^{\frac{h}{2}} m_{xy} dz; Y_{xz} = \int_{-\frac{h}{2}}^{\frac{h}{2}} m_{xz} dz; x \rightleftharpoons y, \{N^T, M^T\} = - \int_{-\frac{h}{2}}^{\frac{h}{2}} \alpha_T (T - T_0) z^{(0,1)} dz.
\end{aligned} \tag{9}$$

We substitute expressions (8) into the motion equations of a smooth plate element in stresses obtained from the Hamilton variational principle. Taking into account (2–5, 9), we obtain a resolving system of motion equations for a micropolar mesh plate in displacements taking into account temperature, vibration and electrostatic influences.

$$\begin{aligned}
& - \left[\frac{h^2(A_{40} + A_{22}\nu)}{12(1-\nu)} + \frac{l^2 A_{22}}{2} \right] \frac{\partial^4 w}{\partial x^4} \\
& - \left[\frac{h^2(2A_{31} + A_{13}\nu)}{12(1-\nu)} - l^2 \left(A_{31} \frac{3}{2} - A_{13} \frac{3}{2} \right) \right] \\
& \frac{\partial^4 w}{\partial x^3 \partial y} - \left[\frac{h^2(A_{40}\nu + 3A_{22} + A_{04}\nu)}{12(1-\nu)} - l^2(3A_{22} - A_{40} - A_{04}) \right] \\
& \frac{\partial^4 w}{\partial x^2 \partial y^2} - \left[\frac{h^2(A_{22}\nu + A_{04})}{12(1-\nu)} + \frac{l^2 A_{22}}{2} \right] \frac{\partial^4 w}{\partial y^4} \\
& - \left[\frac{h^2(A_{31}\nu + 2A_{13})}{12(1-\nu)} - l^2 \left(A_{13} \frac{3}{2} - A_{31} \frac{3}{2} \right) \right] \frac{\partial^4 w}{\partial x \partial y^3} \\
& + \frac{(1+\nu)}{Eh} \left[(A_{40} + A_{22}) \frac{\partial^2 M^T}{\partial x^2} + (A_{22} + A_{04}) \frac{\partial^2 M^T}{\partial y^2} + 2(A_{31} + A_{13}) \frac{\partial^2 M^T}{\partial x \partial y} \right] \\
& + \frac{1}{1-\nu} \left\{ (A_{40} + A_{22}\nu) \frac{\partial^2 u}{\partial x^2} \frac{\partial w}{\partial x} + (A_{40}\nu + A_{22}) \frac{\partial^2 v}{\partial x \partial y} \frac{\partial w}{\partial x} + \frac{1}{2} A_{31} \frac{\partial^2 u}{\partial x \partial y} \frac{\partial w}{\partial x} \right. \\
& + \frac{1}{2} A_{31} \frac{\partial^2 v}{\partial x^2} \frac{\partial w}{\partial x} + (A_{22} + A_{04}\nu) \frac{\partial^2 u}{\partial x \partial y} \frac{\partial w}{\partial y} + (A_{22}\nu + A_{04}) \frac{\partial^2 v}{\partial y^2} \frac{\partial w}{\partial y} \\
& + \frac{1}{2} A_{13} \frac{\partial^2 u}{\partial y^2} \frac{\partial w}{\partial y} + \frac{1}{2} A_{13} \frac{\partial^2 v}{\partial x \partial y} \frac{\partial w}{\partial y} + 2(A_{31} + A_{13}\nu) \frac{\partial^2 u}{\partial x^2} \frac{\partial w}{\partial y} \\
& + 2(A_{31}\nu + A_{13}) \frac{\partial^2 v}{\partial x \partial y} \frac{\partial w}{\partial y} + A_{22} \frac{\partial^2 u}{\partial x \partial y} \frac{\partial w}{\partial y} \\
& \left. + A_{22} \frac{\partial^2 v}{\partial x^2} \frac{\partial w}{\partial y} + 2(A_{31} + A_{13}\nu) \frac{\partial^2 u}{\partial x \partial y} \frac{\partial w}{\partial x} \right\}
\end{aligned}$$

$$\begin{aligned}
& + 2(A_{31}\nu + A_{13}) \frac{\partial^2 v}{\partial y^2} \frac{\partial w}{\partial x} + A_{22} \frac{\partial^2 u}{\partial y^2} \frac{\partial w}{\partial x} \\
& + A_{22} \frac{\partial^2 v}{\partial x \partial y} \frac{\partial w}{\partial x} + (A_{31} + A_{13}\nu) \frac{\partial u}{\partial x} \frac{\partial^2 w}{\partial x \partial y} \\
& + (A_{31}\nu + A_{13}) \frac{\partial v}{\partial y} \frac{\partial^2 w}{\partial x \partial y} + \frac{1}{2} A_{22} \frac{\partial u}{\partial y} \frac{\partial^2 w}{\partial x \partial y} + \frac{1}{2} A_{22} \frac{\partial v}{\partial x} \frac{\partial^2 w}{\partial x \partial y} \Big\} \\
& + \frac{(1 + \nu)}{Eh} \left[(A_{40} + A_{22}) \frac{\partial N^T}{\partial x} \frac{\partial w}{\partial x} \right. \\
& + (A_{40} + A_{22}) \frac{\partial N^T}{\partial x} \frac{\partial w}{\partial x} + (A_{22} + A_{04}) \frac{\partial N^T}{\partial y} \frac{\partial w}{\partial y} \\
& + 2(A_{31} + A_{13}) \frac{\partial N^T}{\partial x} \frac{\partial w}{\partial y} + 2(A_{31} + A_{13}) \frac{\partial N^T}{\partial y} \frac{\partial w}{\partial x} \\
& + 4(A_{31} + A_{13}) N^T \frac{\partial^2 w}{\partial x \partial y} + \frac{(1 + \nu)}{Eh} q \\
& + \frac{(1 + \nu)}{Eh} F_{cuol} = \frac{\rho(1 + \nu)}{E} \frac{\partial^2 w}{\partial t^2} + \frac{\varepsilon\rho(1 + \nu)}{E} \frac{\partial w}{\partial t}; \\
& - \left[\frac{h^2(A_{40} + A_{22}\nu)}{12(1 - \nu)} + \frac{l^2 A_{22}}{2} \right] \frac{\partial^4 w}{\partial x^4} - \left[\frac{h^2(2A_{31} + A_{13}\nu)}{12(1 - \nu)} - l^2 \left(A_{31} \frac{3}{2} - A_{13} \frac{3}{2} \right) \right] \frac{\partial^4 w}{\partial x^3 \partial y} \\
& - \left[\frac{h^2(A_{40}\nu + 3A_{22} + A_{04}\nu)}{12(1 - \nu)} - l^2(3A_{22} - A_{40} - A_{04}) \right] \frac{\partial^4 w}{\partial x^2 \partial y^2} \\
& - \left[\frac{h^2(A_{22}\nu + A_{04})}{12(1 - \nu)} + \frac{l^2 A_{22}}{2} \right] \frac{\partial^4 w}{\partial y^4} - \left[\frac{h^2(A_{31}\nu + 2A_{13})}{12(1 - \nu)} - l^2 \left(A_{13} \frac{3}{2} - A_{31} \frac{3}{2} \right) \right] \frac{\partial^4 w}{\partial x \partial y^3} \\
& + \frac{(1 + \nu)}{Eh} \left[(A_{40} + A_{22}) \frac{\partial^2 M^T}{\partial x^2} + (A_{22} + A_{04}) \frac{\partial^2 M^T}{\partial y^2} + 2(A_{31} + A_{13}) \frac{\partial^2 M^T}{\partial x \partial y} \right] \\
& + \frac{1}{1 - \nu} \left\{ (A_{40} + A_{22}\nu) \frac{\partial^2 u}{\partial x^2} \frac{\partial w}{\partial x} + (A_{40}\nu + A_{22}) \frac{\partial^2 v}{\partial x \partial y} \frac{\partial w}{\partial x} + \frac{1}{2} A_{31} \frac{\partial^2 u}{\partial x \partial y} \frac{\partial w}{\partial x} \right. \\
& + \frac{1}{2} A_{31} \frac{\partial^2 v}{\partial x^2} \frac{\partial w}{\partial x} + (A_{22} + A_{04}\nu) \frac{\partial^2 u}{\partial x \partial y} \frac{\partial w}{\partial y} + (A_{22}\nu + A_{04}) \frac{\partial^2 v}{\partial y^2} \frac{\partial w}{\partial y} \\
& + \frac{1}{2} A_{13} \frac{\partial^2 u}{\partial y^2} \frac{\partial w}{\partial y} + \frac{1}{2} A_{13} \frac{\partial^2 v}{\partial x \partial y} \frac{\partial w}{\partial y} + 2(A_{31} + A_{13}\nu) \frac{\partial^2 u}{\partial x^2} \frac{\partial w}{\partial y} \\
& + 2(A_{31}\nu + A_{13}) \frac{\partial^2 v}{\partial x \partial y} \frac{\partial w}{\partial y} + A_{22} \frac{\partial^2 u}{\partial x \partial y} \frac{\partial w}{\partial y} + A_{22} \frac{\partial^2 v}{\partial x^2} \frac{\partial w}{\partial y} + 2(A_{31} + A_{13}\nu) \frac{\partial^2 u}{\partial x \partial y} \frac{\partial w}{\partial x} \\
& + 2(A_{31}\nu + A_{13}) \frac{\partial^2 v}{\partial y^2} \frac{\partial w}{\partial x} + A_{22} \frac{\partial^2 u}{\partial y^2} \frac{\partial w}{\partial x} + A_{22} \frac{\partial^2 v}{\partial x \partial y} \frac{\partial w}{\partial x} + (A_{31} + A_{13}\nu) \frac{\partial u}{\partial x} \frac{\partial^2 w}{\partial x \partial y} \\
& \left. + (A_{31}\nu + A_{13}) \frac{\partial v}{\partial y} \frac{\partial^2 w}{\partial x \partial y} + \frac{1}{2} A_{22} \frac{\partial u}{\partial y} \frac{\partial^2 w}{\partial x \partial y} + \frac{1}{2} A_{22} \frac{\partial v}{\partial x} \frac{\partial^2 w}{\partial x \partial y} \right\} \\
& + \frac{(1 + \nu)}{Eh} \left[(A_{40} + A_{22}) \frac{\partial N^T}{\partial x} \frac{\partial w}{\partial x} + (A_{40} + A_{22}) \frac{\partial N^T}{\partial x} \frac{\partial w}{\partial x} + (A_{22} + A_{04}) \frac{\partial N^T}{\partial y} \frac{\partial w}{\partial y} \right. \\
& + 2(A_{31} + A_{13}) \frac{\partial N^T}{\partial x} \frac{\partial w}{\partial y} + 2(A_{31} + A_{13}) \frac{\partial N^T}{\partial y} \frac{\partial w}{\partial x} \\
& \left. + 4(A_{31} + A_{13}) N^T \frac{\partial^2 w}{\partial x \partial y} + \frac{(1 + \nu)}{Eh} q + \frac{(1 + \nu)}{Eh} F_{cuol} = \frac{\rho(1 + \nu)}{E} \frac{\partial^2 w}{\partial t^2} + \frac{\varepsilon\rho(1 + \nu)}{E} \frac{\partial w}{\partial t}; \right.
\end{aligned}$$

$$\begin{aligned}
& \frac{1}{1-\nu} \left[[A_{22}\nu + A_{04}] \frac{\partial^2 v}{\partial y^2} + \left[\frac{3}{2} A_{22} + \nu A_{04} \right] \frac{\partial^2 u}{\partial x \partial y} + \frac{1}{2} A_{13} \frac{\partial^2 u}{\partial y^2} \right. \\
& + [A_{31} + A_{13}\nu] \frac{\partial^2 u}{\partial x^2} + \left[A_{31}\nu + \frac{3}{2} A_{13} \right] \frac{\partial^2 v}{\partial x \partial y} + \left. \frac{1}{2} A_{22} \frac{\partial^2 v}{\partial x^2} \right] \\
& - \frac{l^2}{4} \left[\frac{1}{2} A_{20} \frac{\partial^4 v}{\partial x^4} - \frac{1}{2} A_{20} \frac{\partial^4 u}{\partial x^3 \partial y} + A_{11} \frac{\partial^4 v}{\partial y \partial x^3} \right. \\
& - A_{11} \frac{\partial^4 u}{\partial x^2 \partial y^2} + \left. \frac{1}{2} A_{02} \frac{\partial^4 v}{\partial y^2 \partial x^2} - \frac{1}{2} A_{02} \frac{\partial^4 u}{\partial x \partial y^3} \right] \\
& + \frac{(A_{22} + A_{04})(1 + \nu)}{Eh} \frac{\partial N^T}{\partial y} + \frac{(A_{31} + A_{13})(1 + \nu)}{Eh} \frac{\partial N^T}{\partial x} \\
& = \frac{\rho h(1 + \nu)}{Eh} \frac{\partial^2 v}{\partial t^2}.
\end{aligned}$$

The equation of thermal conductivity should be attached to the movement equations of the plate element. In the work, we will consider a three-dimensional stationary equation of thermal conductivity.

$$\frac{\partial^2 T}{\partial x^2} + \frac{\partial^2 T}{\partial y^2} + \frac{\partial^2 T}{\partial z^2} = 0 \quad (13)$$

To complete the differential task, we attach to the equations system (12–13), the boundary conditions for the rigid clamping of the plate

$$\begin{aligned}
w = u = v = \frac{\partial w}{\partial x} = \frac{\partial u}{\partial x} = \frac{\partial v}{\partial x} = 0 \quad \text{at } x = 0, c \\
w = u = v = \frac{\partial w}{\partial y} = \frac{\partial u}{\partial y} = \frac{\partial v}{\partial y} = 0 \quad \text{at } y = 0, b
\end{aligned}$$

zero initial conditions

$$w = \frac{\partial w}{\partial t} = 0 \quad \text{at } t = 0.$$

The boundary conditions of the first kind for the thermal conductivity equation (Dirichlet conditions—the function of heat distribution over the plate surface at any time is set)

$$T|_{\Gamma} = F_0$$

3 Numerical Experiment

To reduce the system of nonlinear partial differential equations to the system of ordinary differential equations by space variables, the finite difference method with the

$O(h^2)$ approximation was applied. The Cauchy problem was solved by the Newmark method. The solution of the static problem was obtained by the steady solution method [21].

Next, we will consider a rectangular plate consisting of two families of mutually perpendicular edges $\varphi_1 = 45^\circ, \varphi_2 = 135^\circ$. The plate is under the action of an electrostatic force. Geometrical and physical parameters of the plate: length $c = 0.5 \mu\text{m}$, width $b = 0.05 \mu\text{m}$, thickness $h = 0.003 \mu\text{m}$, distance between edges $\delta = 0.002; 0.003; 0.004 \mu\text{m}$, edge width $a = 0.003 \mu\text{m}$, dimension-dependent parameter $l = 0.001; 0.002; 0.003 \mu\text{m}$, distance from the plate to the electrode $g_0 = 0.003 \mu\text{m}$ and modulus of elasticity $E = 1 \text{ TPa}$, $T = 293 \text{ K}$, $\alpha_T = -3.7 * 10^{-6} \text{ K}^{-1}$.

Figure 2 shows graphs of the dependence of the deflection in the plate center on the potential difference $w(V)$ depending on the distance between the edges $\delta = 0.002; 0.003; 0.004 \mu\text{m}$ with a dimension-dependent parameter $l = 0.001 \mu\text{m}$.

Figure 3 shows $w(V)$ for different values of the independent additional length parameter $l = 0.001; 0.002; 0.003 \mu\text{m}$ with $\delta = 0.002 \mu\text{m}$.

Fig. 2 $w(V)$ depending on the distance between the edges from the mesh

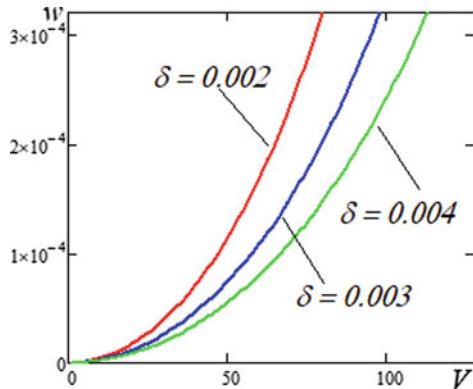
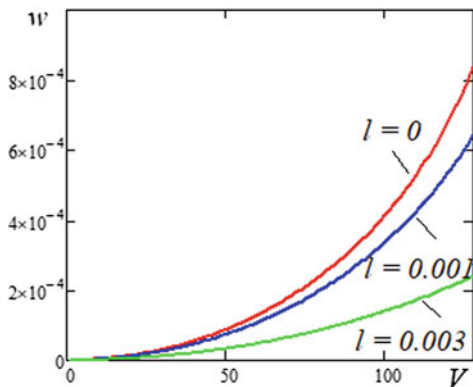


Fig. 3 $w(V)$ depending on the additional independent length parameter



When exposed to the same Coulomb force, the plate deflection decreases with an increase in the distance between the edges of the mesh. Also, the plate deflection decreases at fixed values of the electrostatic force and the mesh geometry with an increase in the value of an additional independent length parameter associated with taking into account higher-order moments in the model.

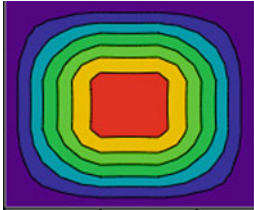
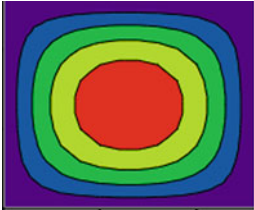
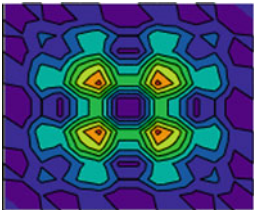
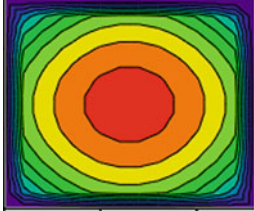
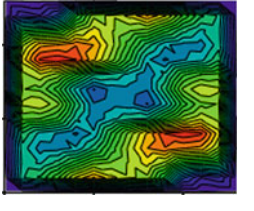
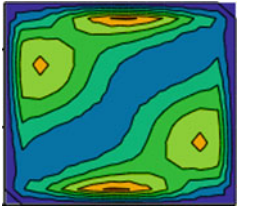
Consider the projections onto the plane XOY of deflections, forces and momentums for the square plate with geometric parameters: $c = b = 0.5 \mu\text{m}$, $h = 0.03 \mu\text{m}$, $\delta = a = 0.002 \mu\text{m}$, $l = 0.002 \mu\text{m}$ and distance from plates to electrode— $g_0 = 0.003 \mu\text{m}$.

In the absence of electrostatic field, the plate heated to $T = 300 \text{ K}$ has domed shape with flattened top. The maximum momentums values are contained in four vertices, which are located symmetrically about the plate center. Forces are distributed symmetrically about the plate center. Three local maxima located in the corner zone vicinity are clearly visible (Table 1).

When the plate is exposed to temperature ($T = 300 \text{ K}$) and electric fields with a potential difference $V = 130 \text{ V}$, the deflection surface also has a dome shape, the momentums surface changes its shape to dome shape, the forces surface are also symmetrical about the center, but two local maxima are visible (Table 1).

Thus, the electrostatic force significantly affects the plate stress–strain state in statics.

Table 1 Deflections surface, momentums surface and forces surface of the plate depending on the electrostatic force

Plate deflections $w(x, y)$	Plate momentums $\frac{M_{xx}+M_{yy}}{2}$	Plate forces $\frac{N_{xx}+N_{yy}}{2}$
T = 300 K, V = 0 B		
		
T = 300 K, V = 130 B		
		

4 Concluding Remarks

The statics and dynamics theory for a flexible nanoplate of a mesh structure under the electrostatic and temperature fields action is constructed.

It is revealed that an additional independent length parameter associated with the accounting of higher-order moments significantly affects the nanoplate deflection.

The electrostatic force significantly affects the plate stress–strain state.

The work was carried out with the support of the RSF № 22-21-00331.

References

1. Chuan, M.W., Riyadi, M.A., Hamzah, A., et al.: Impact of phonon scattering mechanisms on the performance of silicene nanoribbon field-effect transistors. *Results Phys.* **29**, 104714 (2021)
2. Altenbach, H., Eremeyev, V.A.: On the linear theory of micropolar plates. *ZAMM J. Appl. Math. Mech.* **89**(4), 242–256 (2009)
3. Yang, F., Chong, A.C.M., Lam, D.C.C., Tong, P.: Couple stress based strain gradient theory for elasticity. *Int. J. Solids Struct.* **39**, 2731–2743 (2002)
4. Norouzzadeh, A., Ansari, R., Darvizeh, M.: Isogeometric dynamic analysis of shells based on the nonlinear micropolar theory. *Int. J. Non-Linear Mech.* **135**, 103750 (2021)
5. Carrera, E., Zozulya, V.V.: Carrera unified formulation (CUF) for the micropolar plates and shells. I. Higher order theory. *Mech. Adv. Mater. Struct.* **29**(6), 773–795 (2022)
6. Sargsyan, A., Sargsyan, S.: Geometrically nonlinear models of static deformation of micropolar elastic thin plates and shallow shells. *ZAMM Zeitschrift fur Angewandte Mathematik und Mechanik* **101**(5), e202000148 (2021)
7. Zubov, L.M., Kolesnikov, A.M., Rudenko, O.V.: Exact solutions of nonlinear micropolar elastic theory for compressible solids. *Adv. Struct. Mater.* **110**, 771–798 (2019)
8. Varygina, M.: Numerical modeling of elastic waves in micropolar plates and shells taking into account inertial characteristics. *Continuum Mech. Thermodyn.* **32**(3), 761–774 (2020)
9. Krylova, E.Y., Papkova, I.V., Krysko, V.A.: Mathematical modeling of complex oscillations of flexible micropolar mesh cylindrical panels. *Russ. Phys. J.* **62**(9), 1649–1655 (2020)
10. Krysko, V.A., Awrejcewicz, J., Papkova, I.V., Krysko, V.A.: Chaotic vibrations of size-dependent flexible rectangular plates. *Chaos* **31**(4), 043119 (2021)
11. Mazur, O., Kurpa, L., Awrejcewicz, J.: Vibrations and buckling of orthotropic small-scale plates with complex shape based on modified couple stress theory. *ZAMM Zeitschrift fur Angewandte Mathematik und Mechanik* **100**(11), e202000009 (2020)
12. Sargsyan, S.O., Farmanyan, A.Z.: Thermoelasticity of micropolar orthotropic thin shells. *PNRPU Mech. Bull.* **3**, 222–237 (2013)
13. Partap, G., Chugh, N.: Thermoelastic damping in microstretch thermoelastic rectangular plate. *Microsyst. Technol.* **23**(12), 5875–5886 (2017)
14. Karimipour, I., Beni, Y.T., Akbarzadeh, A.H.: Size-dependent nonlinear forced vibration and dynamic stability of electrically actuated micro-plates. *Commun. Nonlinear Sci. Numer. Simul.* **78**, 104856 (2019)
15. dell’Isola, F., Steigman, D.: A two-dimensional gradient-elasticity theory for woven fabrics. *J. Elast.* **118**(1), 113–125 (2015)
16. Eremeev, V.A.: On a nonlinear model of the mesh shell. *Izvestiya of the Russian Academy of Sciences. Solid Mech.* **4**, 127–133 (2018)
17. Krylova, E.Y., Papkova, I.V., Saltykova, O.A., Krysko, V.A.: Features of complex oscillations of flexible micropolar mesh panels. *Izvestiya of Saratov University. Math. Mech. Inf.* **21**(1), 48–59 (2021)

18. Karman, T.: Festigkeitsprobleme in Maschinenbau. Encyklopädie der mathematischen wissenschaften **4**(4), 311–385 (1910)
19. Pshenichnov, G.I.: The Theory of Thin Elastic Mesh Shells and Plates. Nayka, Moscow (1982)
20. Hamilton, W.: Report of the fourth meeting. Br. Assoc. Adv. Sci. 513–518 (1835)
21. Krysko, V.A., Awrejcewicz, J., Komarov, S.A.: Nonlinear deformations of spherical panels subjected to transversal load action. Comput. Methods Appl. Mech. Eng. **194**(27–29), 3108–3126 (2005)

Verification of Wishbone Compliant SPI Using System Verilog



Aditya Yadav, Amit Gupta, Aadarsh Rana, and Aditya Kumar

Abstract In the growing age of technology, there are many capabilities with numerous IP cores that are being combined together on single silicon chip. Component-based validation of these complex SOCs have been very time consuming process. The present era is to have the preconfigured IP cores with their corresponding verification IP. These verification IPs are Self-reliant, adaptable, and also re-purpose validation module. This research is based on open verification methodology (OVM) and UVM-based environment for checking of the wishbone compliant SPI master–slave. A multi-dimensional testbench has been designed which is having a wishbone BFM, SPI slave model, driver, scoreboard, and assertions are been designed using different characteristics of System Verilog (SV) and the UVM library. The System Verilog Language is a very high level language designed by synopsis and it also supports object oriented programming and is easy to use and develop full verification environment The verification results give us the most effective and is suitable for the purposed verification environment.

Keywords UVM · SOC · SPI · Wishbone · TLM · Verification · BFM

1 Introduction

The improvement of cutting-edge incorporated circuits not just expanded the intricacy of IC plan yet additionally IC confirmation similarly testing. Spending 70% on confirmation, is basic way & decreasing time through mechanization [1]. Numerous conventions utilized for any distance correspondence reason, significant conventions are ETHERNET, USB, PCI-EXPRESS. SPI & I2C, utilized as brief correspondence conventions SPI, being sequential information correspondence convention that gives

A. Yadav (✉) · A. Gupta · A. Rana · A. Kumar
Department of ECE, Galgotias College of Engineering and Technology, Greater Noida, Uttar Pradesh, India
e-mail: adityayadav.18gcebec052@galgotiacollege.edu

A. Gupta
e-mail: Amit.gupta@galgotiacollege.edu

© The Author(s), under exclusive license to Springer Nature Singapore Pte Ltd. 2023
V. Bindhu et al. (eds.), *Proceedings of Fifth International Conference on Inventive Material Science Applications*, Advances in Sustainability Science and Technology,
https://doi.org/10.1007/978-981-19-4304-1_18

197

high unwavering quality, smallness and mistake free information transmission & gathering. SPI, created via Motorola [2]. Whole SPI correspondence is isolated among master to endlessly slave to ace divulgence. Convention regularly utilize onto intra chip correspondence. In SPI, master & slave perform double job of transmitter & beneficiary. Principal benefit appertaining to SPI convention speed being exceptionally lofty when contrasted with other conventions viz. I2C [3]. Rapid exhibition of SPI is conceivable in light of the fact that there is compelling reason entail to move slave addresses [4].

SPI has been executed by many organizations with a few furtherance. SPI convention having basic engineering, rapid information transfer and financially savvy execution generally utilized for associating circumferential to the microcontroller or one chip computer. SPI convention with few weaknesses as it does not have any specific tending to plan & it slacks in offering any stream away [5]. The Universal verification Methodology (UVM) comprises set of bases endlessly class library records utilized for the improvement of endorsement environment built & is a re-operable System Verilog in view of Verification environment.

In day-to-day life practically, normally a Microcontroller Core, each & every framework incorporates some insightful control. Universally useful circuits such as LCD drivers, EEPROM, distant I/O ports, RAM, or on the other hand information converters. Application-arranged circuits for correspondence interfaces as well as calculation escalated task. Hence the correspondence allying these modules is very crucial. In similar angle reuse of protected innovation macro-cells is turning into focal point of pull for plan efficiency and lead for having the option to deliver chips which truly work.

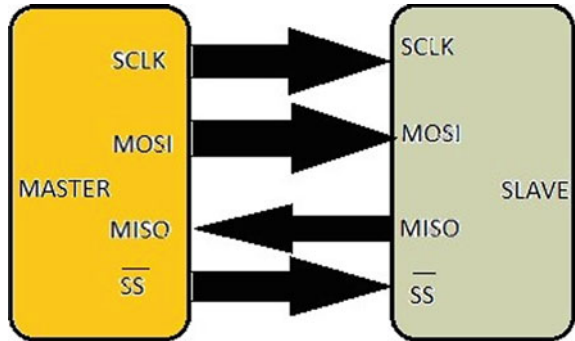
Every one of integrated parts should be associated one another & each SoC should be connected together in an effective manner which permits quick & error-free correspondence. The correspondence amid SoC is lead to allow superior exhibitions: most involved answer for associating SoC is the sequential transport which dispenses extraordinary superiority as far as expenses. With the improvement of the IC fabricating, the communication between equipment gadgets turned out to be especially significant. The currently broadly utilized conventions, for example, WISHBONE bus armistice, etc., let equipment gadgets convey via the arrangement of standards & meet the timing for accomplishing motivation behind trading information.

2 SPI

The Serial Peripheral Interface (SPI) erected by Motorola, is full two folded, coordinated & rapid transport conveying protocol. Its convention utilized in hasty distance correspondence, essentially in drive in structure. Ordinary applications incorporate sensors, cybernated cards, Secure, and liquid precious stone presentation [6].

Figure 1 conveys the illustration of SPI & SPI bus comprises 4 signals: serial clock yield from master & slave selects result from master, MOSI in formation Interface yield from master, (MISO) information yield through slave. SPI accompanies within

Fig. 1 Serial peripheral



solitary master gadget & higher than one slave gadgets. It works in four unique modes, in light of the information sending and getting mutining or falling edge of the sequential clock [7].

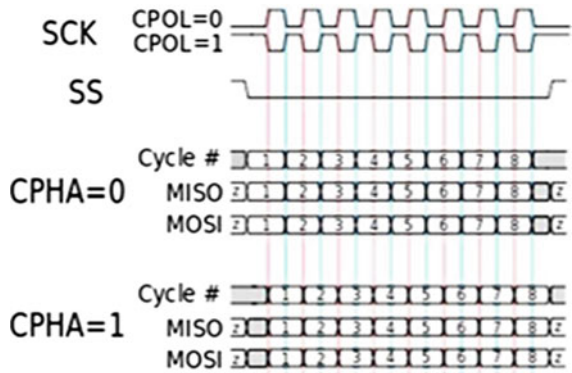
- Master Out Slave In (MOSI)—This is sole bit signal created via ace in view of interior change within shift register available in the Master gadget, this is single bit signal.
- Master In Slave Out (MISO)—This is an individual piece of signal produced via slave in time of moving shift register substance to expert gadget.
- Serial Clock (SC_LK)—The showing dash-line is sequential clock. These signal co-occurring the transmission.
- Slave Select (SS_bar)—The available line is slave select line; dynamic stunted sign utilized via ace gadget to designate specific
- Slave to began transmission.

3 SPI Data Transmission

Clock duality & clock’s stage being significant criterion, maneuver to characterize clock organization to be utilized by SPI bus. Its extremity is utilized to decide condition of clock. In the event that first state as 0 makes polarity as 0 & first state becomes 1 & polarity is 1 [8].

Modes in SPI: The information trade characterized by 2 boundaries, clock extremity (CPOL), & clock stage (C_PHA). Figure 2 briefs circumstance graph about SPI Modes it comprises four vogues.

Fig. 2 Timing representation of SPI modes



3.1 Different Modes of Transmissions

- **Mode 0:**

The information should be acquired prior to muting periphery of initial clock signal. Inactive clock plight is zero & MISO & MOSI lines information should be ordinary stint clock indicator is high & can be commuted when the clock indicator is low. The information is caught on low-to-high clock change & produced on high-to-low clock change.

- **Mode 1:**

Information should be gotten preliminary to mutining contour of main clock signal. Inactive clock plight is zero & MISO & MOSI lines information should be ordinary during clock signal being down & can be altered whenever clock signal is high-enough. Information is caught upon high-to-low clock signal change & produced on low-to-high clock signal progress.

- **Mode 2:**

Information should acquire preparatory to descending periphery of principal clock signal. Inactive clock state is 1 & MISO & MOSI lines should be ordinary stint clock signal is low & can be altered whenever clock signal is high. Information is caught upon high-to-low clock signal change & created on low-to-high clock progress.

- **Mode 3:**

Information should be gotten ahead of descending periphery of main clock signal. Inactive clock state is one, MISO & MOSI lines information should be typical while clock is high & it can be altered when clock signal is low. Information is caught on low-to-high clock signal change & created on high-to-low clock signal progress. Master and slave of SPI owns shift register when expert needs to send the information to the slaves.

4 Wishbone Bus Interface

The WISHBONE System-on-Chip (SoC) alliance Architecture for Compact IP Cores is an adaptable plan strategy for employ with semiconductor IP centers [9]. Its motivation is to quicker configuration reuse by mitigating Framework on-Chip mix issue (Table 1).

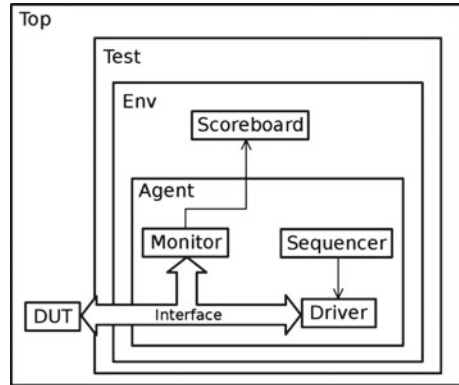
The primary goals of this particular are to make an adaptable interconnection implies for use with semiconductor IP centers. This permits different IP centers to be associated together to shape a System-on-Chip and to make WISHBONE interfaces free of rationaleflagging levels. WISHBONE utilizes an Ace/SLAVE design. That implies that practical modules with MASTER interfaces start information exchanges to taking part SLAVE interfaces. The MASTERS and SLAVES convey through an interconnection interface called the INTERCON. The cloud is considered best for an INTERCON as it has circuits [10]. The above-mentioned circuits permit MASTERS to connect with SLAVES. Following referenced are wishbone interfaced signals which are utilized for our Serial-Fringe-Interface correspondence.

The [clk_i] clock input is mobilized to the revolting boundary, all inside WISHBONE rationale. Thus, master clock chooses information is to be send or not. The reset input [rst_i] powers the center to restart which is dynamically low offbeat. The hinder demand yield is affirmed when center necessities administration from a host framework. Whenever declared, cycle input [cyc_i] demonstrates a legitimate transport cycle is underway. The intelligent AND capacity of [cyc_i] &

Table 1 Wishbone interface signals

Port	Width	Direction	Description
wb_clk_i	1	Input	Master Clock
wb_rst_i	1	Input	Synchronous reset, active high
wb_adr_i	5	Input	Lower address bits
wb_dat_i	32	Input	Data toward the core
wb_dat_o	32	Output	Data from the core
wb_sel_i	4	Input	Byte select signals
wb_we_i	1	Input	Write enable input
wb_stb_i	1	Input	Strobe signal/Core select input
wb_cyc_i	1	Input	Valid bus cycle input
wb_ack_o	1	Output	Bus cycle acknowledge output
wb_err_o	1	Output	Bus cycle error output
wb_int_o	1	Output	Interrupt signal output

Fig. 3 UVM Testbench architecture



[stb_i] demonstrates a legitimate exchange cycle to the core. Thus whenever the cycle input is in high strobe indicator is also in high. When the center is being tended to, the strobe input [stb_i] is attested. Center just answers WISHBONE cycles, when [stb_i] is declared, with an exception of the [rst_i], which continuously get a reaction. The location cluster input [addr_i] is employed to elapse a twofold address deeply [11].

The most critical piece is at on the bigger side of the cluster. When affirmed, the compose empower input [we_i] shows that the current transport cycle is compose cycle. When invalidated, hows that the current transport cycle is an erstood cycle [12]. The information cluster input is utilized to pass double information the current WISHBONE (Fig. 3).

5 System Verification

Universal Verification Methodology (UVM) is a chip of base class System Verilog in view of verification environment.

5.1 UVM Testbench

UVM testbench includes of sequencer, sequence item, driver, test suite, agent, scoreboard, and environment.

Top Testbench: Testbench includes launches of DUT modules and points of interaction that associate DUT with testbench. Exchange Level Modeling (TLM) interfaces in UVM are an extraordinary asset to carry out correspondence work calls for communicating and getting exchanges among modules.

Test: Test part is a class under testbench. Normal errands acted in this are applying the boost to DUT by conjuring groupings, designing qualities in config class. Test class launches high level environs.

Environment: Environment is an exploitable part class which totals scoreboards, specialists also, other UVM check conditions at the same time.

Agent: The Agent as found in the above outline totals a few confirmation parts like sequencer, driver and screen. Specialists can likewise incorporate parts like convention checkers, TLM model, and inclusion gatherers.

Sequence Item: An arrangement thing is an article demonstrating the stack of info sent between two parts at times alluded to as an exchange in the UVM progressive system. It is composed expanding succession thing class.

Sequence: A Sequence is the item which is utilized to produce a bunch of arrangement things to be shipped off the driver.

Sequencer: Sequencer extracts succession things via arrangements produced & accords it to the driver. Sequencer and driver apply TLM interface works to be specific seq thing trade also, seq thing import to interface with each other.

Driver: A Driver is an item that drives DUT pins in view of arrangement things got through the sequencer. It changes over groupings into bitwise values & drives information onto DUT pins.

Monitor: The Monitor grasps DUT bit level qualities what's more, changes them into grouping things that demand over to be conveyed to next UVM parts like the scoreboard inclusion classes. Screen utilizes investigation port for this reason, furthermore, it plays out a transmission activity.

Scoreboard: The Scoreboard executes assayer performance. The assayer coordinates reaction of DUT with the anticipated reaction. It brings a normal reaction through a reference module and gets yield exchanges via the screen.

6 SPI Master & Slave Working

In on excelled SPI correspondence, clock signal (S _ CLK) by way of transport from master to ship off every slave. Every SPI signal can be attended through the present clock signal (Fig. 4).

The number of slave gadgets have, master gadget will have the number of determination signal that are utilized to choose slave gadgets. As of late broadly utilized SPI gadgets are redone by coordinated as an alternative one-to-additional. Within norm SPI, master gadget should have numerous CS signals in the Manifold gadget correspondence. Single-master correspondence which implies multiple master gadget interface with the slave gadget is stringently denied.

Within work mode, a master gadget interface in the company of at least 1 slave gadget, this cannot be replaced right now. Different gadgets need to manage slave gadget that has been constrained by an alternative master gadget, this should break off master device's operation 1st & separate with it, then, at that point, associate with the new gadgets. Along these lines, a master gadget can select various slave

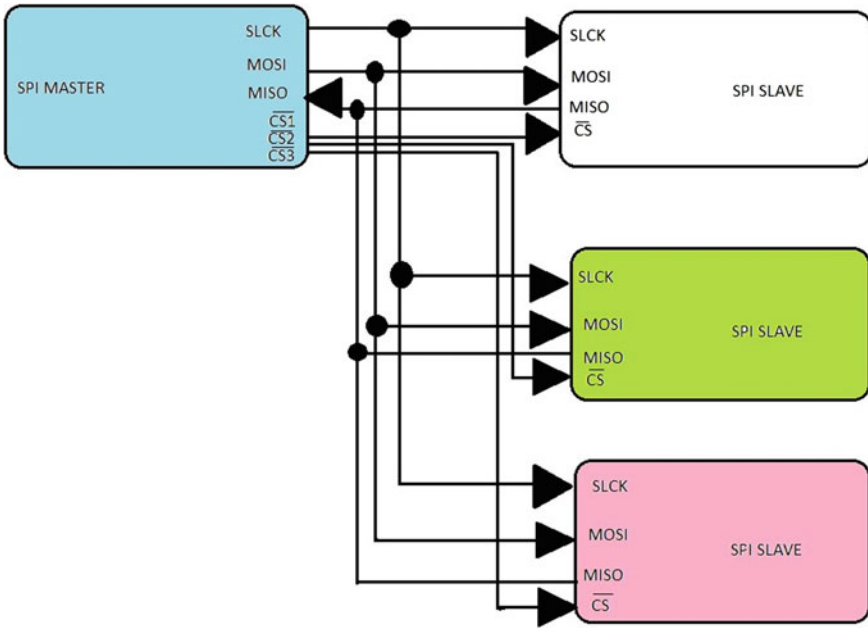


Fig. 4 SPI Multi-device correspondence schematic

gadgets do not need to append additional chip select pins & various master gadgets shall utilize TSM through degree of correspondence need to manage a similar slave gadget without to quit functioning (Fig. 5).

So widespread various gadgets SPI interface IP is more adaptable and successful to remit information of 32 digit, LSB's bit chosen and get off from master to slave, the piece goes to MSB locale & simultaneously slave goes about as left haul register.

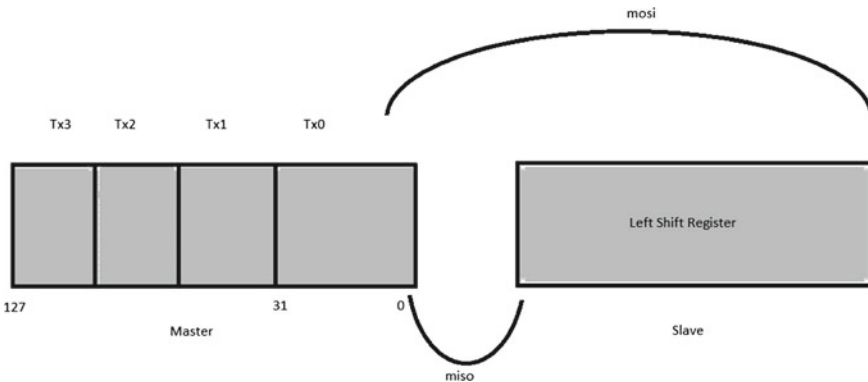


Fig. 5 Operation between master and slave

This is termed as Master Out Slave In (MOSI). Simultaneously LSB bit in slave goes to LSB bit of master. This is yelled as Master in Slave Out (MISO).

The division factor is configurable. The Master Out Slave- In line is the strip line sequential information alert. It is a result from master gadget and a contribution to a slave gadget. The Master in Slave Out line is strip lined sequential information signal. This is a result from slave gadget & a contribution to master gadget.

7 Verification Plan

Re-enactment and confirmation are a vital piece of center plan, since it straightforwardly connected with the accessibility of IP. We re-enact the plan by modalism & do check utilizing framework Verilog language. To confirm SPI information transference the haphazardlyzed sign of wishbone interface, control register, divider register and slave register are created by calling framework inbuilt haphazardlyze function. It is finished by Generator.

The driver a piece of check manages the setup of a few registers which are utilized in information transmission. First and foremost, Slave select register is arranged to choose slave registers of collector. Besides, divider register is designed to produce sequential clk through wb_clk_in of wishbone interface. Thirdly, control register of SPI center is designed to communicate information relying upon character length, LSB, Tx_Neg and so forth boundaries influencing information transmission. For information transmission, the eighth piece of control register “Go_busy” is to synchronize “1” after register configuration. Two occasions are set off one after ss arrangement and one after information conveyancing. The collector a piece of confirmation manages driving of MISO relying upon various occasions. The master information & slave information of scoreboard part manages comparison check. The inclusion replica of our plan comprises a few shield focuses & cross shield focuses that actually looks at all potential situations of information boundary which are influencing information transmission.

To confirm SPI Convention, we have utilized 2 unique sorts of experiments, these are: Directed Test Case & Relapse experiment. Over coordinated experiment, we are giving pre-planned upgrade with expected imperative to confirm anticipated result. In relapse experiment, we are broadening transactor class to various youngster classes where we can compel unlike info boundaries to really look at all potential samples (Fig. 6).

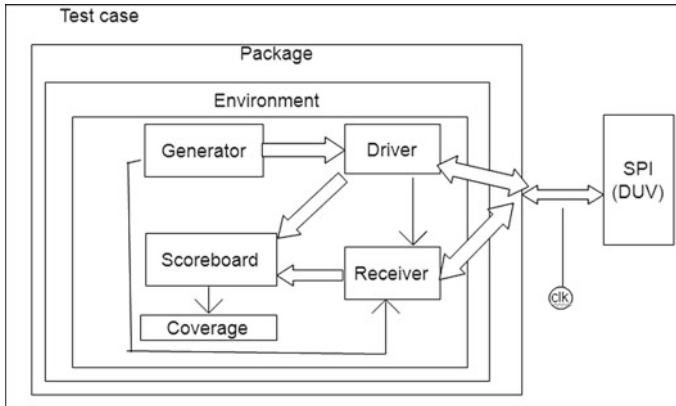


Fig. 6 Verification methodology in system

8 Results

8.1 Testbench Components

The SPI master core is being validated in accordance to SPI slave model. At first, the SPI master and slave are being configured suitably. The Basic idea behind is the verification and to send the data via both master to the slave ends. And when data is transmission is completed it validated the sending and receiving of data at there particular ends.

Test Top

The top-level module is superintend for combining the testbench module with the DUT. In this module it is responsible for the instantiation of two interfaces, one is the master and another slave. And then the master interface is wired with the SPI master core and same as slave interface with SPI slave model. Finally, the module calls the run_test function which begins to run the uvm_root.

- **spi_interface**

The interface block communicate with WISHBONE slave logic signals. The transmission between master and slave core take place with WISHBONE BFM.

- **spi_test**

The test class produced by extending the uvm_test class. Build phase, the lower level SPI environment class is made and composed.

- **spi_environment**

SPI environment is the box inside having agent and scoreboard. And is made use of uvm_env virtual foundation class. In the put up phase module inside the environment are combined together and instantiated. In the connect phase, the connections are made between the module (Fig. 7).

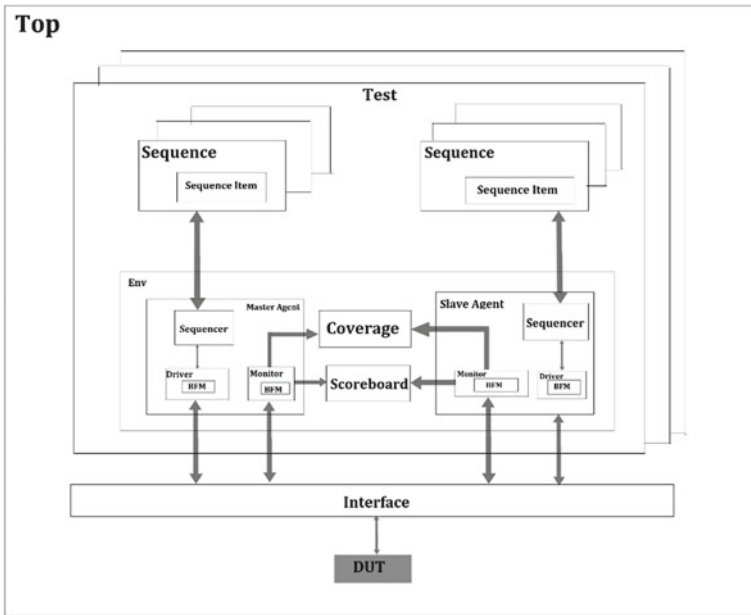


Fig. 7 UVM ARCHITECTURE

- **spi_agent**
Presently, inside the environment there is only one agent box component inside the project. The SPI agent module is composed as an active module.
- **spi_sequence_item**
The data flows inside testbench from module to module in the structure of package called as transaction class or the sequence item.
- **spi_sequence**
The self-declared SPI sequence class utilize uvm_sequence as its virtual base class. This class is restricted class with some parameter being the SPI sequence item associated with this particular class.
- **spi_sequencer**
SPI sequencer is the module which is responsible for the running of sequences. The sequencer is having built-in port called sequence_item sends for the transmission with the driver.
- **spi_driver**
SPI driver is a module accompanied by WISHBONE BFM which takes the processed sequence item from the sequencer and it makes the between DUT with reference to WISHBONE protocol.
- **spi_monitor**
SPI monitor recognizes the coming feedback from the DUT. In accordance to check the data, virtual interface handle sends to the monitor during the build phase. The monitor is made using extending uvm_monitor.

- **spi_scoreboard**
- The SPI scoreboard is a module that includes transaction level checkers as well as coverage collectors. To determine whether our DUT is functionally correct. TLM examines FIFOs in order to join the monitor. The input packet is recovered from the driver during the run phase, while the output packet is recovered from the monitor.
- **wishbone_bfm**

The WISHBONE BFM on the driver side sends transaction level packages within the WISHBONE specific pin level data.

8.2 Testbench Results

The verification environment having main aim to design a functional verification environment for SPI Protocol.

- **Data Transactions**

The results shown in the below table configuration for a regression run of many test cases (Table 2).

WISHBONE to SPI Master Communication using BFM

The correspondance in the mid of the WISHBONE SPI master is made using the WISHBONE BFM. The main motive behind this project is read, write, and reset functionalities w.r.t.WISHBONE B.3 protocol (Fig. 8).

Table 2 Data transactions

Data transmission	Transmit	Transfer	Collect
32 Bit	MSB	posedge	negedge

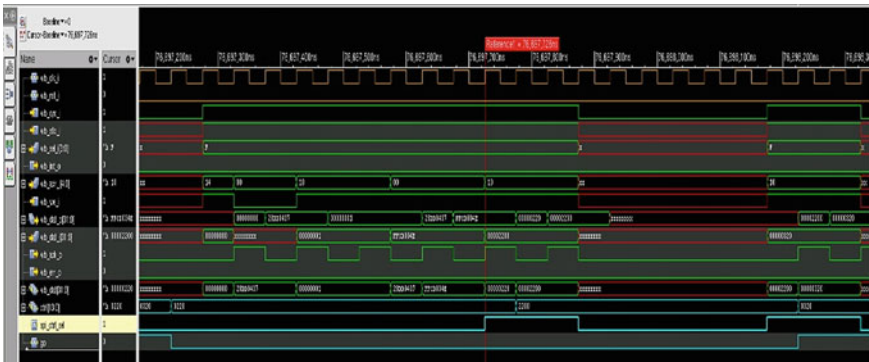


Fig. 8 Wishbone to SPI master communication

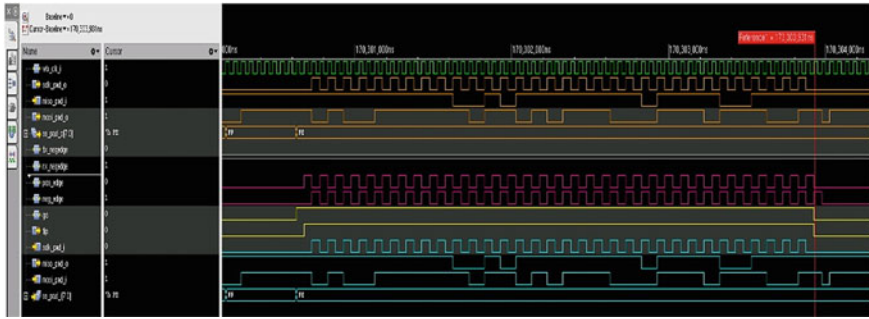


Fig. 9 SPI Master–slave communication

• **SPI Master–Slave communication**

The transmission between the master and slave is coincide to sclk_pad clock, that is again coincide with the wb_clk base clock. Prior the start of the transmission, they are being configure, i.e., the master and slave to the control register. Control register is having flags like tx_nedge/rx_posedge, that is responsible for checking the sampling edge is responsible to check the sending and receiving of signal (Fig. 9).

9 Conclusion

The given research paper, a repupose System Verilog having UVM environment that has been made for the transmission of data from master to slave.

The verification environment is made around the WISHBONE SOC bus and then is makes the core IP, and verification IP very comfortably to join together The testbench makes us easy to combine both and we can aslo easily validate the full duplex data transmission of the data packets between the master and slave easily.

An SPI slave model has been made more feasible and the SPI master core verification to be more reliable. In addition, a WISHBONE BFM was successfully created to make a full fledged bridge between both of them the testbench modules and the DUT. The WISHBONE BFM gives us the basic read and write functionalities.

References

1. Kamireddy, L.S.: UVM Based Reusable authentication IP for Wishbone Compliant SPI Master Core. Int. J. VLSI Design Commun. Syst. 28 Sept 2018
2. Ashok Kumar K.V.: Design & functional authentication of SPI master-slave-core via UVM. Int. J. Sci. Eng. Technol. Res. **04**(51) (2015)
3. Harika, G.: Development of reusable authentication environment for SPI protocol. Int. J. Sci. Eng. Technol. Res. **04**(28) (2015)

4. Salah, K.: A UVM-based smart functional authentication platform: concepts, pros, cons, and opportunities. In: 9th International Design and Test Symposium (2014)
5. Oudjida, A.K.: Design & test of general-purpose SPI Master/Slave Ips on OPB bus. In: 7th International Multi-Conference on Systems, Signals and Devices (2017)
6. Pavithran, T.M.: UVM Based Testbench architecture for logic sub-system authentication. In: IEEE International Conference on Technological Advancements in Power & Energy (2018)
7. Jain, A.: Early development of UVM based authentication environment of image signal processing designs using TLM reference model of RTL. *Int. J. Adv. Comput. Sci. Appl.* **5**(2) (2014)
8. Polsani, P.: Design & authentication of serial peripheral interface(SPI) protocol. *Int. J. Recent Technol. Eng. (IJRTE)* **8**(6) (2020)
9. Gayathri, M.: A SV-UVM framework for Authentication of SGMII IP Core with exploitable AXI to WB Pass Over UVC. In: 3rd International Conference on Advanced Computing and Communication Systems (ICACCS-2016), 22 Jan 2016
10. Roopesh, D.: RTL design & authentication of SPI Master-Slave using UVM. *Int. J. Adv. Res. Electron. Commun. Eng. (IJARECE)* **4**(8) (2015)
11. Vitankar, P.S.: UVM architecture for authentication. *Int. J. Electron. Commun. Eng. Technol. (IJECET)* **7**(3) (2016)
12. Kulkarni, A.: UVM methodology based functional authentication of SPI Protocol. In: National Science, Engineering & Technology Conference (NCSET) (2020)

Design and Simulation of MEMS-Based Two-Directional Capacitive Pressure Sensor



Yellapragada V. S. Sasank, Chennam J. V. K. Sathya Swaroop,
Ghanta Sriram, Satyajeet Sahoo, and M. Taj

Abstract In this paper, MEMS-based pressure sensor is designing using a parallel plate capacitor which can be broadly applied in the electronic technology enhancement circles, increase in pressure tends to equivalent increase in capacitance or reduction in the dielectric value. So, by varying pressure, the respective capacitance can be changed, the individuality of our design gives the analysis of change in capacitance with the respective increase in pressure along with displacement of the proof mass and combs can also be observed by stimulating COMSOL Multiphysics software our design will give more capacitance compared to the other proposed design which we proposed and our design has a huge range of application from jets to measuring the pressure.

Keywords Pressure · MEMS · COMSOL Multiphysics · Two-directional

1 Introduction

Micro Electromechanical Systems (MEMS) is a type of technology by which can extract various types of inputs and has wide range of applications in diverse sectors like: Automobiles, Industries and Biomedical. MEMS-based capacitive pressure sensors is to measure the change in capacitance by applying pressure of certain pascals on the proof mass which is an external force, and it can be used in the various types of systems like modern drone applications, industrial operations, military applications and biomedical applications [1–4].

For the present study, COMSOL Multiphysics® is a tool used for the design and simulation. It is a special software and is a platform for Multiphysics simulation using Finite Element Method (FEM) and with physical models. This software tool consists of many modules like Body, Fluid, Chemical for solving many unsolved issues and it also consists of solid mechanics this will give the stress analysis and

Y. V. S. Sasank · C. J. V. K. Sathya Swaroop · G. Sriram · S. Sahoo · M. Taj (✉)
Department of Electronics and Communication Engineering, Vignan's Foundation for Science
Technology and Research, Vadlamudi, Andhra Pradesh, India
e-mail: mdtaj405@gmail.com

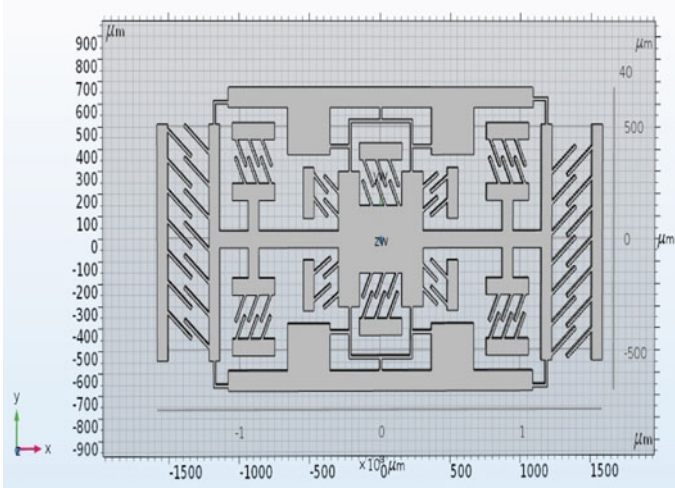


Fig. 1 Structure without air block

flow in solid this two physics solve the different problems in the designed sensor [5–8].

The present 2-dimensional capacitive pressure sensor design will sense pressure applied in two dimensions. When any external pressure is applied on the two dimensions. When external pressure applied to the device angular, linear displacement occur movement occurs 2 dimensionally in the sensor. This results in change in relative area between the electrodes of the capacitors in the device. This results in capacitance change with the help of two parameters. In this paper, stress analysis, capacitance and pressure measurement of the device will be described [9–12].

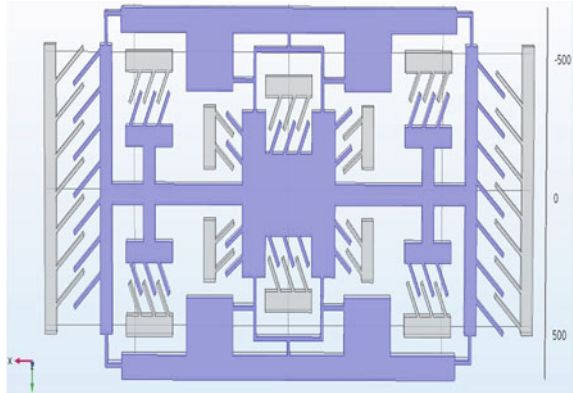
2 Design Concepts

The design has two sets of electrodes to act as capacitance, proof mass is the crux of the design. Where the total pressure is applied on the proof mass capacitance change occurred in the various positions of the design. Polysilicon (Si) are used as sensor material because of its mechanical stability in the fabricated devices of micro electromechanical sensors (Fig. 1).

3 Design of Electrodes

There are electrodes in this design on the inner side of the Base Substrate. Which are used to sense the mechanical changes happens within the design (Fig. 2).

Fig. 2 Enable electrodes in the design



As the area increases the capacitance increases.

$$C = E0A/d \tag{1}$$

The capacitance c_1 that is given in Eq. (1) is used to measure the capacitance between the plates. The parallel plate capacitance will depend on the following parameters: permittivity of the air, dielectric permittivity, area of cross section and distance between two plates.

$$c_1 = \frac{KA}{d} \tag{2}$$

where K is product of air and dielectric permittivity, A is area of cross section and d is distance between two plates. All the remaining capacitances of $c_{2..8}$ is also same as c_1 . Thus, the acceleration depends upon the change of capacitance that depends on the applied momentum.

4 Measurements of Displacement

The displacement is defined as the change in position of an object are the vectorial sum of the distances travelled by the body. The standard unit of displacement in the international system CF units is the kilometre, SI units is metre, CGS is centimetre.

SIMULATION PROCESS USING COMSOL

The simulation process in COMSOL Multiphysics based on the following steps: Selection of physics, Geometry design, Meshing and computation of study. The selection of physics will be determined based on user requirement and the type of step analysis. The selection of study is based on the requirements of the user. Here we study

the stress and capacitance of the materials. Design can be done on the work plane and our design is based on 2-dimensional and this software also supports 3-dimensional and various structures. The COMSOL Multiphysics® supports different kinds of materials such as Metals, Insulators, Semiconductors, Biomaterials and Liquids. If our desired material is not present in library, we can design our own material with material property. This software supports the following physics: It supports the Finite Element Method to simulate the corresponding device. It allows the mathematical analysis. And it simulates the partial differential equations. So, user can use the physics which will be suitable for the device. Meshes on the design is needed to track the changes in the design on applying external forces in very closed manner. Meshes are various types: They are tangential, finer, extra finer and coarse etc., which will be provided with the tool. The computation of study supports the different inputs to the proof mass such that desired results can be obtained for applying the different data analysis to the device. The COMSOL Multiphysics analysis are the 1-Dimensional, 2-Dimensional and 3-Dimensional characteristics with multiple expressions. The user can choose the multiple parameters like surface, points, or boundaries, etc. Here we adopted for the 3-dimensional approach based on our requirements.

5 Simulation Results

Total displacement (Fig. 3)

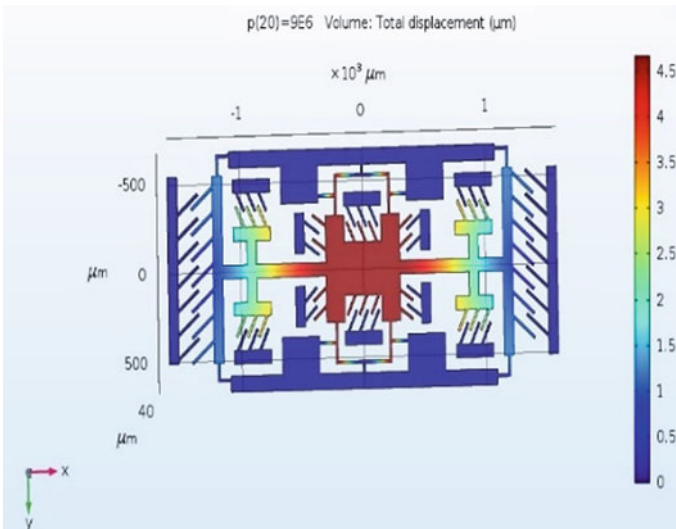


Fig. 3 Total displacement of proof mass

This analysis provides the information of displacement that occurs in the proof mass. The angular displacement is to be measured by either clockwise or anticlockwise direction. And linear displacement is measured along with x and y-direction. The angular displacement analysis is shown in (Figs. 3 and 5). The maximum angular displacement is 4.5×10^{-6} m. Figure 4 shows the surface capacitance for one set of electrodes. Then the value of a capacitance c_1 is 00.39pf (Table 1).

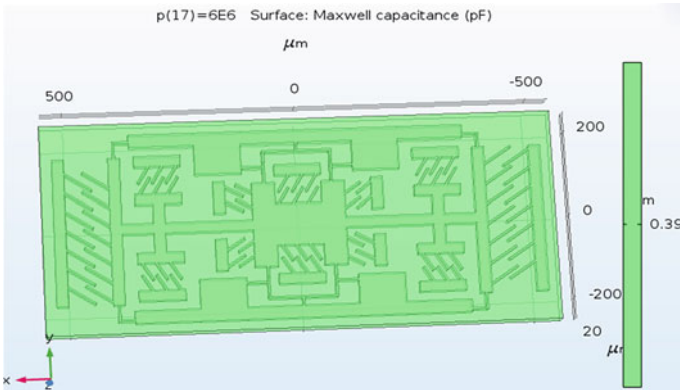


Fig. 4 The surface capacitance of a single electrode

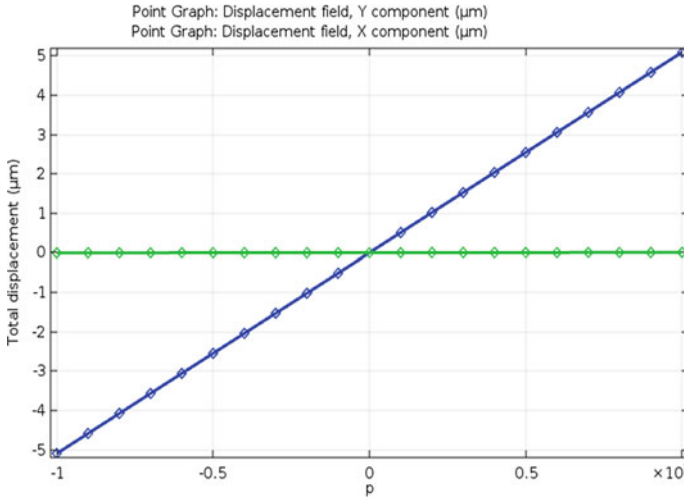


Fig. 5 Displacements versus pressure

Table 1 Measured parameters

S. No	Parameter	With zero displacement	With maximum displacement (pf)
1	Capacitance	0	0.39
2	pressure	0	4.5 μm

6 Conclusion

A new design approach demonstrated for MEMS inertial sensor, with capacitive electrodes. This structure has an eight set of electrodes, which supports to measure multi-directional inertia. High sensitivity for device can be used to determine the possible direction of moment. The simulation is done using the COMSOL Multiphysics®, which is a platform for designing and simulating multi-disciplinary domains. Stress and displacement analysis provide information on the rotational momentum of the proof mass. Then angular acceleration measured with suitable formulations and then capacitance and acceleration parameters are tabulated with boundary conditions. Finally, this design will be suitable to enhance the performance for further simulation of integrated rotational-linear inertial sensors in future.

References

1. Shettar, V., kotin, S.B., Kirankumar, B.B., Sheeparamatti, B.G.: Simulation of different MEMS pressure sensors. *Int. J. Multidiscipl. Res. Adv. Eng. (IJMRAE)* 6(II), 73–81 (April 2014). ISSN 0975-7074
2. Kumar, A., Periasamy, C., Pant, B.D.: Cantilever based MEMS pressure sensor using different piezoelectric materials: a comparative study. *Int. J. Eng. Dev. Res. IJEDR* 2(4). ISSN: 2321-9939 (2014)
3. Kutis, V., Dzuba, J., Paulech, J., Murin, J., Lalinsky, T.: MEMS Piezoelectric pressure sensor—modelling and simulation. *Service Sci. Direct Procedia Eng.* **48**, 338–345 (2012)
4. Ahmadzadeh khosroshahi, N., Karamdel, J.: Simulation and analysis different mems pressure sensor uses comsol multiphysics. In: National Conference on Interdisciplinary Researches in Computer, Electronics, Mechanic and Mechatronic Engineering, June 2016
5. Sahoo, S.: Conduction and switching behavior of e-beam deposited polycrystalline Nb2O5 based nano-ionic memristor for non-volatile memory applications. *J. Alloy. Compd.* **866**, 158394 (2021)
6. Sahoo, S., Prabakaran, S.R.S.: Nano-ionic solid state resistive memories (re-RAM): a review. *J. Nanosci. Nanotechnol.* **17**(1), 72–86 (2017)
7. Chen, D., Hang, M., Chen, K., Brown, K., Zhang, J.X.J.: Piezoelectric PVDF thin films with asymmetric microporous structures for pressure sensing (2015). *IEEE* 978-1-4799-8203-5/15
8. Chen, D., Sharma, T., Zhang, J.X.: Mesoporous surface control of PVDF thin films for enhanced piezoelectric energy generation. *Sens. Actuators A* **216**, 196–201 (2014)
9. Antonio, J.: Analytical and experimental investigations of high-resolution MEMS pressure sensors, Major\ qualifying project. Mechanical Engineering Department, Worcester Polytechnic Institute, Worcester MA (2006)
10. Sahoo, S., Manoravi, P., Prabakaran, S.R.S.: Titania based nano-ionic memristive crossbar arrays: fabrication and resistive switching characteristics. *Nanosci. Nanotechnol. Asia* **9**(4), 486–493 (2019)

11. Kameierski, T.J., Beeby, S.: Energy Harvesting Systems: Principles, Modeling and Applications. Springer science, Berlin, Heidelberg (2011)
12. Yadollah, H., et al (2011) Evaluation for diaphragm's deflection. Arab J. Inf. Technol. **8**(2) (2011)

Memristor and Its Modelling: A Review



Deneyaz Shaik and Satyajeet Sahoo

Abstract This paper provides an overview of memristor methodology, starting from the definition and formulation of memristor progressing through implementation and contemporary literature. Numerous researchers have suggested several modelling methods as well as window functions to analyse the characteristics of memristor device. These models include nonlinear, linear, VTEAM, and TEAM along with different window functions. To handle the boundary issues, various window functions came into existence. From neuromorphic to memory systems, a memristor can be employed in a wide range of scenarios. In comparison with other devices, this device's distinctive features, such as better scalability, non-volatility, compatibility, and minimal feature size, made it more effective. This paper presents a comprehensive description and analysis of the memristor models relying upon their I-V curve.

Keywords Memristor modelling · Window functions · Memristor devices · I-V curve · Non-volatility

1 Introduction

In the year 1971, Professor Leon Chua invented the fourth fundamental circuit element at the University of California, Berkeley [1]. Chua named this element as memristor (memory + resistor). However, the first conception and proposal of memristor were given in the year 1960, by B. Widrow from Stanford University, California [2]. Before the invention of the memristor, three other basic elements inductor, resistor, and capacitor were in existence. After the invention of the memristor, a fourth element was added. Chua designed this fourth element in order to track down the connection in between charge and flux. Memristor has some different

D. Shaik · S. Sahoo (✉)

Department of Electronics and Communication Engineering, Vignan's Foundation for Science, Technology and Research (Deemed to Be University), Vadlamudi, Guntur, Andhra Pradesh 522213, India

e-mail: drss_ece@vignan.ac.in

and unique properties from the properties that are exhibited by those three elements. Even while no physical memristor has been identified without a power supply at the time, Chua claimed that several laboratory models have been produced using active circuits. After that, there has not been any effort in this field for a long time. Stan Williams and his associates at Hewlett Packard Laboratories (HP) made a notable discovery concerning the physical design of memristors in the information and quantum systems (IQS) division in 2008 [3]. Stan Williams and his team developed the first memristor and demonstrated that memristance occurs naturally in nanoscale systems using a simple analytical example.

The relation between the charge (q) and flux (φ) is

$$\varphi = fq \tag{1}$$

$$V = \frac{d\varphi}{dt} \Rightarrow \varphi = \int v dt \tag{2}$$

$$\Rightarrow v = \frac{d}{dt} f(q) = \frac{df(q)}{dq} \cdot \frac{dq}{dt} = M(q) \cdot i(t) \tag{3}$$

$$w(t) = \left(R_{on} \frac{w(t)}{D} + R_{off} \left(1 - \frac{w(t)}{D} \right) \right) i(t) \tag{4}$$

$$w(t) = \mu_v \frac{R_{ON}}{D^2} q(t) \Rightarrow M(q) = R_{OFF} \left(1 - \mu_v \frac{R_{ON}}{D^2} q(t) \right). \tag{5}$$

As indicated in Fig. 1, to characterize the connection between flux (m), voltage (v), electrical charge (q), and current, Leon Chua acknowledged that there should be a fourth element called memristor. These four elements can be combined in the following six ways to form the six combinations [4].

- The equation for the current (i) is $dq = idt$; obtained from the relation between time and charge

Fig. 1 Relationship between the four fundamental elements

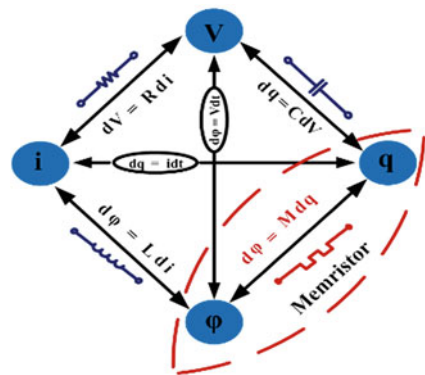


Fig. 2 Symbol of a memristor



- The mathematical expression for voltage (v) is $\mathbf{d} = \mathbf{v}dt$; taken from the relationship between flux and time.
- The expression for resistance (R) is given as, $\mathbf{d}v = Rdi$;
- $\mathbf{d}q = Cdv$ is the derivation of capacitance (c) obtained from voltage and charge
- $\mathbf{d}\phi = Ldi$ is the expression for inductance (L) attained by flux and current;
- Finally, $\mathbf{d}\phi = Mdq$ from Chua's suggested relationship between charge q and flux.

2 Memristor Description

2.1 What is a Memristor?

The term 'memristor' derives from the words 'memory' and 'resistor'. It is a passive element with two terminals and here, the resistance is regulated by the device's internal state. The two terminal devices are known as memristive devices. Because of the memristor's non-volatile memory capabilities [5], numerous scientists have used it in analogue, digital, and digital information processing applications, as well as memory and logic applications [6–10] (Fig. 2).

In such type of devices, by controlling the flow of electrical charge or flux, the nonlinear resistance can be memorized. The amount and direction of electricity flowing through this device determine its resistance. When current travels in one way through the device, resistance tends to increase. If the current moves in another direction, then there will be a reduction in the resistance. When there is no current flow the last value of the resistance will be kept. It is a basic physical structure with high density integration, less power usage, superior alignment, and scalability. Compared to other devices, one of the biggest advantages of memristor is it can be fabricated with feature size as small as 9 nm^2 .

2.2 Overview of the Research Areas

Bernard Widrow proposed the first 'memristor' concept in 1960. In his mind, the memristor was the fundamental component of the ADALINE. The most well-known resistive device, the HP resistive grid, which uses resistance instead of voltage as a significant physical attribute and can accomplish logic functions [11] synchronously,

can also be utilized as a latch (memory) including a gate (logic). Memristors have recently been proved to execute implicative logical functions. Memristor could be illustrated as a ‘real fourth fundamental circuit element’ because these are passive circuit elements, and their behaviour could never be simulated by the other elements such as resistor-inductor-capacitor networks. When the flux and charge formation interpreted like a functionality of charge, it operates like a charge-monitored memristor; when the flux and charge link interpreted as the flux of charge, it governs like a flux-regulated memristor.

$$v(t) = M(q(t))i(t) \quad (6)$$

$$M(q) = d\varphi(q)/dq \quad (7)$$

In the same way, the current via a flux-monitored memristor could be given as

$$i(t) = W(\varphi(t))v(t) \quad (8)$$

$$W(\varphi) = dq(\varphi)/d\varphi \quad (9)$$

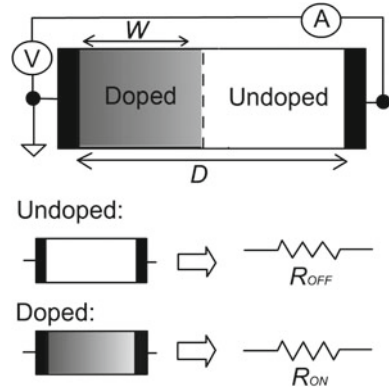
It can be viewed of as both an active and passive circuits, relied on the specific parameters. Those parameters are (a) memristance and (b) dynamic negative differential resistance. A double loop curve is used for the identification of a memristor along with a pinched hysteresis. The magnitude of the given voltage, the width of the bilayer structure, the accessibility of the ions, and the frequency of the applied voltage are all factors that may affect the hysteresis curve.

2.3 Memristor Fabrication and Modelling

2.3.1 Titanium Dioxide Memristor

First memristor was fabricated in the year 2008, by Strukov et al. at HP Laboratory. A TiO_2 material is used during the fabrication process. Between the two platinum electrodes titanium dioxide [12] is placed, one of which has an oxygen vacancy doped area (TiO_{2-x}). The resistivity of the undoped region is higher than that of the doped one. By delivering an appropriate voltage across the device, the doped region can be extended which results a change in the resistance. The device can memorize or remember its last resistance value and the state of the oxygen vacancy carriers remain the same when the voltage is withdrawn. As mentioned in Fig. 3, width of the area is ‘w’ and ‘D’ gives width of the bilayer structure, and this model relies mostly on both the resistors: R_{OFF} and R_{ON} . Where doped resistance is supposed to be mentioned by R_{ON} and undoped resistance is indicated by R_{OFF} [13].

Fig. 3 Doped and undoped regions



Whenever a positive voltage is supplied through the memristor, then there will be a transition of the positively charged oxygen variants from the doped area to the undoped area. Then, there will be a raise in the width of the given region, current conductivity and the level of the total memristance will be fallen.

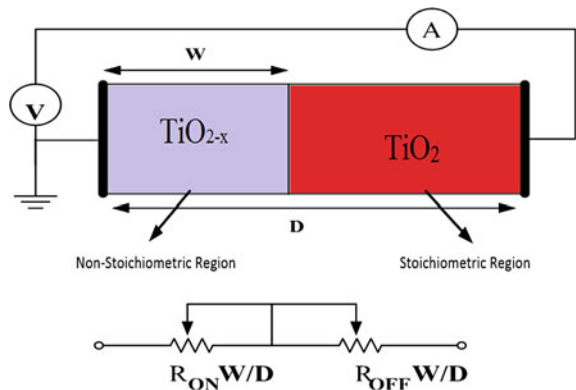
3 Modelling of a Memristor

3.1 Linear Ion Drift Model

This concept was proposed by Strukov et.al, and it can be known as HP model. It was the first the original model witnessed by the HP Laboratories in the year 2008 [4] when they first notified the physical realization of the memristor device (Fig. 4).

The resistivity of the undoped region is higher than that of the doped one. By delivering an appropriate voltage across the device, the doped region can be extended

Fig. 4 Titanium dioxide memristor



which results a change in the resistance [13]. The device can memorize or remember its last resistance value, and the state of the oxygen vacancy carriers remain the same when the voltage is withdrawn. As mentioned in Fig. 3, width of the area is 'w' and 'D' gives width of the bilayer structure, and this model relies mostly on both the resistors: R_{OFF} and R_{ON} [8]. Where doped resistance is supposed to be mentioned by R_{ON} and undoped resistance is indicated by R_{OFF} . Whenever a positive voltage is supplied through the memristor, then there will be a transition of the positively charged oxygen variants from the doped area to the undoped area. Then, there will be a raise in the width of the given region, current conductivity and the level of the total memristance will be fallen [14].

$$\frac{dw}{dt} = \frac{\mu_v R_{on}}{D} i(t) \quad (10)$$

$$M_{(w)} = \frac{v(t)}{i(t)} = \left(R_{on} \frac{w(t)}{D} + R_{off} \left(1 - \frac{w(t)}{D} \right) \right) \quad (11)$$

where $x = \frac{w(t)}{D}$ is known as the state variable and it can be defined as

$$x = \frac{w(t)}{D} = \mu_v \frac{R_{ON}}{D^2} q(t), \quad \text{where } x \in [0, D] \quad (12)$$

Now by substituting the value of 'x' in Eq. (11), the obtained equation is

$$M_{(w)} = (R_{on} \cdot x(t) + R_{off}(1 - x(t))). \quad (13)$$

(Or)

$$M_{(w)} = \left(R_{on} \cdot \mu_v \frac{R_{ON}}{D^2} q(t) + R_{off} \left(1 - \mu_v \frac{R_{ON}}{D^2} q(t) \right) \right) \quad (14)$$

By rearranging and simplifying the above Eqs. (13) and (14), we get

$$M_{(w)} = \mu_v q(t) \left(\frac{R_{on}}{D} \right)^2 + R_{off} \left(1 - \mu_v \frac{R_{ON}}{D^2} q(t) \right) \quad (15)$$

Here, the value of R_{ON} is negligible, i.e. $R_{ON} \ll R_{OFF}$. Hence, the final simplified equation is

$$M(w) = \frac{v(t)}{i(t)} = R_{OFF} \left(1 - \mu_v \frac{R_{ON}}{D^2} q(t) \right). \quad (16)$$

3.2 Nonlinear Ion Drift Model

The assumption that the linear model may not always be able to compensate for the boundary effect leads to the memristor's nonlinear functioning. It also overlooks the fact that the electric field within the memristor is highly nonlinear. Because of this reason, Jogalkar and Wolf devised a new methodology [15] to address the issue. The equation below is part of the nonlinear model

$$\frac{dw(t)}{dt} = \mu_v \frac{R_{ON}}{D} i(t) F\left(\frac{w}{D}\right) \quad (17)$$

The boundary wanders between the doped and undoped sectors where the drift velocity will be ' μ_D '. When it reaches to the edge level $w \sim 0$ or $w \sim D$, this speed will be reduced. As a result, the window function must fulfil the condition $F(0) = F(1) = 0$ to make sure that no drifts are present at the boundaries [16].

3.2.1 Jogelkar's Window Function

Depending upon the choice of the window function, the nonlinear ion model is chosen. In the year 2009, Jogelkar window function was proposed by Yogesh N. Jogelkar while he was trying to suggest some modifications of the HP model [15]. To characterize the polarity of the memristor and address boundary issues, two key elements were added to the present model. To begin, 'n' was inserted to indicate the memristor's polarity. Whenever a positive or higher voltage is provided to the doped area with $n = +1$, the width of the doped zone is expanded. By adding a positive voltage towards the doped sector with $n = -1$, the size of the doped zone will be diminished. Second, to tackle the border issue, new window functionality has been included. The device's drift velocity must be zero for one end and maximum at another end.

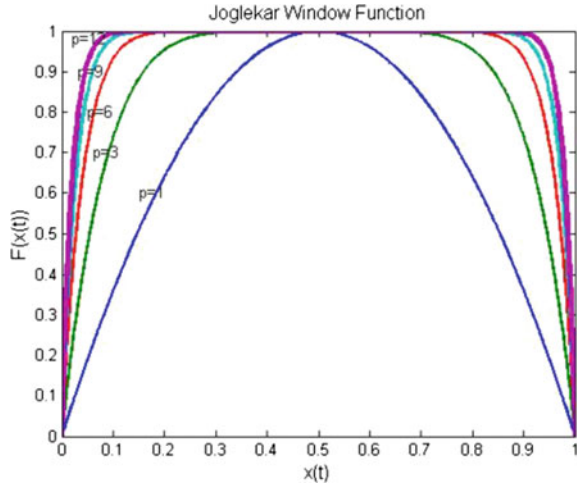
$$\frac{dw(t)}{dt} = \mu_v \frac{R_{ON}}{D} i(t) F\left(\frac{w}{D}\right) \quad (18)$$

$$f(w) = 1 - (2(w/D) - 1)^{2P} \quad (19)$$

The curvature of this function is determined by the control parameter ' p '. When the value of ' p ' is increased, the nonlinear drift problem is reduced. When the value of ' p ' grows, the function also takes on the appearance of a rectangular window function [16] (Fig. 5).

This method is simple and easy to understand and can meet the boundary constraint. The modification in the state variable $(dw(t))/dt$ will be zero if ever the state variable $w(t)$ exceeds one of its boundaries [14].

Fig. 5 Joglekar function for numerous values of ‘p’ [IJE, 107(11), 1362–3060]



3.2.2 Biolek Window Function

For reducing the boundary issues and inaccuracies of Joglekar function and HP models, a new window function was introduced by Zdenek Biolek [15] in the year 2009. This window function is used to realize the fact that after reaching the boundary or if the boundary speeds are different in each voltage bias direction, then the state variable should be moved back by the reversed bias [16]. It is mentioned earlier that there are some issues related to the Joglekar and HP methodologies. Biolek attempted to address these two aspects by proposing a unique window function that differs in border velocity in between the doped and undoped sectors.

$$F(x) = 1 - (x - stp(-i))^{2p} \tag{20}$$

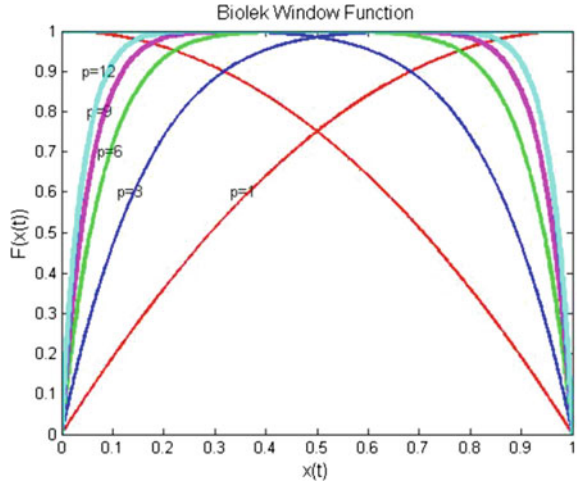
As shown in the above equation, ‘p’ resembles the positive integer. ‘i’ is supposed to be memristor current and the value of $stp(-i)$ will be one if ‘i’ value is greater than or equal to 0 and $stp(-i)$ will be zero if $i < 0$ [14].

$$stp(i) = \begin{cases} 1, & i \geq 0 \\ 0, & i < 0 \end{cases} \tag{21}$$

In this case, $stp(-i)$ is a step function that is a part of the function $f\left(\frac{w(t)}{D}\right) = f(x)$ and it can be given as

$$f(w) = 1 - ((w/D) - u(i))^{2P} \tag{22}$$

Fig. 6 Biolek function provided with various values of 'p' [IJE, 107(11), 1362–3060]

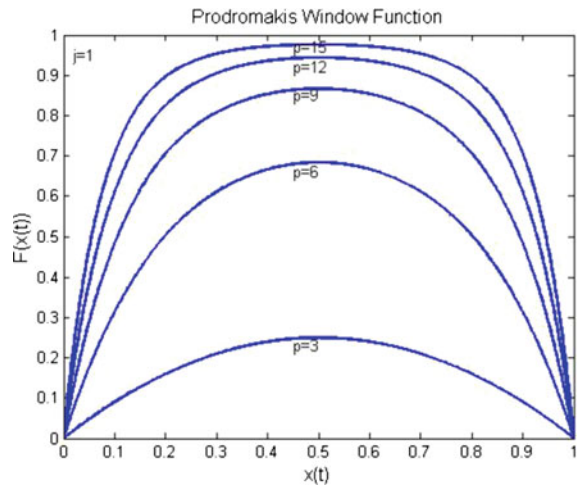


The Biolek window function addresses the memristor’s barrier concerns and nonlinear behaviour, but not its stability and flexibility [16]. The Biolek window function with various 'p' values is shown in Fig. 6.

3.2.3 Prodromakis Window Function

For the window functions, Prodromakis et al. given some valuable advice and expanded the Strukov window function $x-x^2$. It uses the process of completing the square and is relied on a smooth parabolic curve. Moreover, a control parameter is utilized to handle the scalability and flexibility [16] (Fig. 7).

Fig.7 Prodromakis window method at various 'p' values when $j = 1$ [IJE, 107(11), 1362–3060]



Prodromakis et al. discussed a few essential points about the window function. To start, a window function has to be able to incorporate the nonlinear phenomenon. Secondly, only for the edge electronics, the boundary conditions should be maintained. Thirdly, the nonlinear as well as linear dopant drift factors must sustain their relationship. Fourth, an additional control element is needed to accommodate the boundary's nonlinear behaviour [14]. Lastly, the scaling must be updated such that $0 \leq F_{\max}(x) \leq 1$ is the highest range

$$F(x) = j \left(1 - [(x - 0.5)^2 + 0.75]^p \right) \tag{23}$$

As expressed in Eq. (23), 'j' is a scaling factor that is often used to alter the window function's greatest value. Unlike Jogelkar's and Biolek's, where the control factor must be an integer, here 'p' is a real positive integer. A scalable factor [16] can also be used to regulate the function's maximum and minimum values.

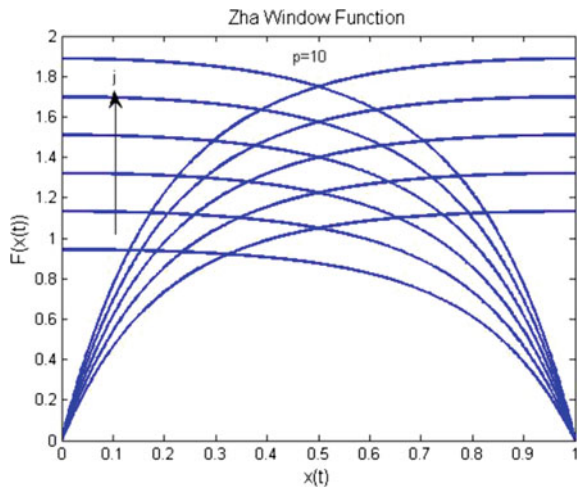
3.2.4 Zha et al. Window Function

Zha et al. proposed a new window function methodology to overcome the issues such as nonlinear affects, boundary lock, and scalability simultaneously [16]. To overcome these three challenges, two control parameters were recommended. The Biolek and Prodromakis functions were combined to form this window function.

$$F(x) = j \left(1 - [0.25(x - stp(-i))^2 + 0.75]^p \right) \tag{24}$$

As given in Eq. (24), 'j' and 'p' are real numbers that are positive. Figure 8 shows the Zha et al. window function model with various 'p' values.

Fig. 8 Zha window function with various 'p' values when j = 1 [IJE, 107(11), 1362–3060]



3.3 Simmons Tunnel Barrier Model

Following Simmon’s method which was postulated in 1963, Picket et al. recommended another model in 2009 [16]. The Simmons tunnel barrier concept contains only one resistor in series, as opposed to the linear ion drift model, which features two resistors in series. For the doped area, one resistor is used and another one is for the undoped areas, whereas this concept simply has one resistor in series. Because the migration of the ionized dopants is exponentially dependent, this theory hypothesizes asymmetrical switching and a nonlinear mechanism.

This model also features nonlinear and symmetric switching properties. According to Picket et al., this concept is an alternate to the HP model [15], in which the resistor as well as the electron tunnel barrier are placed in series. The structural model of the Simmon tunnel barrier concept can be seen in Fig. 9, where ‘ w ’ represents the width of the barrier, ‘ V ’ symbolizes the voltage value, ‘ R_s ’ denotes the channel resistance, ‘ V_g ’ is nothing but the voltage of the oxide zone, and ‘ v ’ resembles the internal voltage [16].

$$i = \frac{j_0 A}{\Delta w^2} \left\{ \varphi_I e^{-B\sqrt{\varphi_I}} - (\varphi_I + e|v_g|) e^{-B\sqrt{\varphi_I + e|v_g|}} \right\} \tag{25}$$

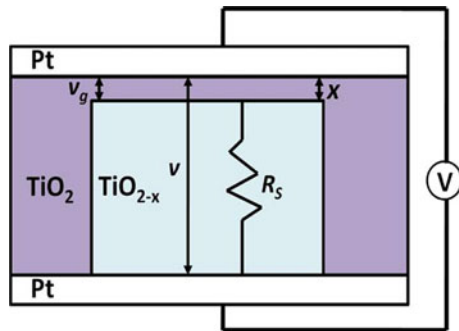
Here, $j_0 = \frac{e}{2\pi h}$, $\Delta w = w_2 - w_1$, $v_g = v - i(t)R_s$ and $B = \frac{4\pi\Delta w\sqrt{2m}}{h}$.

Depending upon the applied voltage ‘ w ’ can be in ON or OFF state. For mobilizing the oxygen vacancies, the nonlinear term $\left(\sin h\left(\frac{i}{i_{off}}\right) \exp \right)$ is used [15]. The below given Eq. (21) shows the ON and OFF states of the voltage. It is in ON position when ‘ i ’ value is less than zero and OFF position if the value of ‘ i ’ is greater than zero.

$$\frac{dw}{dt} = \left\{ \begin{array}{l} f_{off} \sin h\left(\frac{i}{i_{off}}\right) \exp \left[-\exp\left(\frac{w-a_{off}}{w_c} - \frac{|i|}{b}\right) - \frac{w}{w_c} \right], \quad i > 0 \\ f_{on} \sin h\left(\frac{i}{i_{on}}\right) \exp \left[-\exp\left(\frac{w-a_{on}}{w_c} - \frac{|i|}{b}\right) - \frac{w}{w_c} \right], \quad i < 0 \end{array} \right\} \tag{26}$$

As shown in the above Eq. (26), all parameters such as f_{off} , f_{on} , i_{on} , i_{off} , a_{on} , a_{off} , w_c , b are the fitting parameters. Regardless of the

Fig. 9 Simmon tunnel barrier model (IEEE, Vol.22, No.10, P.2054)



fact that this model is supposed to be the most precise model of the memristor and does not require the use of a window function, it also has some drawbacks. It cannot provide the exact relationship between the voltage and current, and it cannot be suitable for all types of memristors [26].

3.4 Threshold Adaptive Memristor Model

TEAM stands for threshold adaptive memristor model [6] which was suggested by Shahar Kvatinisky et al. in 2013. Simmon tunnel barrier method is equivalent to this one and can be fit to any other memristor model, and it is accurate and computationally efficient [14]. This model is moulded based upon some of the assumptions. (a) There should not be any variation in the state variable underneath a specific threshold; (b) the memristor power and the internal state drift component should have a polynomial connection, rather than an exponential dependency.

$$\frac{dw(t)}{dt} = \left\{ \begin{array}{ll} k_{\text{off}} \left(\frac{i(t)}{i_{\text{off}}} - 1 \right)^{\alpha_{\text{off}}} f_{\text{off}}(w), & 0 < i_{\text{off}} < i \\ k_{\text{on}} \left(\frac{i(t)}{i_{\text{on}}} - 1 \right)^{\alpha_{\text{on}}} f_{\text{on}}(w), & i < i_{\text{on}} < 0 \\ 0, & \text{Otherwise} \end{array} \right\}. \quad (27)$$

Here, f_{on} and f_{off} are the functions that are relied on the state variable. In addition, k_{off} , k_{on} , i_{off} , and i_{on} are the constraints where $k_{\text{off}} > 0$ and $k_{\text{on}} < 0$ [17]. Moreover, i_{off} and i_{on} are the current threshold variables. There are two current–voltage relationships in this model, one for nonlinear drift and the other for linear drift. If the relation of current–voltage is deemed to be linear according to the modifications in resistance, the solution becomes

$$f_{\text{off}}(w) = \exp \left[- \exp \left(\frac{w - a_{\text{off}}}{w_c} \right) \right] \quad (28)$$

$$f_{\text{on}}(w) = \exp \left[- \exp \left(\frac{w - a_{\text{on}}}{w_c} \right) \right]. \quad (29)$$

$$v(t) = \left[R_{\text{ON}} + \frac{R_{\text{OFF}} - R_{\text{ON}}}{W_{\text{off}} - W_{\text{on}}} (w - w_{\text{on}}) \right] i(t) \quad (30)$$

If the current–voltage properties match the Simmon tunnel concept significantly, the boundary sizes and resistance will be adjusted accordingly. The solution could then be expressed as follows:

$$v(t) = R_{\text{ON}} e^{\left(\frac{\lambda}{w_{\text{off}} - w_{\text{on}}} \right) (w - w_{\text{on}})} . i(t) \quad (31)$$

In this case, the suitable parameter is ‘ λ ’ and thus, the new equation can be written as

$$\frac{R_{\text{OFF}}}{R_{\text{ON}}} = e^{\lambda} \quad (32)$$

The VTEAM model is a development of the threshold adaptive memristor (TEAM) model. VTEAM means voltage threshold adaptive memristor model [18]. It is a memristor with a voltage control. In this scenario, voltage is supposed to adjust the memristor’s positioning. It means voltage processes as a threshold [19]. The voltage level of a memristor is much more essential than that of the threshold current for logical design and storage implementations.

3.5 Yacopic Neuromorphic Model

Yacopic brought this methodology into existence in the year 2011. This method relied on the voltage–current relation of the Picket et al. model. At a particular voltage threshold, the conductivity level rises automatically. The state variable varies between the values of ‘1’ and ‘0’ only. For this reason, the conductivity may be impacted. The state variable is controlled by two functions $f(w(t))$ and $g(v(t))$. To modify or change the state variable value, the threshold voltage value $g(v(t))$ is used. Moreover, at the boundary, to simplify the state variable value, $f(w(t))$ could be used [16]

$$I(t) = \begin{cases} a_1 w(t) \sin h(bV(t)), & V(t) \geq 0 \\ a_2 w(t) \sin h(bV(t)), & V(t) < 0 \end{cases} \quad (33)$$

As mentioned in the above Eq. (33), $w(t)$ represents the state variable and the fitting variables are a_1 , a_2 , and b .

$$g(V(t)) = \begin{cases} A_p (e^{V(t)} - e^{V_p}), & V(t) > V_p \\ -A_n (e^{-V(t)} - e^{V_p}), & V(t) < -V_n \\ 0, & -V_n \leq V(t) \leq V_p \end{cases} \quad (34)$$

Here, ‘ V_n ’ resembles threshold voltage and it is a negative variable, while ‘ V_p ’ symbolizes for the threshold voltage and it is a positive parameter. The magnitude exponentials are represented by ‘ A_n ’ and ‘ A_p ’.

$$f(w(t)) = \begin{cases} e^{-\alpha_p (w-w_p)} w_p(w, w_p), & w \geq w_p \\ 1, & w < w_p \end{cases} \quad (35)$$

$$f(w(t)) = \begin{cases} e^{-\alpha_n (w+w_n-1)} w_n(w, w_n), & w \leq 1 - w_n \\ 1, & w > 1 - w_n \end{cases} \quad (36)$$

Here, α_n, α_p, w_n & w_p are the fitting parameters

$$w_p(w, w_p) = \frac{w_p - w}{1 - w_p} + 1 \quad (37)$$

$$w_n(w, w_n) = \frac{w}{1 - w_n} \quad (38)$$

$$\frac{dw}{dt} = \eta_g(V(t))f(w(t)) \quad (39)$$

To identify the state variable's direction, the term ' η ' can be used. Because of its variant characteristics, this model can be suitable to the neuromorphic systems.

4 Conclusion

The precise description of the memristor beginning with its formation, basic functioning, various modelling methods such as nonlinear, linear, Simmon tunnel barrier, and TEAM model including various window functions is presented. Mathematical explanation and I-V properties of all the models have been detailed. Following a review of all mathematical models, it was claimed that the linear ion drift model does not demonstrate exact linear behaviour. To resolve and address the boundary problems and to explain the nonlinear behaviour numerous window functions such as Prodromakis, Biolek, Jogelkar, and Zha's have been addressed. In contrast to the nonlinear model, TEAM model was more versatile and easier in modelling. However, the Yacopcic model shows more similarity compared to the TEAM model. Finally, more study could be done to develop a more realistic model, which could be capable of simulating the memristor's experimental behaviour.

References

1. Chua, L.O., Kang, S.M.: Memristive devices and Systems. Proc. IEEE **64**, 209–223 (1976)
2. Widrow.: An adaptive ADALINE neuron using MEMS. Report no: 1553-2 (1960)
3. Stanley Williams, R.: How we found the missing memristor. IEEE Spectrum **45**, 483–489 (2008)
4. Ali, M., Mohamed, S., Elshafey, M., Mostafa, H.: Comparative study for some memristor models in different circuit applications. In: IEEE Conference on Microelectronics, vol. 12, pp. 262–266 (2019)
5. Taj, M., Vikram, G.N.V.R.: Design and simulations of high-sensitivity multi-directional inertial sensor. IEEE Sens. J. **22**(1), 190–194 (2022)
6. Sahoo, S., Prabakaran, S.R.S.: Nano ionic memristor equipped arithmetic logic unit using TEAM model. In: Online International Conference on Green Engineering and Technology (IC-GET), pp. 1–6 (2016)

7. Sahoo, S., Prabakaran, S.R.S.: Nano-ionic solid state resistive memories (ReRAM): a review. *J. Nanotechnol.* **17**, 72–86 (2017)
8. Sahoo, S., Manoravi, P., Prabakaran, S.R.S.: Titania based nano-ionic memristive crossbar arrays: fabrication and resistive switching characteristics. *Nano Sci. Nanotechnol. Asia* **9**(4), 486–493 (2019)
9. Sahoo, S.: Conduction and switching behavior of e-beam deposited polycrystalline Nb₂O₅ for non-volatile memory applications. *J. Alloy. Compd.* **866**, 158394 (2021)
10. Sahoo, S., Raman Murthy, G., Anitha, G.: An efficient design of a memristor augmented BCD to 7 Segment displays. *AIP Proc.* **2405**, 040022 (2022)
11. Sahoo, S., Prabakaran, S.R.S.: Memristor augmented ReRAM cell for Cross-bar memory architecture. In: *International Conference on Nextgen Electronic Technologies: Silicon to software ICNETS2*, pp. 456–462 (2017)
12. Chandra Sekhar, D., Sahoo, S., Prabakaran, S.R.S.: Resistive switching and impedance characteristics of M/TiO_{2-x}/TiO₂/M Nano-ionic memristor. *Solid State Ionics*, **324**, 218–225 (2018)
13. Radwan, A.G., Fouda, M.E.: *Memristor: Models, types and applications*. Springer, pp. 13–49 (2015)
14. Apollos, E.: Memristor theory and mathematical modelling. *Int. J. Comput. Appl.* **178**, 0975–8887 (2019)
15. Kashapaga, S., Sahoo, S.: A review on different memristor modeling and applications. *IEEE-MECON*, 688–695 (2022)
16. Hasan Maruf, M., Ali, S.I.: Review and comparative study of I-V characteristics of different memristor models with sinusoidal input. *Int. J. Electron.* 0020-7217 (2019)
17. Kvatinsky, S., Satat, G., Wald, N., Friedman, E.G., Kolodny, A., Weiser, U.: Memristor based material implication (IMPLY) logic: design principles and methodologies. *IEEE Trans. VLSI Syst.* **22** (2014)
18. Nayak, A., Sahoo, S., Prabakaran, S.R.S.: Memristor Equipped Error Detection Technique, vol. 466, pp. 183–191. Springer Nature (2017)
19. Kvatinsky, S., Friedman, E.G., Kolodny, A., Weiser, U.: TEAM: threshold adaptive memristor model. *IEEE Trans.* **60**, 211–221 (2013)

Performance Characteristics of Vegetable Oil and Its Blended Combinations as Alternate Liquid Insulation



M. Padmavathy and M. Bakruthen

Abstract For many years, petroleum products have dominated the world's energy needs in different application sectors. Natural-based ester oil is presented as alternative liquid insulation considering eco-friendliness to identify a suitable replacement for standard mineral oil. In this study, different ratios of vegetable ester oil were blended to investigate the usual features of blended liquid as liquid insulation. The oils of sunflower, safflower, and rice bran are being studied. According to standards, viscosity, breakdown voltage, flashpoint, fire point, and pour point are tested for various combinations. According to the investigation, individual oil samples can potentially replace typical mineral oil samples. Furthermore, the blended varieties demonstrate that changes occur as a result of the combination of samples, which prompts future investigation.

Keywords Vegetable oil · Blending · Liquid insulation · Transformers

1 Introduction

Transformer oil is indeed the insulating liquid used in electrical power transformers. Fractional distillation and subsequent treatment of crude petroleum yield it. Heat is created inside the transformer whenever a strong electric field is applied. As a result, transformer oil is primarily utilized to suppress corona and arc discharges, cool the transformer, reduce pyrolysis, and prevent direct contact of ambient oxygen with the insulation [1–3].

Mineral oil is a complex combination of hundreds of distinct chemical compounds, with the majority of the molecules consisting of carbon and hydrogen. Mineral oil is divided into three types. A minor amount of naphthenic hydrocarbons is found in

M. Padmavathy
High Voltage Engineering, National Engineering College, Kovilpatti, Tamil Nadu, India

M. Bakruthen (✉)
EEE, National Engineering College, Tamil Nadu, Kovilpatti, India
e-mail: bakruthenme@gmail.com

paraffinic crudes, which are separated into regular paraffin and o-paraffins. Compared to these three oils, naphthenic crudes offer several benefits, including that they contain extremely little wax. Because naphthenic oils are thinner than paraffinic oils, they have a lower viscosity [4–7].

Even if mineral oils continue to be an outstanding technical vs. economic solution, their environmental impact must be considered. Their biodegradability and toxicity are two other characteristics that distinguish them as a viable alternative to mineral oil. Triglycerides are naturally generated by etherification of the tri-alcohol glycerol with three fatty acids in vegetable oil. Ester-based dielectric fluids, both natural and manufactured, have grown in appeal among worldwide academic groups and enterprises interested in liquid dielectrics. The biodegradability of ester-based dielectric fluids, in particular, is an essential feature. As a result, there is a real need and opportunity to expand current understanding and literature on these novel insulating fluids [7–10].

Blended oil is made by combining two insulating liquids and has lately been recommended as a replacement for mineral oil. Blended oil has anti-aging benefits as compared to mineral oil. The dielectric loss, degradation ratio, acid number, and moisture content of this mixed oil are minimal. However, this varies depending on the type of ester oil and the acid concentration. The miscibility of ester oil determines performance qualities. Ester-based dielectric fluids' biodegradability is particularly essential. As a result, the existing state of knowledge and literature on these novel insulating fluids must be updated as soon as possible. This study intends to investigate the properties of natural esters-based oil samples and a blended mixture of natural ester oil based on the literature [7–12].

2 Experimental Details

2.1 Oil Samples

Based on the literature, this research aimed to look into the features of natural esters-based oil samples as well as blended natural ester oil. Based on geographical availability, price, and prior research, sunflower oil (SUO), safflower oil (SAO), and rice bran oil (RBO) were chosen as vegetable oil samples for assessment. Samples of raw vegetable oil are gathered from a neighboring facility. All are filtered to eliminate suspended particles from their composition to fulfill the CIGRE Work Group's Study Committee Report 12.17 standards for high oil quality. Table 1 shows a variety of mixed oil combinations.

Table 1 Proposed oil samples

Sample	Composition
Base Sample 1	100% SUO
Base Sample 2	100% SAO
Base Sample 3	100% RBO
Blended Sample 1	50% SUO + 50% SAO
Blended Sample 2	50% SUO + 25% SAO + 25% RBO
Blended Sample 3	50% SUO + 50% RBO
Blended Sample 4	25% SUO + 25% SAO + 25% RBO
Blended Sample 5	50% SAO + 50% RBO
Blended Sample 6	25% SUO + 50% SAO + 25% RBO

Table 2 Oil quantity required for blended samples

Sample	Oil quantity required in ml		
	SUO	SAO	RBO
Blended Sample 1	250	250	–
Blended Sample 2	250	125	125
Blended Sample 3	250	–	250
Blended Sample 4	125	125	250
Blended Sample 5	–	250	250
Blended Sample 6	125	250	125

2.2 Blended Oil Sample Preparation Process

The sample preparation is done in a 500 mL glass spherical reactor with a thermostat and mechanical stirring. Before adding each vegetable oil sample as per the recommended samples, the reactor is preheated to 75 °C to eliminate moisture. When the reactor reaches the reaction temperature, the stirring system is started, marking this as the reaction's time zero. For the appropriate reaction time, each combination is forcefully agitated and refluxed. Table 2 shows the amount of oil necessary to make the blended sample.

2.3 Measurement of Properties

The relevance of crucial parameters such as breakdown voltage, viscosity, flashpoint, fire point, and pour point, as well as experimental measurement methodologies, is discussed in this section.

The ability of liquid insulation to endure electrical stress created under operating settings is measured by the breakdown voltage of the insulation. When one or more contaminating substances, such as water, dirt, suspended particles, and so on, are

present. The test can be used to measure low-value breakdown voltage (IEEE Std. C57.14, 2018). The breakdown voltage of liquid insulation is tested using a test cell with hemispherical electrodes, according to IEC 60156-11, 2003 [13]. The electrodes are laid out horizontally with a 2.5 mm space between them. Oil samples are placed in a test cell with electrodes wholly immersed.

To avoid deceptive and low voltage breakdown, if bubbles occur in the oil sample, they are adequately eliminated by allowing a longer rest time of more than 15 min at room temperature. The breakdown voltage of oil samples is determined at a certain voltage, which induces breakdown between electrodes under stipulated test circumstances, by delivering a voltage across the electrode at an increasing rate of 2 kV/s across the electrode. The test is performed five to six times to determine the dielectric breakdown voltage of oil samples. The ultimate breakdown voltage of the oil sample is determined by the mean breakdown voltage measured. Figure 1 depicts the breakdown voltage kit.

Because liquid insulation also serves as a coolant, it must have a viscosity within the standard range for usual operating temperatures. Viscosity can influence cooling and the operation of cooling-related equipment. The viscosity of a liquid is a measurement of its resistance to flow (IEEE Std. C57.14, 2018). In a redwood viscometer, the viscosity of liquid insulation is calculated according to ASTM D445 [14]. The time it takes to flow 50 ml of oil samples through an aperture in a viscometer under controlled circumstances is used to calculate it. Figure 2 shows a redwood viscometer.

Fig. 1 Breakdown voltage kit



Fig. 2 Redwood viscometer



One of the most important factors to consider while producing improved liquid insulation is flammability. The lowest temperature at which liquid insulation generates a flammable vapor mixture at the liquid’s surface is known as the flashpoint. In addition, a low flashpoint indicates contamination with liquid insulation (IEEE Std. C57.14, 2018). According to ASTM D92, 2012 [15], the Pensky–Martin closed cup apparatus (Fig. 3) is used to determine the flashpoint and fire point of liquid insulation. The temperature at which flammable vapor on the surface of an oil sample is formed when artificially inserting a flame in a test orifice is determined by heating a 50 ml oil sample under controlled conditions in a test cup.

Among the most essential aspects of liquid insulation’s function in cold climates is its low-temperature performance. The lowest temperature at which liquid flows under certain conditions is known as the pour point of liquid insulation. Oil flow can be complicated below the pour point and viscosity limits flow. In severe 36 operating circumstances, such as frigid locations, pour point measurement can be helpful to in deciding the kind of liquid insulation for particular equipment (IEEE Std. C57.14, 2018). Pour point temperature is determined using a pour point device with four chambers, according to ASTM D97, 2017. In the test tube, 50 ml of oil is taken and placed in a copper container filled with a cooling media. The oil sample in the test tube is examined for solidification by horizontally positioning the test tube after every 3°C reduction by lowering the temperature of the cooling media. The temperature at which oil samples ceased flowing within the test cell is known as the pour point temperature. The setup is shown in Fig. 4.

Fig. 3 Pensky–Martin flash apparatus



Fig. 4 Pour point apparatus kit



Table 3 Properties and its typical values based on standards

Properties	Standard	Typical values
Breakdown voltage (kV)	IEC 60156	≥30 kV
Viscosity at 40 °C (cSt)	ASTM D445	<50 cSt
Flashpoint and fire point (°C)	ASTM D93	≥275 °C
Pour point (°C)	ASTM D97	<-10 °C

Table 4 Properties of base oil samples

Properties	SUO	SAO	RBO
Breakdown voltage (kV)	39	39	35
Viscosity at 40 °C (cSt)	70	80	75
Flashpoint (°C)	325	250	330
Fire point (°C)	335	260	340
Pour point (°C)	-6	-3	-6

IEC and ASTM standards are used to test the qualities of vegetable oils, such as breakdown voltage, viscosity, flashpoint, fire point, and pour point. Table 3 shows the approach standard employed and typical values.

3 Experimental Results and Discussion

3.1 Properties of Oil Samples

Breakdown voltage, viscosity, flashpoint, fire point, and pour point are measured as per standards for preliminary research on selected oils. Values of properties of base oil samples and blended oil samples are listed in Tables 4 and 5, respectively.

3.2 Discussion on Properties of Oil Samples

The relevant conclusions that can be drawn from the experimental data of properties by comparing those to the IEEE guide for acceptance and maintenance of insulating liquid in transformers.

- The breakdown voltage of any liquid insulation is a critical parameter determining the liquid insulation’s capacity to tolerate electrical stress generated inside the transformer during operation. The minimum breakdown voltage, according to IEEE guidelines, should be 30 kV. According to the main study of attributes of selected oil samples for this inquiry, all oil samples (base oil samples and blended oil samples) had a breakdown voltage of more than 30 kV. Based on these findings,

Table 5 Properties of blended oil samples

Oil samples	Breakdown voltage (kV)	Viscosity at 40 °C (cSt)	Flashpoint (°C)	Fire point (°C)	Pour point (°C)
Blended Sample 1	35	75	290	300	-6
Blended Sample 2	36	74	310	320	-6
Blended Sample 3	37	73	325	330	-9
Blended Sample 4	35	75	310	320	-6
Blended Sample 5	33	78	300	310	-6
Blended Sample 6	34	77	290	300	-6

it is discovered that certain natural esters have promise as liquid insulation for use in transformers due to a critical trait of breakdown voltage.

- The viscosity of liquid insulation is a key property that affects its effectiveness as a coolant and other liquid insulation-related components in the transformer. For absorbing liquid insulation, the maximum allowed range for the viscosity value of natural esters given in the IEEE guidance is 50 cSt. The viscosity of vegetable oil-based liquid insulations is often more significant than that of standard mineral oil used in transformers. According to this analysis, the acquired viscosity values for vegetable oil samples are similarly greater than the stipulated standard value. Natural esters may cause difficulties with cooling performance if used directly. Some approaches for lowering viscosity values have been proposed in the literature. As a result, viscosity reduction techniques should be used to operate the researched natural esters as liquid insulation in transformers.
- One of the essential aspects of fire risk assessment is flashpoint and fire point temperature. According to the IEEE guide, natural esters should have a minimum flashpoint temperature of 275 °C. Other than safflower oil, all oil samples' flashpoint temperatures satisfy the standard criteria for accepting liquid insulation. But, flashpoint and fire point have demonstrated more excellent performance and appropriateness as liquid insulation with blended oil combinations. These findings suggest that the oil samples studied had a wide range of flashpoint temperatures suitable for use as liquid insulation in transformers.
- The pour point of liquid insulation is an important feature that shows a temperature range where free circulation is possible. According to the IEEE guidance, the minimum pour point temperature for accepting liquid insulation is -10 °C. Pour point temperatures are more remarkable in all of the samples. These data show that freezing or crystal formation inside oil samples approaching sub-zero temperatures is possible. The findings show that fatty acid components impact pour point values. Because the pour point temperature of researched natural esters should be

lower than the found values for their use in cold climates. Based on the literature available, several approaches for reducing the pour point from its expected value to a defined range should be used.

4 Conclusion

Today, the entire globe is going through a transition period from petroleum-based goods, which are polluting and ecologically unfriendly, to vegetable-based oils, which are renewable and environmentally favorable. These renewable resources have excellent dielectric characteristics and are risk-free to utilize. As a result, the features of natural ester oil-based blended oils are explored in this study. The properties of blended oil combinations are superior to those of raw oil samples. This mixed oil may be used in any electrical equipment based on the application region and essential features. The blended sample under investigation has the potential to be a viable replacement to standard mineral oil. The only issue is that natural esters are more expensive than mineral oil. The findings will pave the way for more liquid insulation research in the future.

References

1. Senthilkumar, S., Karthick, A., Madavan, R., Moshi, A.A.M., Bharathi, S.S., Saroja, S.R., Dhanalakshmi, C.S.: Optimization of transformer oil blended with natural ester oils using Taguchi-based grey relational analysis. *Fuels* **11**, 1813 (2019)
2. Siva, A.S., Balaji, C., Akileshwaran, V., Hemanathan, N.: Experimental analysis on the combination of jatropha oil and silk cotton oil for transformer. In: *International Conference on Science Technology Engineering and Mathematics (ICONSTEM)* (2019)
3. Rakesh, C., Thomas, M.J.: Pongamia oil, an eco-friendly alternative for mineral oil used in high voltage transformers. *IEEE Trans. Dielectr. Electr. Insul.* **5** (2018)
4. Bandara, K.: Fernando: possibility of blending sesame oil with field aged mineral oil for transformer applications. *IEEE Trans. Dielectr. Electr. Insul.* **21**, 7 (2018)
5. Kamal, M.S.A., Bashir, N.: Insulating properties of vegetable oils and their blend. In: *IEEE 7th International Power Engineering and Optimization Conference* (2018)
6. Raof, N., Yunus, R.: Effects of palm-based trimethylolpropane ester/mineral oil blending on dielectric properties and oxidative stability of transformer insulating liquid. *IEEE Trans. Dielectr. Electr. Insul.* **26**, 6 (2019)
7. Liang, S., Wang, F., Huang, Z., Chen, W., Wang, Y., li, J.: Significantly improved electrical breakdown strength of natural ester liquid dielectrics by doping ultraviolet absorbing molecules. *IEEE Trans. Dielectr. Electr. Insul.* (2019)
8. Khaled, U.: Statistical investigation of AC breakdown voltage of natural ester with electronic scavenger additives. *IEEE Trans. Dielectr. Electr. Insul.* **26**, 6 (2019)
9. Trnka, P., Hornak, J., Prosr, P., Michal, O., Wang, F.: Various aging processes in a paper-natural ester insulation system in the presence of copper and moisture. *IEEE Trans. Dielectr. Electr. Insul.* (2020)
10. Cai, S., Zhou, X., Chen, J., Yu, H., Zhou, C.: Transesterification reaction reduce viscosity of vegetable insulating oil. In: *International Conference on High Voltage Engineering and Application (ICHVE)*, pp. 648–650 (2012)

11. Devasia, A., Chattopadhyay, M.: Macroscopic characterization of grating coupled waveguide structures for optical notch filtering. In: International Conference on Innovative Data Communication Technologies and Application, pp. 27–36. Springer, Cham (2019)
12. Saheb, SH, Satish Babu, G.: Modeling and evaluation of performance characteristics of redundant parallel planar manipulator. In: International Conference on Innovative Data Communication Technologies and Application, pp. 229–236. Springer, Cham (2019)
13. IEC 60156.: Insulating liquids- determination of breakdown voltage at power frequency—Test Method, 3rd edn (2003)
14. ASTM D445.: Standard Test Method for Kinematic Viscosity of Transparent and Opaque liquids (and Calculation of Dynamic Viscosity) (2011)
15. ASTM D93.: Standard Test Methods for Flash Point by Pensky-Martens Closed Cup Tester (2012)

Bottom-Up Synthetic Biology Leads to Artificial Cells as Innovative Materials and Calls for the Adoption of Systemic Perspectives



Pasquale Stano

Abstract Relevant advancements in the field of synthetic biology have led to the birth of a new nano-bio-technology based on a new “material”, i.e., the so-called artificial (or synthetic) cells. These terms refer to man-made cell-like systems, which are microcompartments whose size lie in the 0.2–20 μm range that mimic the basic function of biological cells. Artificial cells are generally built for basic science investigations (e.g., what are the minimal requirements for the emergence of life? How did life begin? What phenomena can be spontaneously generated by physico-chemical processes? How complex can an artificial cell be?), but several interesting scenarios can be envisioned in applied science too (e.g., smart drug delivery systems). Artificial cell technology is progressing rapidly, and new exciting reports appear monthly. However, theoretical descriptions of what actually artificial cells are, and how should we conceptually look at them are generally missing. In this contribution we would like to introduce the theme of the need of “systemic perspectives” in artificial cell research, and shortly present three areas for its implementation: (1) the internal reaction network, (2) the artificial cell/environment supra-system, (3) the complexity of artificial cells.

Keywords Synthetic biology · Artificial cells · Systemic perspective · Autopoiesis · Complexity · Information · Communication

1 Bottom-Up Synthetic Biology and the So-Called “Artificial Cells” (ACs)

The new scientific-technological research area called Synthetic Biology (SB) aims at applying engineering approaches to biology [1, 2]. It can be broadly defined as the design and construction of new biological parts, devices and systems, and in

P. Stano (✉)

Department of Biological and Environmental Sciences and Technologies (DiSTeBA), University of Salento, Lecce, Italy

e-mail: pasquale.stano@unisalento.it

redesigning existing natural biological systems in order to make them useful for several purposes.

Since its beginning, in the early 2000s, SB has shown a potential role mainly in applied research. SB classical scopes range from the production of fine chemicals (or chemical intermediates of moderate complexity) for pharmaceutical purposes or for the chemical industry, to the production of bio-fuel, or from the engineering of microorganisms acting as biosensors or for removing pollutants in open areas to the production of bioactive molecules [1, 2]. Further applications of SB can be found in agriculture, food industry, and materials science. Actually all these applications rely on the capacity of controlling the behavior of organisms (more often than not, microorganisms) in order to guide their metabolism or their genetic machinery in a desired, engineered, rewired, and pre-defined direction. Basic science results are also relevant and refers, for instance, to understanding life at its fundamental level, for example by demonstrating that life can be reconstructed in the laboratory, or by constructing living systems with a minimal number of genes.

From the operational viewpoint, SB is typically classified in two fields: top-down and bottom-up. The top-down field refers to those systems generated by modifying pre-existing biological systems (e.g., bacteria), by operations like addition, subtraction, replacement, minimization, rewiring, etc. of elements and sub-systems. An example can be the rewiring of a bacterium metabolism to redirect it toward the production of a compound of interest. The second field, instead, is called bottom-up, and it refers to all those approaches that aim at synthesizing biological systems from scratch, i.e., from isolated molecular component. Such an approach can be intended also as “cell-free”, “in vitro”, and “chemical” SB (with slightly different meanings). Artificial Cells (ACs), also called Synthetic Cells or sometime Protocells can be considered as the most ambitious goal of bottom-up SB, especially when the very challenging (and not at all taken-for-granted) result of building *living* ACs is considered. Today it is not yet possible to build a full-fledged AC from scratch: it is beyond current technical capacity. However, in principle there are no reasons that prevent such an achievement in future. Fortunately, non-living ACs (which are within current experimental reach) attract attention as well, because of their possible applications in biotechnology and nano-medicine (imagine, for example, smart drug delivery systems that actually are chemical robots capable of traveling in the body, reach a target tissue, and heal it by producing a therapeutic agent in situ).

The importance of ACs is, therefore, twofold. From one hand, their construction can help to understand the principles of living organization, the origins-of-life, the onset of “emergent” properties. From the other hand, they can represent excellent new biotechnological tools for applications, for instance in nano-medicine.

Either considering living or non-living ACs, the very practice of building such kind of systems is interesting per se, irrespective from the actual results. In fact, it offers the opportunity of discussing how *systemic perspectives* can impinge on science and technology. Here, by systemic perspective we intend all those conceptual issue related to the wholeness of molecular sets, with emphasis on how elements of the sets are connected to each other rather than on the specific identity of the

elements themselves. Systems theories, in every possible specification, have this peculiar aspect in common.

In this contribution we would like to sketch, in a preliminary manner, three aspects upon which it is possible to highlight how systemic perspectives are determinant for ACs, and in particular how this research field constitutes, actually, a valid platform for conjugating experimental and theoretical investigations dealing with systems theories. The lesson learned for the field of innovative, sustainable materials becomes—thus—quite evident. Coming progresses in the futuristic arena of SB must rely on combination of technical and conceptual innovations, and the latter one can only be systemic.

2 ACs in a Nutshell: Q&A

Since the pioneer 1990s period [3, 4], the construction of SCs has received increasing consideration, and several reviews are available [5–7]. In few words, ACs can be defined as those artificial molecular systems obtained by the encapsulation of reactive molecules inside microcompartments like lipid vesicles (liposomes) aiming at achieving a life-like behavior. Born within the origins-of-life community, the construction of ACs originally was intended as a manner to investigate the emergence of life on Earth, but ACs have become highly relevant as potential biotechnological tool, thus favoring more practical visions. The key aspects of ACs are schematically summarized below, by means of questions and answers.

How are ACs actually made? How long are they stable? Are ACs alive?

ACs are artificial microcompartments (ca. 0.2–20 μm) that contain a set of molecules. As a result of the reactions occurring inside and/or on their boundary surface, ACs can display one or more behavior(s) typical of living cells. Microcompartments (generally liposomes) are allowed to form spontaneously, or in a “directed” way, in the presence of the molecules that need to be entrapped in their lumen or embedded in their surface. What ACs will do, therefore, depends essentially on the nature of the encapsulated and boundary molecules and on the network of reactions they will generate. As any other amphiphile-based colloidal system, ACs integrity and stability are dominated by surface and self-assembly forces. The functioning and stability of ACs macromolecules depend on their 3-D structure, and in turn on interaction with solvent and salts, other macromolecules or lipids, and temperature. Therefore, depending on their structure and storage conditions, ACs stability can range from hours to days. No living ACs have been constructed so far.

What are the technologies involved in ACs research? What is the state-of-the-art of ACs research?

Current research is based on the convergence of: (a) liposome technology and biophysics, (b) in vitro biochemical reconstitution and gene expression, (c) deterministic and stochastic numerical modeling, (d) microfluidics. This powerful multidisciplinary platform slowly crystallized out in the past 25 years, starting from the pioneer phase in the early 1990s [3, 4], with a tremendous acceleration in the past ten years. Literature analysis shows that several milestones have been reached, and that it is possible to carry out complex biomolecular processes in ACs. ACs construction by the droplet transfer method [8], as well as by microfluidic devices, essentially solved the co-encapsulation issue of the many molecules required for gene expression (ca. 100 different molecules). Very efficient cell extracts [9] as well as reconstituted protein synthesis machinery (the PURE system [10]) are available. Water soluble and membrane proteins can be produced from ACs interior, in vitro genetic cascades have been realized, also inside ACs, PCR and RT-PCR, and DNA replication have been reported too, as well as lipid synthesis, signaling, AC-AC communication (comprehensive reviews can be found here [11, 12]).

SCs: quo vadis?

According to the current developments, it is foreseeable that ACs research will move forward in several directions, for example: (a) standardization of the whole approach and the various “modules” developed until now, aiming at their integration to build more complex functions; (b) creation of populations with low between-vesicles diversity by microfluidics [13]; (c) construction of ACs with nested design (vesicles inside vesicles, intended as artificial organellae) for the compartmentalization of otherwise incompatible “modules” and for exploiting trans-membrane vectoriality and gradients [14]; (d) autonomous production of energy (i.e., ATP) [15]; (e) development of a core-and-shell self-reproduction, attempting to synthesize living ACs [16]; (f) shift from studies on isolated ACs to “AC communities”, intended either as structural ensembles (i.e., tissue-like structures) [17], or as functional ensembles (SCs communicating with each other, coordinating their behavior); (g) with respect to ACs communication, improvement of robust, orthogonal, and space–time controlled information processing mechanisms; (h) construction of cognitive ACs.

Can AC compute?

AC can share with natural cells the capability *chemical computing*, i.e., performing a kind of logical operations by manipulating and processing chemical molecules that have been often referred to as signals. Chemical computing consists in molecular recognition, transformation, activation or inhibition of genetic/metabolic pathways. Chemical computing capabilities are intrinsic to the molecular domain and therefore they can be exploited to build nano- and micro-machines that are capable of performing unconventional computation. In SB, new genetic/regulatory/metabolic circuitry can be designed and plugged in natural cells (top-down approach), but with a proper optimization, the same is possible for bottom-up ACs too (genetic/metabolic

circuits with minor complexity). When compared with the engineering of genetic circuits in biological cells, ACs have some advantages: (1) they are built from a minimal number of components, facilitating the modeling and the understanding of their dynamic behavior; (2) the background and potentially interfering processes (always present in natural cells) can be eliminated; and (3) their behavior is largely predictable and programmable because the interaction among their components can be designed a priori.

In conclusion, current AC technology consists in the combination of liposome technology and cell-free technology, possibly integrated by microfluidics. Thanks to the powerful self-assembly properties of lipids, and the resulting encapsulation of free solutes, cell-like systems emerge spontaneously, with minimal manipulation needs. Current research aims at optimizing either the process of AC assembly (more often than not, it is a “guided” self-assembly), either the design of molecular systems inside ACs, in order to let them work in proper (desired, programmable) manner.

3 Three Systemic Perspectives

Systems are everywhere. Despite this common knowledge, systems theories and applications are not often explicitly considered in empirical sci-tech fields, where the objects under investigations are often referred to by a reductionistic viewpoint. By “reductionistic” viewpoint we mean that the focus of research, investigations, discussions, mainly refers to the *individual features* of certain molecular elements. In contrary, a “systemic” viewpoint mainly refers to the *relations* occurring between molecular elements. This change of perspective is decisive for approaching novel phenomenological aspects of the system under scrutiny. We maintain that ACs (and in general SB approaches) can play the role of a sand-box, wherein systemic perspectives can be efficiently tested, because of the facile control—exerted by the experimenter—on the objects under investigation. In other words, ACs can play the role of an experimental platform to test, learn, and exploit systemic theories. What makes SB so exciting, for realizing this conceptual move, is the fact that its resulting constructions, being molecular in nature, have the relevant property of undergoing transformations that modify both structures and functions, while this capacity is very limited in the hardware domain, and too easy (trivial) in the software domain (i.e., without true, realistic, physical constraints). There is no surprise, then, to learn that SB is conceived as the wetware implementation of the Sciences of the Artificial—those dedicated to understanding-by-modeling fundamental concepts such as life and cognition. The novelty, then, consists in the addition of a third way (the wetware one) to the traditional manners of building artificial systems—based on hardware (i.e., robotics) and software (i.e., artificial intelligence).

In the following sections, we will discuss separately three potential arenas where systemic perspectives can be successfully applied: (1) the AC internal reaction network; (2) the AC/environment supra-system; (3) the AC complexity.

3.1 The Internal Reaction Network

ACs were originally intended as tools to demonstrate the emergence of life from inanimate matter—in an origins-of-life perspective, thus employing primitive molecules and primitive chemical transformations. Emphasis was given to the concept of minimal complexity compatible with life (minimal life and minimal cell terminology [18, 19]). To this aim, many practitioners of ACs research often refer to two system-level theories: *autopoiesis*, from the Chilean biologists and neuroscientists Humberto Maturana and Francisco J. Varela [20], and the *chemoton theory*, from the Hungarian biochemist and theoretical biologist Tibor Gánti [21]. Both theories can be employed as conceptual frameworks to guide the construction of ACs. Only the first one will be briefly introduced here.

Autopoiesis (self-production) is considered a key concept to understand how living systems work, and for this reason it has inspired scientists interested in building all kinds of minimal ACs. It reads: (1) the distinctive property of living systems is its autopoiesis, i.e., their capability of producing and maintaining their material identity (themselves) by producing their own components (metabolism), despite the continuous turnover to which all components are subjected; and (2) autopoiesis is a global property; i.e., it does not rely in the physico-chemical properties of components taken separately, but in the way in which these components are dynamically *organized* within living systems.

According to the autopoietic theory, then, the required molecules for constructing living ACs are those strictly required to maintain and sustain the self-production of all cellular components, membrane included. Autopoiesis provides a general recipe for the construction of living ACs, even if such an enterprise is not trivial at all. Major emphasis, in autopoiesis, is given to constitutive (house-keeping) processes.¹ According to recent genomic analysis of small microorganisms (endosymbiont living inside other cells), such a minimal number is around 200 genes, constituting the minimal genome [22]. This is still a quite high number of genes for bottom-up implementation. Current experiments focus instead on the reconstruction of sub-systems (often involving a very small number of genes), just to verify their realizations.

The experimental attempts of constructing autopoietic synthetic units are challenging. They generally focus on the assembly of chemical reacting systems that can produce at least some species of the network. Clearly, the actual implementation depends very much on the chemical nature of the network elements. A popular design makes use of biomolecules such as proteins and nucleic acids encapsulated inside liposomes. Actually, one of the problem is that while the “modern” DNA-RNA–protein implementation of ACs take advantage of the superb performances of these components and allow the generation of sophisticated ACs, on the other hand they pose serious constraints about the processes of their synthesis, requiring very complex mechanisms (e.g., polymerases, ribosomes, post-translational modifications). In turn, because *all* components of an autopoietic network must be produced in order to

¹ However, more sophisticated processes are actually needed when adaptivity and plasticity are considered.

obtain metabolic/organizational/topological closures,² this makes the whole design quite demanding in terms of complexity.

The construction of autopoietic chemical systems is thus relevant for three main reasons. First, it forces the experimenter to think in terms of systems, and in particular of thermodynamically open but organizationally closed systems. Autopoietic cells are thermodynamically open because they require nutrients (building blocks) from their environment (as well as discard therein the waste material), while remaining organizationally closed (the environment plays a co-constructive—not instructive—role, even if the autopoietic system couples its dynamics with environmental changes, see below). Second, it requires a systemic analysis because in order to have a full self-production, the rates of chemical productions must be somehow coherent to each other, otherwise accumulation (or deprivation) of components would lead the network to find itself into “corners” in the chemical viability spaces, and it is not granted at all the situation can be reversed or escaped (with the consequence that the autopoietic system cannot accomplish its function, even partially). Finally, autopoiesis can be seen as a narrower region of the space that defines *autonomy*—a sort of particular case. While, for autopoiesis, the organizationally closed network is made of relations of self-production (it requires the transformative power which is typical of chemical reactions), for autonomy the organizationally closed relation network is, generally speaking, referred to any sort of causal relation (entailment). Accordingly, the assembly of autonomous ACs could be considered as more accessible (and nevertheless quite relevant for the Science of Artificial) than autopoietic ACs, because major constraints are generally associated to chemical transformations.

3.2 *The AC/environment Supra-System*

The Schroeder group reported ACs that synthesize cytotoxic proteins directly in the patient’s body, in the tumor tissue (experiments were done on mice) [23]. Tan and colleagues have shown that ACs produce a bacteria-killing toxin once stimulated by a signal produced by bacteria themselves [24]. These two examples show that one potential direction of applied AC research is the development of smart drug delivery agents, based on properly designed ACs that *perceive* their environment” and act consequently. Such a AC/environment systemic interplay can be applied to two situations: ACs that detect, sense, perceive a chemical in their environment; ACs that communicate with biological cells by chemical exchanges. In both cases, the key elements to which we need to focus attention is the process occurring inside ACs

² By metabolic closure we mean the dynamics of metabolic systems that produce all their own components; by organizational closure we mean that a certain system does not require external guidance or commands, i.e., its own dynamics is self-referential; by topological closure we mean that the system defines its own boundary in autonomous manner. Achieving these three forms of closure at their full extent—certainly a challenging task—implies that the system is autopoietic. On the other hand, it is possible to devise non-autopoietic systems which display these closures in partial, local, and limited (spatial/temporal) manner.

upon receiving a signal. This fascinating pattern can be conceived as a resultant of molecular circuitry inserted inside ACs, specifically designed for chemical signaling. Even if not alive, communicating ACs are therefore highly relevant for conceptual and applicative advancements.

By systemic perspective here we mean moving the focus from isolated ACs to the super-system made of an AC *situated* in an environment, with our attention on the coupled dynamics occurring between the variables describing the environment and those describing the AC. At this aim, the simplest interpretation is limited to non-living ACs, which can be successfully considered machines situated and operating in physico-(bio)chemical environments characterized by certain structures and patterns (i.e., spatio/temporal distributions of physico-chemical variables, such as concentrations, light, temperature, viscosity). Think, for example, to ACs traveling in a capillary of the circulatory system, directed toward a target cell. In these conditions, AC/environmental coupling can be analyzed according to communication and information theories, in particular by referring to standard (Shannon) information theory or considering semantic (meaningful) information (according to very recent approaches [25], which are suitable for AC modeling). Both approaches, for example, allow modeling ACs subjected to environmental patterns in space/time, and conceive the AC/environment as a mutually interacting system. Working models require, for example, probabilistic description of what ACs do upon receiving and perceiving a signal, eliciting interesting analyses about where AC diversity (heterogeneity, extrinsic stochasticity) comes from, if it is (ir)reducible, and what is the role, instead, of intrinsic stochastic behavior.

A still different cue about AC perception can derive from a combination of traditional artificial intelligence (AI) tools with SB. This is the case, for instance, of chemical neural networks grafted inside ACs, as recently proposed [26]. Can SB (i.e., ACs) be useful for the “synthetic exploration” of natural cognition, and in particular minimal cognition? Embodied AI [27], when operating in the biochemical domain—which is the domain where life actually originated—offers several advantages for modeling cognition. Current AC technology is not powerful enough, as mentioned above, and then it is necessary to reduce the complexity of AI-like goals. On the other hand molecular embodiment can be the only way to approach the natural performances of biological systems. The latter, indeed, function by exploiting macromolecules, their interaction with environment and with other molecules, and their structural capability of modify themselves in response to some stimuli. All this means that it would become possible, by starting from minimal ACs, to construct and study minimal autopoietic cognitive systems so to generate a truly embodied AI.

3.3 Complexity and AC Ranking

Finally, the systemic perspective is needed to rank ACs by their complexity. A preliminary suggestion has been recently published [28]. It is well known that defining and measuring complexity in physical, chemical, and biological systems is a challenging

task. Different definitions and measurements are selected on the basis of the features of the object under investigation [29, 30]. The common denominator, however, is that the object under study must be considered a *system* (or a *process*) and great emphasis is given to the relational properties of the system elements both in terms of structure and function.

From the viewpoint of structure, complexity can be related to the amount of information required to specify the arrangement of systems elements in the whole-structure, keeping into account the unique feature of ACs as micro-compartmentalized systems. At this aim, a bottom-line to define the “building blocks” of an AC must be first defined. Is this bottom-line made of individual atoms or of groups of atoms (e.g., functional groups)? Are they simple biomolecules (e.g., a metabolite) or bio-monomers (e.g., amino acids, nucleotides, lipids, intended, respectively, as the building blocks of proteins, nucleic acids, AC membrane). Once this is agreed on, the amount of information associated to the construction of the AC, and therefore the complexity associated to it, can be discussed in an analogous way to a proposed method for estimating the phenotypic complexity of organisms [31].

Looking instead at the functions and at the processes, complexity can be related to the equivalent complexity of an algorithm describing such function/processes, similar to the one defined for computer programs (i.e., the so-called Kolmogorov-Solomonoff-Chaitin complexity [32]). This approach would fit well for machine-like ACs, while there have been theoretical worries about its application to full-fledged autopoietic (and thus living) systems [33]. It should be noted that algorithmic complexity can be safely applied, instead, to AC sub-systems, such as gene networks [34], which often behave as logic gates allowing molecular computation at its basic level.

ACs, moreover, can be conceived as compartmentalized reaction networks, and owing to this interpretation, they can be subjected to the sophisticated toolbox of network analyses, measures, categorization, classification. Dedicated research (which is de facto interdisciplinary) is still missing. Ranking ACs could be quite useful, to monitor in objective manner the development of the field, guiding the experimental efforts toward those systems that would satisfy important complexity milestones, thus favoring the approach to the long-term goal of living ACs.

4 Concluding Remarks—Toward ACs 2.0

Although it is easy to imagine how ACs can be constructed, their actual realization in the laboratory is still difficult. As remarked, current artificial cell-like systems are still quite simple, not alive, but the field is experiencing a momentum that might become determinant for future success in short-medium range. Next generation ACs will represent truly innovative materials (or “active matter”) that can revolutionize biotechnology—because ACs do not resemble anything existing today. Examples of applications range from sophisticated biosensors, to smart drug delivery systems, from agents able to communicate with biological cells, to hybrid constructions made

of biological and artificial cells. For all these applications, as well as the basic science oriented ones, we are convinced that embracing *systemic perspectives* will provide researcher of a better conceptual framework within which develop novel wetware systems.

References

1. Endy, D.: Foundations for engineering biology. *Nature* **438**, 449–453 (2005)
2. Andrianantoandro, E., Basu, S., Karig, D.K., Weiss, R.: Synthetic biology: new engineering rules for an emerging discipline. *Mol. Syst. Biol.* **2**, 2006.0028 (2006)
3. Oberholzer, T., Wick, R., Luisi, P.L., Biebricher, C.K.: Enzymatic RNA replication in self-reproducing vesicles: an approach to a minimal cell. *Biochem. Biophys. Res. Commun.* **207**, 250–257 (1995)
4. Oberholzer, T., Nierhaus, K.H., Luisi, P.L.: Protein expression in liposomes. *Biochem. Biophys. Res. Commun.* **261**, 238–241 (1999)
5. Luisi, P.L., Ferri, F., Stano, P.: Approaches to semi-synthetic minimal cells: a review. *Naturwissenschaften* **93**, 1–13 (2006)
6. Mansy, S.S., Szostak, J.W.: Reconstructing the emergence of cellular life through the synthesis of model protocells. *Cold Spring Harb. Symp. Quant. Biol.* **74**, 47–54 (2009)
7. Schwille, P., Spatz, J., Landfester, K., Bodenschatz, E., Herminghaus, S., Sourjik, V., Erb, T.J., Bastiaens, P., Lipowsky, R., Hyman, A., Dabrock, P., Baret, J.-C., Vidakovic-Koch, T., Bieling, P., Dimova, R., Mutschler, H., Robinson, T., Tang, T.-Y.D., Wegner, S., Sundmacher, K.: MaxSynBio: avenues towards creating cells from the bottom up. *Angew. Chem. Int. Ed. Engl.* **57**, 13382–13392 (2018)
8. Fujii, S., Matsuura, T., Sunami, T., Nishikawa, T., Kazuta, Y., Yomo, T.: Liposome display for in vitro selection and evolution of membrane proteins. *Nat. Protoc.* **9**, 1578–1591 (2014)
9. Caschera, F., Noireaux, V.: Synthesis of 2.3 mg/mL of protein with an all escherichia coli cell-free transcription-translation system. *Biochimie* **99**, 162–168 (2014)
10. Shimizu, Y., Inoue, A., Tomari, Y., Suzuki, T., Yokogawa, T., Nishikawa, K., Ueda, T.: Cell-free translation reconstituted with purified components. *Nat. Biotechnol.* **19**, 751–755 (2001)
11. Stano, P.: Gene expression inside liposomes: from early studies to current protocols. *Chem. Eur. J.* **25**, 7798–7814 (2019)
12. Cho, E., Lu, Y.: Compartmentalizing cell-free systems: toward creating life-like artificial cells and beyond. *ACS Synth Biol* **9**, 2881–2901 (2020)
13. Deshpande, S., Dekker, C.: On-chip microfluidic production of cell-sized liposomes. *Nat. Protoc.* **13**, 856–874 (2018)
14. York-Duran, M.J., Godoy-Gallardo, M., Labay, C., Urquhart, A.J., Andresen, T.L., Hosta-Rigau, L.: Recent advances in compartmentalized synthetic architectures as drug carriers, cell mimics and artificial organelles. *Coll. Surf. B Biointerf* **152**, 199–213 (2017)
15. Altamura, E., Albanese, P., Marotta, R., Milano, F., Fiore, M., Trotta, M., Stano, P., Mavelli, F.: Chromatophores efficiently promote light-driven ATP synthesis and DNA transcription inside hybrid multicompartment artificial cells. *Proc. Natl. Acad. Sci. USA* **118**, e2012170118 (2021)
16. Exterkate, M., Caforio, A., Stuart, M.C.A., Driessen, A.J.M.: Growing membranes in vitro by continuous phospholipid biosynthesis from free fatty acids. *ACS Synth. Biol.* **7**, 153–165 (2018)
17. Carrara, P., Stano, P., Luisi, P.L.: Giant vesicles “Colonies”: a model for primitive cell communities. *ChemBioChem* **13**, 1497–1502 (2012)
18. Luisi, P.L., Varela, F.J.: Self-replicating micelles—a chemical version of a minimal autopoietic system. *Origins Life Evol. Biosphere* **19**, 633–643 (1989)
19. Szostak, J.W., Bartel, D.P., Luisi, P.L.: Synthesizing life. *Nature* **409**, 387–390 (2001)

20. Varela, F.G., Maturana, H.R., Uribe, R.: Autopoiesis: the organization of living systems, its Characterization and a Model. *Biosystems* **5**, 187–196 (1974)
21. Gánti, T.: Organization of chemical reactions into dividing and metabolizing units: the chemotons. *Biosystems* **7**, 15–21 (1975)
22. Gil, R., Silva, F.J., Peretó, J., Moya, A.: Determination of the core of a minimal bacterial gene set. *Microbiol. Mol. Biol. Rev.* **68**, 518–537 (2004)
23. Krinsky, N., Kaduri, M., Zinger, A., Shainsky-Roitman, J., Goldfeder, M., Benhar, I., Hershkovitz, D., Schroeder, A.: Synthetic cells synthesize therapeutic proteins inside tumors. *Adv. Healthc. Mater.* **7**, e1701163 (2018)
24. Ding, Y., Contreras-Llano, L.E., Morris, E., Mao, M., Tan, C.: Minimizing context dependency of gene networks using artificial cells. *ACS Appl. Mater. Interfaces* **10**, 30137–30146 (2018)
25. Kolchinsky, A., Wolpert, D.H.: Semantic information, autonomous agency and non-equilibrium statistical physics. *Interface Focus* **8**, 20180041 (2018)
26. Stano, P.: Chemical neural networks and synthetic cell biotechnology: preludes to chemical AI. In: *Proceedings of CIBB 2021—Computational Intelligence Methods for Bioinformatics and Biostatistics. Springer Lecture Notes in Bioinformatics* (2022), submitted.
27. Shapiro, L.: *Embodied cognition*. Routledge, New York (2011)
28. Stano, P.: Is research on “Synthetic Cells” moving to the next level? *Life* **9**, 3 (2019)
29. Gell-Mann, M., Lloyd, S.: Information measures, effective complexity, and total information. *Complexity* **2**, 44–52 (1996)
30. Lloyd, S.: Measures of complexity: a nonexhaustive list. *IEEE Control Syst. Mag.* **21**, 7–8 (2001)
31. Jiang, Y., Xu, C.: The calculation of information and organismal complexity. *Biol. Direct* **5**, 59 (2010)
32. Kolmogorov, A.N.: Three approaches to the quantitative definition of information. *Int. J. Comp. Math.* **2**, 157–168 (1968)
33. Letelier, J.C., Marín, G., Mpodozis, J.: Autopoietic and (M, R) systems. *J. Theor. Biol.* **222**, 261–272 (2003)
34. Siegal-Gaskins, D., Tuza, Z.A., Kim, J., Noireaux, V., Murray, R.M.: Gene circuit performance characterization and resource usage in a cell-free “Breadboard.” *ACS Synth. Biol.* **3**, 416–425 (2014)

Sensitivity Studies on Low Energetic Pyrotechnic Composition for Future Consumer Fireworks



S. Lionel Beneston, S. P. Asok, and V. Harish

Abstract The pollution caused by the pyrotechnic products is one of the major problems in the environment when it is burned for the celebrations and entertainment purposes. The pollutant from the burning pyrotechnic products causes ill health effects to all the living beings in the environment. The particulate matters like oxides of nitrogen (NO_x) exhausted out due to these pyrotechnic burning remains suspended in the atmospheric air for longer period of time in the size $\text{PM}_{2.5}$ and PM_{10} (Tian et al. in Atmospheric Chemistry And Physics, China, 2014; Lin et al. in Air and Waste Management Association, Taiwan, 2016; Godri et al. in Environmental Science and Technology, U.K, 2010), which are easily diluted in the blood stream of the living beings when inhaled, ingested and injected by direct or indirect mode. So, in this piece of works, the future generation pyrotechnic chemical composition containing sodium oxalate as an oxidizer replacing barium nitrate is studied. A pyrotechnic product namely ground chakkar was made using the existing and proposed chemical composition. Also, in another study modifications in the existing chemical composition is carried out by reducing the dextrin content. Mechanical sensitivity analysis was performed for the existing, modified and alternate chemical composition according to the standard procedure dictated in-EN 13,631–3. The test result shows that the use of an alternate chemical composition is safer and it belongs to class III explosive (sensitive) whereas the existing chemical composition belongs to class IV explosive (very sensitive). The new generation proposed energetic chemical composition mixture is completely free from barium nitrate and it is better as well as safer to handle.

Keywords Oxides of nitrogen (NO_x) · Particulate matter (PM) · Ground chakkar · Barium nitrate · Sodium oxalate

S. Lionel Beneston (✉) · S. P. Asok · V. Harish
Department of Mechanical Engineering, Mepco Schlenk Engineering College, Sivakasi, Tamil Nadu, India
e-mail: lionelbeneston90@gmail.com

© The Author(s), under exclusive license to Springer Nature Singapore Pte Ltd. 2023
V. Bindhu et al. (eds.), *Proceedings of Fifth International Conference on Inventive Material Science Applications*, Advances in Sustainability Science and Technology,
https://doi.org/10.1007/978-981-19-4304-1_23

257

1 Introduction

Fireworks products are widely used by human beings to express their delighted feeling of joy and entertainment purposes by all religions and civilizations around the world dated back from 1000 A.D [4]. From the burned fireworks products ashes and smokes are evolved which pollutes the environment's air, water and soil with their non-degradable heavy metals like barium nitrate [5]. The inorganic compounds present in the fireworks products when burned incompletely will cause ill effects when inhaled, ingested and injected by direct or indirect mode to the living beings in the environment [6]. Oxidizers and fuels are the vital chemical agent sources for the ignition and combustion activity of any pyrotechnic products. Other agents sources like binders, colorants, propellants, sounds and smoke producing agents are added additionally according to the effects it needs to be projected. Binder is a chemical agent which is used in fireworks products for holding the two compositions together in a Homogenous blend [7]. Ground chakkar is a domesticated pyrotechnic product which is used for the purpose of entertainment in outdoors [8]. It consists of long hollow cylindrical high Grams per square meter (GSM) paper tube containing a charge of non-flashing, non-exploding, densely packed pyrotechnic chemical compositions and whirl around with small paper tubes. It is working on the principle of controlled burning of pyrotechnic chemical compositions and outrushes showers of sparks by rotating on its pivot. Ground chakkar gets lightened when igniting the tip and rotation is accompanied by the stream of sparks, twinkles and color. The soluble and insoluble barium compounds like barium nitrate, barium bromide, barium chloride, barium oxalate, barium sulfate, barium carbonate, etc., causes the health effects in humans such as cardiovascular diseases, kidney related diseases, metabolic, neurological and mental disorders [9–11]. To mitigate the pollution caused by the fireworks, Government of India banned the use of chemicals containing barium (heavy metal) and chlorides in the fireworks products [12] and also banned the import and use of Chinese firework products. They also permitted to use of low-emission green pyrotechnic products which are authorized and developed by scientists of Council of Scientific and Industrial Research and National Environmental Engineering Research Institute in accordance with all applicable government norms [13, 14].

To overcome these environmental issues of barium, in this work we have proposed an alternative chemical compositions replacing barium nitrate in ground chakkar with sodium oxalate [15, 16]. This chemical composition is subjected to impact, friction sensitivity tests, performance analysis [17] and it is expected that the sodium oxalate as an oxidizer gives a better result in terms of performance and safety [18].

2 Accident Analysis

India is the world's second-largest manufacturer of fireworks, which is accounted for 94% of fireworks imports by the United States in 2019 [12]. More than 700 factories

in Sivakasi with one million people [12]. They are dependent on the firecracker industry for their livings and they are not aware of the chemical's characteristic [19] and the handling techniques for the safer working. The prolonged storage of the chemicals tends to decompose thermally and causes an accident that occurs mainly due to impact and friction [20–23]. So, the studies are carried out inevitably in this project to know about the sensitivity of the modified and new alternative fireworks mixtures.

3 Materials and Methods

3.1 Chemicals Purchased

The chemicals like Industrial grade barium nitrate, potassium nitrate, sodium oxalate and dextrin was purchased from the Sun Moon Chemicals (India) Private Limited, Sivakasi, Tamil Nadu, India. Industrial grade aluminum 999, 666 and 222 of greater than 99.7% of purity was purchased from the renowned fireworks factory in Sivakasi, Tamil Nadu, India.

3.2 Preparation of Pyrotechnic Mixtures

Each chemical were weighed to the required amount of quantity or by percentage and each chemical were sieved individually according to ISO 9001:2015 standard 150 mesh sieve of 89 μm . The purpose of sieving is to ensure the particle sizes are in the order of 89 microns and also to maintain homogeneity [24]. The chemicals are mixed together by following the safety procedures and then the mixture is sieved and collected which was stored in an air tight container to avoid any interaction with atmosphere.

3.3 Chemicals Mixed

The Existing chemical composition (composition L) consists of mixtures like barium nitrate 40%, potassium nitrate 7%, aluminum 999 35%, aluminum 666 6%, dextrin 12%.

There are six Modified chemical compositions of existing compositions with different percentage of fuel (aluminum 666) and binder (dextrin) such as L_1 , L_2 , L_3 , L_4 , L_5 and L_6 for determining the performance of each chemical composition.

- Composition L_1 consists of mixtures barium nitrate 40%, potassium nitrate 7%, aluminum 999 35%, aluminum 666 8%, dextrin 10%.

- Composition L_2 consists of mixtures barium nitrate 40%, potassium nitrate 7%, aluminum 999 35%, aluminum 666 10%, dextrin 8%.
- Composition L_3 consists of mixtures barium nitrate 40%, potassium nitrate 7%, aluminum 999 35%, aluminum 666 12%, dextrin 6%.
- Composition L_4 consists of mixtures barium nitrate 40%, potassium nitrate 7%, aluminum 999 35%, aluminum 666 14%, dextrin 4%.
- Composition L_5 consists of mixtures barium nitrate 40%, potassium nitrate 7%, aluminum 999 35%, aluminum 666 16%, dextrin 2%.
- Composition L_6 consists of mixtures barium nitrate 40%, potassium nitrate 7%, aluminum 999 35%, aluminum 666 18%.

The new alternate chemical composition LN1 Sodium oxalate is added as an oxidizer added instead of barium nitrate.

- Composition LN1 consists of mixtures Sodium oxalate 40%, aluminum 999 35%, potassium nitrate 7%, aluminum 666 6%, dextrin 12%.

3.4 Sensitivity Analysis

The standard procedures and safety measures are followed up for the sensitivity analysis tests such as impact and friction tests. The Bundesanstalt für Materialforschung und—prüfung (BAM) method is used to examine the impact sensitivity and friction sensitivity behavior of the new alternative and modified chemical composition mixtures of the ground chakkar.

3.4.1 **Impact Sensitivity test.** The Impact Sensitivity test for the chemical compositions are measured as per the German Federal Institute for Testing Materials (GFITM), Bundesanstalt für Materialforschung und—prüfung (BAM), UN Test series.3 method by using impact sensitivity tester as shown in Fig. 1 [25].

The most important part of the impact sensitivity tester is the cast steel block and the base of the column. The drop weight load with the release pin. The apparatus needs to be fixed into the concrete block using four anchoring screws secured in the concrete to the center of the steel block, where the anvil of 2 cm in diameter is the place where to place the sample. The column of length 23 cm are made from seamless drawn steel tube. The movable cast steel block can be placed to the required heights using the Allen keys. A cylinder block of 2 kg is used to hit the sample from height. Top anvil is placed above the mixture; sample of 0.1 g of chemical mixture was taken and placed in the bottom of the anvil. Before revealing the cylinder block from height, the caution is needed to ensure the accurate placing of the chemical sample by spreading it to flattened position.

The impact sensitivity of the chemical samples is expressed in terms of limiting impact energy in Joules (J).

Fig. 1 BAM impact tester
(Source [26])

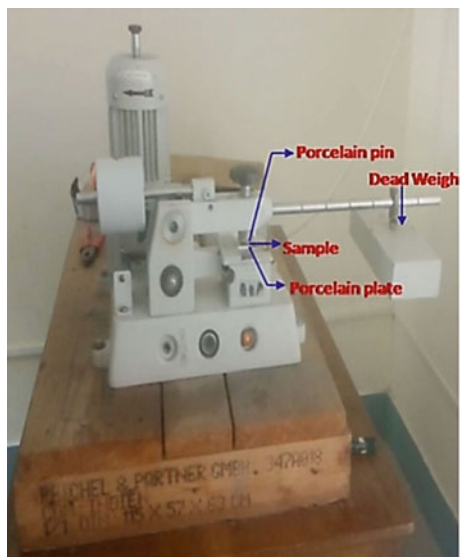


During this experiment, the height at which the explosion takes place is observed by the human assistance (observer). The test procedure is continued in different heights with five trials of test experiment which are done to determine the limiting impact energy of the chemical samples. Then, at least of 3 trials of attempts on the height at which the spark/smoke/sound occurs in the experiment were noted and limiting impact energy was calculated to identify the sample's class/category of explosives.

3.4.2 **Friction Sensitivity test.** The friction sensitivity test for the pyrotechnic composition was measured using friction test apparatus STANAG 4487 as shown in Fig. 2 [27–29]. The test is performed as per the standard procedure dictated in-EN 13,631-3.

The friction sensitivity tester consists of cast metal steel with base plate of gray cast steel on which the motor is fixed with the gear, the friction apparatus with the porcelain pin, load bar and the movable table is driven by the heavy load induction motor. Switching the power supply to the machine and turn on the start button. The porcelain plate under the porcelain pin executes one sliding movement in forward and backward motion overing 10 mm distance. The center off disc stops the motor for each rotation. The load bar has 6 notches for hanging the 9 different loads from 1 to 9 kg. About 0.1 g of sample was placed under a porcelain plate with flattened position. The table with the porcelain plate moves to and fro motion over a distance

Fig. 2 BAM Friction tester
(Source [26])



of about 10 mm with a speed of 141 rpm. Six trials are conducted exactly to identify the exact friction sensitiveness of the sample.

4 Experimental Results and Discussion

The Mechanical Sensitivity for existing modified and alternative chemical compositions are measured by Impact sensitivity and Friction sensitivity tests to determine the limiting impact and friction weight and to avoid accidents during its handling of the chemicals.

4.1 Impact Test

The impact sensitivity of all the chemicals is measured in terms of limiting energy in Joules (J) (Table 1).

The limiting impact energy is calculated by,

$$\text{Limiting Impact Energy (LIE)} = m \times g \times h \quad (1)$$

where

m = mean of the drop weight measured in “kg”.

Table 1 Impact test for Existing composition “L”

Height (m)	Trial 1	Trial 2	Trial 3	Trial 4	Trial 5
0.1	X	X	X	X	X
0.15	X	X	X	X	X
0.18	X	X	X	X	X
0.19	X	X	✓	✓	✓
0.2	✓	✓	✓	✓	✓

Where,

✓ Denotes “occurrence of flash/sound”

X Denotes “no significant occurrences of flash/sound”.

Table 2 Limiting Impact energy for modified and existing

S. No	Chemical composition	Height (m)	Limiting impact energy (J)
1	L1	0.19	3.7278
2	L2	0.25	4.9050
3	L3	0.24	4.7088
4	L4	0.2	3.9240
5	L5	0.21	4.1202
6	L6	0.16	3.1392
7	LN1	0.64	12.5568

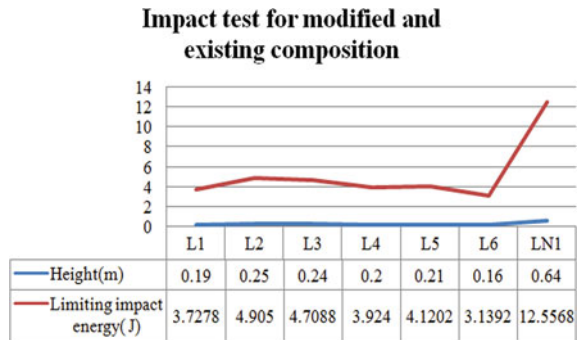
g = acceleration by gravity = 9.81 m/s^2 .

h = height is measured in “ m ”.

For the height 0.2: $LIE = 2 \times 9.81 \times 0.18 = 3.5316 \text{ J}$.

The limiting impact energy for composition L is 3.5316 J . Thus, it belongs to class IV explosive which is very sensitive to impact energy, [30] (Table 2 and Fig. 3).

Fig. 3 Impact test for modified and existing composition



Except the composition LN_1 all the other compositions belongs to class IV explosive which is very sensitive to impact energy, whereas LN_1 belongs to class III explosive which is sensitive to impact energy [30].

4.2 Friction Test

The friction sensitivity of all the chemicals is measured in terms of safe explosion load in Newton (N) (Tables 3 and 4).

The friction sensitivity test was carried out for the existing, modified and alternate chemical compositions with 3 different loads and frictional spark occurred only for the composition “L” at trail 5, whereas no spark was observed in other cases.

Therefore, the friction sensitivity of the proposed modified and alternate chemical compositions are less and is safer to use.

Table 3 Friction test for existing composition “L”

Existing chemical composition	Load (N)	Number of trails					
		1	2	3	4	5	6
<i>L</i>	288	X	X	X	X	X	X
	324	X	X	X	X	X	X
	360	X	X	X	X	✓	X

Where

✓ denotes “occurrence of spark”

X denotes “no significant occurrences of spark”.

Table 4 Friction test for modified and alternate composition

S. No	Chemical composition	Safe explosion load (N)		
		288	324	360
1	L_1	X	X	X
2	L_2	X	X	X
3	L_3	X	X	X
4	L_4	X	X	X
5	L_5	X	X	X
6	L_6	X	X	X
10	LN_1	X	X	X

5 Conclusion

Thus, Sodium oxalate was identified as the good substitution for barium nitrate in ground chakkar based on the sensitivity studies. The existing, modified and alternate chemical compositions are experimented with mechanical sensitivity analysis such as impact sensitivity and friction Sensitivity tests. The impact test results suggest that the mixture belongs to class IV explosives and was moderately sensitive; the friction test results show that the mixture was not prone to friction sensitive. Thus the performance of ground chakkar was observed during the open burning test and the results are fairly satisfactory for modified chemical compositions needs further modifications. Thus, it is inferred that the newfangled energetic chemical compositions is safer to handle and further thermal analysis are to be carried.

References

1. Tian, Y.Z., Wang, J., Peng, X., Shi, G.L., Feng, Y.C.: Estimation of direct & indirect impacts of fireworks on the physicochemical characteristics of atmospheric PM 10 And PM 2.5. In: Atmospheric Chemistry and Physics, China (2014)
2. Lin, C.-C., et al.: The impact of fireworks on particulate matter in ambient air. In: Air and Waste Management Association, Taiwan (2016)
3. Godri, K.J., Green, D.C., Fuller, G.W., Dall'osto, M., Beddows, D.C., Kelly, F.J., Harrison R.M., Mudway, I.S.: Particulate oxidative burden associated with firework activity. In: Environmental Science & Technology, U.K (2010)
4. Naik, V., Patil, K.C.: A Brief History and Chemistry of Fireworks and Rocketry, India (2015)
5. Kulshrestha, U.C., Rao, T.N., Azhaguvel, S., Kulshrestha, M.J.: Emissions and accumulation of metals in the atmosphere due to crackers and sparkles during Diwali festival in India. *Atmos. Environ.* **38**(27), 4421–4425 (2004)
6. Camilleri, R., Vella, A.J.: Emission factors for aerial pyrotechnics and use in assessing the environmental impact of firework displays: case study from Malta. *Propellants Explos. Pyrotech.* **41**(2), 273–280 (2016)
7. Ineichen, H., Berger, B.: Pyrotechnics in fireworks. *CHIMIA Int. J. Chem.* **58**(6), 369–437 (2004)
8. IS 14931 (2001): Fire Works Wheel [CHD 26: Explosives and Pyrotechnics] (2001)
9. Kravchenko, J., Darrah, T.H., Miller, R.K., Kim Lyerly, H., Vengosh, A.: A review of the health impacts of barium from natural and anthropogenic exposure. In: Environment Geochemistry Health, U.S.A (2014)
10. Health effects assessment of barium, U.S.A environmental protection agency, office of health and environment, Washington, U.S.A (1984)
11. Brenniman, G.R., Kojola, W.H., Levy, P.S., Carnow, B.W., Namekata, T., Breck, E.C.: Health effects of human exposure to barium in drinking water. NTIS pb 299968, U.S.A (1979)
12. Palit, R.: Article on Diwali Fails to Light Up India's Pandemic-hit Fireworks Industry, India (2020)
13. Firecracker Emission Testing Facility for Measurement of PM and Gaseous Pollutants by NEERI
14. Steinhäuser, P.G., Klapötke, T.M.: "Green" pyrotechnics: a chemists' challenge. *Angew. Chem. Int. Ed.* **47**(18), 3330–3334 (2008)
15. Sabatini, J.J., Raab, J.M., Hann Jr, R.K., Freeman, C.T.: Brighter- and longer-burning barium-free illuminants for military and civilian pyrotechnics. In: Pyrotechnics Technology and Prototyping Division, USA (2013)

16. Sabatini, J.J., Poret, J.C., Broad, R.N.: Boron carbide as a barium-free green light emitter and burn-rate modifier in pyrotechnic. *Angew. Chem. Int. Ed. (U.S.A)* (2011)
17. Wang, P.S., Hail, G.F.: Friction, impact, and Electrostatic Discharge Sensitivities of Energetic Materials, DE85 01332, U.S.A (1985)
18. Azhagurajan, A., Selvakumar, N., Suresh, A.: Environment Friendly Fireworks Manufacturing Using Nano Scale Flash Powder (2014)
19. Thamburaj F. sdb: A brief report on sivakasi fireworks industries, Tiruchirappalli, India (2016)
20. Palaneeswari, T.: A study on attitude of fireworks manufacturers in Sivakasi towards eco-friendly fireworks. *Int. J. Trade Commer.* **1**, 204–212 (2012)
21. Vijayakumar, A., Veerasimman, A., Ramar, R., Shanmugavel, R., Nallathambi, I.: Fireworks hazards and its consequences—A brief analysis. In: *Materials Today: Proceedings* (2021)
22. Rajathilagam, N., Rajathilagam, N., Azhagurajan, A.: Accident analysis in fireworks industries for the past decade in Sivakasi. *Int. J. Res Soc. Sci.* **2**(2), 170–183 (2012)
23. Sivapirakasam, S.P., HariSivaSri Phanindra, K., Surianarayanan, M.: Hazard assessment for the safe storage, manufacturing and handling of flash compositions. *J. Loss Prev. Process Ind.* **22**(2), 254–256 (2009)
24. Azhagurajan, A., Selvakumar, N., Thanulingam, T.L.: Thermal and sensitivity analysis of nano aluminium powder for firework application. *J. Therm. Anal. Calorim.* **105**(1), 259–267 (2011)
25. Sivapirakasam, S.P., HariSivaSriPhanindra, K., Surianarayanan, M.: Experimental evaluation of the influence of non-metallic contact materials and their surface roughness on the mechanical sensitivity of a safety match head composition. *Process Saf. Prog.* **38**(3), e12023 (2019)
26. Rajendran, M., Ramanathan, R., Ganesan, P., Shanmugavel, R.: Experimental analysis of tamarind seed powder based flash powder composition for eco-friendly firecrackers. *J. Thermal Anal. Calorim. (India)* (2020)
27. STANAG 4487 (2009): Explosives, Friction Sensitivity Tests, NATO (2009)
28. Wharton, R.K., Harding, J.A.: An experimental comparison of three documented test methods for the evaluation of friction sensitiveness. *J. Energ. Mater.* **11**(1), 51–65 (1993)
29. Nalla Mohamed, M.I., Sivapirakasam, S.P., Surianarayanan, M.: Investigation on the friction sensitivity of a match head composition influenced by the surface roughness of contact materials. *Propellants Explos. Pyrotech.* **38**(2), 266–272 (2013)
30. Andreiv-Beliave, classified explosive substances into four classes on the impact sensitivity (i.e. measured in impact energy J (E)) (1965)

Investigation of Desirable Vibrational Energy Harvester Based on Design Structure and Piezoelectric Material



Shaik Riyan, Boppana Bhargav Chowdary, Adil Altom Mohammed Adam, Satyajeet Sahoo, and M. Taj

Abstract Vibrational energy is available as an abundant source in the Environment and this ambient vibrational energy can be scavenged to useful electrical energy with the help of energy harvesters. This paper aims of selecting the best energy harvester by analyzing the different types of structures and their design configurations, as well as various types of piezoelectric materials. Energy harvester with heavy weight proof mass and possessing the large beam length with small width and thickness yields the high efficient output. On analysis, it is observed that arrayed vibrational energy harvester made up of PZT-5H material is chosen to be the best choice as it generates high output voltage and power at low resonating frequency.

Keywords Vibrational energy harvester · MEMS · PZT-5H · Piezoelectric

1 Introduction

Technology is advancing at a rapid pace because of the widespread use of low powered electronic devices. This low power in compact electronic devices is compensated by the use of battery with a finite lifetime that must be replaced or recharged from time to time, affecting the performance of the electronic devices. The use of energy harvester is an effective solution to this problem [1]. Energy harvesters are made of piezoelectric material, which works on the basic principle of transforming vibrational stress to useable electrical energy [1, 2]. This electrical energy can be utilized for variety of purposes, such as to operate the implantable medical devices such as pacemaker, and to power the wireless sensor networks and biofuels [1–3].

Piezoelectric energy harvester are widely used and can be easily integrated into MEMS domain because of simplicity in designing, ease of operation, low cost and easy fabrication and are preferred over other vibrational energy mechanisms as it does not requires any kind of excitation to operate [1, 4]. The electrical performance of the VEH is mostly determined by characteristics such as beam length, thickness,

S. Riyan · B. B. Chowdary · A. A. M. Adam · S. Sahoo · M. Taj (✉)

Department of ECE, Vignana's Foundation for Science, Technology and Research, Guntur, India
e-mail: taj_ece@vignan.ac.in

width, mass position and piezoelectric material type. When a heavy mass is coupled to an energy harvester, it produces a higher displacement as well as higher output power density. When the beam length is long and the thickness and width are small, the output is very efficient [5]. Sasrika et al. [2] discussed a comparison analysis of five different types of piezoelectric materials to determine the best piezoelectric material that delivers the maximum output and came to the conclusion that PZT-5H is the best suitable material that can be used to generate high efficient output.

Anand and Kundu designed a small-scale piezoelectric material for pacemaker applications using ZnO rather than PZT-5H because the latter contains lead, which is hazardous to human health and the environment [1]. According to Taj, the piezoelectric energy harvester is the most sensitive and can offer a power efficiency of 1–10 microwatts [3]. Zhang et al. [6] proposed an AlN-based piezoelectric energy harvester with a unique design structure. AlN is preferred because of its reasonable fabrication costs and environmental friendliness.

According to Wahib et al. [7] arrayed vibrational energy harvesters (VEH) can capture energy over a wide frequency range, whereas single VEH can only harvest energy over a restricted frequency band. As a result, arrayed VEH can generate more power and are more favorable than single VEH. Similarly, Saxena et al. [4] noticed that the resonating frequency is primarily determined by the beam length, which can be adjusted to achieve a lower resonating frequency and thus a more efficient output. According to the researchers Saadon and Wahab, trapezoidal cantilever beam can produce 30% more power and has the ability to generate twice as much energy as rectangular-shaped beam [8].

In this paper different structure of vibrational energy harvesters such as unimorph VEH, bimorph VEH, spiral shaped VEH, miscellaneous VEH and arrayed VEH are compared and analyzed and in addition to that a further analysis is also made with respect to the type of piezoelectric materials, so as to choose the best vibrational energy harvester that produces highly efficient output.

Layout of this paper is as follows. Design structures of vibrational energy harvester is described in Sect. 2. Section 3 explains about various types of piezoelectric materials and Finally Sect. 4 talks about the conclusion of the work [3, 9–11].

2 Design Structures and Configurations of Energy Harvesters

A. Unimorph Vibrational Energy Harvester (VEH)

Unimorph vibrational energy harvester structure can be defined as a cantilever beam with one side covered with piezoelectric material, as shown in Fig. 1.

Proper isolation is provided to prevent the current from flowing through the substance [5].

B. Bimorph Vibrational Energy Harvesters (VEH)

Fig. 1 Unimorph energy harvester [5]

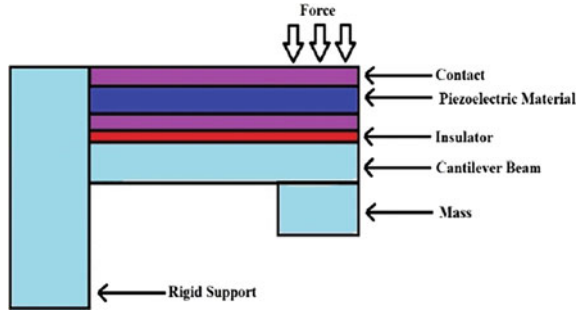
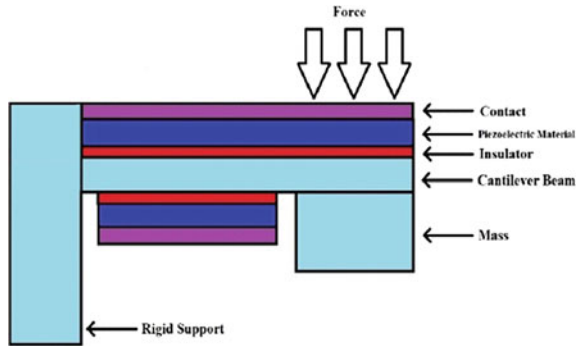


Fig. 2 Bimorph energy harvester [5]



Bimorph vibrational energy harvester structure can be defined as the cantilever beam in which either side of the beam is covered with the piezoelectric material. As shown in Fig. 2.

The structure is insulated with the help of insulator so as to resist the current flow inside the material [5].

C. Unimorph Energy Harvester Versus Bimorph Energy Harvester

A heavy weight proof mass is attached to both structures, allowing them to vibrate when force is applied.

Force applied to a piezoelectric material generates charge, which can be expressed mathematically as follows.

$$Q = d \times F \text{ Coulombs} \tag{1}$$

where Q denotes the charge acquired from the piezoelectric material.

d denotes the crystals charge sensitivity (Coulombs/Newton).

F signifies the amount of mechanical force exerted on the material.

Output voltage can be derived from the basic expression as follows.

$$V_o = \frac{Q}{C} \tag{2}$$

where Q represents charge in coulombs and C represents capacitance of the energy harvester.

$$\text{Capacitance } C = \frac{\epsilon_o \epsilon_r A}{t} \tag{3}$$

$$\text{Output Voltage } V_o = \frac{(d \times F \times t)}{(\epsilon_o \epsilon_r A)} \tag{4}$$

$$V_o = \left(\frac{d}{\epsilon_o \epsilon_r} \right) \times \left(\frac{F}{A} \right) \times (t) \tag{5}$$

$$V_o = g \times P \times t \tag{6}$$

where V_o represents output voltage,

g denotes voltage sensitivity (Vm/N).

P denotes the pressure that is applied on the crystal of the piezoelectric energy harvester (N/m²).

t denotes the crystals thickness (meters) [1, 5].

When both energy harvesters are subjected to the same amount of force, the bimorph vibrational energy harvester with dual piezoelectric patch displaces 4.45% more and provides 40.08% more output than that of the unimorph energy harvester with single piezoelectric patch [5].

D. Spiral Shaped Energy Harvester

Reducing the resonating frequency is one way to improve the efficiency of the generated output. The resonating frequency can be reduced by designing the structure in a spiral shape and to further reduce the resonant frequency, a proof mass is inserted to the structures center [1] (Figs. 3 and 4).

Fig. 3 Spiral shaped piezoelectric energy harvester [3]

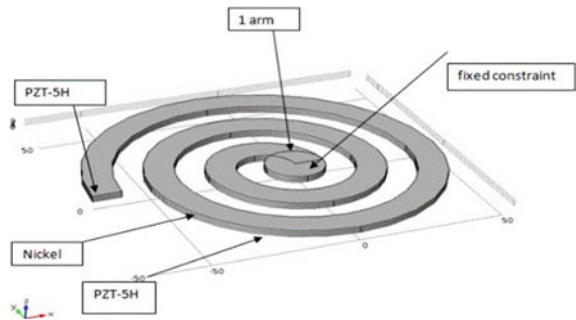
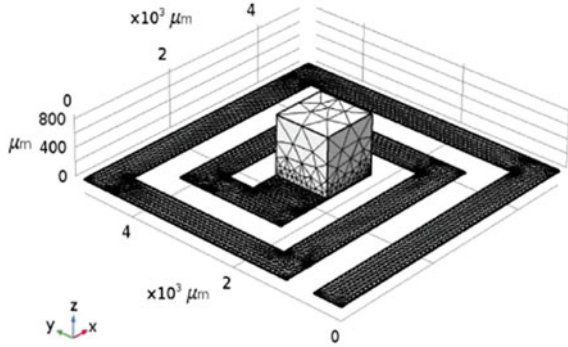


Fig. 4 Spiral shaped piezoelectric cantilever structure [1]



The maximum voltage and power of a piezoelectric energy harvester are obtained at the resonating frequency, which is expressed as follows.

$$\omega = \sqrt{\frac{K}{m}} \tag{7}$$

where **K** denotes the cantilever structure’s stiffness and **m** denotes the cantilever structure’s mass [1].

The most sensitive type of energy harvester is a spiral shaped piezoelectric energy harvester. Spiral shaped energy harvesters are limited to a few millivolts because they can generate output voltages ranging from a few microvolts to a few millivolts [3].

E. Miscellanenous Shaped Energy Harvester

Using (AlN) Aluminum Nitride piezoelectric material, a special unique design of energy harvester was developed. This kind of structure was developed to achieve wide band response at low frequencies (Fig. 5).

AlN piezoelectric material was preferred to design this unique structure because of its ecofriendly nature and biocompatibility. We can be able to generate a wide band of 10 Hz at a low resonating frequency of 57 Hz and an output voltage of 2.5–4 mV can be developed under the acceleration of 0.1–0.6 g [6].

F. Array Shaped Vibrational Energy Harvesters

It is not possible to generate the maximum amount of output with a single element cantilever energy harvester. To address this issue, an array shaped vibrational energy harvester has been developed.

When compared to a single element vibrational energy harvester, an array shaped vibrational energy harvester can generate more power and voltage. When compared to a single element vibrational energy harvester, an arrayed vibrational energy harvester has a lower frequency response [8] (Figs. 6 and 7).

G. Few Types of Array Shaped Vibrational Energy Harvesters (Figs. 8, 9 and 10)

Fig. 5 MEMS-based (ALN) energy harvester [6]

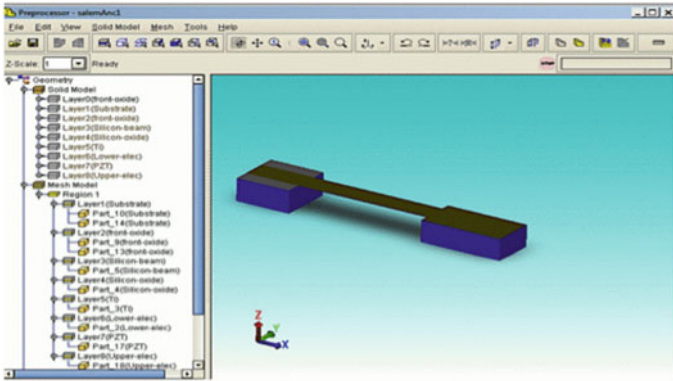
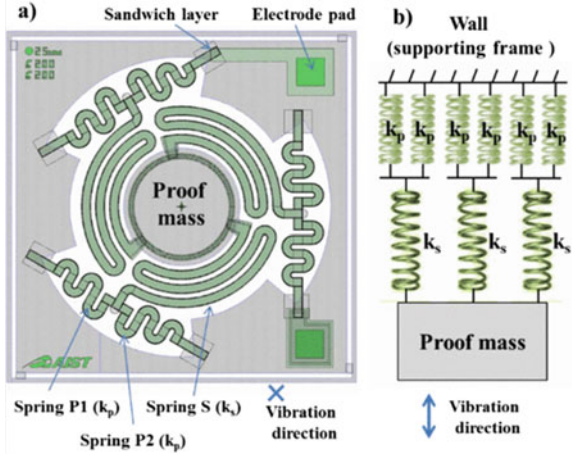


Fig. 6 Single element VEH [8]

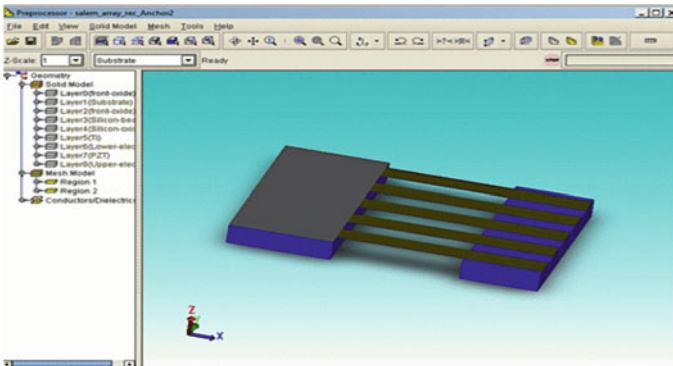


Fig. 7 Five element array shaped VEH [8]

Fig. 8 Top proof mass (TPM) [7]

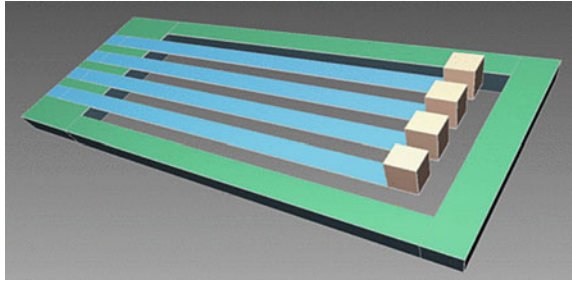


Fig. 9 Back etch mass (BEM) [7]

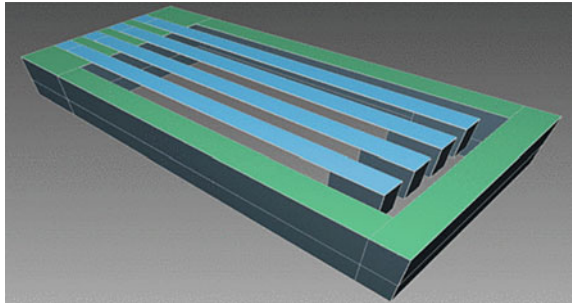
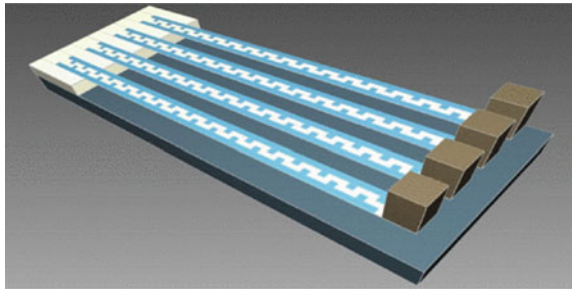


Fig. 10 Interdigitated electrode (ITE) [7]



Among these arrayed vibrational energy harvesters (top proof mass, back etch mass, interdigitated electrode design), top proof mass is found to be an excellent choice because it yields a huge amount of power with small size [7] (Table 1).

3 Types of Piezoelectric Materials

Piezoelectric material is responsible for developing electrical output by the applications of mechanical stress (vibrations) [2]. Most commonly used material are PZT-5H, Zinc Oxide (ZnO), Aluminum Nitride (AlN), etc. [1, 5, 6]. The output voltage

Table 1 Structures and output voltages

S. No	Design structure	Voltage	References
1	Unimorph VEH	200 mV	[5]
2	Bimorph VEH	280.16 mV	[5]
3	Spiral shaped VEH	Up to few milli-Volts	[3]
4	Miscellaneous VEH	4 mV	[6]
5	Arrayed shaped VEH	0.4 V	[8]

and power are particularly influenced by displacement. When the same amount of force is applied to these piezoelectric materials, it is discovered that PZT-5H displaces more and produces a high efficient output [5] (Tables 2 and 3).

Table 2 Piezoelectric materials and there usages

S. No	Piezoelectric material	Usage	References
1	PZT-5H	Typically used in situations where there is a high demand for power	[5]
2	ZnO	Used in implantable devices due to its biocompatibility	[1]
3	AlN	It is preferred due to its low manufacturing cost and eco-friendliness	[6]

Table 3 Vibrational energy harvester design comparisons

Names	Unimorph VEH	Bimorph VEH	Spiral shaped VEH	Miscellaneous VEH	Array shaped VEH
Piezoelectric material	PZT-5H	PZT-5H	–	AlN	PZT
Dimensions	1050 × 80 × 500 μm	1050 × 80 × 500 μm	In terms of μm	7 × 7 mm die size	–
Output voltage	200 mV	280.16 mV	Range From μV-mV	2.5–4 mV	0.4 V
Output power	–	–	1–10 μW	–	6.8 μW
Resonating frequency	–	–	–	57 Hz	67–70 Hz
Acceleration/load	1 N	1 N	–	(0.1–0.6 g)	(0.2 to 1.3 g)/20.1 KΩ

4 Conclusion

Different vibrational energy harvester design structures are seen and analyzed, as well as different types of piezoelectric materials. Highly efficient output with high power density and high voltage at low resonating frequency can be obtained by using arrayed vibrational energy harvester made up of PZT-5H piezoelectric material as it provides more displacement.

References

1. Anand, A., Kundu, S.: Design of mems based piezoelectric energy harvester for pacemaker. In: 2019 Devices for Integrated Circuit (DevIC), Kalyani, India, Mar 2019, pp. 465–469 (2019). <https://doi.org/10.1109/DEVIC.2019.8783311>
2. Sasrika, V., Lakshmi, P., Mangaiyarkarasi, P.: Power enhancement of MEMS based piezoelectric energy harvester for bio-fuel cells. In: 2019 IEEE International Systems Conference (SysCon), Orlando, FL, USA, Apr 2019, pp. 1–7 (2019). <https://doi.org/10.1109/SYSCON.2019.8836736>
3. Taj, M., Vikram, G.N.V.R.: Design and simulations of high-sensitivity multi-directional inertial sensor. *IEEE Sens. J.* **22**(1), 190–194 (2022). <https://doi.org/10.1109/JSEN.2021.3126469>
4. Saxena, S., Sharma, R., Pant, B.D.: Design and development of cantilever-type MEMS based piezoelectric energy harvester. In: 2015 19th International Symposium on VLSI Design and Test, Ahmedabad, India, Jun. 2015, pp. 1–4 (2015). <https://doi.org/10.1109/ISVDAT.2015.7208045>
5. Sil, I., Biswas, K.: Investigation of design parameters in MEMS based piezoelectric vibration energy harvester. In: 2018 IEEE Electron Devices Kolkata Conference (EDKCON), Kolkata, India, Nov. 2018, pp. 64–69 (2018). <https://doi.org/10.1109/EDKCON.2018.8770388>
6. Zhang, L., Takei, R., Lu, J., Makimoto, N., Kobayashi, T., Itoh, T.: Development of wide-band low-frequency MEMS vibration energy harvester for utility infrastructure core monitoring system. In: 2017 Symposium on Design, Test, Integration and Packaging of MEMS/MOEMS (DTIP), Bordeaux, France, May 2017, pp. 1–4 (2017). <https://doi.org/10.1109/DTIP.2017.7984481>
7. Wahib, K.A.A., Wahab, Y., Shakaff, A.Y.M., Saadon, S.: Array design consideration of the MEMS vibration energy harvester cantilever based structure: Top proof mass vs back etch mass vs interdigitated electrode design. In: 2015 IEEE Student Symposium in Biomedical Engineering & Sciences (ISSBES), UiTM, Shah Alam, Malaysia, Nov. 2015, pp. 64–69 (2015). <https://doi.org/10.1109/ISSBES.2015.7435915>
8. Saadon, S., Wahab, Y.: From ambient vibrations to green energy source: MEMS piezoelectric energy harvester for low frequency application. In: 2015 IEEE Student Symposium in Biomedical Engineering & Sciences (ISSBES), UiTM, Shah Alam, Malaysia, Nov. 2015, pp. 59–63 (2015). <https://doi.org/10.1109/ISSBES.2015.7435914>
9. Sahoo, S.: Conduction and switching behavior of e-beam deposited polycrystalline Nb₂O₅ based nano-ionic memristor for non-volatile memory applications. *J Alloys Compounds* **866**, 158394 (2021). <https://doi.org/10.1016/j.jallcom.2020.158394>
10. Sahoo, S., Prabakaran, S.R.S.: Nano-ionic solid state resistive memories (re-RAM): A review. *J. Nanosci. Nanotechnol.* **17**(1), 72–86 (2017)
11. Sahoo, S., Manoravi, P., Prabakaran, S.R.S.: Titania based nano-ionic memristive crossbar arrays: fabrication and resistive switching characteristics. *Nanosci Nanotechnol Asia* **9**(4), 486–493 (2019)

Surface Characterization of $Mn_{1.0}Co_{1.9}Fe_{0.1}O_4$ (MCF) Spinel Coating on Metallic Interconnect Used in Solid Oxide Fuel Cells



N. Manjunath and B. Rajasekaran

Abstract This study deals with the microstructure evaluation and analysis of surface uniformity of $Mn_{1.0}Co_{1.9}Fe_{0.1}O_4$ (MCF) spinel coating deposited by atmospheric plasma spray (APS) on Crofer 22 APU used in solid oxide fuel cells applications. 3-D confocal profilometer and SEM (EDS) have been used to examine the quality of surface, microstructure, and chemical composition. The 3-D analysis of the coated surface showed the variation in uniformity of ridges and grooves of the coated Crofer steel. The microstructure analysis using a scanning electron microscope (SEM) revealed the partially melted particles and microcracks networks.

Keywords Atmospheric plasma spray (APS) · Spinel coatings · Solid oxide fuel cells (SOFC) · Metallic interconnect · 3-D confocal profilometer · Surface isotropy

1 Introduction

Solid oxide fuel cells (SOFCs) have been extensively used as it has exhibited high efficiency in the direct conversion of chemical energy of fuel into electrical energy [1]. SOFC uses dense gas tight solid yttria-stabilized zirconia (YSZ) as electrolyte, Ni-YSZ as anode and lanthanum strontium manganite (LSM) as cathode material [2]. To achieve high output efficiency, fuel cells are stacked in series using interconnects that create a connection between single cells and also separate fuel and oxidant gas [3]. Traditionally used interconnect material, Lanthanum Chromite ($LaCrO_3$), exhibited remarkably high electrical conductivity, good stability in both anode and cathode environments, close match of thermal expansion coefficient with other components. But the decrease in conductivity with the reduction in oxygen partial pressure, limited availability of processing methods, and cost ineffectiveness led to the introduction of

N. Manjunath (✉) · B. Rajasekaran
Department of Metallurgical and Materials Engineering, National Institute of Technology
Karnataka, Surathkal 575025, India
e-mail: manjunathnk91@gmail.com

B. Rajasekaran
e-mail: b.rajasekaran@nitk.edu.in

© The Author(s), under exclusive license to Springer Nature Singapore Pte Ltd. 2023
V. Bindhu et al. (eds.), *Proceedings of Fifth International Conference on Inventive Material Science Applications*, Advances in Sustainability Science and Technology,
https://doi.org/10.1007/978-981-19-4304-1_25

277

metallic interconnects as a substitute to LaCrO_3 ceramic material [4]. Metallic interconnects, especially chromium steels, have been considered because of their excellent electrical conductivity, stability in both oxidative and reducing atmospheres, adaptable thermal expansion coefficient to other components, improved fracture toughness, etc. [1, 3–5]. Water vapor is a common gaseous species found in anode and cathode environments. Although the concentration of water vapor on the cathode end is low, it can inflate the chromium volatilization by altering the oxidation behavior of the interconnect [6]. The chromium-containing steels contain oxides of chromium on the surface that tend to evaporate under a water vapor environment during the high operating temperature (650–850 °C) of SOFC [7]. This chromia deposits on the cathode side of the cell and blocks the active electrochemical sites, ultimately reducing the overall performance of the cells [1, 8].

The proposed mechanisms for preventing chromium evaporation are: protecting by binding the gaseous species of chromium chemically using porous coatings or by dense coatings which block the gas route for migration. As the former method does not prevent chromium evaporation entirely and reduces the lifetime of the SOFC stack, dense coatings on the interconnect are being extensively used [5]. The coatings should exhibit high electrical conductivity, be chemically stable under oxidizing environment, have high density, and have a well-matched thermal expansion coefficient with the interconnect [3, 8]. $\text{Mn}_{1.0}\text{Co}_{1.9}\text{Fe}_{0.1}\text{O}_4$ (MCF) spinel coating have shown promising outcome in preventing chromium evaporation from metallic interconnect, improving the electrical conductivity of the substrate material, and reducing contact resistance with cathode [9]. Atmospheric plasma spraying (APS) is the best-suited method to deposit the protective coating.

The present study aims to characterize surface of $\text{Mn}_{1.0}\text{Co}_{1.9}\text{Fe}_{0.1}\text{O}_4$ (MCF) coated Crofer metallic interconnect and its uniformity and chemical homogeneity. The coated interconnects were characterized using a 3-D confocal profilometer and scanning electron microscopy (SEM). The confocal profilometer was used to study the surface isotropy of the coating, and variation in uniformity of the coating on ridges and grooves. The surface morphology of the coating and chemical analysis was performed by scanning electron microscopy (SEM) equipped with energy-dispersive X-ray spectroscopy (EDS).

2 Experimental Procedure

2.1 Materials and Methods

A manganese-cobalt-iron (MCF) oxide powder having a spinel structure (H.C. Starck, Laufenburg, Germany) was used for the coating on Crofer 22 APU (ThyssenKrupp VDM GmbH, Werdohl, Germany). The deposition of the coating was carried out using Atmospheric Plasma Spray TriplexPro210 gun (Oerlikon Metco, Wohlen, Switzerland). The chemical composition of the coating powder was: 23.5

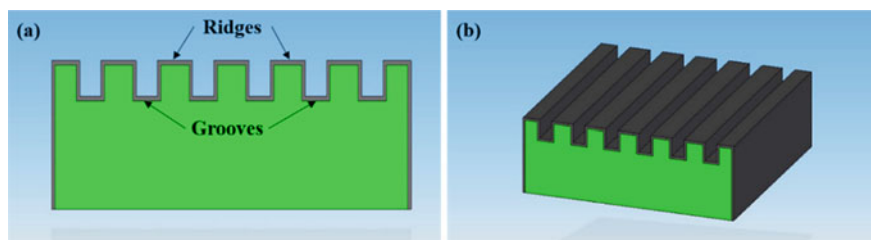


Fig. 1 3-D model of SOFC interconnect with spinel coating indicating ridges and grooves

wt.% Mn, 47.6 wt.% Co, 2.4 wt.% Fe, and 26.5 wt.% O [1, 3, 5]. Figure 1 indicates 3-D model of the linear channel structure replicating the original SOFC interconnect component on which the coating was deposited.

2.2 Characterization

The coated surface was characterized using 3-D Confocal Profilometer (ST400, NANOVEA, USA). A high-speed sensor of resolution $110\ \mu\text{m}$ was used for the scan, and the step size used for the scan was $5\ \mu\text{m}$. The surface isotropy and features of furrows and their parameters were obtained. The topographies captured from the scan were analyzed in Digital Surf Mountain 9 software and parameters related to surface isotropy were obtained to understand the variation in uniformity of the surface. The arithmetic mean of absolute height (R_a) was also assessed on the ridge and groove. The EUR15178N standard was used for roughness and isotropy characterization. A Scanning Electron Microscope (JEOL JSM-6700F, Japan) was used to characterize the surface morphology of the coating. The EDS analysis was performed by considering a spot and area on the coating to estimate the chemical composition of coated surface.

3 Results and Discussion

3.1 Texture Isotropy Analysis

Figure 2 displays the surface furrows and texture isotropy of the ridges and grooves of MCF coated Crofer steel interconnect. Figure 2a, c display the surface furrows where the mean depth of the furrows was estimated. The mean depth of the furrows of the ridge was $11.90\ \mu\text{m}$ and that of the groove was $14.00\ \mu\text{m}$ (Table 1). The correlation of the parameters in Table 1 indicates the uniformity in the surface structure of the ridge in comparison to the groove. The roughness of a surface can be examined

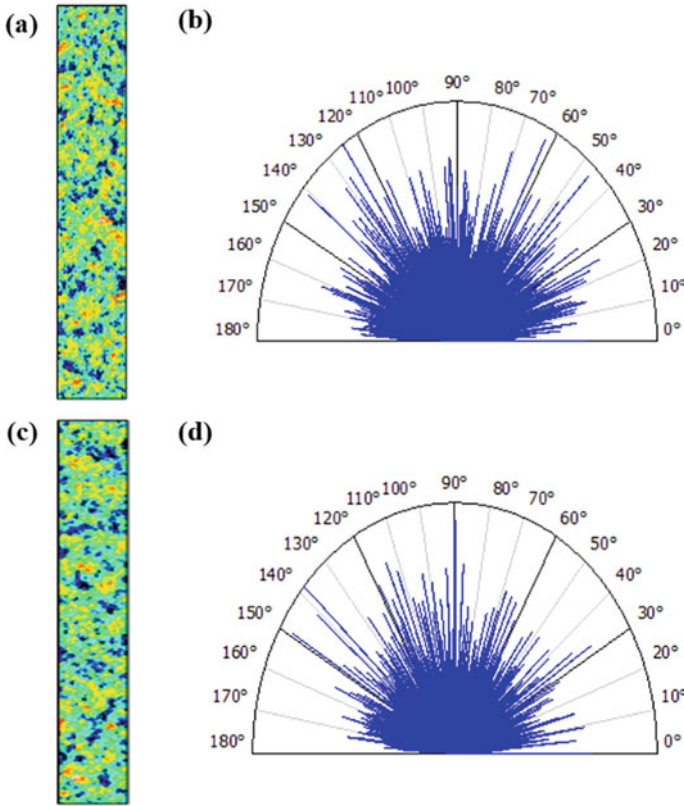


Fig. 2 a Surface furrows of the ridge. b Texture isotropy of ridge. c Surface furrows of the groove d Texture isotropy of groove

Table 1 Parameter of furrows measurement of ridge and groove of interconnect

Parameters	Ridge	Groove
Maximum depth (μm)	31.66	38.66
Mean depth (μm)	11.90	14.00
Mean density (cm/cm^2)	577.0	683.9

by considering the direction of surface irregularities. The surface is isotropic if the topographies are independent of direction or randomly structured and the surface is anisotropic if the surface is oriented in the same direction [10, 11]. Figure 2b, d show that the ridges are comparatively isotropic than the grooves. The isotropy value of a surface nearing 100% is considered to be an isotropic surface, whereas an anisotropic surface represents a value near 0%. It was observed that the characteristics of an isotropic surface reduce as the angle of inclination increases [12]. The evolution of

Table 2 Texture isotropy parameter of ridge and groove of interconnect

Parameters	Ridge	Groove
Isotropy (%)	28.99	3.56
First direction (°)	125.0	138.2
Second direction (°)	140.8	149.3
Third direction (°)	62.20	89.98

the parameters such as surface roughness, texture, and directional isotropy patterns are useful in establishing the quality processing of coating [13].

The parameters determined for surface isotropy from the confocal profilometer are based on ISO 25178 [14]. The calculation of the parameters related to the isotropy of the surface is based on the autocorrelation function (ACF) where the surface of the specimen in one direction, i.e., z -direction, in contrast to the surface in the same direction at a different position, i.e., x and y direction is considered. The corresponding length between the surface profiles is evaluated [11]. The ridge of the coated steel has an isotropy value of 28.99% and that of the groove has a value of 3.56% (Table 2). The arithmetic mean of absolute height (R_a) was 4.82 μm and 5.12 μm for ridge and groove, respectively. This indicates that the ridges have a relatively uniform surface in comparison to the grooves.

3.2 Surface Morphology of MCF Coating

Figure 3 shows the surface morphology of the MCF coating in as-sprayed conditions at different magnifications. Figure 3a indicates the ridges and grooves of the Crofer steel interconnect on which the coating was deposited. Figure 3b displays the coating powder's un-molten or partially melted particles, which is a typical intrinsic defect in atmospheric plasma sprayed coatings [15]. The surface has a relatively coarse structure and phases are densely distributed without the appearance of voids. The coating shows high density with the visibility of cracks (Fig. 3c) [1]. During the atmospheric plasma spraying, the plasma plume contains thermo-chemically transformed particles that are partially or completely melted to form into fused clusters. This is caused

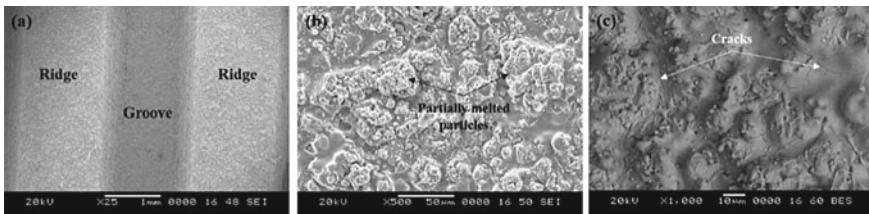


Fig. 3 SEM micrographs of **a** surface indicating ridge and groove of the interconnect, **b** surface morphology of coating (500X), **c** surface morphology of coating (1000X)

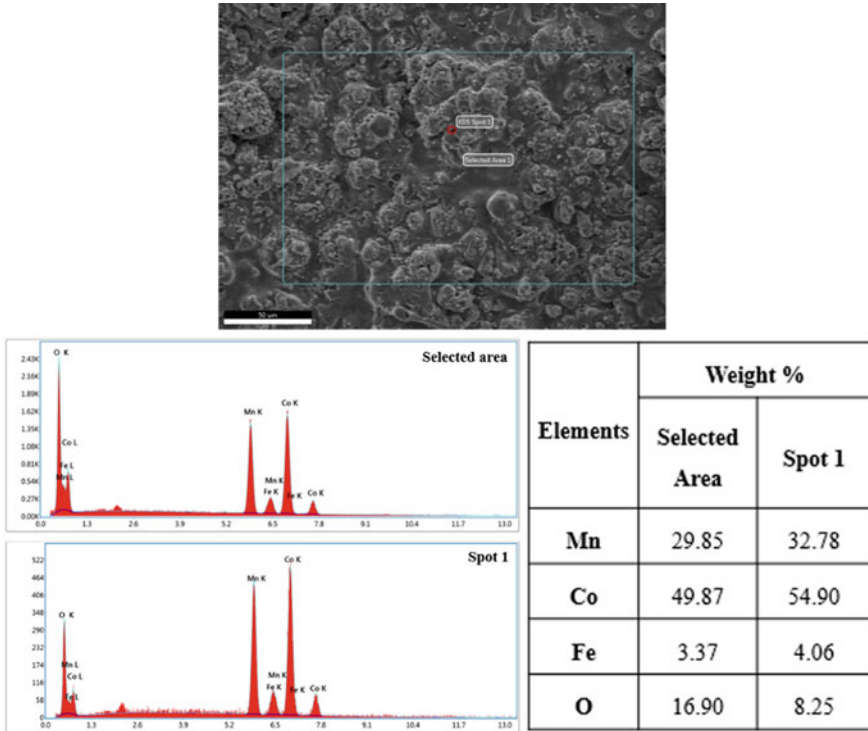


Fig. 4 EDS analysis (spot and selected area) of the coating

due to a very high temperature in the plasma plume, leading to agglomerates of the fused cluster particles on the coating [16].

Figure 4 displays the selected spot and area for EDS analysis and provides comprehensive data on the composition of the elements in the coating in as-sprayed conditions. The data confirmed the presence of Mn, Co, Fe, and O in agreeable weight percentage compared to the coating powder’s nominal composition used in feedstock for APS process. The wt.% of Co is highest and CoO is the main phase in the as-sprayed condition which is a metastable rock salt phase. This is caused due to rapid solidification during the atmospheric spray process [8].

The effect of the plasma plume on the coating enables a good understanding of the distribution of the coating particles on the substrate. The distribution of the particle velocity and the particle temperature was homogeneous over the cross-section of the plume [17, 18]. The spray deposition in atmospheric plasma spray takes place in the core of the plasma plume where the growth rates are very fast. The plasma jet’s fast relative motion (with respect to robot speed) produces a homogenous distribution of feedstock powder on the substrate [17]. The feedstock powder having a diameter of 5 μm melt, spheroidize, and oxidizes whereas the feedstock powder greater than 15 μm softens and undergoes surface oxidation when the particles are near the plasma

plume core. As the concentration of oxygen across the plasma plume is uniform, the time required for the oxidation of the particles, which is tenths of milliseconds, is sufficient for the formation of oxide layers on the deposit [18, 19]. It was also studied that more than 90% of the feedstock powder is passed at the core of the plasma plume whereas 10% of the particles pass through the periphery having low velocity and temperature [20]. In the present study, it can be understood that the plasma plume affected the uniformity of the coating over the ridges and grooves. The core of the plasma plume, where the feedstock powder attains very high temperature and velocity, affected the ridge of the interconnect. This led to a relatively uniform coated surface on the ridge. The grooves were affected by the periphery of the plasma plume which contained un-melted and low velocity particles created anisotropy surface. It should be noted that coating has also been deposited at the side wall of the ridges leads to non-uniformity of coating deposition on the grooves. The difference in uniformity/isotropy was evaluated using confocal profilometer.

4 Conclusions

1. From the surface analysis using a 3-D confocal profilometer, the surface of the ridges is seen to be relatively uniform in comparison to the grooves. The surface isotropy of the ridge was 28.99% and that of the groove was 3.56%. The mean depth of the surface furrows for ridge and groove were 11.99 μm and 14.00 μm , respectively. The non-uniformity in the coated Crofer steel can be attributed to the plasma plume.
2. The surface of the coating characterized by scanning electron microscopy revealed the partially melted particles and network of microcracks.
3. MCF coating chemistry was uniform at the surface and is confirmed by EDS analysis. This implies that the coating retained the chemistry from feedstock powder.

Acknowledgements The authors express sincere thanks to Prof. Dr. Robert Vassen, Deputy Director, (IEK-1:Materials Synthesis and Processing) Institute of Energy and Climate Research, Forschungszentrum, Juelich, Germany, for sharing the MCF coating Crofer 22 APU samples.

References

1. Vaßen, R., et al.: Aging of atmospherically plasma sprayed chromium evaporation barriers. *Surf. Coatings Technol.* **291**, 115–122 (2016)
2. Dwivedi, S.: Solid oxide fuel cell: Materials for anode, cathode and electrolyte. *Int. J. Hydrogen Energy* **45**(44), 23988–24013 (2020)
3. Grünwald, N., Sebold, D., Sohn, Y.J., Menzler, N.H., Vaßen, R.: Self-healing atmospheric plasma sprayed Mn_{1.0}Co_{1.9}Fe_{0.1}O₄ protective interconnector coatings for solid oxide fuel cells. *J. Power Sour.* **363**, 185–192 (2017)

4. Wu, J., Liu, X.: Recent development of SOFC metallic interconnect. *J. Mater. Sci. Technol.* **26**(4), 293–305 (2010)
5. Grünwald, N., Sohn, Y.J., Yin, X., Menzler, N.H., Guillon, O., Vaßen, R.: Microstructure and phase evolution of atmospheric plasma sprayed Mn-Co-Fe oxide protection layers for solid oxide fuel cells. *J. Eur. Ceram. Soc.* **39**(2–3), 449–460 (2019)
6. Niewolak, L., Tietz, F., Quadackers, W.J.: Interconnects (2016)
7. Singheiser, L., Huczowski, P., Markus, T., Quadackers, W.J.: 1.19—High temperature corrosion issues for metallic materials in solid oxide fuel cells A2—Stott, Bob Cottis Michael Graham Robert Lindsay Stuart Lyon Tony Richardson David Scantlebury Howard, pp. 482–517 (2010)
8. Back, H.C., Gibmeier, J., Vaßen, R.: Phase transformation-induced changes in microstructure and residual stresses in thermally sprayed MnCoFeO₄ protective coatings. *J. Therm. Spray Technol.* **29**(6), 1242–1255 (2020)
9. Wang, K., Liu, Y., Fergus, J.W.: Interactions between SOFC interconnect coating materials and chromia. *J. Am. Ceram. Soc.* **94**(12), 4490–4495 (2011)
10. Damiati, L., et al.: Impact of surface topography and coating on osteogenesis and bacterial attachment on titanium implants. *J. Tissue Eng.* **9**(August) (2018)
11. Boettcher, K., Winkeljann, B., Schmidt, T.A., Lieleg, O.: Quantification of cartilage wear morphologies in unidirectional sliding experiments: Influence of different macromolecular lubricants. *Biotribology* **12**(June), 43–51 (2017)
12. Grimm, T., Wiora, G., Witt, G.: Characterization of typical surface effects in additive manufacturing with confocal microscopy. *Surf. Topogr. Metrol. Prop.* **3**(1) (2015)
13. Leroux, P.: Fast & high resolution large surface measurement with 3D fast & high resolution large surface measurement with 3D profilometry Prepared by Duanjie Li , PhD, no. January (2016)
14. Cheng, F., Fu, S., Chen, Z.: Surface texture measurement on complex geometry using dual-scan positioning strategy. *Appl. Sci.* **10**(23), 1–13 (2020)
15. Odhiambo, J.G., Li, W.G., Zhao, Y.T., Li, C.L.: Porosity and its significance in plasma-sprayed coatings. *Coatings* **9**(7), 1–19 (2019)
16. Tummala, R., Guduru, R.K., Mohanty, P.S.: Nanostructured Co₃O₄ electrodes for supercapacitor applications from plasma spray technique. *J. Power Sour.* **209**, 44–51 (2012)
17. Von Niessen, K., Gindrat, M.: Plasma spray-PVD: a new thermal spray process to deposit out of the vapor phase. *J. Therm. Spray Technol.* **20**(4), 736–743 (2011)
18. Von Niessen, K., Gindrat, M., Refke, A.: Vapor phase deposition using plasma spray-PVDTM. *J. Therm. Spray Technol.* **19**(1–2), 502–509 (2010)
19. Anupam, A., et al.: Understanding the microstructural evolution of high entropy alloy coatings manufactured by atmospheric plasma spray processing. *Appl. Surf. Sci.* **505**(June 2019), 144117 (2020)
20. Vardelle, A., Vardelle, M., Fauchais, P.: Influence of velocity and surface temperature of alumina particles on the properties of plasma sprayed coatings. *Plasma Chem. Plasma Process.* **2**(3), 255–291 (1982)

Performance Optimization of IGZO-Based Junctionless Thin Film Transistor for Low Power Application



Shraddha Yogi and Alok Naugarhiya

Abstract This paper proposed design and analysis of an Indium Gallium Zinc Oxide (IGZO)-based Junctionless Thin Film Transistors (JLTFT), using 20 nm Silicon On Insulator (SOI) technology. High dielectric constant (k) material HfO_2 is used as gate insulator and buried oxide layer. The proposed device structure is analyzed using Silvaco TCAD ATLAS™ 2-D simulator. The geometry of the device structure has been successfully optimized by using vertical gate stacking technique and making variations in the channel and buried oxide layer thickness. The proposed device has a very high $I_{\text{ON}}/I_{\text{OFF}} = 2.14 \times 10^7$ and a low subthreshold swing = 72.67 mV/decade ensuring a better current driving capability and high speed of operation. It shows 21.9% improvement in Subthreshold Swing (SS) as compared to device present in reference work. The proposed IGZO-based JLTFT device, which is designed using SOI technology on HfO_2 dielectric, will make it high performance and cost-effective device for low power applications.

Keywords Optimization · Silicon on insulator (SOI) · Junctionless thin film transistor (JLTFT) · Short channel effects (SCEs) · Indium gallium zinc oxide (IGZO) · Silvaco TCAD · Subthreshold swing (SS)

1 Introduction

From the past 50 years, the Moore's law has been the main motivation for the growth in semiconductor industry. According to this law, the no. of transistors in an IC will become double in every 2 years [1]. As a result, the downscaling of the MOSFET devices has continuously been carried out to meet Moore's law and promote device performance, switching speed, low operating power and packing density. However, the main difficulties that arise with the downscaling are the Short Channel Effects (SCEs), which involve velocity saturation, change in threshold

S. Yogi (✉) · A. Naugarhiya

Department of Electronics and Communication Engineering, National Institute of Technology, Raipur 492001, India

e-mail: syogi.mtech2020.etc@nitrr.ac.in

voltage, Hot Carrier Effect (HCE) and Drain induced barrier lowering (DIBL) [2]. Due to this, Subthreshold Swing (SS) degrades and OFF current increases, etc. To solve the problem of SCEs and gate leakage current, various techniques can be used such as, gate electrodes with dual work function, hetero dielectric and making variations in oxide materials and dimensions. The current driving capabilities of the device can be improved by using gate electrodes with dual work function. Usage of high dielectric constant (k) material like HfO_2 improves the performance of the device through the reduction in the gate leakage current [3–6].

The SOI technology plays a significant role in decreasing SCEs and increasing current densities, yet simultaneously allowing continuous miniaturization of the devices. In SOI technology, a semiconductor device is fabricated on layered silicon insulator–silicon substrate. The main advantage of SOI technology is that it improves IC performance and reduces power consumption by improving the current driving capability as well as reducing parasitic capacitance and leakage [3]. However, there are some disadvantages of SOI technology such as SCE's and charge trapping [6, 7]. The main reason for the increase in SCEs and degradation in subthreshold slope is the lateral expansion of the depletion width in the channel region. This issue can be solved by Junctionless Thin film Transistors (JLTFT) [8–11]. An n -type Junctionless TFT (JLTFT) is a variable gated resistor controlled by a gate electrode with homogeneously doped ($n+-n+-n+$) source, drain and channel regions. JLTFTs effectively reduces interface scattering because the current flows as a body current and not as a surface current. A JLTFT is typically used in a device that requires a fully depleted channel or workfunction difference between the gate and the channel to turn off the JLTFT. Therefore, a JLTFT requires an ultrathin body structure to achieve a fully depleted channel region in the OFF state. JLTFT have uniform and heavy doping across the source, drain and channel region, which avoids the formation of any PN junctions. Hence, the necessity of doping concentration gradients can be avoided, which simplifies the fabrication process flow. Therefore, it allows the scalability of the device without increasing the issue of SCEs [12]. The charge trapping is caused by the formation of imperfect crystalline structure at the interface of silicon and different dielectric materials used for gate and buried oxide. There are some deformities at the point of contact between silicon and insulator, which is responsible charge trapping which leads to the surge in leakage current and degrades the device's speed [3, 7]. This charge trapping decreases the ON current and increases the threshold voltage, which further degrades the SS [3]. An IGZO-based JLTFT using SOI technology is proposed to solve such issues.

There are several materials used for making Thin Film Transistors (TFTs), including amorphous silicon (a-Si), low-temperature polycrystalline silicon (LTPS), Zinc Oxide (ZnO) and indium gallium zinc oxide (IGZO). Among all these materials, IGZO is preferred because of its various advantages over other materials like the high value of $I_{\text{ON}}/I_{\text{OFF}}$ ratio, low leakage current and less power consumption [13]. IGZO is a non-toxic, soluble and artificial compound that is transparent and compatible with other materials. The visible wavelength ranging of IGZO transparent is 300–1000 nm. A higher and wider bandgap (3.05 eV) provides better insulation to leakage current and makes it a desirable material for several displays, RF and low

power applications [14–16]. The high mobility of IGZO compound improves the current driving capability of the device and also increases the switching speed [17]. The electrical properties of the IGZO compound mainly depend upon its components: Indium, Gallium and Zinc Oxide. IGZO is doped with Ga_2O_3 and In_2O_3 . Indium provides a high mobility, and Gallium provides a reduction in OFF current [18]. The stability and reduction in power consumption of an IGZO-based TFT device are improved due to the transparency and flexibility of the IGZO compound; hence further research works are going on for its various applications [17, 19].

2 Device Structure and Simulation

2.1 Theory

TFTs are a distinct class of metal-oxide-semiconductor field-effect transistors (MOSFETs) fabricated by depositing a layer of an active semiconductor layer, metallic contacts and the dielectric layer over an insulating substrate. In TFT, the current flow between source and drain is governed by the applied gate voltage. Due to this electric field is developed in the semiconductor layer that attracts and accumulates the charges. It creates the channel between the sources and drains contacts, allowing the flow of charge carriers.

For the operation of Field-Effect Transistor (FET) in saturation region ($V_{DS} > V_{GS} - V_{TH}$), the drain current equation is given as:

$$I_D = \frac{1}{2} \mu_n C_{OX} \frac{W}{L} (V_{GS} - V_{TH})^2$$

where

- μ_n Mobility of electrons,
- C_{OX} Oxide capacitance of the gate oxide layer per unit area,
- I_D Drain current,
- W Channel width,
- L Channel length and
- V_{TH} Threshold voltage of the device

In reported article [20], it is found that IGZO-based TFT shows better results than other TFT devices in terms of performance and other characteristics like SS, I_{ON}/I_{OFF} and leakage currents. Some changes in the calibration of the proposed device is done with reference to published work [20]. The variation in channel and buried oxide thickness is done to optimize the device further. The considered structure of IGZO JLTFT has a vertical gate stacked with a dual material work function to provide insulation to leakage current. Simulation of proposed device is done using

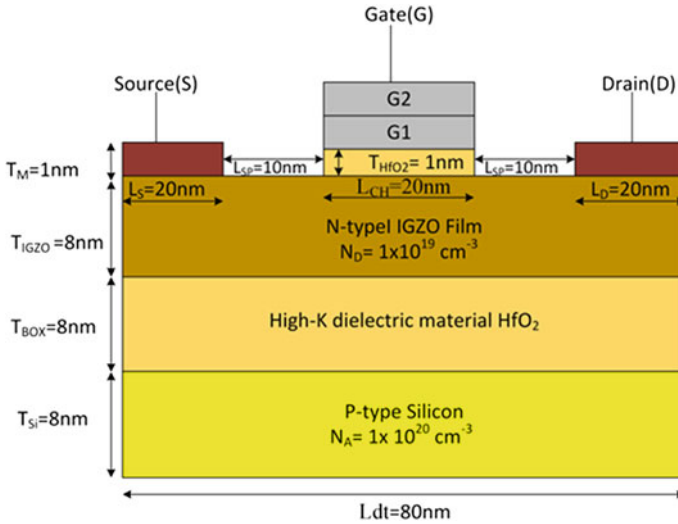


Fig. 1 Simulated 2-D structure of IGZO-based thin film transistor

the SILVACO ATLAS TCAD tool. The 2-D structure of the simulated device is shown in Fig. 1.

The proposed device has three layers which are silicon substrate, buried oxide and N-type doped IGZO layer. The dimensional parameters used for 2-D simulation of the device include gate length (L_G), film thickness (T_{IGZO}) and buried oxide layer (T_{BOX}) thickness as 20 nm, 8 nm and 8 nm, respectively. The device has a channel length of 20 nm and a thickness of 8 nm. High- k dielectric material HfO_2 is used as a gate insulator ($T_{HfO_2} = 1$ nm) and buried oxide ($T_{BOX} = 8$ nm). To make it Junctionless, IGZO layer is uniformly doped with a donor concentration of 1×10^{19} is applied in source, drain and channel region. Gate metal having dual work function with values 4.9 ($G1$) and 4.68 ($G2$) are used for optimization. For device simulation we have used three different materials for gate oxide and buried oxide layer, namely, SiO_2 , Al_2O_3 and HfO_2 . But the best results are obtained for HfO_2 ; as it has a higher dielectric constant; it provides better insulation to leakage currents by increasing the oxide capacitance per unit area. The analysis of the proposed device is carried out by varying the thickness as well as material of the buried oxide and also the gate oxide material. Table 1 consists of a specification of the optimized parameters of the device, which is taken for the simulation purpose.

For 2-D simulation of the device drift–diffusion model without impact ionization is used. This model is used for transport phenomenon of charge carriers. AUGER and SRH (Shockley Read Hall) models are used to calculate minority lifetime and recombination rate of the device. The bandgap variation caused by heavy doping of the device is modeled by bandgap narrowing (BGN) and Fermi Dirac is used to find the probability of availability of electrons in heavily doped region. In addition to

Table 1 Optimized parameter of the device

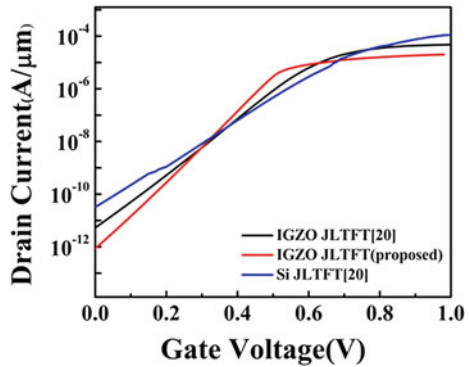
Specification	Symbol	IGZO JLTFE
Length of the device	L_{dt}	80 nm
Length of source and drain	L_D, L_S	20 nm
Spacer length	L_{SP}	10 nm
Gate and channel length	L_G, L_{CH}	20 nm
Gate oxide thickness	T_{HfO_2}	1 nm
Film material		IGZO
Film thickness	T_{IGZO}	8 nm
Buried oxide thickness	T_{BOX}	8 nm
Substrate thickness	T_{Si}	8 nm
Substrate concentration	N_A	1×10^{20}
Drain, source and channel concentration	N_D	1×10^{19}

this, constant field mobility (CONMOB) is used to consider the effect of low field mobility.

2.2 Results and Discussion

In this section, the various parameters like SS and I_{ON}/I_{OFF} are discussed for different devices. Variation in transfer characteristics and output characteristics of proposed device has also been analyzed w.r.t. change in buried oxide thickness. For validation of transfer characteristics of the proposed device, those parameters and models are considered which is reported in [20]. In Fig. 2, I_D versus V_{GS} characteristics of Silicon JLTFE, IGZO TFE and of the proposed device are compared. The graph in Fig. 2 shows that better results are obtained for the proposed device having channel length 20 nm and width 8 nm with HfO_2 as a buried oxide and gate oxide material. High

Fig. 2 I_D - V_{GS} curve of Silicon TFE, IGZO TFE and proposed device



I_{ON}/I_{OFF} current ratio and lower SS is advisable for better current drive capability and high speed operation of the device. OFF current (I_{OFF}) = 8.97×10^{-13} A/ μm and ON current (I_{ON}) = 1.92×10^{-5} A/ μm was obtained hence I_{ON}/I_{OFF} improves to 2.14×10^7 as compared to reference work [20].

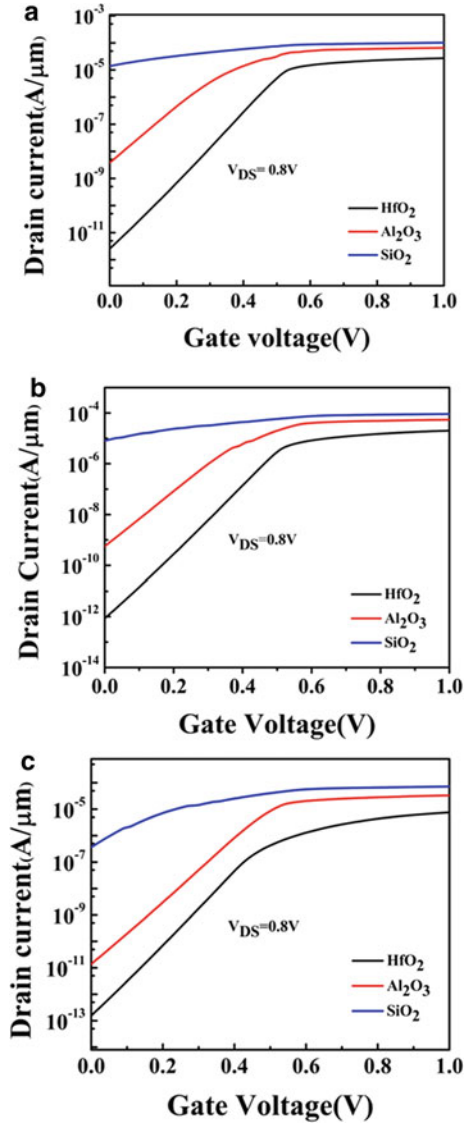
The vertical gate stacking technique provides better insulation to leakage current [21]. High dielectric constant material provides better controllability over the gate and increases gate capacitance without increasing the gate leakage current. Due to which I_{OFF} decreases and I_{ON}/I_{OFF} ratio increases which lead to improvement in SS also. The next graph in Fig. 3a–c shows the drain current variation with different oxides such as SiO_2 , Al_2O_3 and HfO_2 as gate oxide and buried oxide material with various thicknesses as 10 nm, 8 nm and 5 nm, respectively. For channel thickness 8 nm, $I_{ON}/I_{OFF} = 2.14 \times 10^7$ and $\text{SS} = 72.67$ mV/dec is obtained for HfO_2 as buried oxide at $V_{GS} = 1$ V and $V_{DS} = 0.8$ V. Assuming same data for Al_2O_3 , $I_{ON}/I_{OFF} = 1.05 \times 10^5$ and $\text{SS} = 90.08$ mV/dec and for SiO_2 , SS is 324.62 mV/dec with very poor I_{ON}/I_{OFF} ratio was observed. The results show that HfO_2 proves to be a better candidate to improve device performance. This is because replacing the SiO_2 gate insulator layer with a high dielectric material increases gate capacitance without increasing the associated leakage effects. Hence, HfO_2 provide better insulation to gate leakage. It is observed from simulation studies that on increasing the buried oxide thickness, I_{ON}/I_{OFF} and SS are degrading, but threshold voltage improves while decreasing the oxide thickness has an inverse effect. This is because on increasing the buried oxide thickness, OFF current increases that means leakage also increases which further degrades SS.

In Fig. 4a–c, variation of output characteristics curve with buried oxide thickness has been analyzed for gate voltages 0.6 V, 0.7 V and 0.8 V, respectively. On increasing the V_{DS} , the horizontal electric field increases in the device which enhance the drain current. But after certain value of V_{DS} , drain current saturates due to channel depletion hence current becomes independent of V_{DS} .

The analysis of device structure has also been done using the work function engineering technique. Figure 5 shows the drain current variation with change in work function of gate G2 from 4.3–4.8 eV, keeping the work function of G1 constant at 4.9 eV. It is observed that there is improvement in the SS when the work function of the dual material gate is varied. This is because an increment in work function improves the controllability over the gate, which leads to a decrease in OFF current. Hence, I_{ON}/I_{OFF} ratio also improves to a great level. However, the increase in work function also increases the value of threshold voltage, which degrades the switching speed performance of a device. This is because barrier lowering effect reduced with increase in work function. Hence, proper value of work function as $\phi_1 = 4.9$ eV and $\phi_2 = 4.68$ eV is taken for simulation purpose.

Table 2 shows the effect of work function variation of gate G2 keeping the work-function of gate G1 = 4.9 eV on various device parameters like V_{TH} , I_{ON} , I_{OFF} and SS. Table 3 shows the performance parameter of various TFT based devices proposed earlier. From the data of Table 2, it is clear that proposed IGZO JLTFT device shows better results in terms of SS and I_{ON}/I_{OFF} ratio.

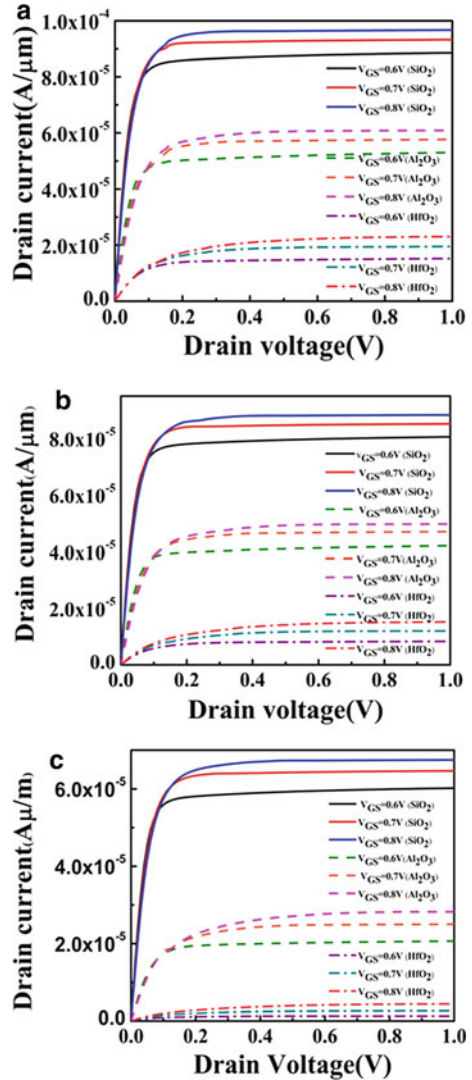
Fig. 3 a–c Shows I_D versus V_{GS} curve for different oxides as gate and buried oxide material for $T_{BOX} = 10$ nm, 8 nm and 5 nm, respectively



2.3 Conclusion

This paper proposes the performance optimization of Junctionless IGZO TFT using SOI technology. The simulation of the 2-D device is done using the SILVACO TCAD ATLAS 2-D simulator. Its performance parameters are also compared with other types of TFT devices proposed earlier in terms of SS and I_{ON}/I_{OFF} ratio. The simulation result of IGZO TFT revealed that the proposed device shows better results

Fig. 4 a–c I_D versus V_{DS} variation with oxide materials and thickness of buried oxide with 10 nm, 8 nm and 5 nm respectively



when vertical gate stacking has been used with high-k dielectric material such as HfO₂. It has been used as gate dielectric and buried oxide material. Proposed device have high I_{ON} / I_{OFF} ratio of 2.14×10^7 and SS of 72.67 mV/dec at lower gate and drain voltages. SS swing improved by 21.9% as compared to conventional device. Workfunction variation and use of high-k dielectric material also help to improve the device's performance; So that it can be further used for low power applications.

Fig. 5 I_D versus V_{GS} curve with varying workfunction of G_2 from 4.3–4.8 eV keeping workfunction of G_1 constant

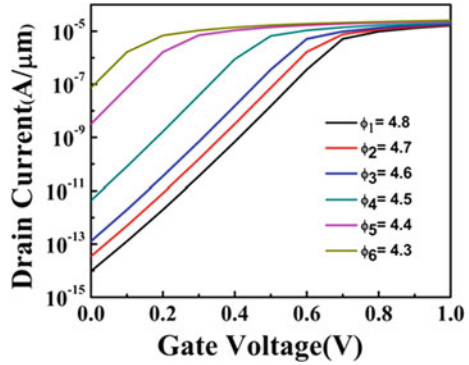


Table 2 Effect of workfunction variation on various parameters

ϕ_2 (eV)	I_{ON} (A/ μm)	I_{OFF} (A/ μm)	I_{ON}/I_{OFF}	SS (mV/dec)	V_{TH}
4.85	1.60×10^{-5}	5.79×10^{-15}	2.76×10^9	73.02	0.56
4.80	1.75×10^{-5}	5.48×10^{-14}	3.19×10^8	72.94	0.51
4.75	1.81×10^{-5}	5.47×10^{-14}	3.30×10^8	72.94	0.46
4.68	1.92×10^{-5}	8.97×10^{-13}	2.14×10^7	72.67	0.38
4.65	1.97×10^{-5}	1.86×10^{-12}	1.05×10^7	72.62	0.36

Table 3 Comparison of performance parameters for various devices

Device	I_{ON} (A/ μm)	I_{OFF} (A/ μm)	I_{ON}/I_{OFF}	SS (mV/dec)
SOI MOSFET [22]	8.56×10^{-4}	1.23×10^{-9}	6.95×10^5	112.69
ZnO-based TFT [23]	2.78×10^{-4}	8.06×10^{-13}	3.23×10^8	131
Silicon JLTFET (20 nm) [20]	2.49×10^{-4}	1.41×10^{-11}	1.75×10^7	106.58
IGZOTFT (20 nm) [20]	3.96×10^{-5}	9.97×10^{-12}	3.97×10^6	93.18
Proposed device (20 nm)	1.92×10^{-5}	8.97×10^{-13}	2.14×10^7	72.67

References

1. Bhushan, S., Kumar, A., Gola, D., Tiwari, P.K.: An analytical subthreshold current model of short-channel symmetrical double gate-all-around (DGAA) field-effect-transistors. In: Devices for Integrated Circuit (DevIC), pp. 211–215 (2017)
2. Yu, B., Yuan, Y., Song, J., Taur, Y.: A two-dimensional analytical solution for Short-Channel effects in nanowire MOSFETs. IEEE Trans. Electron Devices **56**, 2357–2362 (2009)
3. Banerjee, P., Saha, P., Dash, D. K., Sarkar, S. K.: Surface potential based analytical modeling of graded channel strained high-k gate stack dual-material double gate MOSFET. In: Devices for Integrated Circuit (DevIC) IEEE, pp. 240–244 (2019)
4. Long, W., Ou, H., Kuo, J., Chin, K.: Dual-material gate (DMG) field effect transistor. IEEE Trans. Electron Devices **46**, 865–870 (1999)
5. Migita, S., Watanabe, Y., Ota, H., Ito, H., Kamimuta, Y., Nabatame, T., Toriumi, A.: Design and demonstration of very high-k ($k \sim 50$) HfO₂ for ultra-scaled Si CMOS. In: IEEE Symposium

- on VLSI Technology, pp. 152–153 (2008)
6. Hsia, J.K., Shih, C.H., Kang, T.S., Chien, N.D., Van Kien, N.: Fringing field and short channel effects in thin-body SOI MOSFETs with shallow source/drain. In: IEEE International Conference on Ultimate Integration on Silicon (ULIS), pp. 129–132 (2013)
 7. Leray, J.L., Paillet, P., Autran, J.L.: An overview of buried oxides on silicon: new processes and radiation effects. *Journal de Physique* **III**(6), 1625–1646 (1996)
 8. Colinge, J.P.: Junctionless transistors. In: IEEE International Meeting for Future of Electron Devices, Kansai, pp. 1–2 (2012)
 9. Kumar, A., Swami, Y., Rai, S.: Modeling of surface potential and fringe capacitance of selective buried oxide junctionless transistor. *SILICON* **13**, 389–397 (2021)
 10. Singh, S., Raman, A., Kumar, N., Ranjan, R., Shekhar, D., Anand, S.: Linearity analysis of gate engineered Dopingless and Junctionless silicon nanowire FET. In: IEEE International Conference on Signal Processing and Integrated Networks (SPIN), pp. 215–219 (2019)
 11. Korolev, M.A., Klyuchnikov, A.S., Efimov, D.I.: Junctionless MOS-transistor with a low subthreshold current. *Russ. Microelectron.* **48**, 457–461 (2019)
 12. Lee, C.W., Afzalian, A., Akhavan, N.D., Yan, R., Ferain, I., Colinge, J.P.: Junctionless multigate field-effect transistor. *Appl. Phys. Lett.* **94**, 053511 (2009)
 13. Singh, A.K., Kharache, V.V., Chakrabarti, P.: Performance optimization of ZnO based thin film transistor for future generation display technology. In: IEEE India Council International Conference (INDICON), pp. 1–5 (2017)
 14. Hosono, H.: How we made the IGZO transistor. *Nat. Electron.* **1**, 428–428 (2018)
 15. Shim, G.W., Hong, W., Cha, J.H., Park, J.H., Lee, K.J., Choi, S.Y.: TFT channel materials for display applications: from amorphous silicon to transition metal dichalcogenides. *Adv. Mater.* **32**, 1907166 (2020)
 16. Uhm, H., Lee, S., Kim, W., Park, J.: A two-mask process for fabrication of bottom-gate IGZO-based TFTs. *IEEE Electron Device Lett.* **33**, 543–545 (2012)
 17. Park, J., Maeng, W., Kim, H., Park, J.: Review of recent developments in amorphous oxide semiconductor thin-film transistor Devices. *Thin Solid Films* **520**, 1679–1693 (2012)
 18. Dargar, S., Srivastava, V.: Design and analysis of IGZO thin film transistor for AMOLED pixel circuit using double-gate triactive layer channel. *Heliyon* **5**, 01452 (2019)
 19. Zhang, L., Wei, J., Zhou, K., Wan, C., Sun, H.: Highly transparent IGZO-TFTs uses IGZO source and drain electrodes with a composite insulation layer structure. *Optik* **204**, 163654 (2020)
 20. Singh, R.P., Khosla, M., Saini, I., Kumar, N.: Design and analysis of IGZO based junctionless thin film transistor using SOI technology. *SILICON* **13**, 2309–2318 (2020)
 21. Mathew, J., Nesamani, I.F.: Stack gate technique for minimizing leakage current in multigate MOSFETs. In: IEEE International Conference on Circuit, Power and Computing Technologies (ICCPCT), pp. 1–5 (2016)
 22. Ehteshamuddin, M., Loan, S., Haris, M., Rafat, M.: Enhanced subthreshold characteristic in SOI MOSFET with non-uniform drain doping profile. In: International Conference on Microelectronic Devices, Circuits and Systems (ICMDCS), pp. 1–4 (2017)
 23. Kandpal, K., Gupta, N., Singh, J., Shekhar, C.: On the threshold voltage and performance of ZnO-based thin-film transistors with a ZrO₂ gate dielectric. *J. Electron. Mater.* **49**, 3156–3164 (2020)

Author Index

A

Adam, Adil Altom Mohammed, [267](#)
Adebayo, A. S., [115](#)
Ajide, O. O., [115](#)
Aogo, O. A., [115](#)
Asok, S. P., [257](#)

B

Bakruthen, M., [17](#), [97](#), [235](#)
Banerjee, Anirudh, [27](#)
Banubakode, Aalapi, [131](#)
Baoji, Ma, [145](#)

C

Chacana, Sebastián, [1](#)
Chowdary, Boppana Bhargav, [267](#)

D

Dada, T. O., [115](#)
Dohare, Rajeev Kumar, [155](#)

F

Fleming, Wagner, [1](#)

G

Gayathri, P., [77](#)
Ghuge, Shrinath, [131](#)
Gupta, Amit, [197](#)

H

Harichandran, R., [47](#)
Harish, V., [257](#)
Herrera, Diego, [1](#)
Honghong, Gao, [145](#)

I

Idusuyi, N., [115](#)

J

Jayaprakash, S., [17](#)
Jinxiang, Huo, [145](#)

K

Krishna, K. Vamsi, [77](#)
Krylova, E. Y., [185](#)
Kumar, Aditya, [197](#)
Kumar, L. Santhosh, [17](#)
Kumar, N., [115](#)
Kumar, S. Dhileep, [59](#)

L

Lionel Beneston, S., [257](#)

M

Mainuddin, [155](#)
Manjunath, N., [277](#)
Maqsood, Nabeel, [87](#)
Mishra, Guru Prasad, [107](#)
Musa, F. A., [115](#)

© The Editor(s) (if applicable) and The Author(s), under exclusive license to Springer Nature Singapore Pte Ltd. 2023

V. Bindhu et al. (eds.), *Proceedings of Fifth International Conference on Inventive Material Science Applications*, Advances in Sustainability Science and Technology, <https://doi.org/10.1007/978-981-19-4304-1>

N

Naugarhiya, Alok, [285](#)
Nemad, Atharva, [131](#)

O

Olcay, Ruben, [33](#)

P

Padmavathy, M., [235](#)
Potharaju, Abhishek, [175](#)
Prakash, P., [17](#)
Prasanth, S., [97](#)
Puri, Gaurav, [131](#)

Q

Quiero, Aldo, [33](#)

R

Raja, J. Salamon, [97](#)
Rajasekaran, B., [277](#)
Rajesh, M., [97](#)
Rana, Aadarsh, [197](#)
Ravindran, M., [47](#)
Ravula, Meghana Rao, [175](#)
Rimašauskas, Marius, [87](#)
Riyan, Shaik, [267](#)

S

Sahoo, Satyajeet, [77](#), [211](#), [219](#), [267](#)
Salazar, Iván, [1](#)

Sasank, Yellapragada V. S., [211](#)
Sathya, P., [47](#)
Sathya Swaroop, Chennam J. V. K., [211](#)
Seethraman, M., [17](#)
Selvakumar, S., [97](#)
Shaik, Deneyaz, [219](#)
Singhal, Gaurav, [155](#)
Singha, Satadru, [163](#)
Sriram, Ghanta, [211](#)
Stano, Pasquale, [245](#)

T

Taj, M., [77](#), [211](#), [267](#)
Teware, Devyani, [131](#)
Tiwari, S. K., [163](#)
Toro, Norman, [1](#), [33](#)

V

Vathsalya, Kasireddy, [59](#)
Venkatesh, Chitikina Neeraj, [107](#)
Vidyadhar, R. Phani, [59](#), [175](#)
Vineetha, J., [77](#)

W

Waghmare, Gopaldas, [131](#)

Y

Yadav, Aditya, [197](#)
Yogi, Shraddha, [285](#)
Yuanpeng, Zhu, [145](#)